Modeling molecular transport in the brain : a coarse-grid multiscale model capturing the microscale dynamics of embedded microvascular networks

David Pastor Alonso

Université de Toulouse

THÈSE

En vue de l'obtention du

DOCTORAT DE L'UNIVERSITÉ DE TOULOUSE

Délivré par :

Institut National Polytechnique de Toulouse (Toulouse INP)

Discipline ou spécialité :

Dynamique des fluides

Présentée et soutenue par :

M. DAVID PASTOR ALONSO

le mardi 14 novembre 2023

Titre :

Modélisation du transport moléculaire dans le cerveau : un modèle multi-échelle capturant la dynamique microscopique du réseau vasculaire

---

École doctorale :

Mécanique, Énergétique, Génie civil, Procédés (MEGeP)

Unité de recherche :

Institut de Mécanique des Fluides de Toulouse (IMFT)

Directeurs de Thèse :

MME SYLVIE LORTHOIS

M. YOHAN DAVIT

Rapporteurs :

M. JOSE-MARIA FULLANA, UNIVERSITE SORBONNE

M. PAOLO ZUNINO, POLITECNICO DE MILAN

Membres du jury :

M. FRANCK BOYER, UNIVERSITE PAUL SABATIER, Président

MME CATHERINE HALL, UNIVERSITY OF SUSSEX, Membre

MME FRANCA SCHMID, ARTORG, Membre

MME SYLVIE LORTHOIS, TOULOUSE INP, Membre

M. MICHEL QUINTARD, TOULOUSE INP, Invité

M. YOHAN DAVIT, TOULOUSE INP, Membre

Table of Contents

Acknowledgements

My most profound thank you to my parents for always being there for every difficulty, teaching me resilience in the face of adversity, and always motivating me to always aim higher.

Thank you Valeriia for your steady support through this long process. Your sacrifices and presence, even during your own difficulties, have been a source of immense strength.

Sylvie, thank you for everything – your dedication, knowledge, fairness, and kindness. I've learned countless lessons from you, both scientific and personal. It's been a real pleasure working with you, and I'm truly proud and happy for the experience.

Abstract

Through nutrient delivery, waste clearance, and adaptation to changes of the metabolic demand, the brain microcirculation supports the wide range of tasks performed by neural cells. For that purpose, vascular networks ensure proximity to all cells in the brain through an efficient spatial organization that encompasses a wide range of scales. Such networks include capillaries, i.e., the smallest vessels (1-10 μm in diameter), which are fed and drained by the arterial and venular trees (10-100 μm and over in diameter), respectively. Due to its critical role in brain homeostasis, the cerebral microvascular system is intricately linked to various pathologies, spanning from stroke to neurodegenerative diseases. In some cases, microvascular dysfunction is even the primary cause.

In recent decades, a multitude of advanced imaging techniques have surfaced that enable accurate depictions of microvascular anatomy in the brain. These techniques also provide valuable data on blood flow dynamics and molecular transport. Theoretical models on the transport of molecules have been developed in parallel to interpret and expand the insights provided by these imaging methods. Such models have shown that fine scale features taking place at the cellular scale, notably large perivascular concentration gradients, significantly impact molecular transport. However, capturing these features using conventional numerical tools proves prohibitively expensive. As a result, their applicability is generally constrained to a mere handful of vessels, which is not enough to examine the non-local properties of microvascular networks that drive molecular transport. Numerous alternative approaches have emerged, including in other fields (e.g. geosciences) to address analogous challenges associated with the underlying mathematical structure of transport processes in embedded networks.

In this thesis, we first review these existing approaches to adapt the most relevant features to our specific problem. In doing so, we develop a multiscale model that optimally tackles the spatial constraints of the molecular transport problem in the brain microcirculation. This results in an operator splitting approach firmly rooted in a sound mathematical foundation based on Green's third identity. This aids in the precise assessment of the underlying assumptions in 2D configurations (Chapter 3). Beyond this theoretical analysis of the modeling assumptions, we perform thorough testing through numerical experimentation, which enables us to evaluate the magnitude of errors introduced by the multiscale model, therefore providing a precise estimation of the model's accuracy. Subsequently, we extend the multiscale model to 3D configurations enabling the simulation of large microvascular networks, with more than 18000 vessels (Chapter 4).

The multiscale model developed in this thesis allows to increase substantially the scope of molecular transport simulations in the brain microcirculation, simplifying the problem significantly while preserving a non-linear description of metabolic consumption in neural cells.

This, in turn, will enable future investigations of the non-local properties of the microvasculature that were not accessible previously. In particular, coupled to an intravascular transport model that better represents the non-linear binding of oxygen to hemoglobin, it will provide a new research tool to further investigate the emergence of hypoxia in Alzheimer's disease. It may also provide a basis to account for temporal dynamics, then offering a window into neurovascular coupling. Overall, the multiscale model addresses the bottleneck of spatial constraints posed by the microvasculature, thus bridging the gap between the description of transport at the microscale and at the scale of microvascular networks.

Résumé

Grâce à l'apport de nutriments, à l'élimination des déchets et à l'adaptation aux changements de la demande métabolique, la microcirculation cérébrale soutient l'ensemble des tâches accomplies par les cellules neuronales. À cette fin, l'organisation spatiale du réseau vasculaire, s'étendant sur différentes échelles, assure la proximité de chaque cellule avec un vaisseau capillaire. Ces vaisseaux, avec des diamètres de 1 à 10 µm, sont alimentés et drainés par les arbres artériolaires et veineux (10-100 µm et plus en diamètre). En raison de son rôle crucial dans l'homéostasie cérébrale, le système microvasculaire cérébral est intimement lié à diverses pathologies, de l'accident vasculaire cérébral aux maladies neurodégénératives, parfois en tant que cause principale.

Au cours des dernières années, de nombreuses techniques d'imagerie avancée ont émergé qui permettent de décrire avec précision l'anatomie microvasculaire cérébrale. Ces techniques fournissent également des données précieuses sur la dynamique du flux sanguin et le transport moléculaire. Des modèles théoriques du transport moléculaire ont été développés en parallèle afin d'interpréter et d'élargir les connaissances fournies par ces méthodes d'imagerie. Ces modèles ont montré que les forts gradients de concentration périvasculaire, qui s'établissent à l'échelle cellulaire, ont un impact significatif sur le transport moléculaire. La prise en compte de ces gradients à l'aide d'outils numériques conventionnels représente un coût inabordable. Par conséquent, leur applicabilité est généralement limitée à quelques vaisseaux, ce qui est insuffisant pour examiner les propriétés non locales des réseaux microvasculaires qui déterminent le transport moléculaire. De nombreuses approches alternatives ont été développées, y compris dans d'autres domaines (par exemple les géosciences), pour relever des défis analogues associés à la structure mathématique sous-jacente des processus de transport autour de réseaux multi-échelles.

Dans cette thèse, nous faisons d'abord le point sur ces approches existantes afin d'en adapter les ingrédients les plus pertinents à notre problème spécifique. Ainsi, nous développons un modèle multi-échelle qui répond de manière optimale aux contraintes spatiales du problème de transport moléculaire dans la microcirculation cérébrale. Pour cela, nous mettons en œuvre une approche de séparation des opérateurs dont la formulation est basée sur la troisième identité de Green. Cette base mathématique solide facilite l'évaluation précise des hypothèses sous-jacentes dans des configurations 2D (chapitre 3). Au-delà de cette analyse théorique, nous réalisons des tests numériques exhaustifs pour estimer l'erreur introduite par le modèle multi-échelle, fournissant une évaluation rigoureuse de sa précision. Par la suite, nous étendons le modèle multi-échelle à des configurations 3D permettant la simulation de grands réseaux microvasculaires, avec plus de 18000 vaisseaux (chapitre 4).

Le modèle multi-échelle développé dans cette thèse améliore considérablement la capacité de simulation de transport moléculaire dans la microcirculation cérébrale, en simplifiant le

problème tout en préservant une description non linéaire de la consommation métabolique dans les cellules neuronales. Ceci ouvre la voie à l'étude des propriétés non locales de la microvasculature, auparavant inaccessibles. En particulier, couplé à un modèle de transport intravasculaire plus fidèle à la liaison non linéaire de l'oxygène à l'hémoglobine, il fournira un nouvel outil de recherche pour étudier l'émergence de régions hypoxiques dans la maladie d'Alzheimer. Il pourra également servir de base pour décrire la dynamique temporelle du transport, en lien avec le couplage neurovasculaire. Ainsi, ce modèle multi-échelle surmonte les contraintes spatiales de la microvasculature, en comblant le fossé entre la description du transport à l'échelle microscopique et celle des réseaux microvasculaires.

Acknowledgements

My most profound thank you to my parents for always being there for every difficulty, teaching me resilience in the face of adversity, and always motivating me to always aim higher.

Thank you Valeriia for your steady support through this long process. Your sacrifices and presence, even during your own difficulties, have been a source of immense strength.

Sylvie, thank you for everything – your dedication, knowledge, fairness, and kindness. I've learned countless lessons from you, both scientific and personal. It's been a real pleasure working with you, and I'm truly proud and happy for the experience.

Nomenclature

Acronyms

AD	Alzheimer's disease
ASL	Arterial Spin Labeling
ATP	Adenosine Tri-Phosphate
BBB	Blood Brain Barrier
BIE	Boundary Integral Equation
BOLD	Blood Oxygen Level Dependent
BVP	Boundary Value Problem
CBF	Cerebral Blood Flow
CBV	Cerebral Blood Volume
CNS	Central Nervous System
DWI	Diffusion Weighted Imaging
ECS	Extra Cellular Space
EV	Extra Vascular
fMRI	functional Magnetic Resonance Imaging
IV	Intra Vascular
MRI	Magnetic Resonance Imaging
NVC	Neuro Vascular Coupling
NVM	Neuro Metabolic Coupling
OCT	Optical Coherence Tomography
PET	Positron Emission Tomography
RBC	Red Blood Cell
REV	Representative Elementary Volume
ROM	Reduced Order Model
SPECT	Single-Photon Emission Computed Tomography

Domains

Λ	Centerlines of the vessel network
λ	Vessel cross-section
$\mathscr{F}$	Set containing all the FV cells
$\mathscr{N}_k$	Set containing the direct neighbours of V_k
$\mathscr{P}$	Total number of non-null entries within a matrix
$\mathscr{S}$	Set containing all the sources
Ω	3D domain of computation
Ω_β	Blood
Ω_σ	Parenchyma
$\partial\lambda$	Circumference of a vessel cross-section
$\partial\Omega$	Boundaries of the domain of computation
$\partial\Omega_\beta$	Vessel wall
$\partial\Omega_\sigma$	Boundaries of the parenchyma (includes the vessel wall)
$\widehat{V}$	Neighbourhood made up of individual discrete sub-spaces (V_k)
$\widehat{V}^d$	Extended neighbourhood used for reconstruction/interpolation
V_k	Subspace arising from the 3D discretization of the domain of computation

Variables

δ_Λ	Lineic delta distribution (m^{-2})
δ_{ij}	Kronecker delta
ϵ	Vessel wall thickness (m)
γ	Q^1 element in three dimensions
$\langle C_v \rangle$	Average cross-sectional intravascular concentration (mol m^{-3})
$\mathbf{b}_{\partial\Omega_\beta}$	Vector containing the relevant values to satisfy the boundary conditions on the inlets and outlets of the network
$\mathbf{b}_{\partial\Omega}$	Vector containing the relevant values to satisfy the boundary conditions on the limits of the domain of computation
$\mathbf{S}_{metab}$	Vector containing the values of the metabolic reaction within each FV cell
$\mathbf{U}$	Blood velocity (m s^{-1})
$\mathscr{G}$	Vessel conductance (m^3 s^{-1} mmHg^{-1})
$\mathscr{I}_\phi$	Interpolation function (mol m^{-3})
$\mathscr{r}$	Rapid term (mol m^{-3})
$\mathscr{r}_i^c$	Corrected rapid term (mol m^{-3})
$\mathscr{r}_k$	Locally continuous rapid term over the sub-space V_k (mol m^{-3})
$\mathscr{R}_{km}$	Flux of the rapid term over the interface between V_k and V_m (mol s−1)
$\mathscr{s}$	Slow term (mol m^{-3})

$\mathfrak{s}_j$	Average value of the slow term over the vessel wall of source j
$\mathfrak{s}_k$	Locally continuous slow term over the sub-space V_k (mol m^{-3})
$\mathcal{S}_{km}$	Flux of the slow term over the interface between V_k and V_m (mol s−1)
μ^{app}	Apparent viscosity (mmHg s)
$\overline{\phi}$	Average extravascular concentration over a vessel cross-section (mol m^{-3})
ϕ	Extrascular concentration (mol m^{-3})
ϕ_d	Value of the concentration set on a Dirichlet boundary (mol m^{-3})
ϕ_{PA}	Value of the concentration field within a penetrating arteriole (mol m^{-3})
ε_ϕ^g	Global error on the concentration field
ε_ϕ^j	Relative local error on concentration for the FV cell k
$\varepsilon_{\widehat{V}}$	Error introduced by the FV discretization when considering a neighbourhood
ε_q^g	Global error of the vessel-tissue exchanges
ε_q^j	Relative local error on the vessel-tissue exchanges for the source j
ε_{FV}	Error introduced by the FV discretization
$\widetilde{\mathfrak{r}}$	Average value of the rapid term on the sub-space V_k (mol m^{-3})
$\widetilde{\mathfrak{s}}$	Discrete value of the slow term of the sub-space V_k (mol m^{-3})
C_v	Intravascular concentration (mol m^{-3})
d	Vessel diameter (m)
D_p	Effective diffusion coefficient in the parenchyma (m^2 s^{-1})
D_v	Effective diffusion coefficient in blood (m^2 s^{-1})
D_{eff}	Effective, upscaled diffusion coefficient in blood (m^2 s^{-1})
G	Fundamental solution/Green's function
G_j	Single layer potential for the source j(mol m^{-3})
G_j^{line}	Estimation of the single layer potential using the line approximation (mol m^{-3})
G_j^{point}	Estimation of the single layer potential using the point approximation (mol m^{-3})
G_{ij}	Average value of the single layer potential of cylinder i over cylinder j
h_Λ	Discretization size of the 1D mesh (m)
h_λ	Sub-discretization size used for the numerical integration of the self-influence coefficients (m)
h_Ω	Discretization size of the 3D mesh (m)
H_j	Double layer potential for the source j(mol m^{-3})
H_{ij}	Average value of the single layer potential of cylinder i over cylinder j
$J_{k,m}$	Integral of the rapid that satisfies mass conservation over the interface between V_k and V_m
K	Value of the concentration for which the reaction speed is half its maximum (mol m^{-3})

K_D	Hydraulic conductivity tensor (m $mmHg^{-1}$ s^{-1})
K_m	Vessel wall permeability (m s^{-1})
K_{eff}	Effective permeability (s^{-1})
l	Vessel length (m)
M	Maximum reaction rate (mol m^{-3} s^{-1})
N	Value of the molecular flux set on Neumann boundary ()
P	Pressure (mmHg)
P	Source potential (mol m^{-3})
PO_2	Partial pressure of oxygen (mmHg)
Q	Blood flow (m^3 s^{-1})
q	Vessel-tissue exchanges (mol m^{-1} s^{-1})
q_w	Fluid flux provided by a well (m s^{-1})
R	Radius (m)
R_{cyl}	Radius of the capillary free cylinder around a penetrating arteriole (m)
U_{eff}	Effective velocity coefficient in blood (m s^{-1})
F	Total number of FV cells
S	Total number of sources

Chapter 1

Introduction

The microcirculation is comprised of the small vessels that irrigate the organs [1]. The brain possesses minimal energy reserves, making the neurons and glia reliant on the microvasculature to supply nutrients [1–3]. This continuous dependence on the blood flow of nutrients likely plays a significant role in shaping the structural arrangement of the microvasculature [4]. These requirements have led to the development of a captivating network of vessels spanning various scales, ensuring nourishment to every cell in the irrigated tissue. Nevertheless, due to these reasons, the well-being of the brain is closely tied to vascular health, an aspect that has been somewhat overshadowed by neuronal research in the investigation of various forms of dementia like Alzheimer's disease (AD) [5].

Beyond its primary role in delivering nutrients, the brain microcirculation performs a myriad of essential functions. It dynamically modulates cerebral blood flow (CBF) and cerebral blood volume (CBV), plays a role in temperature regulation, maintains ionic balance, plays a role in the maintenance of the blood brain barrier (BBB) [2], among other crucial tasks. Thus, the microcirculation emerges as an intricate and remarkably complex system that orchestrates a diverse array of functions essential for a healthy brain [6]. Given its importance, the microcirculatory system exhibits redundancies to ensure reliability and robustness. In short, the many tasks fulfilled by the cerebral microcirculation underscores its crucial contribution to sustaining the proper functioning of the central nervous system (CNS).

Additionally, metabolic activity in the brain varies widely in both space and time, necessitating the microvasculature to dynamically adjust to surges in oxygen demand in real-time. This phenomenon is referred to as neurovascular coupling (NVC). Despite its widespread application in various imaging methods, the precise linkage between blood perfusion and neural activity remains incomplete [2; 7]. Nevertheless, strong assumptions about the quantitative relationships between blood flow, oxygen exchanges, and metabolic activity are often used in many imaging techniques [8] that constitute a cornerstone of cognitive research [9]. The ongoing exploration of neurovascular coupling demands an improved understanding of the physiological mechanisms that govern the intricate interplay among blood flow, metabolic activity, and neuronal function [10; 11]. This presents an opportunity for theoretical and numerical models to bridge the gap between observed physiological responses and the present

1. A specific definition of what is considered "small vessels" is provided in Section 1.1 where we delve into the detailed anatomy of the vasculature

2. the barrier between blood and parenchyma created by the endothelial lining of the vessels and other structures discussed in Section 1.2.3

understanding of the underlying mechanisms. Particularly when dealing with the dynamics of molecular transport.

1.1 A multiscale overview of the microvasculature

While the terms "microcirculation" and "microvasculature" are commonly used interchangeably, we acknowledge an important distinction : the microvasculature specifically refers to blood vessels, while the microcirculation comprises fluid mechanical aspects, including blood flow and molecular exchanges with the surrounding tissue.

At the most basic level, we can categorize the small vessels into arterioles, venules, and capillaries. Arterioles and venules have a similar hierarchical quasi-fractal structure [12]. Much like the branches of a tree, the largest vessels that stem from the heart progressively branch into smaller vessels (figure 1.1C and 1.1D), until the capillaries where they form a space-filling mesh. This mesh, often called the capillary bed connects the terminal branches of the arterio-venular trees (figure 1.1D). In a healthy brain, there are no anastomoses that connect the arterial to the venular trees, thus ensuring that the oxygenated blood needed to feed the tissue flows through the capillaries.

Arterioles serve as the primary sites for blood flow regulation, as their thicker walls incorporate smooth muscle cells that govern their diameter, thus influencing the hemodynamic resistance. Meanwhile, the majority of cerebral blood volume remains within the capillaries. In contrast, venules assume a more passive role, primarily serving as conduits for deoxygenated blood drainage from the capillary bed [4; 13].

The capillary bed, consisting of the smallest and most abundant blood vessels, is responsible for ensuring proper supply of oxygen, nutrients, and other molecules to every cell in the brain tissue (neurons and glial cells). This remarkable efficiency is facilitated by its thin walls and expansive surface area. Arterioles also contribute to the molecular exchanges [4; 13] as they carry the oxygenated blood from the heart. However, the extent of their contribution remains a subject of debate, primarily due to the lack of accurate models capable of quantifying these molecular exchanges [14].

Various classifications methods exist to differentiate between arterioles or venules and capillaries. It is generally accepted that the capillaries comprise the vessels with diameter of $d \approx 10\mu m$ and below, although more sophisticated characterization methods exist based on the vessel resistance for instance [16]. We do not delve into the specificities of these classification methods in this thesis, given the early nature of our exploration into the theoretical modeling of molecular transport. According to [6], the arteriolar and capillary side of the cortical angioarchitecture is structured as follows :

— First tier, the pial arteries that cover the surface of the cortex, as shown in Fig. 1.1A. They form a 2 dimensional pial network that connects the 3 large arteries that supply the brain (the anterior, middle and posterior cerebral arteries), with the penetrating arteries.

— Second tier, the penetrating intracortical arterioles that connect the network of pial arteries with the sub-surface circulation, as illustrated in 1.1B. These arterioles have been identified as the bottlenecks of the cerebral microcirculation [17], as the entire microcirculatory system is endowed with redundancies to safeguard neuronal nourishment against occlusions or microstrokes, except for the penetrating arterioles and venules.

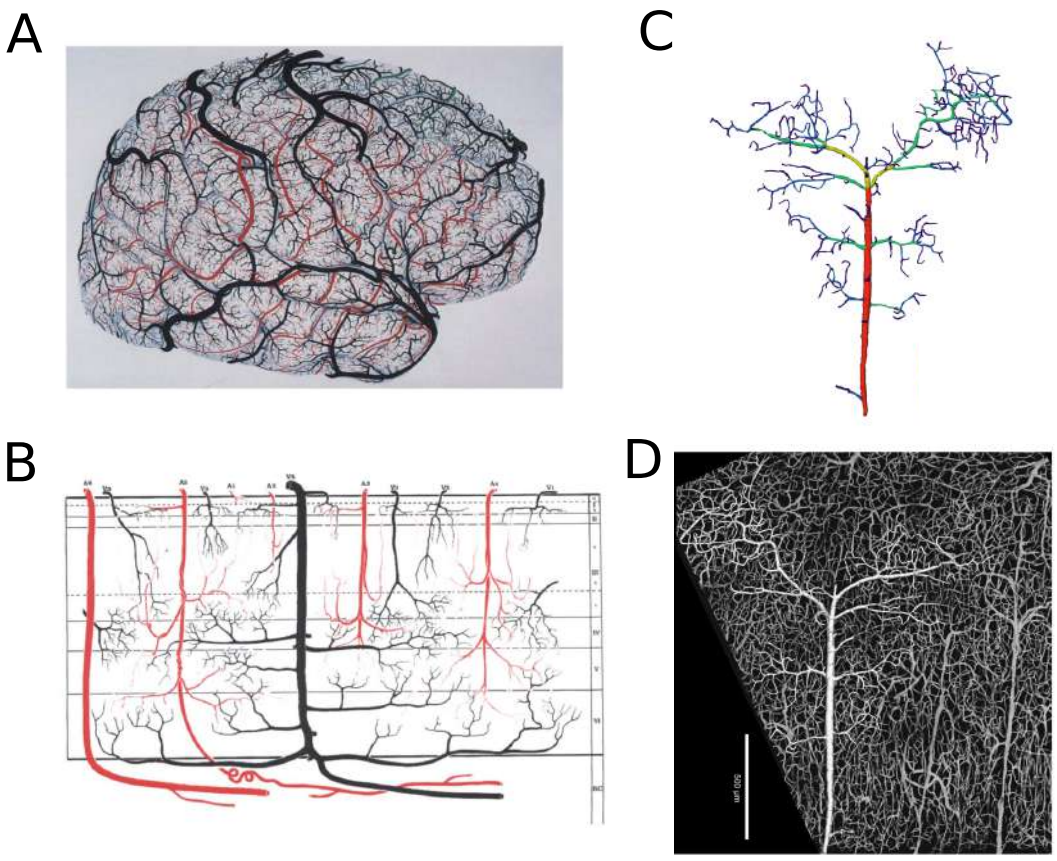

FIGURE 1.1 – **Terminology and notations for parenchyma and vessel spaces.** Panel A : The pial arteries (red) and veins (black) each forming a 2D network covering the surface of the cortex [15]. Panel B : Representation of the penetrating arterioles and veins that stem from the pial network [6]. Panel C : Computer representation of an venular tree in the human cortex that includes 4 branching orders [16]. Panel D : This same venular tree with its interconnected capillary bed and upstreamed arteriole. Image obtained through confocal laser microscopy [16].

— Third tier, the sub-surface microcirculation, as shown in grey in Fig.1.1B. As penetrating arterioles descend into the cortex, they gradually ramify into pre-capillary arterioles that, in turn, feed into the subsurface capillary network. This capillary network is fully three-dimensional. All cerebral blood flow must pass through this network in order to exit the brain, as there are no direct arteriole to venule anastomoses in the healthy brain. The capillary bed offers the largest surface area for the molecular exchanges to take place [18].

The venular network, responsible for draining the blood that reaches the subsurface microcirculation, mirrors the structural traits of the arterial network but with inverted direction of blood flow. Here, the sub-surface venules feed the penetrating venules, culminating in the two-dimensional surface network on the brain's cortical surface (see Fig. 1.1B). In essence, the emerging network exhibits the characteristics of a redundant two-dimensional cortical network (the pial arteries and veins) linked to a three-dimensional, space-filling capillary mesh through the penetrating arterioles and venules. This network serves as a resilient source of nourishment for the neurons and glia in the cortex, with the exception of the penetrating arterioles and venules, where circulation is more delicate and prone to ischemia due to occlusions [6]. In summary, the microcirculation forms an extensive network of approximately twelve billion vessels [19] which can be classified as arterioles or venules that have a quasi-fractal structure [12], and the capillaries, which collectively form the capillary bed. This space filling

network offers the largest hemodynamic resistance [20] and ensures proper oxygen delivery to every cell in the tissue.

1.2 Beyond the microvasculature : brain compartments involved in molecular transport

We have presented the cortical microcvasculatre as the intricate network of vessels responsible for nourishing the neurons and glia within the cortex. This Section is now dedicated to three components of interests in the brain cortex that have different permeabilities to oxygen : the parenchyma, the microvasculature and the BBB.

Let us illustrate the role of these components by qualitatively describing the journey of an oxygen molecule beginning its path from the left ventricle of the heart through the aorta. It traverses successive arterial bifurcations until it reaches the pial arteries, as detailed in Section 1.1. Subsequently, the molecule enters the cortex via the penetrating arterioles, which are oriented perpendicular to the cortex (Fig. 1.1B). At this point, the molecule either remains within the microvasculaure and it continues to flow until drained downstream by a venular tree, or it diffuses into the brain parenchyma through the BBB. Should the molecule successfully cross the BBB, it will either be metabolized within the parenchyma or drained by re-crossing the BBB to reach the bloodstream or via the glymphatic system.

Throughout this journey, we emphasize four essential transport processes : advection-dispersion within the vessels, diffusion across the BBB and diffusion-reaction within the parenchyma. In the subsequent paragraphs, we offer a concise overview of each process without delving into the specific theoretical and numerical modeling frameworks. These frameworks will be the primary focus of the upcoming Chapter.

1.2.1 Parenchyma

The term ”parenchyma” commonly refers to an organ’s functional cells. In the brain, it encompasses neurons responsible for transmitting and processing electrical signals, as well as glial cells that provide essential support to neurons. In this thesis, our focus lies on molecular transport at a scale beyond individual cells. Consequently, we broaden the parenchyma’s definition to encompass the entire extravascular space—comprising the brain tissue not occupied by blood, i.e., 97% of the brain volume [21]. Approximately 80% of this extravascular space is occupied by neurons and glial cells, the extracellular space (ECS, comprising between 5 and 20% of brain volume [22]), and other minor compartments like the perivascular spaces. The cellular structures within the parenchyma are extensively studied for their role in chemical and electrical communication, thought processing, memory storage, and more. The neurons produce the electrical signals responsible for the characteristic communication of the central nervous system. The glial cells, that include astrocytes, microglia, oligodendrocytes and ependymal cells, perform a great multitude of support functions that include structural support, electrical insulation, maintaining homeostasis, controlling blood flow, and many others. The ECS serves as a reservoir of ions and therefore plays an important role for non synaptic cell to cell communication, K^+- and glutamate- buffering during neuronal signaling, and cellular nutrient uptake [23]. In this thesis, however, we shift our attention away from individual extravascular structures that have minimal impact on molecular transport and focus on the overall transport properties of the parenchyma.

Small non-polar molecules diffuse freely through the parenchyma due to their ability to cross the lipid bilayer that encloses the cells, other larger and polar molecules diffuse through the tortuous paths of the ECS. Any movement of molecules at the scale of the cells arises from the random movement of the individual molecules. This implies that large gradients are needed in order to move significant quantities of oxygen to the neurons [24]. Robust nutrient delivery is ensured by the space filling capillary bed of the brain that places a capillary no further than 50 μm away from any point of parenchyma [24–26]. It has even been hypothesized that each neuron has a capillary for nourishment [27]. The development of such a network highlights the important role of the microcirculation to ensure nutrient delivery. Thus, availability of nutrients within the parenchyma is closely linked to capillary health.

1.2.2 Microcirculation

Central to the molecular transport in the human body lies the vasculature due to its capacity to move molecules within blood through a pressure gradient provided by the heart. The blood circulation establishes a direct connection among all the organs in the body, providing a pathway for communication through chemical signalling molecules (e.g., neurotransmitters, hormones) or for transport of nutrients and waste, thus irrigating every organ within our body. This blood circulation guarantees a continuous supply of oxygenated blood to the brain. Specifically, the oxygen molecule binds to the hemoglobin contained within the RBCs and also remains dissolved in the blood plasma, creating concentration gradients that lead to dispersion within the vessels. Although advection is the dominant transport mechanism, it's important to note that significant radial concentration gradients have been observed across a wide range of physiological conditions [14]. Therefore, advection and dispersion are the transport processes present within the vessels of the microcirculation.

Due to locality of the tasks within the brain, the microvasculature has to adapt dynamically to local surges in metabolic activity. The microvessels, notably arterioles and capillaries that are the main sites of exchange of nutrients to the brain parenchyma [4; 13], are in constant communication with the neurons and glia of the brain to provide this dynamic adaptation. This communication is made possible by the BBB, a structure exclusive to the brain that protects the brain parenchyma from toxic molecules and provides a via of communication between neurons, glia and the vasculature.

1.2.3 Blood brain barrier

The BBB is a unique and intricate structure that contributes to the distinct biochemical environment of the brain. Functioning as a highly selective semipermeable membrane, it partitions the circulating blood from what we denominate as brain parenchyma ; it effectively blocks 98% of small molecules and virtually all big molecules [28]. This selectivity is achieved through the closely arranged endothelial cells within brain capillaries, creating a barrier that limits the transit of molecules and ions from the bloodstream into the brain tissue [29].

Furthermore, the BBB, depicted in Figure 2A, consists of several distinct components working in concert to tightly regulate the exchange of substances between the bloodstream and the brain parenchyma. It commences with a layer of endothelial cells enveloping the inner lining of capillaries throughout the body. These endothelial cells are interconnected by tight junctions, which serve as robust barriers, allowing only essential nutrients and molecules to diffuse into the brain parenchyma. Beyond this selective filtering function, endothelial cells also perform a multitude of other roles, including immune response regulation, chemical signaling, and

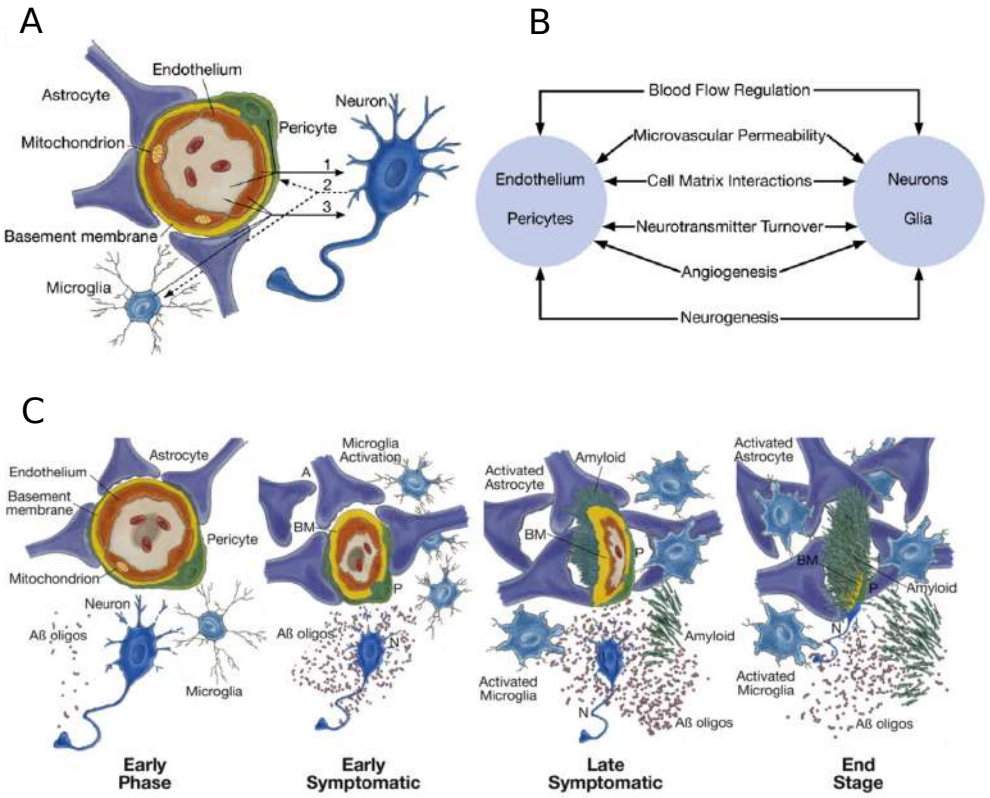

FIGURE 1.2 – **The multicellular structure of the blood-brain-barrier (BBB** and the neurovascular unit (NVC). The core structures comprising the NVU (Panel A) are the glial cells, notably astrocytes and microglia, the neurons, the pericytes and the endothelial cells. The endothelial cells envelope the vessel lumen through tight junctions that neatly seal the blood. Pericytes and astrocytes end-feet extend along the outer vessel wall and perform important tasks of communication allowing the dynamic addaptation of the vessels to metabolic demands. Panel A shows the main structures involved in the NVU, and Panel B shows the tasks managed by the communication between the vascular structures and the neurons and glia. Panel C shows a common pathway of BBB dysfunction caused by the accumulation of toxic waste characteristic of AD.

control of blood vessel tone.

In addition to endothelial cells, pericytes (as shown in Figure 2A) constitute specialized cells within the BBB. They contribute significantly to functions such as regulating blood flow, promoting angiogenesis, and maintaining vessel stability, among other critical roles [30]. Additionally, there exists a region known as the Virchow-Robin space between the endothelium and the astrocyte end-feet. These fluid-filled compartments encircle the vessels and play a crucial role in waste clearance through a mechanism referred to as the glymphatic system, [31]. Astrocytes and glial end-feet are also integral components of the BBB, playing essential roles within the neurovascular unit (NVU), which we will discuss further in the following Section.

Transport across the BBB is a complex process, often requiring active transport mechanisms that consume energy in the form adenosine triphosphate (ATP), particularly for larger molecules like glucose and polar molecules such as sodium (Na^+), chloride (Cl^-) and potassium (K^+). In contrast, smaller non-polar molecules like oxygen (O_2) and carbon dioxide (CO_2) can passively diffuse through the BBB, facilitated by concentration gradients between the bloodstream and brain tissue.

The concentration gradient across the vessel wall is created by the inflow of oxygenated blood

through the arterial circulation and the consumption of oxygen within the brain parenchyma. This gradient drives the diffusion of oxygen and other small molecules across the vessel wall, enabling exchanges between the bloodstream and the surrounding tissue. Importantly, capillaries represent the primary site for oxygen exchange due to their large surface area available for vessel-tissue molecular exchanges [18] and their thin walls, which enhance diffusivity.

1.2.4 The neurovascular unit

The vasculature within the brain maintains a close developmental, structural, and functional relationship with the surrounding parenchyma, collectively forming a crucial functional domain known as the neurovascular unit (NVU) [9; 32]. Given the brain's limited energy reserves, the NVU is a dynamic system where the parenchyma, BBB, and vasculature collaborate in harmony to adapt to varying metabolic demands. This intricate coordination occurs at the smallest functional level of the brain, where these three components communicate through chemical signaling to regulate crucial processes such as blood flow and molecular exchanges (see Figure 1.2A and B).

The phenomenon of adjusting local blood perfusion in response to changes in neuronal activity is known as neurovascular coupling (NVC). Unraveling the mechanisms underlying NVC is a thriving area of research [2; 29; 33; 34]. Together, the NVU and NVC exemplify the intricate interplay between the structural and functional elements of the brain. This collaborative effort ensures the brain's metabolic demands are adequately met, facilitating efficient cognitive processes and overall brain health.

Nevertheless, many aspects of the communication between neurons and blood vessels, as well as the mechanisms governing local hemodynamic changes, remain unknown [9; 32]. For example, the phenomenon of local blood flow increasing to a degree that surpasses metabolic requirements is widely acknowledged, yet the reasons for this overcompensation are not fully understood [35]. Theoretical and numerical modeling approaches that delve into the intricate interplay between blood flow and metabolic activity hold significant potential in shedding light on these aspects of the NVU.

1.3 Exploring clinical and research questions linked to the brain microcirculation

Thus far, we have presented the structural intricacies of the brain microcirculation and underscored its significance in relation to brain health. Also, we have highlighted the main transport processes relevant to the brain microcirculation. In this Section, we explore key areas where advances in numerical and theoretical models of transport within the microcirculation can effectively address existing research limitations and establish connections to address clinical inquiries. We begin by outlining the current state of some widely used imaging methods in Section 1.3.1 and subsequently, in Section 1.3.2, we explore distinct pathologies where hypotheses suggest that hypoxia and impairment of the transport capacities within the microcirculation may contribute to the progression of the disease.

1.3.1 Imaging methods

In the last decades, numerous techniques have emerged in the field of brain imaging that aid in the exploration of both the micro- and macroscopic aspects of brain structure and function.

These methods come in different sizes, so to speak, catering to the multiscale nature of the microcirculation. We deem the microscopic scale as the phenomena with a characteristic length similar to the diameter of a capillary, or O(10 μm), whereas the macroscopic scale represents vessel networks of the order of tens of thousands, or O(1 mm^3). The mesoscopic scale is everything that lies in between of the two.

On the microscopic end, there are imaging techniques like multiphoton microscopy [3; 6] that allow to zoom in and explore the finer details within tiny brain sections with extremely high resolution (see Fig. 1.1D for an example of the image of a venular tree using confocal microscopy [16]). These methods aid in our comprehension of cellular interactions and the intricate functioning of the tiniest vessels. These small vessels are primarily responsible for communicating with neurons, thereby offering a unique perspective into the inner workings of the NVU, which therefore provides valuable insights into the microscale processes that underpin brain function. On the macroscopic end, we find clinical approaches like magnetic resonance imaging (MRI), positron emission tomography (PET) imaging that offer a broader view, capturing larger brain areas and providing a sense of average quantities, but lack the spatial resolution, and therefore, do not include the intricate details of the angioarchitecture at the capillary level. In this Section, we delve into some relevant imaging techniques at the microscale and macroscale.

Microscopic scale

Multiphoton scanning microscopy [3; 36] is a form of fluorescence microscopy that relies on the simultaneous absorption of multiple low-energy photons to excite fluorescent molecules that permits the spatio-temporal investigation of hemodynamics and oxygen concentration at very high resolutions. It has enabled an exceptional exploration of the cortical microcirculation [2; 7; 17; 37–40]. It allows for *in vivo* mapping of the microvascular anatomy with unprecedented cortical penetration (see Fig. 1.3). We can observe in Fig. 1.3 how in the same experiment Mächler et al. [41], could obtain very accurate representations of the vascular anatomy sufficiently deep to map the vasculature of the first four cortical layers. Even more interesting, in Fig. 1.3D and E, we observe the photon count and its associated oxygen concentration profile around a penetrating arterioles. It is reasonable to assume that, when coupled with robust theoretical methods, multiphoton microscopy has the potential to unravel useful insights regarding oxygen transport and consumption, thereby providing important quantitative data regarding the NVU and neurometabolic coupling. Nevertheless, the spatial extent of observation is limited with multiphoton microscopy, so that, due to the interconnected nature of the microvascular network, they implicitly provide incomplete data. Ligh sheet microscopy recently emerged as an alternative that allows the acquisition of much larger volumes [42], but only *post mortem*. Overall, these tools offer a powerful window into the microvascular anatomy. Nevertheless, they are difficult to interpret without a suitable numerical and theoretical framework of the transport processes that occur in the brain

Perfusion imaging and hemodynamically-based functional imaging techniques

The brain performs and extremely diverse array of functions, from maintaining basic human function in the hypothalamus, to stimulating muscle contraction. The capacity to perform many different tasks is possible due to the ability to locally activate specific regions. There is therefore a huge incentive in enabling the measure of this local activity in the brain; that is the field of perfusion and hemdynamically-based functional imaging techniques at the

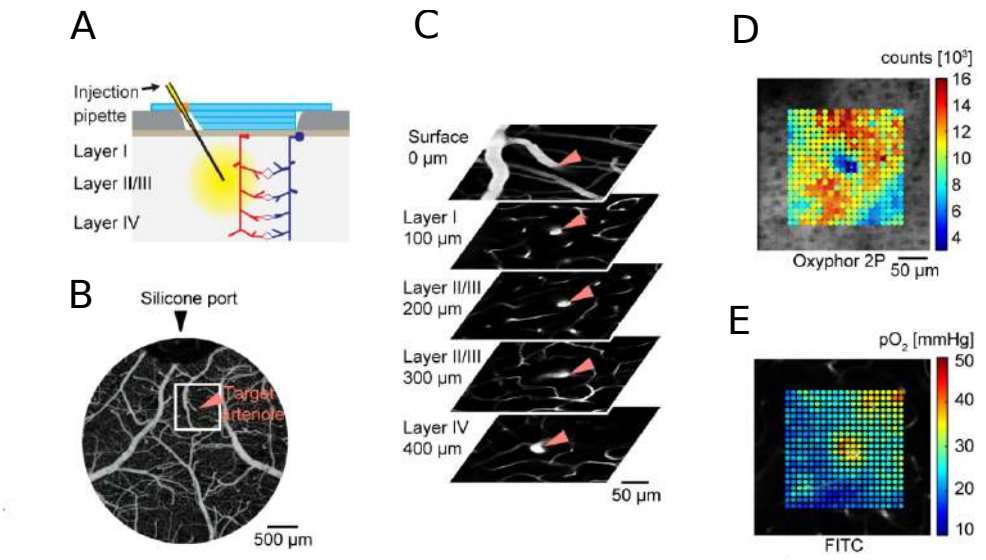

FIGURE 1.3 – **Schematic of the obtainment of oxygen concentration data using multiphoton scanning microscopy.** Panels A and B show the schematic of the measure data and the selection of a target arteriole that is, as much as possible, perpendicular to the plane of view. Panel C shows the obtained anatomical data for each cortical depth highlighting the position of the penetrating arteriole. Panels D and E show the photon count and its associated oxygen concentration field. Modified figure from [41].

macroscopic level i.e., resolution O(1 mm^3).

At the macroscopic level, several neuroimaging techniques are available to study brain function, including blood oxygenation-dependent functional magnetic resonance imaging (BOLD fMRI), positron emission tomography (PET), diffusion-weighted imaging (DWI), single-photon emission computerized tomography (SPECT), Doppler optical coherence tomography (OCT), arterial spin labeling (ASL), and more. These modalities provide insights into various aspects, such as angioarchitecture, blood perfusion, oxygen exchange, and more, across large volumes of tissue. Among these techniques, two stand out due to their relevance and effectiveness in quantifying changes in blood flow and molecular exchange : PET and BOLD fMRI. Both PET and BOLD fMRI rely on the use of tracers, albeit with different approaches. BOLD fMRI measures changes in the hemoglobin content of blood, while PET involves the injection of an exogenous radioactive tracer, making it a more invasive technique.

From a hemodynamic perspective, PET directly measures the average quantity of an exogenous radioactive tracer. This allows for the deduction of various physiological parameters, such as metabolism (if using radioactive glucose as tracer) or blood flow. In contrast, the BOLD signal relies on the principle of neurometabolic coupling, where an increase in brain metabolic activity triggers an overcompensation in blood flow [35; 45–47]. In essence, neurometabolic coupling relies on the expected shift from oxygenated to deoxygenated hemoglobin in regions with heightened metabolic activity. However, it's worth noting that neither of these techniques directly measures neuronal activity ; instead, they are often used as proxies, especially the BOLD signal.

Furthermore, neurometabolic coupling, which links changes in neuronal activity to metabolic demands via the NVU [48; 49], presents challenges. The relationship between metabolic activity and neural activation remains unclear, partly due to energy-consuming inhibitory synaptic connections [35; 45; 50]. Consequently, there is a strong limitation to the interpre-

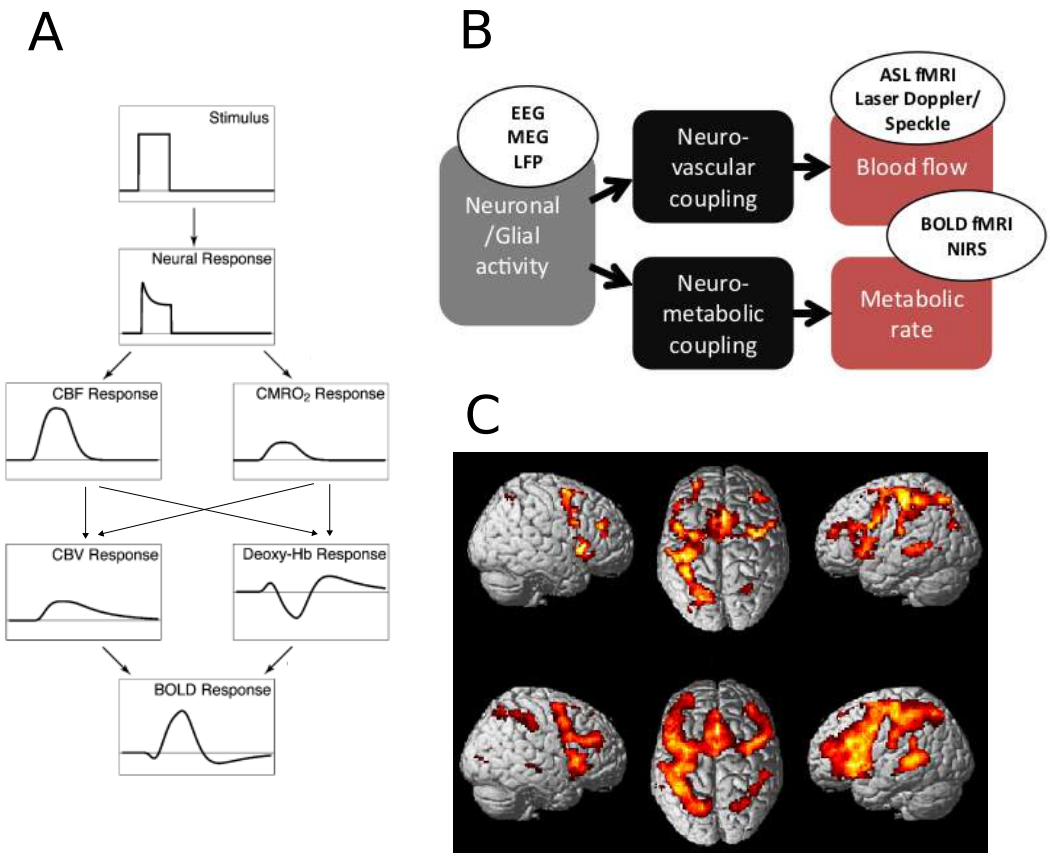

FIGURE 1.4 – **Neurovascular and neurometabolic coupling as the underlying mechanisms for the BOLD signal and other fMRI modalities.** The origin of the functional signals including BOLD and ASL fMRI have their roots in the increase in blood flow (neuro-vascular coupling) and increase in oxygen metabolism (neuro-metabolic coupling) that occurs when neuronal activity increases. Panel A shows an illustration of the shape of the different quantities following a neuronal stimulus [10]. Panel B show the origin of the overcompensation of the vascular system with increased blood flow and oxygen delivery to the activated cortical regions and their associated imaging modalities [43]. Panel C illustrates an example of the BOLD signal for a sensory stimulus (row on top) and visual stimulus (row on bottom) [44].

tability of the BOLD signal. To address this limitation, the field of "calibrated fMRI" has emerged, aiming to provide models describing this neurovascular relationship [48]. Currently, the information gained from functional imaging is often constrained not by engineering limitations but by our limited understanding of neurovascular coupling [50].

Therefore, no existing model comprehensively captures the precise microscale physics that occur in these processes. Additionally, neither PET nor BOLD fMRI adequately considers the intricacies of the microvasculature within the cortex. To bridge the gap between the spatial resolution of the BOLD signal (approximately 1 mm^3 for clinical scanners operating at 1-1.5 Teslas) and the transport processes occurring at the capillary level, a more accurate understanding of microscale physics and vascular anatomy is required. Thus, theoretical and numerical models are crucial for bridging the gap between metabolic activity in the brain parenchyma and the vascular response and to accurately quantify the transport phenomena in the microcirculation.

1.3.2 Vascular mechanism of neurodegeneration : Alzheimer's disease and vascular mediated dementia

Alzheimer's disease (AD) stands as a prominent form of dementia, characterized by the pathological buildup of amyloid-β plaques and tau tangles within the brain parenchyma. In particular, amyloid plaques are believed to be the main cause of cognitive impairment in AD since they are neurotoxic, interfere with synaptic connections and produce an inflammatory response [51]. The accumulation of this metabolic waste is closely related to vascular dysfunction [52; 53] though it is unclear whether vascular dysfunction is the precursor to amyloid-β accumulation or vice versa. Undoubtedly, vascular dysfunction is highly correlated with AD [5; 54–56], and it is estimated that more than half of AD cases could be prevented by control of cardiovascular factors [57].

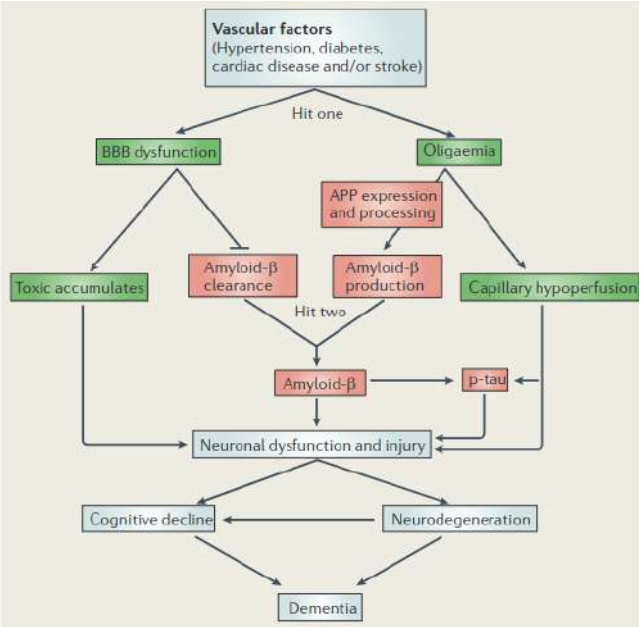

FIGURE 1.5 – **Two hit hypothesis vascular hypothesis for AD.** Schematic of hypothesized underlying causes of the development of AD through vascular dysfunction. It is hypothesized that vascular risks converge to either BBB dysfunction, mild hypoperfusion (oligaemia), or both to cause an increase of amyloid-β accumulation in the brain parenchyma, or to be independent causes of neuronal dysfunction and injury [29]

.

While AD is the most common dementia diagnosis, vascular contributions to cognitive impairment remain important independent causes or contributors of dementia [56]. These vascular factors encompass conditions such as atherosclerosis, arteriosclerosis, microinfarcts, and silent strokes, all of which are associated with an increased risk of dementia [55]. Moreover, more than half of the cases of AD include mixed pathologies, with amyloid-β and vascular disease being the most frequent combination. For this reason, the contribution of vascular factors and their underlying mechanisms remains an intense areas of research [5; 29; 55]. However, the molecular and cellular mechanisms for the development of the disease process for each risk factor remain unclear. Nevertheless, vascular factors may all converge toward a common final disease pathway that involves chronic hypoperfusion-hypoxia, and/or amyloid-β and tau accumulation [29], see Fig. 1.5. These shared pathways accelerate the onset of neuronal dysfunction and neurodegeneration, and in the worst cases, dementia.

Furthermore, both BBB dysfunction and mild hypoperfusion (termed oligaemia in Fig. 1.5)

tend to occur together, potentially intensifying the accumulation of amyloid-β in the parenchyma. The break down of the BBB is often associated with capillary rarefraction, leading to decreased capillary density, which ultimately results in hypoperfusion and hypoxia, particularly in vulnerable regions like the hippocampus [7] or the white matter [5]. Additionally, hypoperfusion has been shown to induce endothelial dysfunction, perpetuating a harmful cycle of hypoxia and BBB breakdown [58].

To sum up, the impact of vascular dysfunction in the development of neurodegenerative diseases is clear. From being the earliest biomarker of neurodegeneration in humans [59], to being considered as the main underlying cause of the disease [5; 27; 32; 49; 60]. The mechanistic nature of neurodegeneration due to vascular factors primarily affects the transport processes facilitated by the vascular system. Notably, these include BBB dysfunction caused by hypoxia [5; 58], hypoperfusion caused by decrease of capillary density [61–63] and impaired waste clearance associated with increased BBB permeability [32; 49]

Despite substantial progress in understanding vascular factors contributing to various types of dementia, there is a lack of comprehensive theoretical models that allow careful investigation of the progression of the disease. Considering also the wide range of pathologies that arise from the malfunctioning or deterioration of the microcirculation (specific to the brain in this case, e.g., AD, hypo- and hypertension, etc. [11; 64; 65]), clearly there is a need for a deeper understanding of the underlying microvascular structure and its implications on CBF, nutrient transport, and waste disposal.

1.4 Objectives of the present work and general strategy

Understanding and modeling the transport of molecules in the brain is a crucial step in the interpretation of imaging data at the microscale [7; 36; 41; 66], and at the macroscale [33; 35]. It also plays an important role in the understanding of neurovascular coupling [9; 34] and the progression of multiple diseases such as AD [67] or vascular mediated dementiae [55; 68]. In particular, the transport of oxygen is of great importance due to its direct link with oxidative metabolism and hypoxia. However, beyond the structural patterns that govern the brain microvasculature, we have limited knowledge of the mechanisms controlling oxygen delivery to the brain parenchyma [50]. Moreover, the multiscale architecture of the microvasculature challenges the integration of information across various scales due to non-local network effects [69] leading to other non-local properties such as the heterogeneous capillary oxygen distribution [4]. Overall, these properties hinder the extrapolation of studies with a low number of vessels to the larger landscape of the brain microcirculation.

In this thesis, we thus undertake the development of an efficient, simple and accurate multiscale molecular transport model applicable to large volumes of cortical tissue. Our primary goal revolves around the application of established physical laws governing solute transport through advanced numerical techniques, all aimed at addressing the specific challenges arising from the intricate nature of brain microcirculation. That way, attempting to shed light on the complex transport phenomena occurring in the brain cortex. In simpler terms, we aim at creating a comprehensive numerical model that enhances our understanding of how oxygen moves within the brain's cortex without the extreme computational requirements characteristic of this system.

The primary objective of this PhD thesis is thus to develop a numerical approach that can be used on large microvascular datasets. This approach will aid in the interpretation of images

acquired through the aforementioned microscopic and macroscopic imaging techniques. Such a model would serve as a strong asset in generating physics-informed interpretations to decipher signals like BOLD. Additionally, it would shed light on the interaction between vessels and parenchyma, which is also needed in order to provide a physics-based approach to interpret the data garnered through microscopic imaging modalities such as multiphoton microscopy [4; 36; 41]. Additionally, it can improve our understanding of the development of diseases like AD and other types of vascular dementiae.

The main idea developed in this thesis, is to use mathematical techniques to reduce the complexity of the numerical resolution of the molecular transport problem. The challenges of the problem arise as a consequence of the apparently chaotic brain microvasculature and the rapid variation of vessel sizes within the same region. In the next Chapter, we will thus explore the current techniques to model blood flow and molecular transport in the brain microcirculation. An extensive overview is done of the numerical and mathematical techniques aiming at reducing the complexity of similar problems from a wide range of subjects, from geoscience engineering, to more similar fields such as blood flow in tumours. We will extend this exploration to highlight the relevant mathematical techniques employed in each subject, and then develop a multiscale model tailored to the brain microcirculation.

1.5 References

[1] Richard B. Buxton and Lawrence R. Frank. A Model for the Coupling between Cerebral Blood Flow and Oxygen Metabolism during Neural Stimulation. *Journal of Cerebral Blood Flow & Metabolism*, 17(1) :64–72, January 1997. 1

[2] David A. Boas, Stephanie R. Jones, Anna Devor, Theodore J. Huppert, and Anders M. Dale. A vascular anatomical network model of the spatio-temporal response to brain activation. *NeuroImage*, 40(3) :1116–1129, April 2008. 1, 7, 8

[3] Sven Hirsch, Johannes Reichold, Matthias Schneider, Gábor Székely, and Bruno Weber. Topology and Hemodynamics of the Cortical Cerebrovascular System. *Journal of Cerebral Blood Flow & Metabolism*, 32(6) :952–967, June 2012. 1, 8

[4] Sava Sakadžić, Emiri T. Mandeville, Louis Gagnon, Joseph J. Musacchia, Mohammad A. Yaseen, Meryem A. Yucel, Joel Lefebvre, Frédéric Lesage, Anders M. Dale, Katharina Eikermann-Haerter, Cenk Ayata, Vivek J. Srinivasan, Eng H. Lo, Anna Devor, and David A. Boas. Large arteriolar component of oxygen delivery implies a safe margin of oxygen supply to cerebral tissue. *Nature Communications*, 5(1) :5734, December 2014. 1, 2, 5, 12, 13

[5] Costantino Iadecola. The Pathobiology of Vascular Dementia. *Neuron*, 80(4) :844–866, November 2013. 1, 11, 12

[6] Andy Y. Shih, Charlotta Rühlmann, Pablo Blinder, Anna Devor, Patrick J. Drew, Beth Friedman, Per M. Knutsen, Patrick D. Lyden, Céline Matéo, Lisa Mellander, Nozomi Nishimura, Chris B. Schaffer, Philbert S. Tsai, and David Kleinfeld. Robust and Fragile Aspects of Cortical Blood Flow in Relation to the Underlying Angioarchitecture. *Microcirculation*, 22(3) :204–218, April 2015. 1, 2, 3, 8

[7] K. Shaw, L. Bell, K. Boyd, D. M. Grijseels, D. Clarke, O. Bonnar, H. S. Crombag, and C. N. Hall. Neurovascular coupling and oxygenation are decreased in hippocampus compared to neocortex because of microvascular differences. *Nature Communications*, 12(1) :3190, May 2021. 1, 8, 12

[8] Richard B. Buxton. Interpreting oxygenation-based neuroimaging signals : the importance and the challenge of understanding brain oxygen metabolism. *Frontiers in Neuroenergetics*, 2010. 1

[9] Costantino Iadecola. The Neurovascular Unit Coming of Age : A Journey through Neurovascular Coupling in Health and Disease. *Neuron*, 96(1) :17–42, 2017. 1, 7, 12

[10] Richard B. Buxton, Kâmil Uludağ, David J. Dubowitz, and Thomas T. Liu. Modeling the hemodynamic response to brain activation. *NeuroImage*, 23 :S220–S233, January 2004. 1, 10

[11] Helene Girouard and Costantino Iadecola. Neurovascular coupling in the normal brain and in hypertension, stroke, and Alzheimer disease. *Journal of Applied Physiology*, 100(1) :328–335, January 2006. 1, 12

[12] Sylvie Lorthois and Francis Cassot. Fractal analysis of vascular networks : Insights from morphogenesis. *Journal of Theoretical Biology*, 262(4) :614–633, February 2010. 2, 3

[13] Marcos Intaglietta, Paul C. Johnson, and Robert M. Winslow. Microvascular and tissue oxygen distribution. *Cardiovascular Research*, 32(4) :632–643, October 1996. _eprint : https ://academic.oup.com/cardiovascres/article-pdf/32/4/632/735042/32-4-632.pdf. 2, 5

[14] Maxime Berg, Yohan Davit, Michel Quintard, and Sylvie Lorthois. Modelling solute transport in the brain microcirculation : is it really well mixed inside the blood vessels ? *Journal of Fluid Mechanics*, 884 :A39, February 2020. 2, 5

[15] H.M. Duvernoy, S. Delon, and J.L. Vannson. Cortical blood vessels of the human brain. *Brain Research Bulletin*, 7(5) :519–579, November 1981. 3

[16] Francis Cassot, Frederic Lauwers, Céline Fouard, Steffen Prohaska, and Valerie Lauwers-Cances. A Novel Three-Dimensional Computer-Assisted Method for a Quantitative Study of Microvascular Networks of the Human Cerebral Cortex. *Microcirculation*, 13(1) :1–18, January 2006. 2, 3, 8

[17] Nozomi Nishimura, Chris B. Schaffer, Beth Friedman, Patrick D. Lyden, and David Kleinfeld. Penetrating arterioles are a bottleneck in the perfusion of neocortex. *Proceedings of the National Academy of Sciences*, 104(1) :365–370, January 2007. 2, 8

[18] Timothy W. Secomb. Hemodynamics. In Ronald Terjung, editor, *Comprehensive Physiology*, pages 975–1003. Wiley, 1 edition, March 2016. 3, 7

[19] Marilyn J. Cipolla. *The Cerebral Circulation*. San Rafael (CA), 2009. Book Title : The Cerebral Circulation. 3

[20] Ian Gopal Gould, Philbert Tsai, David Kleinfeld, and Andreas Linninger. The capillary bed offers the largest hemodynamic resistance to the cortical blood supply. *Journal of Cerebral Blood Flow & Metabolism*, 37(1) :52–68, January 2017. 4

[21] N. P. Smith, A. J. Pullan, and P. J. Hunter. An Anatomically Based Model of Transient Coronary Blood Flow in the Heart. *SIAM Journal on Applied Mathematics*, 62(3) :990–1018, January 2002. 4

[22] Charles Nicholson. Diffusion and related transport mechanisms in brain tissue. *Reports on Progress in Physics*, 64(7) :815–884, July 2001. 4

[23] Gideon Idumah, Erkki Somersalo, and Daniela Calvetti. A spatially distributed model of brain metabolism highlights the role of diffusion in brain energy metabolism. *Journal of Theoretical Biology*, 572 :111567, September 2023. 4

[24] T.W. Secomb, R. Hsu, N.B. Beamer, and B.M. Coull. Theoretical Simulation of Oxygen Transport to Brain by Networks of Microvessels : Effects of Oxygen Supply and Demand on Tissue Hypoxia. *Microcirculation*, 7(4) :237–247, August 2000. 5

[25] Amy F. Smith, Vincent Doyeux, Maxime Berg, Myriam Peyrounette, Mohammad Haft-Javaherian, Anne-Edith Larue, John H. Slater, Frédéric Lauwers, Pablo Blinder, Philbert Tsai, David Kleinfeld, Chris B. Schaffer, Nozomi Nishimura, Yohan Davit, and Sylvie Lorthois. Brain Capillary Networks Across Species : A few Simple Organizational Requirements Are Sufficient to Reproduce Both Structure and Function. *Frontiers in Physiology*, 10 :233, March 2019.

[26] Rebecca J Shipley, Amy F Smith, Paul W Sweeney, Axel R Pries, and Timothy W Secomb. A hybrid discrete–continuum approach for modelling microcirculatory blood flow. *Mathematical Medicine and Biology : A Journal of the IMA*, March 2019. 5

[27] Berislav V. Zlokovic. Neurovascular mechanisms of Alzheimer's neurodegeneration. *Trends in Neurosciences*, 28(4) :202–208, 2005. 5, 12

[28] William M. Pardridge. Blood–brain barrier delivery. *Drug Discovery Today*, 12(1-2) :54–61, January 2007. 5

[29] Berislav V. Zlokovic. Neurovascular pathways to neurodegeneration in Alzheimer's disease and other disorders. *Nature Reviews Neuroscience*, 12(12) :723–738, December 2011. 5, 7, 11

[30] N. Joan Abbott, Adjanie A.K. Patabendige, Diana E.M. Dolman, Siti R. Yusof, and David J. Begley. Structure and function of the blood–brain barrier. *Neurobiology of Disease*, 37(1) :13–25, January 2010. 6

[31] Lulu Xie, Hongyi Kang, Qiwu Xu, Michael J. Chen, Yonghong Liao, Meenakshisundaram Thiyagarajan, John O'Donnell, Daniel J. Christensen, Charles Nicholson, Jeffrey J. Iliff, Takahiro Takano, Rashid Deane, and Maiken Nedergaard. Sleep Drives Metabolite Clearance from the Adult Brain. *Science*, 342(6156) :373–377, October 2013. 6

[32] Berislav V. Zlokovic. The Blood-Brain Barrier in Health and Chronic Neurodegenerative Disorders. *Neuron*, 57(2) :178–201, 2008. 7, 12

[33] Richard B. Buxton, Eric C. Wong, and Lawrence R. Frank. Dynamics of blood flow and oxygenation changes during brain activation : The balloon model. *Magnetic Resonance in Medicine*, 39(6) :855–864, June 1998. 7, 12

[34] Patrick J. Drew. Neurovascular coupling : motive unknown. *Trends in Neurosciences*, 45(11) :809–819, 2022. 7, 12

[35] Nikos K. Logothetis and Brian A. Wandell. Interpreting the BOLD Signal. *Annual Review of Physiology*, 66(1) :735–769, March 2004. 7, 9, 12

[36] Sava Sakadžic, Mohammad A. Yaseen, Rajeshwer Jaswal, Emmanuel Roussakis, Anders M. Dale, Richard B. Buxton, Sergei A. Vinogradov, David A. Boas, and Anna Devor. Two-photon microscopy measurement of cerebral metabolic rate of oxygen using periarteriolar oxygen concentration gradients. *Neurophotonics*, 3(4) :045005, October 2016. 8, 12, 13

[37] Anna Devor, Sava Sakadžić, Payam A. Saisan, Mohammad A. Yaseen, Emmanuel Roussakis, Vivek J. Srinivasan, Sergei A. Vinogradov, Bruce R. Rosen, Richard B. Buxton, Anders M. Dale, and David A. Boas. "Overshoot" of O_2 Is Required to Maintain Baseline Tissue Oxygenation at Locations Distal to Blood Vessels. *The Journal of Neuroscience*, 31(38) :13676–13681, September 2011. 8

[38] Thom P. Santisakultarm, Nathan R. Cornelius, Nozomi Nishimura, Andrew I. Schafer, Richard T. Silver, Peter C. Doerschuk, William L. Olbricht, and Chris B. Schaffer. In vivo two-photon excited fluorescence microscopy reveals cardiac- and respiration-dependent pulsatile blood flow in cortical blood vessels in mice. *American Journal of Physiology-Heart and Circulatory Physiology*, 302(7) :H1367–H1377, April 2012.

[39] Baoqiang Li, Tatiana V Esipova, Ikbal Sencan, Kıvılcım Kılıç, Buyin Fu, Michele Desjardins, Mohammad Moeini, Sreekanth Kura, Mohammad A Yaseen, Frederic Lesage, Leif Østergaard, Anna Devor, David A Boas, Sergei A Vinogradov, and Sava Sakadžić. More homogeneous capillary flow and oxygenation in deeper cortical layers correlate with increased oxygen extraction. *eLife*, 8 :e42299, July 2019.

[40] L. Gagnon, S. Sakad i, F. Lesage, J. J. Musacchia, J. Lefebvre, Q. Fang, M. A. Yucel, K. C. Evans, E. T. Mandeville, J. Cohen-Adad, J. R. Polimeni, M. A. Yaseen, E. H. Lo, D. N. Greve, R. B. Buxton, A. M. Dale, A. Devor, and D. A. Boas. Quantifying the Microvascular Origin of BOLD-fMRI from First Principles with Two-Photon Microscopy and an Oxygen-Sensitive Nanoprobe. *Journal of Neuroscience*, 35(8) :3663–3675, February 2015. 8

[41] Philipp Mächler, Natalie Fomin-Thunemann, Martin Thunemann, Marte Julie Sætra, Michèle Desjardins, Kıvılcım Kılıç, Layth N. Amra, Emily A. Martin, Ichun Anderson Chen, Ikbal Şencan Eğilmez, Baoqiang Li, Payam Saisan, John X. Jiang, Qun Cheng, Kimberly L. Weldy, David A. Boas, Richard B. Buxton, Gaute T. Einevoll, Anders M. Dale, Sava Sakadžić, and Anna Devor. Baseline oxygen consumption decreases with cortical depth. *PLOS Biology*, 20(10) :e3001440, October 2022. 8, 9, 12, 13

[42] Erlen Lugo-Hernandez, Anthony Squire, Nina Hagemann, Alexandra Brenzel, Maryam Sardari, Jana Schlechter, Eduardo H Sanchez-Mendoza, Matthias Gunzer, Andreas Faissner, and Dirk M Hermann. 3D visualization and quantification of microvessels in the whole ischemic mouse brain using solvent-based clearing and light sheet microscopy. *Journal of Cerebral Blood Flow & Metabolism*, 37(10) :3355–3367, October 2017. 8

[43] Clément Huneau, Habib Benali, and Hugues Chabriat. Investigating Human Neurovascular Coupling Using Functional Neuroimaging : A Critical Review of Dynamic Models. *Frontiers in Neuroscience*, 9, December 2015. 10

[44] Barbara Tomasino, Ilaria Del Negro, Riccardo Garbo, Gian Luigi Gigli, Serena D'Agostini, and Maria Rosaria Valente. Multisensory mental imagery of *fatigue* : Evidence from an fMRI study. *Human Brain Mapping*, 43(10) :3143–3152, July 2022. 10

[45] Nikos K Logothetis, Jon Pauls, Mark Augath, Torsten Trinath, and Axel Oeltermann. Neurophysiological investigation of the basis of the fMRI signal. 412 :8, 2001. 9

[46] David Attwell and Costantino Iadecola. The neural basis of functional brain imaging signals. *Trends in Neurosciences*, 25(12) :621–625, December 2002.

[47] Elizabeth M.C. Hillman. Coupling Mechanism and Significance of the BOLD Signal : A Status Report. *Annual Review of Neuroscience*, 37(1) :161–181, July 2014. 9

[48] C.Y. Shu, B.G. Sanganahalli, D. Coman, P. Herman, and F. Hyder. New horizons in neurometabolic and neurovascular coupling from calibrated fMRI. In *Progress in Brain Research*, volume 225, pages 99–122. Elsevier, 2016. 9, 10

[49] Joanna M. Wardlaw, Stephen J. Makin, Maria C. Valdés Hernández, Paul A. Armitage, Anna K. Heye, Francesca M. Chappell, Susana Muñoz-Maniega, Eleni Sakka, Kirsten Shuler, Martin S. Dennis, and Michael J. Thrippleton. Blood-brain barrier failure

as a core mechanism in cerebral small vessel disease and dementia : evidence from a cohort study. *Alzheimer's & Dementia*, 13(6) :634–643, 2017. _eprint : https ://alz-journals.onlinelibrary.wiley.com/doi/pdf/10.1016/j.jalz.2016.09.006. 9, 12

[50] Nikos K. Logothetis. What we can do and what we cannot do with fMRI. *Nature*, 453(7197) :869–878, June 2008. 9, 10, 12

[51] L. Mucke and D. J. Selkoe. Neurotoxicity of Amyloid -Protein : Synaptic and Network Dysfunction. *Cold Spring Harbor Perspectives in Medicine*, 2(7) :a006338–a006338, July 2012. 11

[52] Melanie D. Sweeney, Kassandra Kisler, Axel Montagne, Arthur W. Toga, and Berislav V. Zlokovic. The role of brain vasculature in neurodegenerative disorders. *Nature Neuroscience*, 21(10) :1318–1331, October 2018. 11

[53] Joseph M. Castellano, Rashid Deane, Andrew J. Gottesdiener, Philip B. Verghese, Floy R. Stewart, Tim West, Andrew C. Paoletti, Tristan R. Kasper, Ronald B. DeMattos, Berislav V. Zlokovic, and David M. Holtzman. Low-density lipoprotein receptor overexpression enhances the rate of brain-to-blood A clearance in a mouse model of -amyloidosis. *Proceedings of the National Academy of Sciences of the United States of America*, 109(38) :15502–15507, September 2012. Place : United States. 11

[54] Albert Hofman, Alewijn Ott, Monique MB Breteler, Michiel L Bots, Arjen JC Slooter, Frans van Harskamp, Cornelia N van Duijn, Christine Van Broeckhoven, and Diederick E Grobbee. Atherosclerosis, apolipoprotein E, and prevalence of dementia and Alzheimer's disease in the Rotterdam Study. *The Lancet*, 349(9046) :151–154, January 1997. 11

[55] Roderick A. Corriveau, Francesca Bosetti, Marian Emr, Jordan T. Gladman, James I. Koenig, Claudia S. Moy, Katherine Pahigiannis, Salina P. Waddy, and Walter Koroshetz. The Science of Vascular Contributions to Cognitive Impairment and Dementia (VCID) : A Framework for Advancing Research Priorities in the Cerebrovascular Biology of Cognitive Decline. *Cellular and Molecular Neurobiology*, 36(2) :281–288, March 2016. 11, 12

[56] Philip B. Gorelick, Angelo Scuteri, Sandra E. Black, Charles Decarli, Steven M. Greenberg, Costantino Iadecola, Lenore J. Launer, Stephane Laurent, Oscar L. Lopez, David Nyenhuis, Ronald C. Petersen, Julie A. Schneider, Christophe Tzourio, Donna K. Arnett, David A. Bennett, Helena C. Chui, Randall T. Higashida, Ruth Lindquist, Peter M. Nilsson, Gustavo C. Roman, Frank W. Sellke, and Sudha Seshadri. Vascular contributions to cognitive impairment and dementia : a statement for healthcare professionals from the american heart association/american stroke association. *Stroke*, 42(9) :2672–2713, September 2011. Place : United States. 11

[57] Deborah E Barnes and Kristine Yaffe. The projected effect of risk factor reduction on Alzheimer's disease prevalence. *The Lancet Neurology*, 10(9) :819–828, September 2011. 11

[58] Abraham Al Ahmad, Max Gassmann, and Omolara O. Ogunshola. Involvement of oxidative stress in hypoxia-induced blood–brain barrier breakdown. *Microvascular Research*, 84(2) :222–225, 2012. 12

[59] Y. et al. Iturria-Medina. Early role of vascular dysregulation on late-onset Alzheimer's disease based on multifactorial data-driven analysis. *Nature Communications*, 7(1) :11934, June 2016. 12

[60] Philip B Gorelick. World Stroke Day Proclamation 2015. 12

[61] Cecilia Czakó, Tibor Kovács, Zoltan Ungvari, Anna Csiszar, Andriy Yabluchanskiy, Shannon Conley, Tamas Csipo, Agnes Lipecz, Hajnalka Horváth, Gábor László Sándor, Lilla István, Trevor Logan, Zoltán Zsolt Nagy, and Illés Kovács. Retinal biomarkers for Alzheimer's disease and vascular cognitive impairment and dementia (VCID) : implication for early diagnosis and prognosis. *GeroScience*, 42(6) :1499–1525, December 2020. 12

[62] Anne Joutel, Marie Monet-Leprêtre, Claudia Gosele, Céline Baron-Menguy, Annette Hammes, Sabine Schmidt, Barbara Lemaire-Carrette, Valérie Domenga, Andreas Schedl, Pierre Lacombe, and Norbert Hubner. Cerebrovascular dysfunction and microcirculation rarefaction precede white matter lesions in a mouse genetic model of cerebral ischemic small vessel disease. *Journal of Clinical Investigation*, 120(2) :433–445, February 2010.

[63] Rune B. Nielsen, Lærke Egefjord, Hugo Angleys, Kim Mouridsen, Michael Gejl, Arne Møller, Birgitte Brock, Hans Brændgaard, Hanne Gottrup, Jørgen Rungby, Simon F. Eskildsen, and Leif Østergaard. Capillary dysfunction is associated with symptom severity and neurodegeneration in Alzheimer's disease. *Alzheimer's & Dementia*, 13(10) :1143–1153, October 2017. 12

[64] S. Lorthois, F. Cassot, and F. Lauwers. Simulation study of brain blood flow regulation by intra-cortical arterioles in an anatomically accurate large human vascular network : Part I : Methodology and baseline flow. *NeuroImage*, 54(2) :1031–1042, January 2011. 12

[65] Laura K. Teune, Anna L. Bartels, Bauke M. de Jong, Antoon T. M. Willemsen, Silvia A. Eshuis, Jeroen J. de Vries, Joost C. H. van Oostrom, and Klaus L. Leenders. Typical cerebral metabolic patterns in neurodegenerative brain diseases : Typical Cerebral Metabolic Patterns. *Movement Disorders*, 25(14) :2395–2404, October 2010. 12

[66] Marte J. Sætra, Andreas V. Solbrå, Anna Devor, Sava Sakadžić, Anders M. Dale, and Gaute T. Einevoll. Spatially resolved estimation of metabolic oxygen consumption from optical measurements in cortex. *Neurophotonics*, 7(03), August 2020. 12

[67] Xiulian Sun, Guiqiong He, Hong Qing, Weihui Zhou, Frederick Dobie, Fang Cai, Matthias Staufenbiel, L. Eric Huang, and Weihong Song. Hypoxia facilitates Alzheimer's disease pathogenesis by up-regulating *BACE1* gene expression. *Proceedings of the National Academy of Sciences*, 103(49) :18727–18732, December 2006. 12

[68] Brina Snyder, Brent Shell, J. Thomas Cunningham, and Rebecca L. Cunningham. Chronic intermittent hypoxia induces oxidative stress and inflammation in brain regions associated with early-stage neurodegeneration. *Physiological reports*, 5(9), May 2017. Place : United States. 12

[69] F. Goirand, B. Georgeot, O. Giraud, and S. Lorthois. Network community structure and resilience to localized damage : Application to brain microcirculation. *Brain Multiphysics*, 2 :100028, 2021. 12

Chapter 2

Current methods for modeling blood flow and molecular transport

In the previous Chapter, we underscored the increasing demand for the development of large-scale models for molecular transport. This Chapter is dedicated to examining the challenges inherent in such models, along with the existing strategies documented in the literature. We place particular emphasis on the various techniques employed to simplify the resolution of the governing equations. Our objective is to identify key components that can enhance the capabilities of molecular transport models. This focus aligns with the central aim of this thesis : to reduce the complexity of molecular transport modeling, resulting in smaller and less dense matrix systems for faster and more resource-efficient problem-solving. Based on the strategy determined through this review, we will detail the model formulations in 2D and 3D in Chapters 3 and 4, respectively.

In Section 2.1, we introduce the concept of representing the vascular system as a connected graph, a widely adopted approach for the structured and intuitive analysis of network connectivity and flow characteristics. In Section 2.2, we briefly discuss the modeling techniques used to derive velocity fields within the vessels. Section 2.3 introduces the fundamental equations governing molecular transport. Finally, in Section 2.4, we delve into the prevalent models employed to solve these equations within the microcirculation and analogous systems.

2.1 Graph representation of the microvasculature

The vasculature is generally represented as a graph composed of interconnected vertices and edges [1–4], as illustrated in Fig. 2.1. In this representation, each edge corresponds to a vessel with an associated diameter d, and length l ; the vertices represent the junctions between vessels. As shown in Fig. 2.1, each edge connects two vertices. We therefore denote each edge by the vertices it connects ; for instance, $d_{2,3}$ represents the diameter of the edge connecting the inner vertex 2 with the boundary vertex 3 in Fig. 2.1. For the sake of simplicity, let us consider the diameter of each edge is constant, although it is worth noting that variability may be simply included by introducing the curvilinear abscissa s along each vessel and defining $d(s)$. The simplicity of graphs makes them a widespread method in the field of microcirculation. They represent the topology of networks in a concise manner, allowing us to extract a wide range of quantitative data.

Such a graph representation has been thoroughly used in network models of blood flow

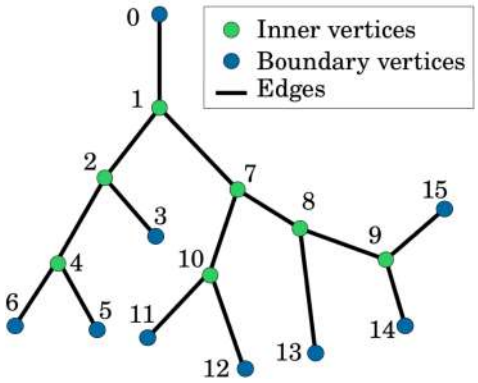

FIGURE 2.1 – **Example of the graph representation of an arterial tree.** The edges are represented as straight lines joined by vertices. The inner vertices are represented in green, while the boundary vertices are in blue.

and molecular transport associated to reduced-order models of flow and advection-diffusion-reaction that are applied to each edge.

2.2 Modeling blood flow in microvascular networks

Transport models are crucially dependent on the properties of the media considered. The diffusivity of oxygen in both blood and the parenchyma is commonly approximated to that in water [5–11]. Conversely, estimating the advective properties of the microcirculation through experimentation remains difficult, which has prompted the development of a multitude of blood flow models [2; 8; 12–15]. It is important to underscore that flow models offering insights into the characteristics of the cortical microcirculation [16; 17] are immensely valuable in their own right. In particular, these models are considerably simpler than molecular transport models and can simulate larger cortical volumes [3]. Nevertheless, a blood flow map is a prerequisite for any molecular transport model as the flow problem is independent from the transport problem but not the other way around. In this context, we consider the flow model to be a pre-processing step, as our primary focus is on the transport model itself.

In this Section, we detail the challenges arising when modeling blood flow in the microcirculation and briefly discuss the strategy adopted to obtain the velocity distribution in our networks.

2.2.1 Blood rheology at the scale of single vessels

Human blood primarily consists of two main components : red blood cells (RBCs) and their suspending fluid, called plasma, constituting approximately 40-45% and 55-60% of the blood volume, respectively [1]. Plasma is an acqueous solution containing ions (e.g., Na^+, Cl^-), proteins and other solutes, including oxygen.

RBCs are specialized oxygen carriers containing hemoglobin, a protein with high affinity to oxygen molecules. In the context of fluid dynamics, plasma behaves as a Newtonian fluid [12]. RBCs on the other hand are bound by the lipid bilayer characteristic of human cells. Consequently, RBCs are the primary contributor to the non linear behaviour of blood. In larger vessels whose diameter is much larger than the size of a single RBC (approximately

1. The volume fraction of RBCs in blood is commonly referred to as the systemic hematocrit.

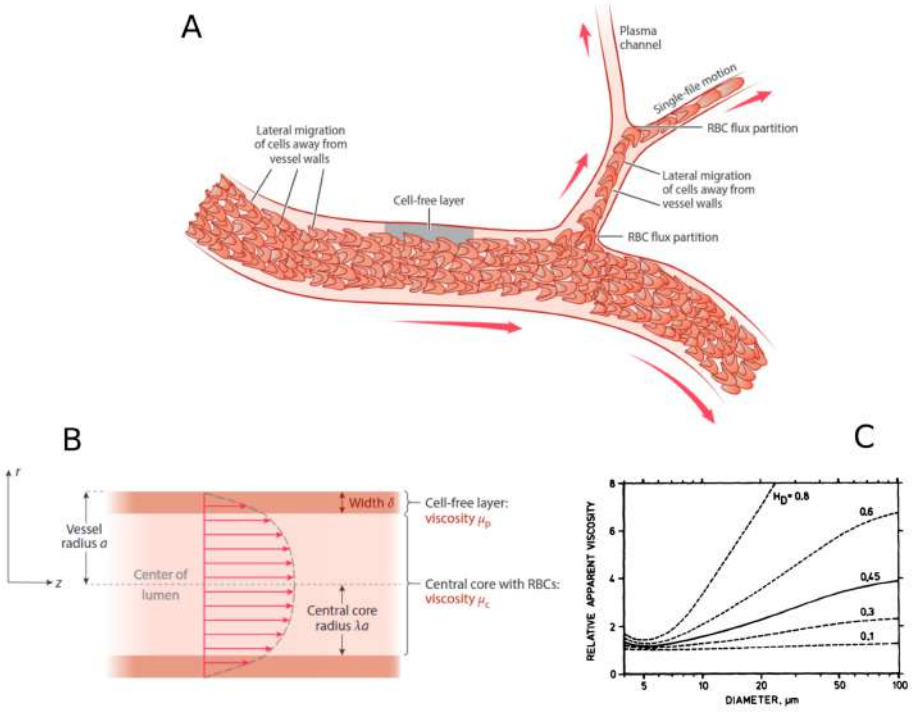

FIGURE 2.2 – **Schmetatics of the red blood cell structuration in microvessels that contribute to the non-linear behaviour of blood.** Panel A displays the features contributing to the phase separation effect i.e., the non proportional distribution of red blood cells at diverging bifurcations. Panel B illustrates the blunted velocity profile contributing to the Fåhræus effect i.e., relative decrease of the tube hematocrit in comparison with the discharge hematocrit. Panel C shows the non-linear curves traced from experiments that illustrate the dependence of apparent blood viscosity on vessel diameter and hematocrit. Panels A and B come from [18], and Panel C from [19].

$8\mu m$ [18]), blood can be approximated as homogeneous solution behaving as a Newtonian fluid where RBCs act as solutes [2; 8; 12; 20–23].

In contrast, when dealing with smaller vessels, the two-phase nature of blood must be considered. Here, blood exhibits a semi-solid state due to the non-negligible size of RBCs and it organizes itself by increasing the concentration of RBCs towards the center of the vessel (see Fig. 2.2A and B). This is caused by the interactions between RBCs and the vessel walls, which give rise to a cell-depleted layer, the so called cell-free layer around the vessel walls. This spatial structuration of RBCs contributes to several non-linear effects characteristic of blood flow in small vessels, as illustrated in Figure 2.2A. This, and other phenomena caused by the two phase nature of the blood influence the velocity profile found within vessels (see Fig. 2.2B), which causes a difference between the tube hematocrit (H_T), i.e., the volume fraction of RBCs within a vessel, and the discharge hematocrit (H_D), i.e., the fraction of RBCs delivered by the flow of the vessel.

In the small vessels, i.e., the vessels where the RBC-free layer is not negligible relative to the vessel diameter, the blood's behavior deviates from that of a simple Newtonian fluid and accounting for the interactions between RBCs and the vessel walls is essential. The non-linear phenomena caused by the two-phase nature of blood in small vessels include :

— Fåhræus effect : relative decrease of the tube hematocrit by comparison with discharge hematocrit. This effect is caused by the greater concentration of RBCs at the center of the vessel where the velocity is greater. Fig. 2.2B illustrates how the blunted velocity

profile inside the vessels in combination with the existence of the cell-free layer produces a higher proportion of RBCs leaving the vessel than contained within.

— Fåhræus-Lindqvist effect : dependence of the apparent blood viscosity upon the vessel diameter and the hematocrit that occurs in small vessels due to the vessel wall-to-RBCs interactions. Fig. 2.2C shows the dependence of relative apparent viscosity with diameter for several values of discharge hematocrit. For larger vessels (diameter well above 10 μm) the relationship is rather linear, which is clearly not the case for smaller vessels with diameter around 10 μm.

— The phase separation effect : non-proportional distribution of hematocrit at diverging bifurcations as a direct consequence of the existence of the cell free layer and the discrete nature of the RBCs. For example, on the higher side of Fig. 2.2A, we can observe a plasma channel. It occurs when a small vessel divides and, due to the existence of the cell-free layer, one vessel receives a disproportionately larger amount of RBCs than the other, which constitutes a clear example of the phase separation effect.

The Fåhræus and Fåhræus-Lindqvist effects impact directly the flow field due to their capacity to modify the apparent viscosity of blood. On the other hand, the phase-separation effect strongly influences the distribution of RBCs in the capillaries, which has a strong influence on oxgyen transport since RBCs are specialized oxygen carriers [20; 24]. We note that the relationship between the apparent viscosity of blood, the hematocrit and the vessel diameter is a complicated one and an active area of research, as well as the prediction of partitioning of RBCs after bifurcations [12; 24–30]. One of the most widely used expression of the apparent viscosity μ^{app} has been obtained by combining experimental measurements *in vitro* and inverse modeling of blood flow for human blood *in vivo* [12] and is given by :

$$\mu^{app} = \mu_p \left[1 + (\mu^{0.45} - 1)\frac{(1 - H_D)^C - 1}{(1 - 0.45)^C - 1} \cdot \left(\frac{d}{d - 1.1}\right)^2\right] \left(\frac{d}{d - 1.1}\right)^2 \tag{2.1}$$

where C is a coefficient describing the dependence upon discharge hematocrit

$$C = (0.8 + e^{-0.075d}) \left(-1 + \frac{1}{1 + 10^{-11} d^{12}}\right) + \frac{1}{1 + 10^{-11} d^{12}} \tag{2.2}$$

and $\mu^{0.45}$ represents the apparent viscosity representative of a blood vessel with 45% in RBC flow ($H_D = 0.45$). The curve in Fig. 2.2C is parametrized by the following expression :

$$\mu^{0.45} = 6e^{-0.085d} + 3.2 - 2.44e^{0.06d^{0.645}} \tag{2.3}$$

Moreover, the varying sizes of blood vessels give rise to a diversity of flow patterns. For instance, the aorta exhibits turbulent and pulsatile flow, while the capillaries maintain a continuous and laminar flow. We concentrate on laminar flow due to its prevalence within the microcirculation. Our approach to obtain a velocity map within each vessel of the microcirculation begins with a graph that depicts the vasculature (see Fig. 2.1). The blood flow Q ($\mathrm{m}^3\ \mathrm{s}^{-1}$) in each vessel is directly proportional to the pressure difference (mmHg) between the vertices.

$$Q_{\beta\gamma} = \mathscr{G}_{\beta\gamma}(P_\beta - P_\gamma) \tag{2.4}$$

where the initial and end vertices are given by the sub-indices β and γ respectively, P represents the pressure at each vertex (mmHg) and $\mathscr{G}$ is the conductance ($m^3\ s^{-1}\ mmHg^{-1}$) defined as :

$$\mathscr{G}_{\beta\gamma} = \frac{\pi d_{\beta\gamma}^4}{128\mu_{\beta\gamma}^{app} l_{\beta\gamma}} \tag{2.5}$$

In conclusion, this Section has introduced a reduced-order model (ROM) that leverages empirical laws to calculate blood viscosity to establish a relationship between the pressure decay and flow within circular conduits. By doing so, we significantly simplify the computational complexity associated with direct numerical modeling of the 3D Stokes equations for laminar flow within a single vessel. This type of strategy is a recurring theme in this thesis since it allows for larger simulations than previously possible, as exemplified by the single-vessel flow model presented in this Section. Furthermore, this methodology extends to a network model, as discussed in the next Section.

2.2.2 Network models

A vascular network is a complex, interconnected system of blood vessels that transport blood throughout the body. Graph representations of the network are used to aid in the modeling tasks. Within a single vessel, the equations presented in the previous Section are used to model the blood flow taking into account the non-linearities arising due to the Fåhræus and the Fåhræus-Lindqvist effects. Additionally, on each inner vertex of the network (green vertices in Fig. 2.1), mass conservation is imposed

$$\sum_{\gamma \in \mathscr{N}_\beta} Q_{\beta\gamma} = 0 \tag{2.6}$$

where $\mathscr{N}_\beta$ represents the set of vertices connected to γ. Equation 2.6 constructs the full system provided pressure or flow condition are given at each boundary vertex and the discharge hematocrit is known in each vessel. The network approach provides a sparse matrix with a narrow bandwidth due to the low connectivity of vascular networks, which constitutes an ideal structure for linear solvers. Besides mass conservation at each bifurcation, there is the need to predict the hematocrit within each daughter branch, which, due to the phase separation effect, constitutes a challenging task. It is important to note that the hematocrit heavily influences the apparent viscosity of blood as shown in equation 2.3. Detailing the intricacies of the phase separation effect, however, lie outside of the scope of this thesis. We note that, for the obtaining of the flow field we use the iterative approach described in detail in [31]. Moving forward, we focus on the main objective of this thesis : modeling solute transport. In Section 2.3, we expand upon the notions of molecular transport discussed in the previous Chapter by introducing the underlying theoretical framework that will be used as the bases for the model developed in subsequent Chapters.

2.3 The physics of molecular transport

In this Section, we revisit the transport phenomena introduced in the previous Chapter to expand upon the underlying physical principles and present the theoretical models employed

in the literature. We recall that the focus of this thesis lies in modeling large microvascular networks while preserving the microscale dynamics that constitute a crucial component of an accurate numerical model [6]. For that reason, we avoid modeling phenomena at the cellular level (e.g., explicitly modeling the geometry of each cell such as neurons (Fig. 2.3C) or RBCs, and instead use effective descriptions of the media considered. Thus, we model blood and parenchyma as continuous media [5; 6; 8; 15; 32–35] corresponding to a description of the associated phenomena at the mesoscale (Fig. 2.3B). In this continuum description, blood and parenchyma are each represented as binary solvent/solute mixtures which allows to leverage available theoretical models [5; 9; 11; 33; 36] to bridge the gap between the mesoscopic and microscopic scales.

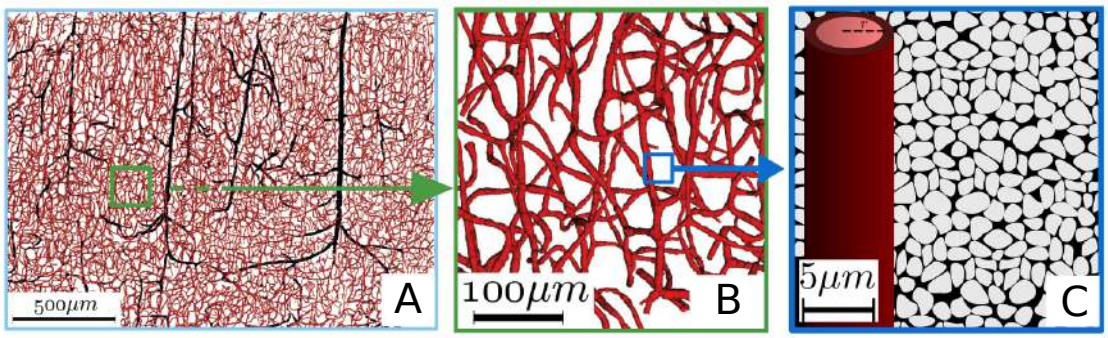

FIGURE 2.3 – **Different scales of interest in the brain microcirculation.** Panel A : the macroscopic scale where the larger vessels (with semi-fractal architecture) are shown in black and the smaller capillary vessels in red. Panel B : the mesoscopic scale which represents the focus of this thesis. It involves already a considerable amount of vessels so it is considered the scale of microvascular networks. Panel C : the microscopic scale where RBCs (not shown) and cells in the parenchyma (shown in grey) represent important structures at this scale. Figures taken from [3].

The modeling strategy consists in a two compartment description where the intra and extra-vascular transport are coupled via the diffusion of solutes through the permeable blood brain barrier (BBB), which yields a coupled blood-parenchyma transport problem. As illustrated in Fig. 2.4. In the following Sections, we introduce the transport equations governing the transport processes at the mesoscale.

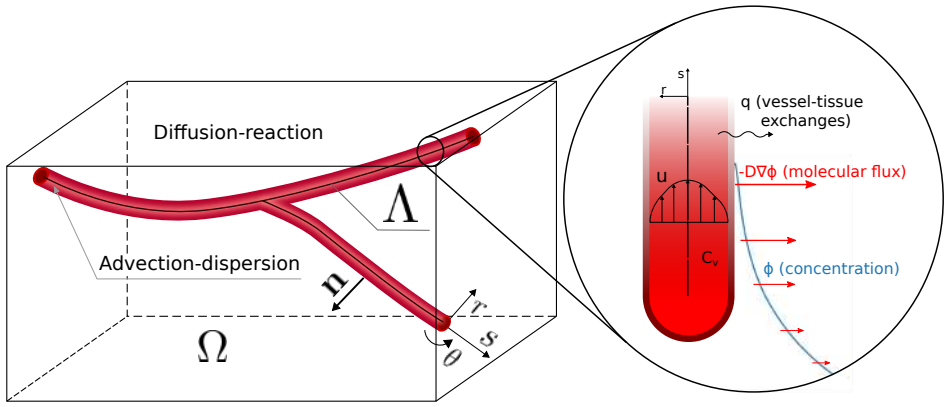

FIGURE 2.4 – **Schematics representing the main transport phenomena in the brain.** On the left, the two compartment description is illustrated : advection-dispersion coupled to diffusion-reaction. On the right, we show the large perivascular concentration gradients caused by the vessel tissue exchanges.

2.3.1 Intravascular advection-dispersion

Within blood vessels, bulk flow is driven by the pressure difference between arteries and veins (see equation 2.4). As blood is a fluid, diffusive transport also plays a role, quantified by Fick's law. Thus, conservation at the microscale can be expressed as follows :

$$\frac{\partial C_v}{\partial t} = \nabla \cdot (-\mathbf{U} C_v + D_v \boldsymbol{\nabla} C_v) \tag{2.7}$$

where C_v represents the intravascular concentration field (mol m^{-3}), $\mathbf{U}$ represents the velocity vector field of blood (m s^{-1}) , and D_v is the effective diffusion coefficient (m^2 s^{-1}) of the solute in blood. The blunted velocity profile appearing in vessels (illustrated in Fig. 2.2B and Fig. 2.4) combined with radial diffusion generates dispersion and enhanced mixing [33; 37; 38]. Direct numerical resolution of these phenomena, i.e., resolution of equation 2.7 in 3D in the vessels, is cumbersome and expensive. For that reason, ROMs are often used in order to simplify the resolution of the problem, similarly as in Section 2.2.1 for the blood flow problem [2]. The reduced order version of the intravascular transport problem is presented in Section 4.2.10.

2.3.2 Extravascular diffusion and consumption

The brain parenchyma is composed of densely packed glial cells (mostly microglia and astrocytes) and neurons with interstitial fluid in between. Nicholson [11] and Holter et al. [36] showed how the movement of molecules in this medium can be approximated by a molecular diffusion process with an effective diffusion coefficient. Moreover, the metabolic consumption is a highly complex process that requires multiple intermediate reactions. Therefore, at the scale we are working with, Michaelis-Menten kinetics is commonly used to estimate the metabolism of oxygen [6; 9; 39–41] and glucose [42]. Both diffusion and metabolic reaction can be integrated within the mass conservation equation in the parenchyma yielding :

$$\frac{\partial \phi}{\partial t} = \nabla \cdot (D_p \boldsymbol{\nabla} \phi) - M \frac{\phi}{\phi + K} \tag{2.8}$$

where the first term in the right-hand side models diffusive transport and the second represents the metabolic consumption modeled through Michaelis-Menten kinetics. The concentration field is given by ϕ (mol m^{-3}), D_p represents the effective diffusion coefficient (m^2 s^{-1}) in the parenchyma, M is the maximum reaction rate (mol m^{-3} s^{-1}), and K is the value of the concentration (mol m^{-3}) for which the reaction speed is half its maximum.

It is worth noting that the diffusion term in equation (equation 2.8) effectively models the random walk of molecules at a macroscopic level, which results in a molecular flux from higher to lower concentration zones. Moreover, equation 2.8 offers an upscaled view of the estravascular space where D_p represents an effective diffusion coefficient in the parenchyma. Such view is well supported in the literature [6; 8; 11; 32; 34; 36]. This exemplifies how upscaling methods are a powerful tool in fluid mechanics to model fluid flow and solute transport since they constitute a theoretical framework that allows a considerable reduction

2. Although we did not include the original set of equations in the text in the interest of readability, the blood flow models originate from the Stokes equations in cylindrical tubes that are later reduced to obtain the formulation discussed in Section 2.2.1.

in complexity in the modeling strategy by incorporating the microscale dynamics into a macroscale equation exemplified in equation 2.8.

2.3.3 Diffusion through the blood brain barrier

We model the BBB as an infinitesimally thin membrane where no sorption takes place and that is permeable to some solutes. As discussed in the previous Chapter, these solutes include small non-polar molecules e.g., oxygen and carbon dioxide, and some big molecules driven by active transport through dedicated channels e.g., glucose and proteins. Due to the no sorption condition, we assume mass balance across the BBB in the following manner :

$$-\mathbf{n} \cdot (D_v \nabla C_v) = -\mathbf{n} \cdot (D_p \nabla \phi) \tag{2.9}$$

where $\mathbf{n}$ is the unit normal pointing inward toward the parenchyma (see Fig. 2.4). Furthermore, there is a jump in concentration across the BBB controled by its permeability to the given solute

$$-\mathbf{n} \cdot (D_p \nabla \phi) = K_m (C_v - \phi) \quad \text{on} \quad \partial\Omega_\beta \tag{2.10}$$

that effectively couples the intravascular concentration field (C_v) to the concentration field in the parenchyma (ϕ). Equation 2.10 represents a Robin boundary condition since it effectively relates the molecular flux ($D_p \nabla \phi$) to the concentration (ϕ) at the boundary created by the vessel wall ($\partial\Omega_\beta$). The molecular flux is proportional to the jump in concentration [43], and controlled by the selective diffusive permeability K_m (m s^{-1}) of the BBB to the particular solute. For the case of oxygen, for which the BBB is fully permeable, we can estimate the value of the permeability as

$$K_m = \frac{D_B}{\epsilon} \tag{2.11}$$

where D_B is the diffusion coefficient of oxygen in the endothelial tissue of the vessel wall, and ϵ represents its thickness (m) [33]. In the limit cases, when $K_m = 0$, the vessel wall is impermeable, blocking solutes from crossing and effectively uncoupling intra- and extravascular transport. When $K_m = \infty$, the vessel wall effectively poses no barrier to diffusion, which, according to equation 2.10, is equivalent to imposing continuity of concentration across the blood-parenchyma boundary.

2.4 Current approaches for modeling molecular transport

Solving the above equations coupled in spatial domains that correspond to a collection of vessels (Fig. 2.4) is highly challenging for conventional numerical methods. First, blood vessels are slender (i.e., high aspect ratio) structures, which pose a challenge requiring a mesh of characteristic size smaller than the smallest dimension. Second, these slender objects are embedded in a three-dimensional volume that also needs to be meshed (excluding the vessels). Consequently, the direct numerical resolution of equations 2.7 - 2.10 is prohibitively expensive.

The use of ROMs is a prevalent practice when dealing with microcirculatory dynamics given the large size of microvascular networks and the above mentioned challenges. An example of ROM includes the network approach represented in Section 2.2, wherein the Stokes equation governing blood flow within vessels is simplified into a linear relationship between pressure

difference and flow. Such techniques allow for a considerable decrease of computational complexity while preserving the accuracy of the original physical model.

From this point onward, we focus on the steady state version of equations 2.7-2.8, where the temporal derivative is null. In fact, the complexity of the transport problem mostly stems from the great size of the microvasculature, its intricate organization and its multiscale nature. Therefore, the challenge in modeling large networks lies in the spatial complexity of the problem, which is the focus of this thesis.

2.4.1 Intravascular transport

In an effort to reduce the complicated task of modelling 3D vascular flow and transport inside the slender cortical vessels (equation 2.7), radial transport inside the vessels is commonly neglected and the intravascular problem is thereby reduced to a 1D ordinary differential equation (ODE) [6; 8; 32; 34; 35; 44; 45]. This formulation arises naturally when working with a graph representation of the vascular system (see Fig. 2.1) and eliminates the need of a 3D mesh of the vessels, which, as mentioned previously, requires a substantial computational effort.

In the present work, we use a generalization of this formulation which accounts for the radial gradients of molecular concentration and enhanced mixing through Taylor's dispersion [38]. Taylor's dispersion was indeed found important in a significant proportion of capillaries [37]. To our knowledge, only [33] includes dispersion into the transport equation, although only rigorously demonstrated for weakly coupled regimes (high Peclet number in the vessel and high Damköhler number in the tissue [3]), corresponding to the following reduced-order model (ROM) for steady-state intravascular transport

$$U_{eff}\frac{\partial\langle C_v\rangle(s)}{\partial s} - D_{eff}\frac{\partial^2\langle C_v\rangle(s)}{\partial s^2} + \frac{4q(s)}{\pi d^2} = 0 \text{ on } \Lambda \tag{2.12}$$

where s represents the intravascular abscisa as illustrated in Fig. 2.4, Λ represents the topological space containing the vessel centerlines ($\Lambda \subset \mathbb{R}$), $\langle\cdot\rangle$ is the cross-sectional average operator

$$\langle\cdot\rangle = \frac{4}{\pi d^2}\iint_{\lambda(s)} \cdot\, dS \tag{2.13}$$

and $q(s)$ represents the vessel-tissue exchanges (mol m^{-1} s^{-1}) given by the line integral molecular flux through the vessel wall, defined as :

$$q(s) = K_{eff}(\langle C_v\rangle(s) - \overline{\phi}(s)) \tag{2.14}$$

The effective transport coefficients for advection, diffusion, and permeability U_{eff}, D_{eff} and K_{eff} respectively, depend on the velocity, the velocity profile, and the diffusive permeability of the vessel wall and are given in [33]. Furthermore, the operator $\bar{\cdot}$ represents the averaging over the circumference of the vessel :

$$\bar{\cdot} = \frac{1}{\pi d}\int_{\partial\lambda(s)} \cdot\, dl \tag{2.15}$$

3. The Peclet and Damköhler numbers refer to the non dimensional numbers quantifying the velocity within the vessel and the tissue consumption within the tissue. For a further description of these quantities see [33]

It is noteworthy how the diffusive permeability of the BBB yields a term (K_{eff}) that is formally identical to a reaction term (see equations 2.12 and 2.14). This equivalence arises from simplifying intravascular transport into a 1D equation. In our model, molecular exchanges are incorporated as a reaction term. Consequently, we refer to our effective intravascular equation as one that encompasses advection, diffusion, and reaction transport processes.

In short, this ROM allows to model intravascular transport with a 1D effective advection-dispersion-reaction equation (equation 2.12). This effective equation accounts for the radial gradients of concentration that have an important impact on vessel-tissue exchanges for physiological values of the BBB diffusive permeability [33].

2.4.2 Current approaches for extravascular transport

The use of a graph representation for the vascular network, along with simplified blood flow and molecular transport equations, greatly simplifies intravascular problem. However, these methods do not address the complexity of the extravascular transport problem, which remains the main challenge in modeling large microvascular networks.

Due to the large aspect ratio of the vessels, large concentration gradients build up around them to drive diffusive transport deep into the parenchyma (see Fig. 2.3). When using conventional numerical methods for the extravascular transport, a fine mesh would be needed in order to capture these rapid variations around the vessels. This implicates the use of meshes where the location of the vessels is explicitly taken into account (i.e., conforming/body-fitted mesh illustrated in Fig. 2.5A). If not (i.e., non-corfoming mesh used as illustrated in Fig. 2.5B), then additional ingredients should be included to represent the microscale dynamics at subgrid scale. Such approach has not been yet used in the brain, thus the detailed modeling strategies used in other fields could be leveraged for that purpose. Particularly, we focus on flow in porous media and in fractured reservoirs [46–48] due to the similarities of these problems with ours.

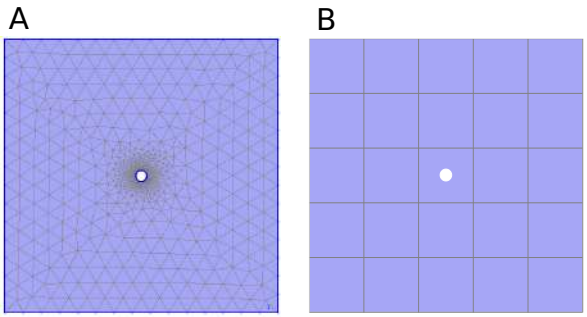

FIGURE 2.5 – **Conforming fine grid with 1288 elements and coarse cartesian grid with 25 elements.** Panel A : conforming mesh i.e., mesh that surrounds and accomodates the circular source that is representative of a fine-grid configuration. Panel B : coarse cartesian grid that disregards the precise location of the circular source and is representative of models that employ some type of coupling scheme.

In the following Sections, we thus discuss the advantages and shortcomings of other approaches that might be used to model solute transport in the brain microcirculation in order to state the specific requirements of a large scale model which are introduced in Section 2.5. In particular, in Section 2.4.2, we introduce the problem of flow in porous media due to its similar underlying mathematical structure to the molecular transport problem. We discuss how the pressure gradients building up around the fractures or wells are akin to the concentration gradients that appear around the vessels in the parenchyma. Then, in Sections 2.4.2 - 2.4.2,

we discuss the strategies found in the literature that tackle the same or similar problems in an efficient manner and that might be conducive to our goal of accurately modeling transport in large microvascular networks. Finally in Section 2.5, we discuss the necessary requirements of a multiscale model and how different ingredients of the strategies introduced here can be leveraged.

Mathematical form of single phase, uncompressible flow in porous media

The mathematical resemblance of Darcy's law for flow in a porous medium and Fick's law of diffusion provide a link with the many similar problems that have been tackled for years in reservoir engineering, geosciences, and many others. In reservoirs, when certain characteristics are present (e.g., semi-periodicity of the pore network, newtonian fluid, large-scale mechanical equilibrium), the Stokes equations of flow at the pore scale (equivalent to the microscale in our case, as displayed in Fig. 2.2C) can be averaged to obtain an upscaled description in terms of the large-scale pressure [49] through Darcy's equation

$$\nabla \cdot (K_D \nabla P) = 0 \tag{2.16}$$

where K_D represents the hydraulic conductivity tensor (m mmHg^{-1} s^{-1}) and P denotes the large-scale average pressure (mmHg). For simplicity, we consider an isotropic and homogeneous porous medium that allows to write K as an scalar parameter. It is worth noting that despite the entirely different physical processes governing flow in porous media compared to steady state diffusion-reaction in the parenchyma, their underlying mathematical formulations are remarkably similar. In fact, if we consider metabolic consumption to be null ($M = 0$) in the parenchyma, the steady state diffusion problem in the parenchyma reads

$$\nabla \cdot (D_p \nabla \phi) = 0 \tag{2.17}$$

Due to the large aspect ratio of blood vessels, a common strategy employed consists of representing the vessels in the microcirculation as line sources of solute in the parenchyma

$$\nabla \cdot (D_p \nabla \phi) + q\delta_\Lambda = 0 \tag{2.18}$$

where q represents the molecular exchanges between vessels and parenchyma (see equations 2.12 and 2.14), and δ_Λ, which is a delta function, restricts the flux q to the centerlines of the network given the following property

$$\iiint_\Omega f\delta_\Lambda d\mathbf{x} = \int_\Lambda f dl \quad \forall f \tag{2.19}$$

Similarly, in oil reservoirs, a notable challenge is the modeling of wells due to the scale difference between well diameters and the size of the reservoir. Analogous to equation 2.18, these wells are often modeled as line source terms in the mass conservation equation [46; 47; 50; 51]

$$\nabla \cdot (K_D \nabla P) + q_w \delta_w = 0 \tag{2.20}$$

where q_w is the fluid flux provided by the well (m s^{-1}) constrained to the centerline of the well δ_w,. This flux is proportional to the difference in pressure between the well and the reservoir.

It's important to distinguish between the sizes of the different systems. For instance, a well typically has a diameter ranging from 10 to 100 cm, whereas a reservoir can extend over several kilometers. On the other hand, the diameter of blood vessels in microcirculation varies from 5-10 μm in capillaries to 10-20 μm in penetrating arterioles, while in the context of solute transport simulations in microcirculation, it's common to work with volumes smaller than 1 mm^3 [6; 34; 52]. Consequently, the difference in scale between wells and oil reservoirs is more significant compared to the scale difference between blood vessels and the surrounding tissue. This implies that simplifications such as modeling as line sources may be applicable in reservoir modeling but may not necessarily hold true in the microcirculation.

Our interest is using coarse meshes in order to 1) introduce few unknowns in the parenchyma and 2) avoid using the more complicated unstructured meshing procedures that adapt to the network geometry such as the one shown in Fig. 2.5A. Due to the proximity between vessels and the different spatial scales present in brain networks, separation of scales between the transport phenomena at the vessel scale and that of the network is not possible. Nevertheless, blood vessels remain slender structures embedded in a diffusive matrix (parenchyma), where similar modeling difficulties arise due to the large gradients arising around the vessels, similarly to the large gradients of pressure arising in the vicinity of the well in an oil reservoir. The modeling strategy of including the vessels as line sources (equation 2.18) allows us to focus on the modeling strategies that can be leveraged from the reservoir modeling literature [46–48; 51; 53] that deal with the modeling of the large near source gradients of the scalar field i.e., concentration or pressure.

Thus, in the following Sections, we explore various approaches from the literature that address solute transport challenges in microcirculation and related problems, such as fluid flow in reservoirs. The focus lies in the resolution of the extravascular problem, modeled via equation 2.18. Therefore, when discussing the matrix structure obtained, we focus on the transport problem in the prenchyma, while not dealing with the coupling with intravascular transport (equation 2.12) for now. We present these approaches in descending order of fidelity to the fine-scale features. We begin in Section 2.4.2, where the original tubular geometry of blood vessels is preserved. Subsequently, we introduce different models that employ the simplified delta formulation introduced earlier in this Section. Finally, our review of approaches ends in Section 2.4.2, where we examine models that permit the coarsest meshes of the parenchyma, which constitute the most significant reductions in computational costs.

Fine-grid models - original network geometry

To perform direct numerical simulations of the problem, it is essential to employ a mesh that conforms to or is body-fitted to the network's geometry. This is exemplified in the work by Fang et al. [54], whose mesh is equivalent to that in Fig. 2.6A. The primary challenge of this approach lies in mesh generation. It necessitates a fine-grid to accurately represent the network's geometry, leading to a substantial increase in the number of unknowns owing to the required fine resolution, while the resolution of the problem in an unstructured grid with FE is straight forward [55]. Nevertheless, the unstructured grid produces a sparse but disorganized matrix depicted in the left panel of Fig. 2.6A. This, and the great size of the mesh needed even for a few vessels renders this approach unpractical for large networks. Essentially, this represents a brute force approach where the complicated perivascular dynamics are tackled by increasing the numerical resolution around the sources, as in [54]. Due to the 3D nature of the resolution of transport in both compartments we denote this approach as a 3D intravascular

- 3D extravascular (3DIV-3DEV) coupled transport model.

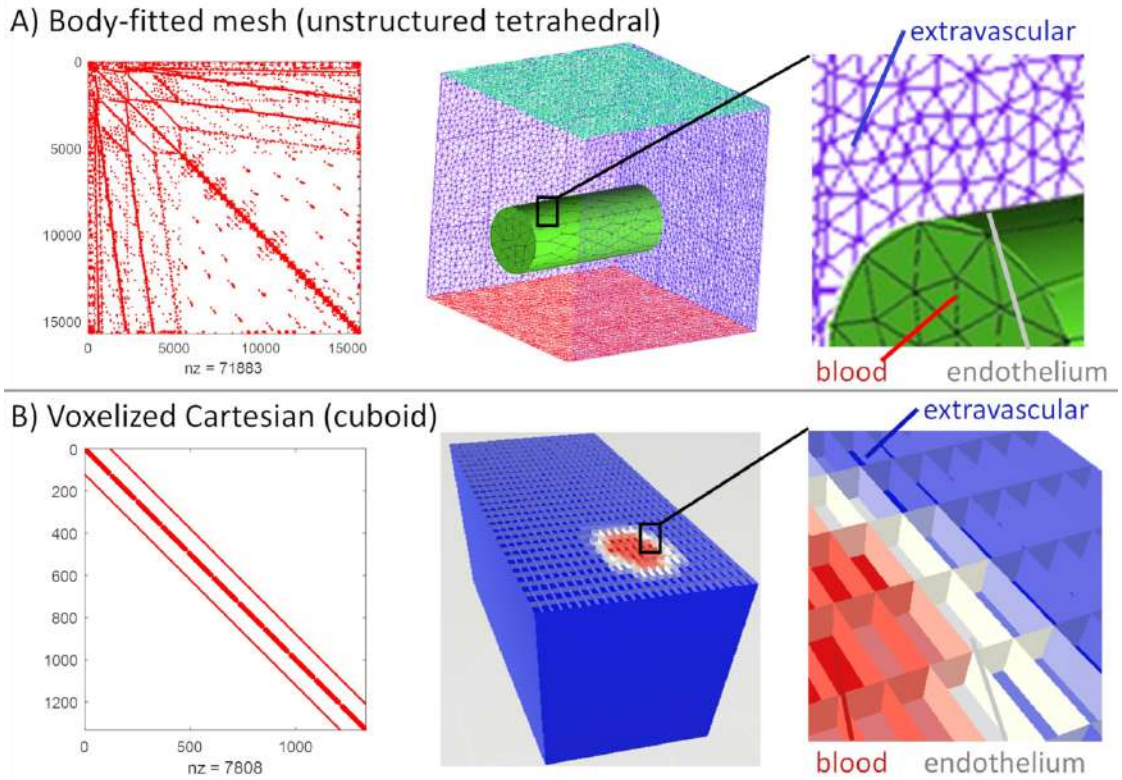

FIGURE 2.6 – **Illustrations of two fine grid approaches conforming to the geometry of the vascular system**. Panel A : unstructured mesh in the same spirit of [54]. Both the extravascular and the intravascular meshes conform to the cylindrical geometry of the vessels, while the endothelium is represented by the interface between the two domains. On the left side, the density profile of the resulting matrix associated with the linear problem in the parenchyma is shown. Panel B : structured cartesian ("voxelized") mesh not conforming to the geometry of the vessels. The mesh size is small enough to capture the endothelium represented in white. Cartesian meshes of this type combined with a FV discretization of the diffusion problem provide a sparse and structured matrix shown on the left side of the panel. Figure taken from [35]

Another fine-grid strategy involves the use of a cartesian grid so small that it can accommodate the smallest geometrical structures taking place in the vascular system [35; 56], as illustrated in Fig. 2.6B. This approach avoids the cumbersome body-fitted meshing procedure by increasing even more the resolution of the grid. The increase in the size of the system is somewhat compensated by the resulting sparse matrix with diagonal structure and narrow bandwidth shown in Fig. 2.6B. However, the fact that the grid needs to be of characteristic size of the same order as the vessel wall (approximately 1 µm), renders it impractical for large networks. Any greater mesh size than the smallest details of the vessel wall would misrepresent the endothelial wall, and therefore, would provide an inaccurate estimation of the vessel-tissue exchanges. Thus, due to size constraints, this approach is also impractical for large vascular networks.

Fine-grid models - simplified network geometry

We now discuss the models that take advantage of the delta formulation in equation 2.18 to represent the vessels as a network of infinitesimally thin lines. Following the same convention as in Section 2.4.2, these approaches fall under the 1DIV-3DEV models.

One notable feature of these models is their treatment of vessels as lines without explicitly

modeling microscale dynamics around them. Instead, they rely on local refinement strategies focused on the line sources, as detailed in [57]. This approach offers distinct advantages. The resulting matrices are exceptionally sparse, aligning well with conventional Finite Element (FE) or finite volume (FV) schemes, which efficiently handle elliptic equations, e.g., (equation 2.18). Additionally, accommodating non-linearities and different types of boundary conditions (BCs) is straightforward.

However, a drawback emerges from the necessity of local refinement and unstructured meshing (see Fig. 2.7). This leads to larger system sizes that are not scalable. Additionally, the unstructured mesh does not provide a banded matrix, but rather a sparse but unstructured matrix similar to the depiction in Fig. 2.6A. Inherently, this approach goes against our primary goal of modeling large microvascular networks due to the great amount of unknowns produced by locally refined meshes.

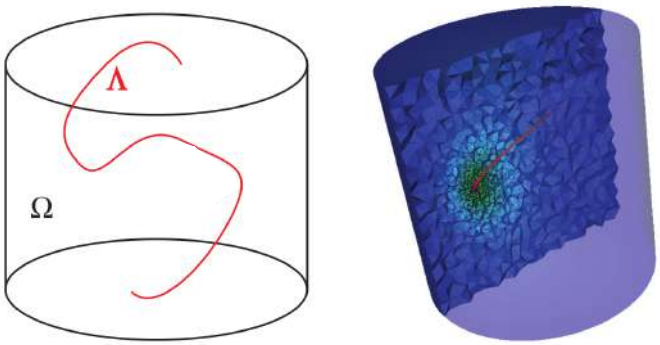

FIGURE 2.7 – **Illustration of a graded mesh around the a vessel reduced to an infinitesimally thin line.** On the left : the 3D domain $\Omega \subset \mathbb{R}^3$ and the embedded line $\Lambda \subset \mathbb{R}$. On the right : cross-section of the graded mesh around the embedded line. Figure taken from [58].

Semi-analytical models

By semi-analytical models, we refer to models based on a Green's function approach [6; 32], which are prevalent in the field oxygen transport in the brain cortex [23; 59–64]. The strategy consists in reducing the vascular system to a collection of point sources distributed along the vessels' centerlines. The extravascular concentration field is thus reconstructed by summing the impulse response (i.e., fundamental solution or Green's function) of the non-reactive mass transport equation (equation 2.8 with $M = 0$). The approach is inherently linear, as it relies on the summation of independent impulse responses, making it particularly suitable for scenarios with either negligible or constant metabolic consumption. These methods are referred to as 'semi-analytical' because they reconstruct the spatial dynamics of the concentration field using the fundamental solution, i.e., Green's function, which comprises a sum of analytical functions. Nevertheless, due to the complex organization of the vascular system, the vascular network needs to be meshed, introducing some numerical ingredients, notably the discretization of the vascular system.

Moreover, the inevitable challenge for Green's function type approaches is the satisfaction of the boundary conditions, which is the most computationally intensive part [52]. These semi-analytical methods belong to a a larger class of boundary integral methods (e.g., the boundary element method), in which the idea is to avoid a volume mesh of the domain by meshing only the boundaries. That way, the satisfaction of the boundary conditions can be achieved by finding the bounded Green's function, i.e., finding an impulse response that

both satisfy the non-reactive mass conservation equation and the boundary conditions (the bounded Green's function of the problem) as in[6; 18; 52], or by also meshing the boundary of the parenchyma as commonly done in the boundary element method [55; 65] and using the free-space fundamental solution, which is easier to obtain.

The main advantage of Green's function methods is the lack of a volume mesh of the parenchyma, which results in a great decrease in the size of the matrix system while maintaining accuracy regarding the perivascular dynamics due to their analytical nature. This decrease in size comes at the expense of severely increasing the density of the matrix system. In conventional finite element or finite volume, generally, the matrices obtained are quite sparse due to the locality of the methods. Conversely, due to the infinite support of the fundamental solution, semi-analytical methods provide a matrix with no null values. This prevents parallelization and effectively renders the method not scalable. The lack of a sparse matrix system also challenges the resolution via iterative linear solvers. Additionally, the lack of a volume mesh reduces severely the size of the system, but prevents the inclusion of a reaction term via conventinal means, i.e., since there is no volume mesh, a reaction term is not straight forward to include. In Secomb et al., [6], they deal with the issue of non-linear metabolism in the parenchyma by homogeneously distributing a set of point sinks of mass throughout the parenchyma. Thereby, effectively negating the computational gain obtained by the lack of volume mesh. Overall, the aforementioned drawbacks render these approaches impractical for physiological configurations due to computational constraints.

Analytical coupling models

By analytical coupling models, we refer to those often used in reservoir modeling to include the highly conductive well [47; 48; 51; 66] when separation of scales is present (e.g., well/vessel much smaller than reservoir/parenchyma). These models originate from the Peaceman well model [46] which we reference often throughout this text. The shared characteristic among these is the use of an analytical solution for the near well pressure gradients (equivalent to our perivascular concentration gradients) to couple the scalar field inside the well to the coarse numerical solution of the much larger reservoir. In reservoir simulations, the scalar field is often the pressure. Due to the similar underlying mathematical structure of both problems (equations 2.18 and 2.20), similar numerical challenges arise, notably the modeling of large gradients around the sources. For that reason, many coupling methods would remain mostly unchanged when applied to the brain microcirculation. The main advantage of these methods is that they allow a coarse, cartesian mesh. A coarse mesh signifies fewer unknowns and cartesian signifies no need for a meshing algorithm and a structured sparse and diagonal matrix (see Fig. 2.6A).

A direct extension of these methods appears in [3] where they propose a hybrid approach that combines an explicit network model of flow as the one introduced in Section 2.2 with an upscaled description of the blood flow in the capillary bed through a Darcy-type law, which we denote as hybrid model. The influence of the arterio-venular trees appears as point sources of flux in the upscaled description of the capillary bed in a very similar manner as in equation 2.18. This is a challenging configuration where large gradients occur in the vicinity of the lower dimensional source. In Peyrounette et al. [3], the pressure field is modeled analytically in the neighbouring cells shown in blue and yellow in Fig. 2.8B. However, in this case, the separation of scales is not clear, i.e., the size of the vessels is not negligible compared to the size of the tissue. Therefore, the model necessitates of an additional treatment than traditional

well models.

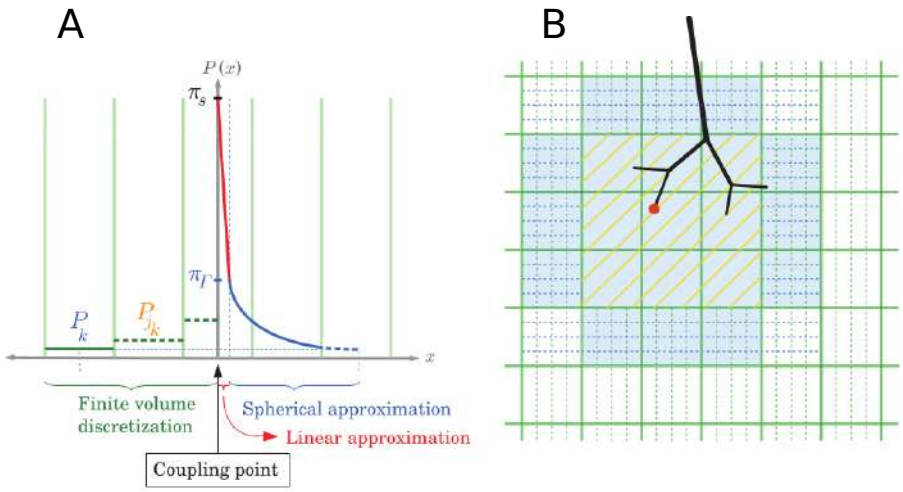

FIGURE 2.8 – **Example of analytical coupling schemes from [3].** Panel A : In blue and red the analytical coupling used for the point source of mass. Due to the lack of separations of scales a linear decay is added to the spherical decay characteristic of a point source of flux in 3D. Panel B : the colored cells (blue and yellow) illustrate the ones whose value is computed by the analytical coupling.

Another recent development of coupling models includes [67], where the delta distribution appearing in the mass conservation equation in the parenchyma (see equation 2.18) is spread into a cylinder of larger volume than the original vessel. The shape of the scalar field within the cylinder is computed a-priori (similarly to the linear-spherical profile shown in Fig 2.8A). This strategy allows to solve a secondary system that does not have such large gradients around the vessels due to the spreading and is more easily applied to the brain microcirculation due to the independence between the vessel position and the coupling scheme. However, this analytical approach necessitates strong assumptions that are usually not satisfied in the brain microcirculation, such as the lack of superposition of the cylinders that spread the source. This represents the main drawback of the a-priori computed perivascular field : these models require to compute a-priori the shape of the field around the sources that is usually acquired via a single source simulation or analytical solution. Evidently, this does not hold up in high density configuration due to the interactions between multiple nearby sources.

Overall, analytical coupling methods offer a flexible approach to include microscale dynamics into a larger structured mesh, which significantly reduces the meshing procedure, and therefore, the computational complexity of the problem. Thus, they allow an inexpensive solution to multiscale problems as long as scale separation is satisfied. The main disadvantage of these methods is the independence of each coupling function, that is, each microscale feature (e.g., line source representing a well in a reservoir, point source representing the end of the arterio-venular tree), is equipped with an analytical coupling function that normally resembles the fundamental solution of the problem. This poses a problem when the density of the lower dimensional sources is high, as it is in the brain microcirculation. Independent coupling functions do not account for interactions with nearby sources, which is expected to introduce errors in the solution when sources lie close together. Additionally, these methods generally lack flexibility regarding the support of the analytical coupling (e.g. yellow and blue regions in Fig. 2.8), which effectively locks the resolution of the coarse grid to a given value that must remain unchanged regardless of other constraints of the problem.

Coarse-grid models

In this Section, we encompass all models that use a coarse grid (as in Section 2.4.2) but do not use an analytical coupling model to relate the vascular concentration with the neighbouring cells in the 3D mesh. A clear example of such models is [8] where a coarse unstructured mesh is used together with a 1D simplification of the vascular system. This model does not use an analytical coupling scheme (Section 2.4.2), nor local mesh refinement (2.4.2 and 2.4.2) around the capillaries to accurately quantify the microscale dynamics. Therefore, we do not consider it as a plausible strategy since it does not model the perivascular gradients, thus neglecting the microscale dynamics.

Other approaches use a operator splitting framework [68–71] where a simpler problem is solved, generally using the semi-analytical methods discussed in Section 2.4.2, whose solution captures the perivascular concentration gradients. This analytical solution is then subtracted from the original problem with the goal of writing a new (third) problem. This third problem lacks the large gradients around the sources (since they are explicitly modeled by the analytical solution) and, therefore, can be solved numerically without the need for mesh refinement around the sources. The two solutions are then added to obtain a final concentration field. The need for mesh refinement is eliminated by subtracting the impact of the vessels on the overall concentration field, and the costly computation of the bounded fundamental solution (i.e., main drawback of the models in Section 2.4.2) is avoided as well.

However, since they are using the semi-analytical methods, there remains the challenge to deal with the non-local nature of the fundamental solution. Due to its infinite support, the problem remains highly coupled, which challenges parallelization and scalability of the approach. Nevertheless, these methods provide a good foundation due to the combination of the flexibility of semi-analytical methods (independence of network geometry) with the efficiency of analytical coupling methods.

Another operator splitting approach is the multiscale finite volume method (MSFV) [72; 73], which represents a versatile and efficient technique for tackling multiscale problems. Specifically, the MSFV method calculates microscale dynamics by solving a smaller numerical model beforehand of the dynamics around the sources/sinks. This eliminates the need for implementing a localization strategy, as microscale dynamics are modeled through a bounded numerical problem resolved in a pre-processing step. The key aspect of this approach is the coupling of a microscale solution around the sources with the coarse-grid FV discretization of the domain. In the subsequent Chapters, we draw inspiration from the MSFV method to establish a connection between coarse grid discretization and the microscale depiction of perivascular dynamics.

2.5 Strategy adopted

As presented in this Chapter, different types of ROMs exist that contribute to an important computational gain due to the associated reduction of the number of unknowns. We presented them in ascending order of computational efficiency, i.e., reduction in the quantity of unknowns, as well as the density of each associated matrix that dictates the ease to solve the linear system as well as the possibility of parallelization.

In the following Chapters, we aim at developing a multiscale model that expands upon the advantages of the models discussed in this Chapter. We now focus on the problem of interest

in this thesis : diffusion-reaction problem in the brain parenchyma coupled to advection-dispersion-reaction problem inside the vessels. In order to properly address the challenges faced by the specific configurations that arise in the microcirculation, in the next Section 2.5.1, we first discuss the characteristics required from an efficient numerical model for solute transport. Then, in Section 2.5.2, we discuss the strategy adopted to tackle the complex problem of solute transport in the brain microcirculation.

2.5.1 Characteristics of an efficient numerical model

The high density and amount of blood vessels generates a lack of scale separation between vessels and the parenchyma that remains a challenge for numerical methods. Our objective is to leverage the ingredients of the existing methods of Section 2.4 to develop a viable approach for modeling solute transport in the brain microcirculation. Below, we summarize our requirements for a multiscale model that bridges the micro and mesoscale and allows for the simulation of large microvascular networks

— Accuracy : concentration gradients drive extravascular transport [9; 11; 36; 74]. Therefore, an accurate approach must include the microscale spatial dynamics that take place around the capillaries. There will inevitably be errors associated with the modeling assumptions employed to reduce the size of the problem. For instance, the aforementioned models, with the exception of the direct numerical simulation of Section 2.4.2, all introduce simplifications of the geometry of the vessels to either cylindrical shapes or to thin lines. In the interest of accuracy, we use the approach introduced in Section 2.4.2 as reference solution for extravascular transport due to the accurate representation of the vascular network.

— Scalability : while representing microscale dynamics, the model must be applicable to large microvascular networks. This implies an intrinsic local nature of the numerical approach. Thus, we avoid the semi-analytical methods of Section 2.4.2 since they produce a fully coupled system where each source (i.e., vessel) depends on the molecular flux supplied by all the other vessels in the domain. Fine-grid models also pose a problem for scalability due to the need of a refined mesh around the sources. This results in rapid increase of the size of the problem when modeling larger volumes, explaining why such models generally remain within the range of around 100 vessels [34; 54; 58].

— Theoretical simplicity and conservativeness : One of the goals of this research includes direct application to imaging methods and to answer clinical questions. That implies the approaches described here must be tractable for non-mathematicians. We therefore prioritize the FV discretization scheme of the equations over FE due to its greater simplicity and similar accuracy. The FV discretization establishes a direct connection between physical quantities, such as molecular fluxes, and the discrete equations for each unknown. This results in a numerical scheme that is more intuitive and easier to comprehend, as it bridges the gap between physics and numerical computations. Furthermore, FV schemes enable the straightforward implementation of advective transport, which is valuable when modeling various media, such as tumors [75; 76]. Importantly, FV schemes are intrinsically conservative, which may not always be the case with FE methods. For these reasons, FV schemes are widely employed, particularly in microcirculation problems. [3; 8; 35; 44; 56]

2.5.2 Strategy of a multiscale model for solute transport modeling in the brain microcirculation

As discussed in Section 4.2.10, Berg et al., [33] introduced an effective intravascular transport model with one dimensional support. Due to the great reduction in complexity offered by a 1D model and the accuracy in modeling intravascular radial concentration gradients, we employ this approach to model the intravascular advection-dispersion-reaction.

For the parenchyma, the available solutions are more varied. We avoid the fine-grid methods (Sections 2.4.2 and 2.4.2) due to the large volume meshes used. Additionally, these methods lack the scalability necessary to model large microvascular networks. On the other hand, semi-analytical methods provide a theoretical framework that reduces substantially the size of the system through the use of the fundamental solution of the problem. However, they too lack scalability due to their fully coupled nature. We suggest to take advantage of the theoretical framework of Green's functions to obtain an analytical description of the perivascular gradients that is later coupled to a coarse cartesian mesh. That way, we can take advantage of the approaches in Section 2.4.2, i.e., coarse cartesian meshes that are not computationally expensive but allows conventional treatment of the boundary conditions and the reaction terms in the parenchyma.

In order to develop such a multiscale model that also satisfies the requirements cited in the previous Section, there are multiple features that do not yet exist in the literature. For instance, a localization scheme that couples an analytical description of the concentration field with the coarse mesh, or the integration of the non linear reaction term together with the analytical description of the perivascular gradients. Thus, in Chapters 3 and 4, we focus on the development of a multiscale model with these characteristics for 0DIV-2DEV and 1DIV-3DEV, respectively.

Therefore, we suggest to use the Green's function framework to design the analytical coupling between the network and a coarse mesh broadly leveraging the flux based formulation similarly to the MSFV developed in [72]. In particular, in the next Chapter, we develop the groundwork of the model through a 2D equivalent problem. A closely related problem was previously addressed using the MSFV approach in Wolfsteiner et al. [73]. Due to the explicit numerical computation of the gradients around the sources, the models based on the MSFV [72] offer an ideal balance between accuracy and computational complexity. Nevertheless, due to the the high vascular density in our case, a direct application of the MSFV would reduce to a fine-grid solution in the same spirit as the models discussed in Section 2.4.2. In the following Chapters, we propose a model that conserves the advantages of the MSFV while removing the pre-processing step by including many of the tools provided by the Green's function approaches.

2.6 References

[1] Johannes Reichold, Marco Stampanoni, Anna Lena Keller, Alfred Buck, Patrick Jenny, and Bruno Weber. Vascular Graph Model to Simulate the Cerebral Blood Flow in Realistic Vascular Networks. *Journal of Cerebral Blood Flow & Metabolism*, 29(8) :1429–1443, August 2009. 21

[2] S. Lorthois, F. Cassot, and F. Lauwers. Simulation study of brain blood flow regulation by intra-cortical arterioles in an anatomically accurate large human vascular network : Part I : Methodology and baseline flow. *NeuroImage*, 54(2) :1031–1042, January 2011. 22, 23

[3] Myriam Peyrounette, Yohan Davit, Michel Quintard, and Sylvie Lorthois. Multiscale modelling of blood flow in cerebral microcirculation : Details at capillary scale control accuracy at the level of the cortex. *PLOS ONE*, 13(1) :e0189474, January 2018. 22, 26, 35, 36, 38

[4] Amy F. Smith, Vincent Doyeux, Maxime Berg, Myriam Peyrounette, Mohammad Haft-Javaherian, Anne-Edith Larue, John H. Slater, Frédéric Lauwers, Pablo Blinder, Philbert Tsai, David Kleinfeld, Chris B. Schaffer, Nozomi Nishimura, Yohan Davit, and Sylvie Lorthois. Brain Capillary Networks Across Species : A few Simple Organizational Requirements Are Sufficient to Reproduce Both Structure and Function. *Frontiers in Physiology*, 10 :233, March 2019. 21

[5] Sylvie Lorthois, Paul Duru, Ian Billanou, Michel Quintard, and Pierre Celsis. Kinetic modeling in the context of cerebral blood flow quantification by H215O positron emission tomography : The meaning of the permeability coefficient in Renkin–Crones model revisited at capillary scale. *Journal of Theoretical Biology*, 353 :157–169, July 2014. 22, 26

[6] Timothy W. Secomb, Richard Hsu, Eric Y. H. Park, and Mark W. Dewhirst. Green's Function Methods for Analysis of Oxygen Delivery to Tissue by Microvascular Networks. *Annals of Biomedical Engineering*, 32(11) :1519–1529, November 2004. 26, 27, 29, 32, 34, 35

[7] K. Shaw, L. Bell, K. Boyd, D. M. Grijseels, D. Clarke, O. Bonnar, H. S. Crombag, and C. N. Hall. Neurovascular coupling and oxygenation are decreased in hippocampus compared to neocortex because of microvascular differences. *Nature Communications*, 12(1) :3190, May 2021.

[8] A. A. Linninger, I. G. Gould, T. Marinnan, C.-Y. Hsu, M. Chojecki, and A. Alaraj. Cerebral Microcirculation and Oxygen Tension in the Human Secondary Cortex. *Annals of Biomedical Engineering*, 41(11) :2264–2284, November 2013. 22, 23, 26, 27, 29, 37, 38

[9] Daniel Goldman. Theoretical Models of Microvascular Oxygen Transport to Tissue. *Microcirculation*, 15(8) :795–811, January 2008. 26, 27, 38

[10] Mark A. Mintun, Brian N. Lundstrom, Abraham Z. Snyder, Andrei G. Vlassenko, Gordon L. Shulman, and Marcus E. Raichle. Blood flow and oxygen delivery to human brain during functional activity : Theoretical modeling and experimental data. *Proceedings of the National Academy of Sciences*, 98(12) :6859–6864, June 2001.

[11] Charles Nicholson. Diffusion and related transport mechanisms in brain tissue. *Reports on Progress in Physics*, 64(7) :815–884, July 2001. 22, 26, 27, 38

[12] A R Pries, T W Secomb, P Gaehtgens, and J F Gross. Blood flow in microvascular networks. Experiments and simulation. *Circulation Research*, 67(4) :826–834, October 1990. 22, 23, 24

[13] David A. Boas, Stephanie R. Jones, Anna Devor, Theodore J. Huppert, and Anders M. Dale. A vascular anatomical network model of the spatio-temporal response to brain activation. *NeuroImage*, 40(3) :1116–1129, April 2008.

[14] Ian G. Gould and Andreas A. Linninger. Hematocrit Distribution and Tissue Oxygenation in Large Microcirculatory Networks. *Microcirculation*, 22(1) :1–18, January 2015.

[15] Rebecca J Shipley, Amy F Smith, Paul W Sweeney, Axel R Pries, and Timothy W Secomb. A hybrid discrete–continuum approach for modelling microcirculatory blood flow. *Mathematical Medicine and Biology : A Journal of the IMA*, March 2019. 22, 26

[16] Pablo Blinder, Philbert S Tsai, John P Kaufhold, Per M Knutsen, Harry Suhl, and David Kleinfeld. The cortical angiome : an interconnected vascular network with noncolumnar patterns of blood flow. *Nature Neuroscience*, 16(7) :889–897, July 2013. 22

[17] Nozomi Nishimura, Chris B. Schaffer, Beth Friedman, Patrick D. Lyden, and David Kleinfeld. Penetrating arterioles are a bottleneck in the perfusion of neocortex. *Proceedings of the National Academy of Sciences*, 104(1) :365–370, January 2007. 22

[18] Timothy W Secomb. Blood Flow in the Microcirculation. page 21, 2016. 23, 35

[19] A.R. Pries, K. Ley, M. Claassen, and P. Gaehtgens. Red cell distribution at microvascular bifurcations. *Microvascular Research*, 38(1) :81–101, July 1989. 23

[20] Romain Guibert, Caroline Fonta, and Franck Plouraboué. Cerebral Blood Flow Modeling in Primate Cortex. *Journal of Cerebral Blood Flow & Metabolism*, 30(11) :1860–1873, November 2010. 23, 24

[21] Brendan C. Fry, Jack Lee, Nicolas P. Smith, and Timothy W. Secomb. Estimation of Blood Flow Rates in Large Microvascular Networks : Flow Estimation in Microvessel Networks. *Microcirculation*, 19(6) :530–538, August 2012.

[22] Franca Schmid, Philbert S. Tsai, David Kleinfeld, Patrick Jenny, and Bruno Weber. Depth-dependent flow and pressure characteristics in cortical microvascular networks. *PLOS Computational Biology*, 13(2) :e1005392, February 2017.

[23] Paul W. Sweeney, Simon Walker-Samuel, and Rebecca J. Shipley. Insights into cerebral haemodynamics and oxygenation utilising in vivo mural cell imaging and mathematical modelling. *Scientific Reports*, 8(1) :1373, December 2018. 23, 34

[24] Adlan Merlo, Maxime Berg, Paul Duru, Frédéric Risso, Yohan Davit, and Sylvie Lorthois. A few upstream bifurcations drive the spatial distribution of red blood cells in model microfluidic networks. *Soft Matter*, 18(7) :1463–1478, 2022. 24

[25] Timothy W. Secomb and Axel R. Pries. Blood viscosity in microvessels : Experiment and theory. *Comptes Rendus Physique*, 14(6) :470–478, June 2013.

[26] A. R. Pries and T. W. Secomb. Microvascular blood viscosity in vivo and the endothelial surface layer. *American Journal of Physiology-Heart and Circulatory Physiology*, 289(6) :H2657–H2664, December 2005.

[27] B. Kaoui, G. H. Ristow, I. Cantat, C. Misbah, and W. Zimmermann. Lateral migration of a two-dimensional vesicle in unbounded Poiseuille flow. *Phys. Rev. E*, 77(2) :021903, February 2008. Publisher : American Physical Society.

[28] David Leighton and Andreas Acrivos. The shear-induced migration of particles in concentrated suspensions. *Journal of Fluid Mechanics*, 181 :415–439, 1987. Publisher : Cambridge University Press.

[29] Luca Lanotte, Johannes Mauer, Simon Mendez, Dmitry A. Fedosov, Jean-Marc Fromental, Viviana Claveria, Franck Nicoud, Gerhard Gompper, and Manouk Abkarian. Red cells' dynamic morphologies govern blood shear thinning under microcirculatory flow conditions. *Proceedings of the National Academy of Sciences*, 113(47) :13289–13294, November 2016.

[30] Gwennou Coupier, Badr Kaoui, Thomas Podgorski, and Chaouqi Misbah. Noninertial lateral migration of vesicles in bounded Poiseuille flow. *Physics of Fluids*, 20(11) :111702, November 2008. 24

[31] maxime Berg. Modélisation de l'écoulement sanguin et du transport de molécules dans la microcirculation sanguine cérébrale : impact des occlusions capillaires dans la maladie d'Alzheimer. page 160, 2019. 25

[32] C. Pozrikidis and D. A. Farrow. A Model of Fluid Flow in Solid Tumors. *Annals of Biomedical Engineering*, 31(2) :181–194, February 2003. 26, 27, 29, 34

[33] Maxime Berg, Yohan Davit, Michel Quintard, and Sylvie Lorthois. Modelling solute transport in the brain microcirculation : is it really well mixed inside the blood vessels ? *Journal of Fluid Mechanics*, 884 :A39, February 2020. 26, 27, 28, 29, 30, 39

[34] Luca Possenti, Alessandro Cicchetti, Riccardo Rosati, Daniele Cerroni, Maria Laura Costantino, Tiziana Rancati, and Paolo Zunino. A Mesoscale Computational Model for Microvascular Oxygen Transfer. *Annals of Biomedical Engineering*, 49(12) :3356–3373, December 2021. 27, 29, 32, 38

[35] Grant Hartung, Shoale Badr, Mohammad Moeini, Frédéric Lesage, David Kleinfeld, Ali Alaraj, and Andreas Linninger. Voxelized simulation of cerebral oxygen perfusion elucidates hypoxia in aged mouse cortex. *PLOS Computational Biology*, 17(1) :e1008584, January 2021. 26, 29, 33, 38

[36] Karl Erik Holter, Benjamin Kehlet, Anna Devor, Terrence J. Sejnowski, Anders M. Dale, Stig W. Omholt, Ole Petter Ottersen, Erlend Arnulf Nagelhus, Kent-André Mardal, and Klas H. Pettersen. Interstitial solute transport in 3D reconstructed neuropil occurs by diffusion rather than bulk flow. *Proceedings of the National Academy of Sciences*, 114(37) :9894–9899, September 2017. 26, 27, 38

[37] David G. Levitt. Capillary-tissue exchange kinetics : An analysis of the krogh cylinder model. *Journal of Theoretical Biology*, 34(1) :103–124, 1972. 27, 29

[38] GI Taylor. Conditions under Which Dispersion of a Solute in a Stream of Solvent can be Used to Measure Molecular Diffusion. *Proceedings of the Royal Society A*, 225(1163) :473–477, 1954. 27, 29

[39] Anthony J. McGoron, Pankajam Nair, and Roy W. Schubert. Michaelis-Menten kinetics model of oxygen consumption by rat brain slices following hypoxia. *Annals of Biomedical Engineering*, 25(3) :565–572, May 1997. 27

[40] P. W. Atkins and Julio De Paula. *Physical chemistry for the life sciences*. W.H. Freeman and Co. ; Oxford University Press, New York : Oxford, 2nd ed edition, 2011. OCLC : ocn695528594.

[41] Gideon Idumah, Erkki Somersalo, and Daniela Calvetti. A spatially distributed model of brain metabolism highlights the role of diffusion in brain energy metabolism. *Journal of Theoretical Biology*, 572 :111567, September 2023. 27

[42] David Attwell and Simon B. Laughlin. An Energy Budget for Signaling in the Grey Matter of the Brain. *Journal of Cerebral Blood Flow & Metabolism*, 21(10) :1133–1145, October 2001. 27

[43] J. D. Hellums. The resistance to oxygen transport in the capillaries relative to that in the surrounding tissue. *Microvascular Research*, 13(1) :131–136, 1977. 28

[44] Timo Koch, Martin Schneider, Rainer Helmig, and Patrick Jenny. Modeling tissue perfusion in terms of 1d-3d embedded mixed-dimension coupled problems with distributed sources. *Journal of Computational Physics*, 410 :109370, June 2020. 29, 38

[45] Ingeborg G. Gjerde, Kundan Kumar, Jan M. Nordbotten, and Barbara Wohlmuth. Splitting method for elliptic equations with line sources. *ESAIM : Mathematical Modelling and Numerical Analysis*, 53(5) :1715–1739, September 2019. 29

[46] D W Peaceman. Interpretation of Well-Block Pressures in Numerical Reservoir Simulation. *Society of Petroleum Engineers*, page 17, 1978. 30, 31, 32, 35

[47] I. Aavatsmark and R.A. Klausen. Well Index in Reservoir Simulation for Slanted and Slightly Curved Wells in 3D Grids. *SPE-75275-PA*, 8(01) :41–48, March 2003. Publisher : Society of Petroleum Engineers. 31, 35

[48] D. Y. Ding. Near-Well Upscaling for Reservoir Simulations. *Oil & Gas Science and Technology*, 59(2) :157–165, March 2004. 30, 32, 35

[49] Michel Quintard and Stephen Whitaker. Transport in chemically and mechanically heterogeneous porous media—III. Large-scale mechanical equilibrium and the regional form of Darcy's law. *Advances in Water Resources*, 21(7) :617–629, June 1998. 31

[50] Y. Ding and L. Jeannin. A Multi-Point Flux Approximation Scheme for the Well Modelling in Reservoir Simulations. 2000. Publisher : European Association of Geoscientists &amp ; Engineers. 31

[51] Savithru Jayasinghe, David L. Darmofal, Eric Dow, Marshall C. Galbraith, and Steven R. Allmaras. A Discretization-Independent Distributed Well Model. *SPE Journal*, 24(06) :2946–2967, December 2019. 31, 32, 35

[52] Richard Hsu and Timothy W. Secomb. A Green's function method for analysis of oxygen delivery to tissue by microvascular networks. *Mathematical Biosciences*, 96(1) :61–78, September 1989. 32, 34, 35

[53] D.Y. Ding, Y.S. Wu, and L. Jeannin. Efficient simulation of hydraulic fractured wells in unconventional reservoirs. *Journal of Petroleum Science and Engineering*, 122 :631–642, October 2014. 32

[54] Qianqian Fang, Sava Sakadžić, Lana Ruvinskaya, Anna Devor, Anders M. Dale, and David A. Boas. Oxygen advection and diffusion in a three-dimensional vascular anatomical network. *Optics Express*, 16(22) :17530, October 2008. 32, 33, 38

[55] D. Pepper, A. Kassab, and E. Divo. *Introduction to Finite Element, Boundary Element, and Meshless Methods : With Applications to Heat Transfer and Fluid Flow.* ASME Press, 2014. 32, 35

[56] Thomas Ventimiglia and Andreas A Linninger. MESH-FREE HIGH-RESOLUTION SIMULATION OF CEREBROCORTICAL OXYGEN SUPPLY WITH FAST FOURIER PRECONDITIONING. preprint, Bioengineering, January 2023. 33, 38

[57] Carlo D'Angelo and Anna Scotti. A mixed finite element method for Darcy flow in fractured porous media with non-matching grids. *ESAIM : Mathematical Modelling and Numerical Analysis*, 46(2) :465–489, March 2012. 34

[58] Carlo D'Angelo. Finite Element Approximation of Elliptic Problems with Dirac Measure Terms in Weighted Spaces : Applications to One- and Three-dimensional Coupled Problems. *SIAM Journal on Numerical Analysis*, 50(1) :194–215, January 2012. 34, 38

[59] Paul W. Sweeney, Angela d'Esposito, Simon Walker-Samuel, and Rebecca J. Shipley. Modelling the transport of fluid through heterogeneous, whole tumours in silico. *PLOS Computational Biology*, 15(6) :e1006751, June 2019. 34

[60] Yidan Xue, Theodosia Georgakopoulou, Anne-Eva van der Wijk, Tamás I. Józsa, Ed van Bavel, and Stephen J. Payne. Quantification of hypoxic regions distant from occlusions in cerebral penetrating arteriole trees. *PLOS Computational Biology*, 18(8) :e1010166, August 2022.

[61] Angela d'Esposito, Paul W. Sweeney, Morium Ali, Magdy Saleh, Rajiv Ramasawmy, Thomas A. Roberts, Giulia Agliardi, Adrien Desjardins, Mark F. Lythgoe, R. Barbara Pedley, Rebecca Shipley, and Simon Walker-Samuel. Computational fluid dynamics with imaging of cleared tissue and of in vivo perfusion predicts drug uptake and treatment responses in tumours. *Nature Biomedical Engineering*, 2(10) :773–787, October 2018.

[62] Louis Gagnon, Amy F. Smith, David A. Boas, Anna Devor, Timothy W. Secomb, and Sava Sakadžić. Modeling of Cerebral Oxygen Transport Based on In vivo Microscopic Imaging of Microvascular Network Structure, Blood Flow, and Oxygenation. *Frontiers in Computational Neuroscience*, 10, August 2016.

[63] Jose T Celaya-Alcala, Grace V Lee, Amy F Smith, Bohan Li, Sava Sakadžić, David A Boas, and Timothy W Secomb. Simulation of oxygen transport and estimation of tissue perfusion in extensive microvascular networks : Application to cerebral cortex. *Journal of Cerebral Blood Flow & Metabolism*, 41(3) :656–669, March 2021.

[64] Gang Liu, Feilim Mac Gabhann, and Aleksander S. Popel. Effects of Fiber Type and Size on the Heterogeneity of Oxygen Distribution in Exercising Skeletal Muscle. *PLoS ONE*, 7(9) :e44375, September 2012. 34

[65] Costas Pozrikidis and Joel H. Ferziger. Introduction to Theoretical and Computational Fluid Dynamics. *Physics Today*, 50(9) :72–74, September 1997. 35

[66] D.W. Peaceman. A New Method for Representing Multiple Wells With Arbitrary Rates in Numerical Reservoir Simulation. *SPE Reservoir Engineering*, 10(04) :253–258, November 1995. 35

[67] Timo Koch, Rainer Helmig, and Martin Schneider. A new and consistent well model for one-phase flow in anisotropic porous media using a distributed source model. *Journal of Computational Physics*, 410 :109369, June 2020. 36

[68] L. C. Woods. The relaxation treatment of singular points in Poisson's equation. *The Quarterly Journal of Mechanics and Applied Mathematics*, 6(2) :163–185, 1953. 37

[69] F. Drechsler, C.H. Wolters, T. Dierkes, H. Si, and L. Grasedyck. A full subtraction approach for finite element method based source analysis using constrained Delaunay tetrahedralisation. *NeuroImage*, 46(4) :1055–1065, July 2009.

[70] Ingeborg G. Gjerde, Kundan Kumar, and Jan M. Nordbotten. A Singularity Removal Method for Coupled 1D-3D Flow Models. Technical Report arXiv :1812.03055, arXiv, August 2019. arXiv :1812.03055 [cs, math] type : article.

[71] Ingeborg G. Gjerde, Kundan Kumar, and Jan M. Nordbotten. A singularity removal method for coupled 1D–3D flow models. *Computational Geosciences*, 24(2) :443–457, April 2020. 37

[72] P. Jenny, S. H. Lee, and H. A. Tchelepi. Adaptive Multiscale Finite-Volume Method for Multiphase Flow and Transport in Porous Media. *Multiscale Modeling & Simulation*, 3(1) :50–64, January 2005. 37, 39

[73] Christian Wolfsteiner, Seong H. Lee, and Hamdi A. Tchelepi. Well Modeling in the Multiscale Finite Volume Method for Subsurface Flow Simulation. *Multiscale Modeling & Simulation*, 5(3) :900–917, January 2006. 37, 39

[74] T.W. Secomb, R. Hsu, N.B. Beamer, and B.M. Coull. Theoretical Simulation of Oxygen Transport to Brain by Networks of Microvessels : Effects of Oxygen Supply and Demand on Tissue Hypoxia. *Microcirculation*, 7(4) :237–247, August 2000. 38

[75] C. Pozrikidis and J.M. Davis. Blood Flow Through Capillary Networks. In *Transport in Biological Media*, pages 213–252. Elsevier, 2013. 38

[76] Rebecca J. Shipley and S. Jonathan Chapman. Multiscale Modelling of Fluid and Drug Transport in Vascular Tumours. *Bulletin of Mathematical Biology*, 72(6) :1464–1491, August 2010. 38

Chapter 3

Oxygen transport in the parenchyma : 2D configuration

As we have seen in the previous Chapter, the problem of solute transport in the brain microcirculation is highly challenging. In particular, coupled transport between the intra- and extra-vascular compartments (i.e., microcirculation and parenchyma) presents significant difficulties because different modeling strategies are employed in each system. Furthermore, the hierarchical architecture and high vessel density in the brain tissue prevent the application of multiscale methods commonly used in other fields, such as well models [1; 2], or direct extension of flow models in the microcirculation [3; 4].

To advance our understanding of solute transport in brain microcirculation, it is essential to integrate the microscale dynamics into a mesoscale model capable of efficiently handling a large number of vessels. Notably, these microscale dynamics involve large perivascular concentration gradients around vessels that play a crucial role in oxygen delivery [5; 6]. However, accurate numerical modeling of these gradients is challenging because it requires either fine-grid models [7; 8], which are computationally expensive, or semi-analytical models [9; 10], which lack scalability.

In this chapter, we thus focus on transport in the parenchyma, aiming to establish the foundation for a multiscale solute transport model tailored to microcirculation. With the ultimate goal of developing a 1DIV-3DEV model, we lay the mathematical foundation through 0DIV-2DEV configurations in order to systematically test the limits of the modeling framework. This allows us to maintain the readability of the development and to establish the groundwork for the subsequent chapter. Our primary focus is to accurately quantifying the perivascular concentration gradients in an efficient manner, a significant challenge in the modeling of molecular transport, and a central aspect when interpreting experimental oxygenation data [11; 12]. Additionally, we emphasize the validation of assumptions made to ensure precise estimations of oxygen delivery and consumption, even as we simplify computational complexity. We conduct various tests to assess errors resulting from deviations from ideal configurations, providing a thorough evaluation of accuracy before applying the model to realistic microvascular scenarios.

The following section reproduces a manuscript submitted to PLOS Computational Biology.

3.1 Coarse grid approach for oxygen transport

Modeling oxygen transport in the brain: an efficient coarse-grid approach to capture perivascular gradients in the parenchyma.

David Pastor-Alonso[1], Maxime Berg[1,2], Franck Boyer[3], Natalie Fomin-Thunemann[4], Michel Quintard[1], Yohan Davit[1], Sylvie Lorthois*[1],

1 Institut de Mécanique des Fluides de Toulouse (IMFT), UMR 5502, Université de Toulouse, CNRS, Toulouse, France.
2 Department of Mechanical Engineering, University College London, London, United Kingdom.
3 Institut de Mathématiques de Toulouse (IMT), UMR 5219, Université de Toulouse, CNRS, UPS, Toulouse, France.
4 Department of Biomedical Engineering, Boston University, Boston, Massachusetts, United States of America.

*sylvie.lorthois@imft.fr

Abstract

Recent progresses in intravital imaging have enabled highly-resolved measurements of periarteriolar oxygen gradients (POGs) within the brain parenchyma. POGs are increasingly used as proxies to estimate the local baseline oxygen consumption, which is a hallmark of cell activity. However, the oxygen profile around a given arteriole arises from an interplay between oxygen consumption and delivery, not only by this arteriole but also by distant capillaries. Integrating such interactions across scales while accounting for the complex architecture of the microvascular network remains a challenge from a modelling perspective. This limits our ability to interpret the experimental oxygen maps and constitutes a key bottleneck toward the inverse determination of metabolic rates of oxygen.

We revisit the problem of parenchymal oxygen transport and metabolism and introduce a simple, conservative, accurate and scalable direct numerical method going beyond canonical Krogh-type models and their associated geometrical simplifications. We focus on a two-dimensional formulation, and introduce the concepts needed to combine an operator-splitting and a Green's function approach. Oxygen concentration is decomposed into a slowly-varying contribution, discretized by Finite Volumes over a coarse cartesian grid, and a rapidly-varying contribution, approximated analytically in grid-cells surrounding each vessel.

Starting with simple test cases, we thoroughly analyze the resulting errors by comparison with highly-resolved simulations of the original transport problem, showing considerable improvement of the computational-cost/accuracy balance compared to previous work. We then demonstrate the model ability to flexibly generate synthetic data reproducing the spatial dynamics of oxygen in the brain parenchyma, with sub-grid resolution. Based on these synthetic data, we show that capillaries distant from the arteriole cannot be overlooked when interpreting POGs, thus reconciling recent measurements of POGs across cortical layers with the fundamental idea that variations of vascular density within the depth of the cortex may reveal underlying differences in neuronal organization and metabolic load.

Author summary

The cerebral microvascular network is the logistics system that provides energy to brain cells at the right time and place. Blood flow and oxygen can now be observed dynamically in living rodents, which transformed our knowledge of the system and its role in ageing and disease. However, oxygen concentration at a given location is the result of a subtle balance between local cellular consumption, supply by neighboring vessels and their interconnections to distant ones. Thus, measurements are difficult to interpret without integrating this multi-scale component, which requires advanced computational models. This hinders our ability to bridge the gap between experiments in rodents and clinical applications in humans.

In this work, we focus on oxygen transport between vessels, leveraging recent advances in multi-scale modelling and their mathematical foundations. By this way, we formulate for the first time a simple, conservative, accurate and scalable computational model for cerebral oxygen across scales, that is able to integrate the spatially heterogenous distribution of vessels. We illustrate how this model, combined to imaging, will pave the way towards better estimates of oxygen consumption, a hallmark of neural activity that cannot be directly measured.

1 Introduction

Due to its highly specialized function, the brain is one of the organs with the highest basal energy demand. With essentially no substantial energy reserves, it is thus extremely vulnerable to sudden interruptions in oxygen and nutrients delivery by the blood, which can induce neuronal death within minutes with devastating consequences, e.g., for stroke victims [1]. It is also highly sensitive to chronic cerebral hypoperfusion, which can lead to progressive neurodegeneration and cognitive decline, not only in hypoperfusion dementia [2] but also, as increasingly accepted, in Alzheimer's disease [3–6]. However, despite its critical role in the transition between health and disease, many aspects of oxygen transport and metabolism in the brain remain poorly understood.

This motivated the development of high-resolution brain imaging techniques [7]. Together with the increased sophistication of experimental protocols, which enabled the brain of living rodents to be studied in various conditions including sleep, resting and awake states, these provide an unprecedented window on microvascular dynamics (e.g. diameters, red blood cell velocities, blood and tissue oxygenation, neural activity) [7–10]. However, due to the intrinsically heterogeneous and non-local nature of network flows [11–13], the results obtained in different conditions have been difficult to interpret. As we shall see next, this contributed to casting doubt on previously accepted ideas, including the fundamental idea that both structure and function of the brain microcirculation are subservient to cerebral metabolic demand.

With regard to brain function, the physiological role of neurovascular coupling, i.e. local surges in blood flow driven by increased neuronal activity (also referred to as functional hyperamia), has been questioned. On the one hand, even the baseline level of blood flow is indeed globally sufficient to supply oxygen to neurons with elevated levels of activity [12]. On the other hand, in the words of Drew [12], *"low-flow regions are an inescapable consequence of the architecture of the cerebral vasculature"* and *"cannot be removed by functional hyperemia"*. In fact, *"increases in blood flow – whether local or global – will serve only to move the location of the low-blood-flow regions, not eliminate them [13]"*.

With regard to structure, the local variations of vascular density have been believed for decades to reveal underlying differences in neuronal organization and metabolic

load [14–16], as a result of cerebral angiogenesis being driven by their oxygen requirements [17–19]. Recent breakthroughs in brain-wide vascular network imaging and reconstruction in rodents, associated to scaling analyses, support this vision at the scale of the whole brain [20]. However, detailed measurements of periarteriolar oxygen profiles across cortical layers in awake mice, associated with estimates of the corresponding cerebral metabolic rate of oxygen, recently suggested that baseline oxygen consumption may decrease with cortical depth, from Layer I to Layer IV [10], in contrast to the known increase of capillary density [20, 21].

Solving these apparent contradictions requires the development of models integrating the non-local nature of microvascular blood flow [11, 13, 22], which account for the complex architecture of brain microvascular networks but simplify or neglect transport and metabolism within the tissue, with models of oxygen dynamics going beyond the geometrical oversimplifications associated to Krogh-type analytical descriptions [10, 23–28].

However, the computational cost of simulating oxygen transport and consumption in the brain parenchyma by standard numerical methods, such as finite volume or finite element methods, is prohibitive. In fact, they imply to finely mesh the extravascular tissue so as to resolve the strong oxygen concentration gradients building up in the vicinity of each vessel (e.g. [29]), not to mention the technical challenge of automatically meshing its complex three-dimensional volume. A popular alternative, specifically designed to solve oxygen transport in the microcirculation, formulates the problem using Green's functions [30–34]. The non-local nature of this formulation allows the description of concentration gradients around microvessels while circumventing the need for meshing the intricate geometry of the extravascular space. However, it generally relies on the infinite domain form of the Green's function, making difficult the application of boundary conditions at the limits of the tissue domain (e.g. periodic boundary conditions). Additionally, oxygen metabolism exhibits non-linear behavior [23, 35], which is challenging to describe using Green's function and generally requires additional meshing [30, 36]. This, coupled with the non-local formulation at the core of the approach, requires the creation of large and dense matrices that are computationally costly to invert. Therefore, solving oxygen transport whether using standard methods or the Green's function approach limits the size of the regions that can be considered and hinders the potential of such methods to be used in inverse problems, where measured spatial oxygen dynamics are used to deduce local metabolic rate constants or permeability coefficients, which requires to run the direct problem many times. In the latter case, the spatial resolution of the solver is much higher than that of the measurements, which requires averaging of the numerical results, deviating from an optimal allocation of computational resources.

Such challenges have been bypassed by introducing dual mesh techniques, where the extravascular domain is coarsely meshed independently of microvessel locations [37], or by simplifying the mesh structure, e.g. based on cartesian grids, to approximate the extravascular domain [38]. These approaches decrease the computational cost, but do not leverage recent progresses in other fields, where analytical solutions to similar problems (analogous form of equations with same underlying mathematical structure) could be used to capture the smallest features of the extravascular oxygen field (perivascular gradients). This would circumvent the need of mesh refinement around the sources. In geosciences (well or fractured reservoir modelling), for example, coupling models are often used where analytical functions help provide a relationship between the highly conductive slender structures (commonly modeled as 1D sources) and the 3D simulation domain [39–45]. In particular, in operator-splitting approaches [46–48], the scalar field (concentration, pressure, heat, etc.) is decomposed into a slowly varying contribution and a rapidly varying contribution. The former can be solved numerically

over a coarse cartesian mesh, while the later can be approximated analytically, thus enabling a precise estimation of exchanges at the vessel-tissue interface as well as an *a posteriori* highly-resolved reconstruction of the concentration field in each mesh cell.

The goal of the present paper is to revisit the problem of oxygen transport and metabolism in the brain parenchyma to introduce a simple, scalable and accurate numerical method for its direct resolution. By simplicity, we mean the ability to use cartesian mesh cells independent of vessel locations, thus avoiding meshing the extravascular space, as well as the ability to impose various boundary conditions at the outer limits of the computational domain. By scalability, we refer to a mathematical formulation of the problem at the core of which is a low-bandwidth linear system of equations, so that the numerical resolution can be fully and efficiently parallelized. By accuracy, we mean the ability to control the numerical errors even in the case of a coarse mesh. Here, we present the associated concepts in two dimensions (Section 2), so as to increase the readability of the mathematical developments. This also permits to exploit current commercial finite element solvers, which enable to obtain reference solutions of the initial boundary value problem. This enables to carefully study how the underlying simplifications translate into numerical errors in idealized test cases that sequentially challenge these assumptions (Section 3). We then show how this model helps understanding the recent counter-intuitive experimental results on cortical oxygenation and metabolism [10, 24, 26] (Section 4). Finally, we discuss how this novel approach compares to previous work and how it will provide the groundwork for computationally affordable oxygen transport and metabolic simulations, fully coupled with intravascular transport in large microvascular networks.

2 Model and Methods

We first focus on the diffusive transport of oxygen in the brain parenchyma, i.e. the brain tissue except for blood vessels, denoted Ω_σ in Fig 1A, for which we present the general three-dimensional formulation in Section 2.1. We then restrict ourselves to a 2D configuration, where vessels are reduced to a collection of circular sources, as schematized in Fig 1B. This enables to maintain the readability of the mathematical developments, introduced from Section 2.2 onwards, without significant loss of generality. We finally consider oxygen consumption in Section 2.4.

2.1 Diffusive transport in the brain parenchyma

Following [22, 29, 49, 50], oxygen transport in the brain parenchyma is modeled through the following boundary-value problem (BVP):

$$\begin{cases} \nabla^2\phi = 0 & \text{in } \Omega_\sigma & \text{(1a)} \\ -\mathbf{n}\cdot(D\boldsymbol{\nabla}\phi) = K_m(C_v|_{R_j,\theta} - \phi|_{R_j,\theta}) & \text{on } \partial\Omega_{\beta,j}\ \forall j \in E(\Omega) & \text{(1b)} \\ \phi = \phi_D & \text{on } \partial\Omega & \text{(1c)} \end{cases}$$

where spatial domains Ω, $\partial\Omega$ and $\partial\Omega_{\beta,j}$ and outer normal $\mathbf{n}$ are defined in Fig 1 and ϕ [$\text{mol}\cdot\text{m}^{-3}$] and D [$\text{m}^2\cdot\text{s}^{-1}$] are the molar concentration field and the diffusion coefficient in the parenchyma, C_v [$\text{mol}\cdot\text{m}^{-3}$] is the intravascular molar concentration, K_m [$\text{m}\cdot\text{s}^{-1}$] is the diffusive permeability of the vessel wall and R_j [m] the radius of vessel $j \in E(\Omega)$. $E(\Omega)$ is the set of all vessels located in the domain, so that the total number of sources (S) is equal to the number of vessels, i.e., to the cardinality of $E(\Omega)$ ($S = \text{Card}(E(\Omega))$). In the example displayed in Fig 1A, $E(\Omega) = \{1, 2\}$ and $S = 2$. To keep the developments as simple as possible, we present the model with Dirichlet boundary conditions (BCs) (Eq. 1c), but our approach is readily available using

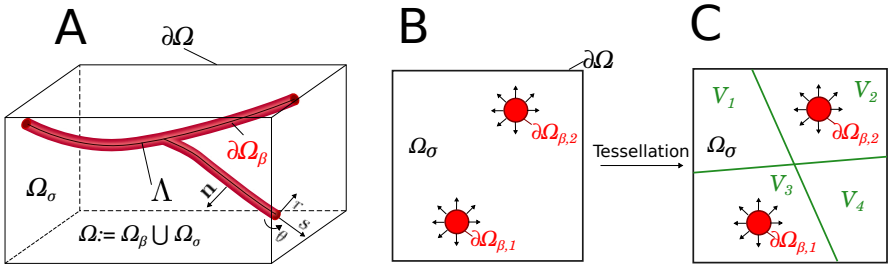

Fig 1. Terminology and notations for parenchyma and vessel spaces. Panel A represents a 3D region Ω of the brain tissue, which includes the parenchyma Ω_σ and the vessel space Ω_β. The external boundary is denoted by $\partial\Omega$, the vessel walls by $\partial\Omega_\beta$, the vessels center-lines by Λ, the curvilinear coordinate system for the vessels by (s, r, θ) and the outer normal to the vessel walls by $\mathbf{n}$. Panel B illustrates a 2D geometry, as used in the present paper to establish the modeling framework in Section 2, with two sources. The source walls are denoted by $\partial\Omega_{\beta,1}$ and $\partial\Omega_{\beta,2}$. Panel C displays one example of a tesselation of space Ω_σ into 4 sub-spaces V_k for $k = \{1, 2, 3, 4\}$. Here, only two sub-spaces contain sources, *i.e.*, $E(V_1) = E(V_4) = \varnothing$, $E(V_2) = \{2\}$, and $E(V_3) = \{1\}$.

Neumann and Periodic BCs as shown in the Results Section. Moreover, we follow [29, 36] and formulate the problem in terms of molar concentration, while most authors in the field use oxygen partial pressures [30, 37, 51, 52]. Partial pressures are indeed only strictly defined for a gas in a mixture of gases. The concept of partial pressure of oxygen in blood implicitly refers to gas-liquid equilibrium and can be manipulated in the case of a system at constant temperature and total pressure. Thus, we prefer to adopt in this paper a more general description of a multicomponent liquid mixture based on concentrations, as illustrated for instance in [53]. This can be accurately applied to any thermodynamic conditions, and offers a more versatile description of gas-liquid equilibrium, avoiding problems when, for instance in free-diving or high altitude, Henry's law coefficient is pressure dependent.

Due to the large aspect ratio of vessels and their low density in the tissue space, we neglect the azimuthal variations of the concentration field around the vessel walls so that Eq. 1b simplifies to:

$$-\mathbf{n} \cdot (D\boldsymbol{\nabla}\phi) = \frac{q_j(s)}{2\pi R_j} \text{ on } \partial\Omega_{\beta,j} \tag{2}$$

where $q_j(s)$ $[\text{mol} \cdot \text{m}^{-1} \cdot \text{s}^{-1}]$ is the integral molecular flux per unit length through the vessel wall at curvilinear abscissa s, defined as [22]:

$$q_j(s) = K_{eff}(\langle C_v(s)\rangle_j - \overline{\phi}_j(s)) \tag{3}$$

Here, $\langle C_v(s)\rangle$ is the cross-section averaged intravascular concentration:

$$\langle C_v(s)\rangle_j = \frac{1}{\pi R_j^2} \iint_{\Omega_{\beta,j}} C_v(s, r, \theta) dS \tag{4}$$

$\overline{\phi}_j$ is the perimeter-averaged extravascular concentration:

$$\overline{\phi}_j(s) = \frac{1}{2\pi R_j} \int_{\partial\Omega_{\beta,j}} \phi(s, R_j, \theta) dl \tag{5}$$

Finally, K_{eff} $[\text{m}^2 \cdot \text{s}^{-1}]$ can be deduced from the adimensional effective reaction rate that accounts for the impact of intravascular concentration gradients on the overall flux

at the vessel wall: $K_{eff} = 8\pi \frac{D_\beta}{1+\frac{4D_\beta}{K_m R_j}}$, where D_β is the diffusion coefficient in blood and K_m $[\mathrm{m} \cdot \mathrm{s}^{-1}]$ is the diffusive permeability of the vessel wall, as established for weak vessel-tissue couplings in [22]. This enables the use of the cross-section average intravascular concentration in Eq. 3.

Thus, the previous BVP simplifies into:

$$\begin{cases} \nabla^2 \phi = 0 & \text{in } \Omega_\sigma \quad (6a) \\ -\mathbf{n} \cdot (D \nabla \phi) = \dfrac{q_j(s)}{2\pi R_j} & \text{on } \partial\Omega_\beta \quad (6b) \\ \phi = \phi_D & \text{on } \partial\Omega \quad (6c) \end{cases}$$

together with Eqs. 3-5 which are needed to estimate $q_j(s)$ in Eq. 6b. Of course, a transport model in the intravascular network [22] is also needed to define $C_v(s)$, hence q_j, so that the developments in the present work focus on transport in the parenchyma and its coupling with the embedded intravascular network.

From now on, we restrict ourselves to a 2D configuration so that we can eliminate s from Eqs. 3-5 and 6b. As we shall see in Section 5, the 2D problem allows us to focus on radial transport, which provides the high perivascular concentration gradients and therefore poses the greatest challenge for the development of numerical approaches.

2.2 Operator-splitting

Getting inspiration from a large body of literature about mixed-dimensional problems, from well or fractured reservoir modelling in geosciences [39, 41, 54, 55] to multi-scale finite volume or operator-splitting methods in applied mathematics [45, 48, 56–58], we rewrite the previous BVP (Eqs. 6) by decomposing the concentration field into a slowly varying contribution $\mathfrak{z}$ and a rapidly varying contribution $\mathfrak{r}$:

$$\phi(\mathbf{x}) = \mathfrak{z}(\mathbf{x}) + \mathfrak{r}(\mathbf{x}) \quad (7)$$

so that $\mathfrak{r}$ will account for the large near-source concentration gradients while $\mathfrak{z}$ will account for the slower contributions of the domain boundary and the sources located further away.

We further introduce a tesselation $\mathscr{F}$ of space Ω_σ into F sub-spaces V_k, so that $\Omega_\sigma := \bigcup_{k \in \mathscr{F}} V_k$ as schematized Fig 1C. The rationale for this will be apparent in Section 2.3.2, where we present the specific analytical expression chosen for the rapid term, with a localization strategy that maintains conformity with the finite volume (FV) mesh introduced to discretize the equations in Section 2.3.

For now, let us decompose $\mathfrak{r}$ and $\mathfrak{z}$ as sums of functions which must be continuous-by-part on tesselation $\mathscr{F}$:

$$\mathfrak{r}(\mathbf{x}) = \sum_{k \in \mathscr{F}} \mathfrak{r}_k(\mathbf{x}) \quad \text{with} \quad \mathfrak{r}_k(\mathbf{x}) = 0 \; \forall \mathbf{x} \notin V_k \quad (8a)$$

$$\mathfrak{z}(\mathbf{x}) = \sum_{k \in \mathscr{F}} \mathfrak{z}_k(\mathbf{x}) \quad \text{with} \quad \mathfrak{z}_k(\mathbf{x}) = 0 \; \forall \mathbf{x} \notin V_k \quad (8b)$$

and let us define $\mathfrak{r}_k$ as any function that satisfies:

$$\begin{cases} \nabla^2 \mathfrak{r}_k = 0 & \text{in } V_k \quad (9a) \\ -\mathbf{n} \cdot (D \boldsymbol{\nabla} \mathfrak{r}_k) = \dfrac{q_j}{2\pi R_j} & \text{on } \partial\Omega_{\beta,j} \; \forall j \in E(V_k) \quad (9b) \end{cases}$$

where $E(V_k)$ is the set of sources located inside V_k. This general definition ensures that $\mathfrak{r}_k$ accounts a minima for the rapid contribution of all sources within V_k. This, in turn, ensures the regularity of $\mathfrak{z}_k$ within V_k.

Substituting Eqs. 7 - 9 in Eq. 6 yields a BVP for each ϑ_k:

$$\begin{cases} \nabla^2 \vartheta_k = 0 & \text{in } V_k \quad (10a) \\ \mathbf{n} \cdot \boldsymbol{\nabla} \vartheta_k = 0 & \text{on } \partial\Omega_\beta \quad (10b) \\ \vartheta_k = \phi_D - \varkappa_k & \text{on } \partial\Omega \quad (10c) \end{cases}$$

These BVPs will be at the basis for the numerical finite-volume resolution of ϑ on a coarse mesh in the next Section. For that purpose, we also need to close the problem 10 by imposing continuity of concentrations ϕ and fluxes at the interfaces between any contiguous sub-spaces V_k and V_m of $\mathscr{F}$:

$$\begin{cases} \mathbf{n} \cdot (\boldsymbol{\nabla} \phi)\big|_{\partial V_{k,m}} = \mathbf{n} \cdot (\boldsymbol{\nabla} \phi)\big|_{\partial V_{m,k}} & (11a) \\ \phi\big|_{\partial V_{k,m}} = \phi\big|_{\partial V_{m,k}} & (11b) \end{cases}$$

where $\partial V_{k,m} = \partial V_{m,k}$ is the interface between these contiguous sub-spaces.

Using Eqs. 7 and 8 to substitute for ϕ, and reorganizing, we obtain:

$$\begin{cases} \mathbf{n} \cdot (\boldsymbol{\nabla} \vartheta_k - \boldsymbol{\nabla} \vartheta_m)\big|_{\partial V_{k,m}} = \mathbf{n} \cdot (\boldsymbol{\nabla} \varkappa_m - \boldsymbol{\nabla} \varkappa_k)\big|_{\partial V_{k,m}} & (12a) \\ (\vartheta_k - \vartheta_m)\big|_{\partial V_{k,m}} = (\varkappa_m - \varkappa_k)\big|_{\partial V_{k,m}} & (12b) \end{cases}$$

Therefore, the final BVP for each ϑ_k is:

$$\begin{cases} \nabla^2 \vartheta_k = 0 & \text{in } V_k \quad (13a) \\ \mathbf{n} \cdot \boldsymbol{\nabla} \vartheta_k = 0 & \text{on } \partial\Omega_\beta \quad (13b) \\ \vartheta_k = \phi_D - \varkappa_k & \text{on } \partial\Omega \quad (13c) \\ \mathbf{n} \cdot \boldsymbol{\nabla} \vartheta_k = 0 & \text{on } \partial\Omega_\beta \quad (13d) \\ \mathbf{n} \cdot (\boldsymbol{\nabla} \vartheta_k - \boldsymbol{\nabla} \vartheta_m)\big|_{\partial V_{k,m}} = \mathbf{n} \cdot (\boldsymbol{\nabla} \varkappa_m - \boldsymbol{\nabla} \varkappa_k)\big|_{\partial V_{k,m}} & (13e) \\ (\vartheta_k - \vartheta_m)\big|_{\partial V_{k,m}} = (\varkappa_m - \varkappa_k)\big|_{\partial V_{k,m}} & (13f) \end{cases}$$

where $\varkappa_k$will be given as analytic functions of variables q_j in Section 2.3.2 and ϑ_k will be obtained numerically. Such a set of BVPs could typically be further discretized and solved by domain decomposition methods [56]. Here however, the strong perivascular gradients are accounted for by the rapid term. To minimize the number of unknowns, we introduce in the next Section a FV discretization where a single grid-cell is associated to each sub-space V_k of tessellation $\mathscr{F}$.

2.3 Assembly of a system of discrete algebraic equations

For that purpose, we set tessellation $\mathscr{F}$ to match a cartesian grid of cell side-length $h = |\partial V_{k,m}|$, where m is a direct neighbour of k (i.e $m \in \mathscr{N}^k$) with:

$$\mathscr{N}^k := \{n, s, e, w\} \quad (14)$$

as defined in Fig 2.

From this point forward, we use symbol $\tilde{}$ to represent the discrete average values of a field on each FV cell k. Noteworthy, for harmonic functions such as $\vartheta(\mathbf{x})$, from Gauss's harmonic function theorem [59], if we neglect the small volume occupied by the

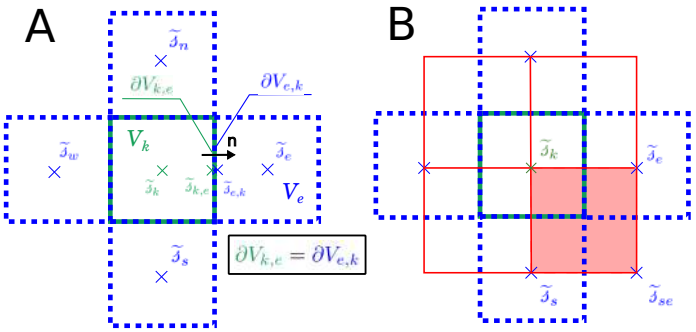

Fig 2. Terminology and notations for the FV discretization (A) and sub-grid interpolation (B). Panel A displays the current cell k of the cartesian mesh in green and its direct neighbours $\mathcal{N}^k = \{n, s, e, w\}$ in blue. $\widetilde{\jmath}_k$ is the value of the slow term at the center of cell k. The dummy variables $\widetilde{\jmath}_{k,e}$ and $\widetilde{\jmath}_{e,k}$ represent the values of the slow term on both sides of the interface $\partial V_{k,e}$. Generally, $\widetilde{\jmath}_{k,e} \neq \widetilde{\jmath}_{e,k}$ due to the jump introduced by Eqs. 12. Panel B displays the dual mesh used for sub-scale interpolation in red. This dual mesh is constructed by joining the centers of the FV grid. Its cells are denoted by numbers $(0, 1, 2$ and $3)$.

vasculature ($\approx 3\%$ [60]), this average value can be approximated at second-order by the value at the cell's center.

Therefore, the unknowns of the system are the values of the slow term at the center of each FV cell $\widetilde{\jmath}_k$, and the vessel-tissue flux for each source q_j. These are represented by two vectors of discrete variables $\boldsymbol{\jmath} = \{\widetilde{\jmath}_1, \widetilde{\jmath}_2, \widetilde{\jmath}_3, ..., \widetilde{\jmath}_F\}$ and $\mathbf{q} = \{q_1, q_2, q_3, ..., q_S\}$, respectively.

2.3.1 FV discretization for the slow term

The gradient of the slow term is approximated by the Two Point Flux Approximation (TPFA):

$$(D\boldsymbol{\nabla}\jmath_k(\mathbf{x}) \cdot \mathbf{n})\Big|_{\partial V_{k,m}} \approx D\frac{\widetilde{\jmath}_{k,m} - \widetilde{\jmath}_k}{h/2} \tag{15}$$

where h is the size of the FV cell face $h = |\partial V_{k,m}|$ and $\widetilde{\jmath}_{k,m}$ are dummy variables, to be eliminated by substitution from the final system, which represent the values of the slow term on interfaces $\partial V_{k,m}$.

Additionally, we use the classic FV formulation by integrating Eq. 13a over each FV cell k (see Section A in S1 Methods for more detail). This yields:

$$-4\widetilde{\jmath}_k + \sum_{m \in \mathcal{N}^k} \widetilde{\jmath}_{k,m} = 0 \tag{16}$$

The discrete versions of boundary conditions 13e and 13f are:

$$\begin{cases} D\dfrac{\widetilde{\jmath}_{k,m} - \widetilde{\jmath}_k}{h/2} - D\dfrac{\widetilde{\jmath}_m - \widetilde{\jmath}_{m,k}}{h/2} = \dfrac{1}{h}\displaystyle\int_{\partial V_{k,m}} \mathbf{n} \cdot (D\boldsymbol{\nabla}\curlyvee_m(\mathbf{x}) - D\boldsymbol{\nabla}\curlyvee_k(\mathbf{x}))dl & \text{(17a)} \\ \widetilde{\jmath}_{k,m} - \widetilde{\jmath}_{m,k} = \dfrac{1}{h}\displaystyle\int_{\partial V_{k,m}} (\curlyvee_m - \curlyvee_k)dl & \text{(17b)} \end{cases}$$

From the above equations, we can express the dummy variables $\widetilde{\jmath}_{k,m}$ as follows:

$$\widetilde{\jmath}_{k,m} = \frac{\widetilde{\jmath}_k + \widetilde{\jmath}_m}{2} + \frac{J_{k,m}}{2} \tag{18}$$

with:

$$J_{k,m} = \frac{1}{2}\int_{\partial V_{k,m}} \mathbf{n}\cdot(\boldsymbol{\nabla}\text{ɾ}_m - \boldsymbol{\nabla}\text{ɾ}_k)dl + \frac{1}{h}\int_{\partial V_{k,m}} (\text{ɾ}_m - \text{ɾ}_k)dl \tag{19}$$

where $J_{k,m}$ is a function of the sources $\mathbf{q}$ as we shall see in Section 2.3.2, and it accounts for the discontinuities of the rapid term across the interfaces of the FV. We can express equation 16 as a function of the unknowns of the system:

$$-4\widetilde{\jmath}_k + \sum_{m\in\mathcal{N}^k}\left(\widetilde{\jmath}_m + J_{k,m}\right) = 0 \tag{20}$$

where $\widetilde{\jmath}_k$ and $\widetilde{\jmath}_m$ are found under the vector $\boldsymbol{\jmath}$.

Moreover, if the current mesh cell k belongs to a boundary, the boundary condition 10c is used instead of 17, yielding:

$$\widetilde{\jmath}_{k,\partial\Omega} = \phi_D - \text{ɾ}_{k,\partial\Omega} \quad \text{if} \quad \partial V_{k,\partial\Omega} \in \partial\Omega \tag{21}$$

Therefore, the discretized version of BVP 13 can be assembled from Eqs. 20 and 21 into an algebraic system with as many equations as grid-cells:

$$\mathbf{A}\cdot\boldsymbol{\jmath} + \mathbf{J} = \mathbf{b}_{\partial\boldsymbol{\Omega}} \tag{22}$$

where matrix $\mathbf{A}$ contains the classic diffusion stencil, and the vector $\mathbf{J}$ contains the values of J given by Eq. 19. Therefore, for each row k, $\mathbf{A}$ contains one diagonal value and 4 off-diagonal values associated to its neighbours, while the vector $\mathbf{b}_{\partial\boldsymbol{\Omega}}$ contains the entries relevant to enforce the BCs 21.

We have constructed a system of algebraic equations that enforces mass balance of the concentration field in each FV cell through Eq. 20. To go further, we must specify the choice of the rapid term that will allow the the entries of $\mathbf{J}$ to be deduced from Eq. 19. We note ɾ could be obtained numerically as in [56, 57], or approximated analytically based on the Green's function formulation, as detailed in the next Section.

2.3.2 Potential-based localized formulation for the rapid term ɾ

We first recall that, as written in Section 2.2, ɾ_k must be harmonic functions that satisfy Eqs. 9 for all k, ensuring to consider, a minima, the rapid contribution of all sources within V_k.

Straightforward analytical approximations for ɾ_k in 2D are therefore:

$$\text{ɾ}_k = \sum_{j\in E(\widehat{V}_k)} P_j \tag{23}$$

where $\widehat{V}_k$ represents any extension of V_k, i.e. any region of space containing V_k, and P_j is the single-source potential associated to source j.

According to potential theory [61–63], P_j can be written as (see Section B in S1 Methods):

$$P_j = \begin{cases} \overline{\phi}_j + \dfrac{q_j}{2\pi D}\ln\Big(\dfrac{R_j}{||\mathbf{x}-\mathbf{x}_j||}\Big) & \text{if } ||\mathbf{x}-\mathbf{x}_j|| > R_j \\ \overline{\phi}_j & \text{if } ||\mathbf{x}-\mathbf{x}_j|| \le R_j \end{cases} \tag{24}$$

With this explicit definition of the potentials, the expression of the rapid term (Eq. 23) only depends on the vessel-tissue exchanges ($\mathbf{q}$) and on the position $||\mathbf{x}-\mathbf{x}_j||$, so that $\text{ɾ}_k = \text{ɾ}_k(\mathbf{q};\mathbf{x})$. From this expression of the rapid term, now we have an explicit definition of $\mathbf{J}$ from Eq. 22 as a function of the vessel-tissue exchanges $\mathbf{q}$. We can thus assemble the discrete system of equations with $\boldsymbol{\jmath}$ and $\mathbf{q}$ as follows:

$$\mathbf{A} \cdot \mathfrak{z} + \mathbf{B} \cdot \mathbf{q} = \mathbf{b}_{\partial\mathbf{\Omega}} \tag{25}$$

Noteworthy, $\mathscr{r}_k$ strictly fulfills the constraints corresponding to Eqs. 9 if and only if there is a single source i in $\widehat{V}_k$, for which $\mathbf{x}_i \in V_k$. Any additional source j in $\widehat{V}_k$ induces a perturbation $\varepsilon^q_{i,j}$:

$$\varepsilon^q_{i,j} = -\mathbf{n} \cdot (D\boldsymbol{\nabla} P_j)\big|_{\partial\Omega_{\beta,i}} \tag{26}$$

of the normal flux around source i (see Section C in S1 Methods), which is not accounted for in the model. However, the integral contribution of these errors is null so the model remains conservative (Section C in S1 Methods). The impact of this perturbation will be examined in the Results Section 3.3.

Inspired by our previous work in [64], we set $\widehat{V}_k$ to correspond to a finite number n^2 of cells in the finite-volume mesh, with $n \geq 3$ to avoid a special treatment for sources lying on the interface between two mesh cells.

By this way, n sets up the characteristic size of the region in which we account for the contribution of nearby sources to $\mathscr{r}_k$, while the contribution of sources outside $\widehat{V}_k$ is only implicitly treated through $\mathfrak{z}_k$, as illustrated in Fig 3. Thus, increasing n leads to a better approximation of the concentration field (see Section 2.3.4), but at the same time increases the density of matrix $\mathbf{B}$ in Eq. 25. In the limit case where $\widehat{V}_k = \Omega$, we would obtain an element-wise non-zero $\mathbf{B}$, leading to a non-sparse system similar to [30, 51, 65] where the boundary integrals of the classic Green's function formulation are estimated by $\mathfrak{z}$. Since the goal here is to obtain a sparse linear system, $\widehat{V}$ ($\widehat{V} \subset \Omega$) is chosen to be small in comparison to the domain of computation, but large enough to include the near source gradients.

The estimation of the single source potential based on the Green's integral formulation has a natural extension to 3D. The circular sources that appear in the 2D model provide a simple formulation to the potential since the double layer potential is null (see Section B in S1 Methods). In contrast, an open cylinder provides a non-null value for the double layer integral resulting in a second potential in Eq. 24 [51] which accounts for the axial variations. The rest of the developments presented in Section 2.3, including FV discretization and localization of the slow term, can be simply extrapolated to 3D.

2.3.3 Sub-grid reconstruction to estimate vessel-tissue exchanges (q)

The vessel-tissue exchanges are governed by Eq. 3, which in 2D translates into:

$$q_j = K_{eff}(\langle C_v \rangle_j - \overline{\phi}_j) \tag{27}$$

for each source $j \in E(\Omega)$. In 3D, this equation should be coupled to an intravascular transport problem that introduces a discrete 1D description of average intravascular concentrations along vessel centerlines [22] as additional unknowns (see e.g. [45, 66]). In our 2D case, however, sources are disconnected, so that the values of $\langle C_v \rangle_j$ are provided as boundary conditions. The average wall concentration is given by:

$$\overline{\phi}_j = \frac{1}{2\pi R_j} \oint_{\partial\Omega_{\beta,j}} \phi(\mathbf{x}) dl \tag{28}$$

However, the numerical model only provides an approximation of the concentration field at the grid-cell centers $\mathbf{x}_k$:

$$\widetilde{\phi}_k = \widetilde{\mathfrak{z}}_k + \mathscr{r}_k(\mathbf{q}, \mathbf{x}_k) \tag{29}$$

and, from Eq. 21, at the boundary nodes.

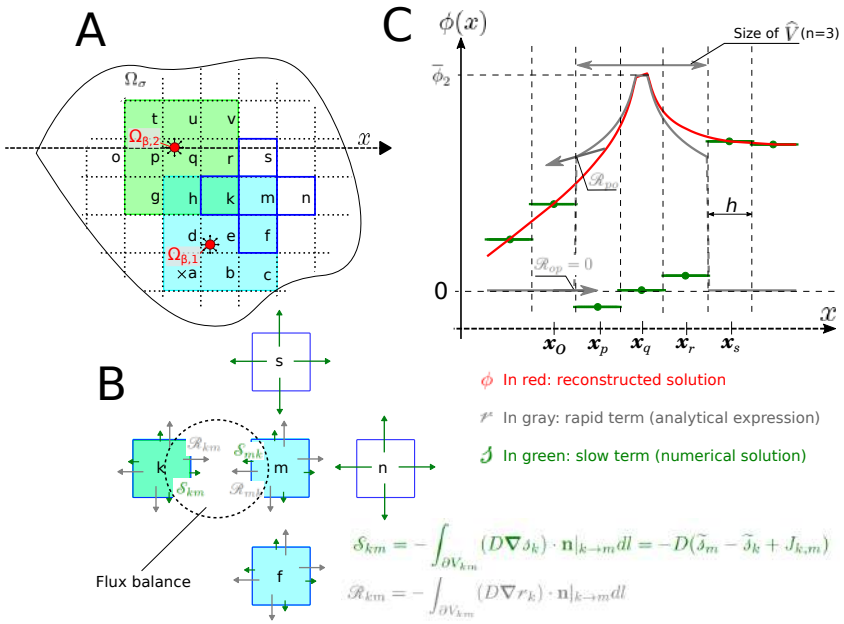

Fig 3. Localization strategy illustrated for two sources with neighbourhood $\widehat{V}_k$ of size 3x3 grid-cells (i.e., $n = 3$). Panel A: Cells where the rapid term accounts for source 1 and source 2 are displayed in blue and green respectively, with superposition in cells h and k, so that $\mathscr{r}_w = P_1\ \forall w \in \{a, b, c, d, e, f, m\}$, $\mathscr{r}_w = P_2$ $\forall w \in \{g, p, q, r, t, u, v\}$ and $\mathscr{r}_w = P_1 + P_2\ \forall w \in \{h, k\}$; cells lying further from sources 1 and 2 are displayed in white. In these cells, $\mathscr{r}_w = 0$; Panel B: Flux balance for all cells highlighted in dark blue in panel A. Green arrows represent the contributions of slow terms while grey arrows those of rapid terms. The latter may exhibit jumps, e.g. at interfaces V_{km} and V_{nm} due to the localization-induced discontinuities in the rapid term. Panel C: Concentration field decomposition (Eq. 7) along the x-axis crossing the center of source 2 (dashed axis in Panel A). We show in red the fine-grid reconstructed solution through Eq. 30, in green the coarse-grid slow term and in grey the rapid term.

To estimate $\overline{\phi}_j$ from Eq. 28, we must reconstruct the concentration field everywhere in Ω_σ. For that purpose, we interpolate the slow term from its values at x_k and $x_{k,\partial\Omega}$ using a classical set of linear shape functions γ_i associated to these points, as defined in Section D in S1 Methods. We also introduce a extended rapid term $\mathscr{r}_i^c$ bridging the discontinuities across the interfaces of the FV cells $\partial V_{k,m} \forall k \in \mathscr{F}\ \&\ m \in \mathscr{N}^k$, as detailed in Section D in S1 Methods. The resulting interpolation function $\mathscr{J}_\phi$ reads:

$$\mathscr{J}_\phi(\boldsymbol{\mathscr{J}}, \mathbf{q}; \mathbf{x}) = \sum_{i\in\mathscr{T}} \gamma_i(\mathbf{x})(\widetilde{\mathscr{J}}_i + \mathscr{r}_i^c(\mathbf{q}; \mathbf{x})) \tag{30}$$

where $\mathscr{T}$ represents the set of FV grid-cell centers x_k and of boundary nodes $x_{k,\partial\Omega}$.

Since both $\mathscr{J}_k$ and $\mathscr{r}_k$ are harmonic functions in V_k, the average needed to estimate $\overline{\phi}_j$ in Eq. 28 can be deduced from Gauss's harmonic function theorem, yielding $\overline{\phi}_j = \mathscr{J}_\phi(\boldsymbol{\mathscr{J}}, \mathbf{q}; \mathbf{x}_j)$ so that Eq. 27 becomes:

$$q_j = K_{eff}(\langle C_v\rangle_j - \mathscr{J}_\phi(\boldsymbol{\mathscr{J}}, \mathbf{q}; \mathbf{x}_j)) \tag{31}$$

We can now assemble Eq. 31 into a discrete linear system of S equations with $\boldsymbol{\mathscr{J}}$ and $\mathbf{q}$ as vectors of unknowns:

$$\mathbf{C}\cdot\boldsymbol{\mathscr{J}} + \mathbf{D}\cdot\mathbf{q} = \mathbf{b}_{\partial\boldsymbol{\Omega}_\beta} \tag{32}$$

Noteworthy, the interpolation function $\mathscr{I}_\phi$ uses the nearby sources as well as the four nearest FV unknowns of the mesh grid (see Section D in S1 Methods). Therefore, matrix $\mathbf{C}$ is sparse, with 4 non-zero entries per line, while the density of matrix $\mathbf{D}$ depends on the size of $\widehat{V}$. Additionally, vector $\mathbf{b}_{\partial\mathbf{\Omega}_\beta}$ contains the values of intravascular concentrations ($\langle C_v \rangle_j$) treated here as boundary conditions.

2.3.4 Full discrete system and error induced by localization

The full discrete system is therefore:

$$\begin{cases} \mathbf{A} \cdot \boldsymbol{\mathscr{s}} + \mathbf{B} \cdot \mathbf{q} = \mathbf{b}_{\partial\mathbf{\Omega}} \\ \mathbf{C} \cdot \boldsymbol{\mathscr{s}} + \mathbf{D} \cdot \mathbf{q} = \mathbf{b}_{\partial\mathbf{\Omega}_\beta} \end{cases} \tag{33}$$

with a total of $F + S$ unknowns, $F = Card(\mathscr{F})$ being the total number of FV grid-cells and S the number of sources. This general form is independent of the specific choice made for the size of extensions $\widehat{V}_k$ used to define $\mathscr{r}_k$ as linear combinations of potentials based on the Green's formulation. This size, however, strongly influences the densities of matrices $\mathbf{B}$ and $\mathbf{D}$. Nevertheless, matrices $\mathbf{A}$ and $\mathbf{C}$ always remain sparse since $\mathbf{A}$ is the classic FV diffusion matrix with only 5 non-zero terms per line and $\mathbf{C}$ only depends on the interpolation function $\mathscr{I}_\phi$, resulting in 4 non-zero elements per line.

Of course, the global error resulting from approximating BVP 13 by the above system depends on the size of $\widehat{V}_k$. This global error $\varepsilon_{\widehat{V}}$ induced by the localization strategy can be estimated by considering the neglected contribution of sources outside of $\widehat{V}_k$ to the concentration field ($\sum_{j \notin E(\widehat{V}_k)} P_j$).

The error associated to FV methods is commonly given by [44]:

$$\varepsilon_{FV} < C_0 h^2 \tag{34}$$

where C_0 is bounded by the norm of the second derivative of the estimated field. Using Eq. 24 and considering that the minimal distance between a source in V_k and one outside $\widehat{V}_k$ is of order $(n-1)h/2$, we get an upper-bound of $\varepsilon_{\widehat{V}}$:

$$\varepsilon_{\widehat{V}} \leq \sum_{j \notin \widehat{V}_k} \frac{4 q_j}{2\pi D (n-1)^2 h^2} O(h^2) \tag{35}$$

Simplifying, we obtain:

$$\varepsilon_{\widehat{V}} < \sum_{j \notin \widehat{V}_k} \frac{4 q_j}{2\pi D (n-1)^2} O(1) \tag{36}$$

Therefore the localization error $\varepsilon_{\widehat{V}}$ is expected to decrease with n^2, i.e., $\varepsilon_{\widehat{V}} \propto \dfrac{1}{(n-1)^2}$.

2.4 Metabolism

Now that we have introduced the concepts and formulation for the non-reactive problem (BVP 6), we introduce tissue consumption, that we model by a Michaelis-Menten reaction kinetic [67]. In the resulting reactive problem, Eq. 6a is thus substituted by the following non-linear PDE:

$$D \nabla^2 \phi = M \frac{\phi}{\phi + K} \text{ in } \Omega_\sigma \tag{37}$$

where M [mol·m^{-3} · s^{-1}] is the maximal cerebral metabolic rate of oxygen, often denoted $\mathrm{CMRO}_{2,max}$, and K [mol · m^{-3}] represents the concentration where consumption is half of its maximum, often denoted EC_{50} for O_2 activating oxidative

phosphorylation [68]. The boundary conditions on ∂V_k given in Eqs. 13c - 13f remain unchanged. We consider D and M homogeneous to rewrite the PDE 13a

$$D\nabla^2 \mathscr{z}_k - M\left(1 - \frac{K}{K+\phi}\right) = 0 \quad \text{for } \mathbf{x} \in V_k \tag{38}$$

The new discrete system is:

$$\begin{cases} \mathbf{A}\cdot\boldsymbol{\mathscr{z}} + \mathbf{B}\cdot\mathbf{q} + \mathbf{S_{metab}} = \mathbf{b}_{\partial\boldsymbol{\Omega}} \\ \mathbf{C}\cdot\boldsymbol{\mathscr{z}} + \mathbf{D}\cdot\mathbf{q} = \mathbf{b}_{\partial\boldsymbol{\Omega}_\beta} \end{cases} \tag{39}$$

where $\mathbf{S_{metab}}$ is a vector containing the integral contributions of the metabolism per FV cell:

$$\mathbf{S_{metab}} = -\begin{Bmatrix} M(1 - \int_{V_1}\left(\frac{K}{K+\widetilde{\mathscr{z}}_1 + \mathscr{r}_1(\mathbf{x})}\right)dV) \\ M(1 - \int_{V_2}\left(\frac{K}{K+\widetilde{\mathscr{z}}_2 + \mathscr{r}_2(\mathbf{x})}\right)dV) \\ M(1 - \int_{V_3}\left(\frac{K}{K+\widetilde{\mathscr{z}}_3 + \mathscr{r}_3(\mathbf{x})}\right)dV) \\ \vdots \\ M(1 - \int_{V_F}\left(\frac{K}{K+\widetilde{\mathscr{z}}_F + \mathscr{r}_F(\mathbf{x})}\right)dV) \end{Bmatrix} \tag{40}$$

2.5 Numerical implementation

The problem is assembled and solved using an in house code written in Python. Due to the large reduction in size allowed by the multiscale model presented, the libraries scipy and numpy for solving linear problems are adequate for the 2D simulations and test cases. An extension to 3D is possible under careful consideration and optimization of the code.

The integrals in Eq. 19 and 40 are evaluated using the second order accurate Simpson's rule of integration [59]. Furthermore, the non-linear system assembled in Eq. 39 is classically solved through an iterative Newton-Raphson method (see Section E in S1 Methods).

2.6 Summary of model assumptions

Before examining the robustness, consistency and limitations of the above model in Section 3, we recall the two main assumptions introduced in the developments:

- *Assumption 1:* We considered that the concentration field could be split into a rapid and a slow component ($\mathscr{r}$ and $\mathscr{z}$, respectively). In practice, we thus considered the scale of variations of $\mathscr{z}$ to be much larger than the size of the coarse grid h, so that the slow field could be accurately evaluated using Eq. 20. Recalling that the slow term accounts for the contribution of the domain boundaries and of the sources located outside of $\widehat{V}$ (Section 2.2), this assumption should break down in the following cases:
  - *Case 1.1*: when h is not sufficiently small compared to the scale of variation driven by the boundary conditions, i.e., in simple cases, the size of the computational domain;
  - *Case 1.2*: when a source lies near the domain outer boundaries $\partial\Omega$;

- *Case 1.3*: when the neighbourhood $\widehat{V}$ is too small to accommodate accurately for the potentials arising from nearby sources.

- *Assumption 2:* We neglected the azimuthal variations of concentration around each source ($\phi|_{\partial\Omega_j} \approx \overline{\phi}_j$). As a result of Eq. 6b, we thus neglected the azimuthal variations of flux around the source's walls. This assumption is crucial to write the potential for a single source based on Eq. 24. Noteworthy, in contrast to Krogh-type models [10], these azimuthal variations are neglected only locally on the source walls. We expect this assumption to break down in the following cases:

  - *Case 2.1*: when two or more sources are lying close together, that is, when the density of sources becomes locally too large;
  - *Case 2.2*: when a source lies near $\partial\Omega$.

In the next Section, we use idealized test cases of increasing complexity that help decouple the impact of these different sources of errors and clarify the associated size constraints.

3 Results: error estimation

In this Section, we first consider test cases involving a single source (Section 3.1) and a single dipole, i.e., the combination of a single source and a single sink (Section 3.2). Then, in Section 3.3, we turn to multiple sources and sinks. Noteworthy, we generically designate by "source" any vessel j whose concentration is greater than the local tissue concentration, i.e., for which the resulting flux q_j will be positive. In the same way, we use "sink" for any vessel j whose concentration is lower than the local tissue concentration, i.e., for which the resulting flux q_j will be negative. This enables "diffusional shunts" in the parenchyma, which have been evidenced experimentally between arterioles and venules [69], to be considered.

Thus, for all simulations we assign $\langle C_v \rangle_j = \phi_{max}$ to all sources and $\langle C_v \rangle_j = 0$ to all sinks, where ϕ_{max} represents the oxygen concentration in penetrating arterioles at the inlet of the brain cortex. We also use a diffusion coefficient $D = 2 \times 10^{-5} \mathrm{cm}^2 \cdot \ \mathrm{s}^{-1}$ [25, 30, 70], an effective permeability for the capillaries of $K_{eff} = 2 \times 10^{-5} \mathrm{cm}^2 \cdot \mathrm{s}^{-1}$ [29, 30] and a maximum metabolic consumption of $M = 2.4\,\mu\mathrm{mol} \cdot \ \mathrm{cm}^{-3} \cdot \ \mathrm{min}^{-1}$ which falls within physiological range (see Table 1).

Moreover, for all test cases considered in this Section, we purposely put ourselves in *Case 1.1* above by considering relatively small domains of side $L = 240\mu$m, i.e., only 50 times larger than the source/sink radii ($R = 4.8\mu$m). In doing so, we aim at providing reasonable estimates for the upper bounds of the numerical errors.

Errors are estimated by comparison with a fine mesh finite element (FE) solution of the original BVP (Eqs. 1 for the linear problem or Eq. 37 for the non-linear problem) without any additional modeling assumptions, in the same spirit as [29]. This reference FE solution, ϕ_{ref}, was obtained with COMSOL Multiphysics using a triangular mesh fine enough to accommodate the contours of the circular sources, to handle the azimuthal variations of the concentration field around the sources and to ensure convergence in the estimation of q_{ref}, obtained by integrating the normal derivative of ϕ_{ref} along the vessel wall.

We define the following metrics to compare our multiscale model with this reference solution. The local errors on the vessel-tissue exchanges for each source (q_j) are given by:

$$\varepsilon_q^j = \frac{|q_j - q_{j,ref}|}{q_{j,ref}} \tag{41}$$

Variable	Value	Units	References
Microvascular parameters			
R_{PA}	20	μm	[10]
R_{cap}	4.8	μm	[10]
R_{cyl}	100	μm	[10]
Capillary length density	$[0.8, 1.2]$	$\mathrm{m} \cdot \mathrm{mm}^{-3}$	[20]
ϕ_{max}	137	$\mathrm{nmol} \cdot \mathrm{cm}^{-3}$	from [9,34,71]
Tissue transport and consumption			
D	2×10^{-5}	$\mathrm{cm}^2 \cdot \mathrm{s}^{-1}$	[25,30,70]
K_{eff}	2×10^{-5}	$\mathrm{cm}^2 \cdot \mathrm{s}^{-1}$	[29,30]
α	1.39×10^{-3}	$\mathrm{mol} \cdot \mathrm{m}^{-3} \cdot \mathrm{mmHg}^{-1}$	[24,28]
K	$\sim \phi_{max}/10$		from [23,30]
M	$[0, 2.4]$	$\mu\mathrm{mol} \cdot \mathrm{cm}^{-3} \cdot \mathrm{min}^{-1}$	[10,23,29]

Table 1. Parameter values. Radii R: see Fig 7; ϕ_{max}: oxygen concentration in penetrating arterioles at the inlet of the brain cortex; D: diffusion coefficient in the parenchyma; K_{eff}: effective diffusive permeability of the capillary walls; α: oxygen solubility in water at atmospheric pressure; M: maximum metabolic rate of oxygen; K: concentration where consumption is half of its maximum.

and the local errors on the concentration field at the center of each grid-cell are given by:

$$\varepsilon_\phi^k = \frac{|\widetilde{\phi}_k - \phi_{k,ref}|}{\phi_{k,ref}} \tag{42}$$

where $\widetilde{\phi}_k$ is given by Eq. 29. We then define the global errors as the average of the local errors:

$$\varepsilon_\phi^g = \frac{1}{F} \sum_{k \in [1,F]} \varepsilon_\phi^k \tag{43}$$

and:

$$\varepsilon_q^g = \frac{1}{S} \sum_{j \in [1,S]} \varepsilon_q^j \tag{44}$$

where where F is the number of discrete grid-cells in the cartesian mesh and S is the total number of sources, i.e., $S = Card(E(\Omega))$.

We consider the error on vessel-tissue exchanges (ε_q^g) as the main metric to assess the model's accuracy, since proper estimation of q_j's relies on an accurate evaluation of the microscale dynamics and provides crucial information on oxygen exchanged between blood and tissue. The error on the concentration field serves as a secondary metric, offering valuable insights into the interactions between sources.

We compare these errors with the errors resulting from a coarse-grid FV approach without multiscale coupling, in the same spirit as [37]. Such an approach solves the simplified BVP (Eqs. 6 for the linear problem or Eq. 37 for the non-linear problem) by approximating the average concentration on the vessel wall ($\overline{\phi}_j$) by the value of the concentration field in the nearest FV cell k ($\overline{\phi}_j = \widetilde{\phi}_k$ for $\Omega_{\beta,j} \in V_k$). As a result, the exchange term is given by

$$q_j = K_{eff}(\langle C_v \rangle_j - \widetilde{\phi}_k) \tag{45}$$

where k is the grid-cell containing source j. This coupling condition is not a multiscale coupling condition, as it doesn't integrate any description of the near source

concentration gradients that could compensate for the scale gap with the coarse-grid for the estimation of q_j. At its core, it assumes a well-mixed concentration within each mesh cell, i.e., it neglects the effect of concentration gradients near sources when using a coarse grid, generating significant errors in the estimation of q_j (see Figs 4-6). On the one hand, increasing mesh discretizations can solve this issue and allow to (asymptotically) recover the influence of such gradients [38], with the significant trade-off of increased computational cost. On the other hand, including a multiscale component by reconstructing analytically the local concentration near sources as done in Section 2, allows to capture the influence of the gradients whilst allowing to use a coarse-grid discretization of the tissue space. The FV solution with resolution matching that of the coarse-grid is thus useful to illustrate the interest of the multiscale coupling at the core of the developments presented in Section 2.

For the sake of comparison, the following conventions are used in all figure legends in this Section:

- Blue lines are used for the present multiscale method while red ones are used for the coarse-grid FV model.
- Continuous lines are used for the linear, non-reactive model (Eqs. 33) while discontinuous ones are used when metabolism is considered, i.e. reactive model (Eqs. 39).
- Square markers are used to display the global errors on the vessel-tissue exchanges while triangular ones are used to display errors on the concentration field.

3.1 Single source

In this Section, we focus on single source configurations, where we first assess the dependence of numerical errors on mesh size, in the case of coarse meshes (*Case 1.1*). We thus consider grid-cell sizes (h) varying from 20μm to 80μm, i.e. larger than the source radius and not so small compared to the domain side. In this case, we don't need to consider potentials arising from other sources (Eq. 26), thus drawing emphasis away from the size n of the neighborhood $\widehat{V}$ since its purpose is to control the cross influence among sources. We therefore opt for an approximately constant size of $\widehat{V}$ relative to the radius of the source R, fixed to $30R$. This corresponds to $n = 3$ in a 5x5 grid, as displayed in Fig 4A. The exact size of $\widehat{V}$ may slightly vary according to the discretization size h used, as $\widehat{V}$ consists of a discrete number of grid-cells.

Figure 4B illustrates the error evolution with respect to grid-cell size h for a single source, located at the center of the computational domain, and for a combination of boundary conditions (Dirichlet, Neuman, Periodic), as displayed in Fig 4A. Our multiscale model demonstrates remarkable accuracy, achieving global errors below 1% for both flux (q) and concentration (ϕ) estimates even with the coarser grids. Furthermore, these errors are about one order of magnitude smaller than those of the coarse-grid FV approach, since the later lacks a coupling scheme to bridge the scale gap between the source and the coarse-grid. Moreover, the multiscale model errors decrease monotonously with decreasing grid size. In contrast, the coarse-grid FV approach displays a minimum for grid-cells sizes of about $5R$, as expected from the Peaceman well model [39]. This model bridges the scale gap between the source and the coarse-grid scale as commonly done in geosciences, by relating the value of the scalar field inside the source to the grid via the following flux relationship:

$$q = \frac{K_{eff}(C_v - \widetilde{\phi}_k)}{1 + \frac{K_{eff}}{2\pi D}\ln(\frac{R}{0.2h})}$$

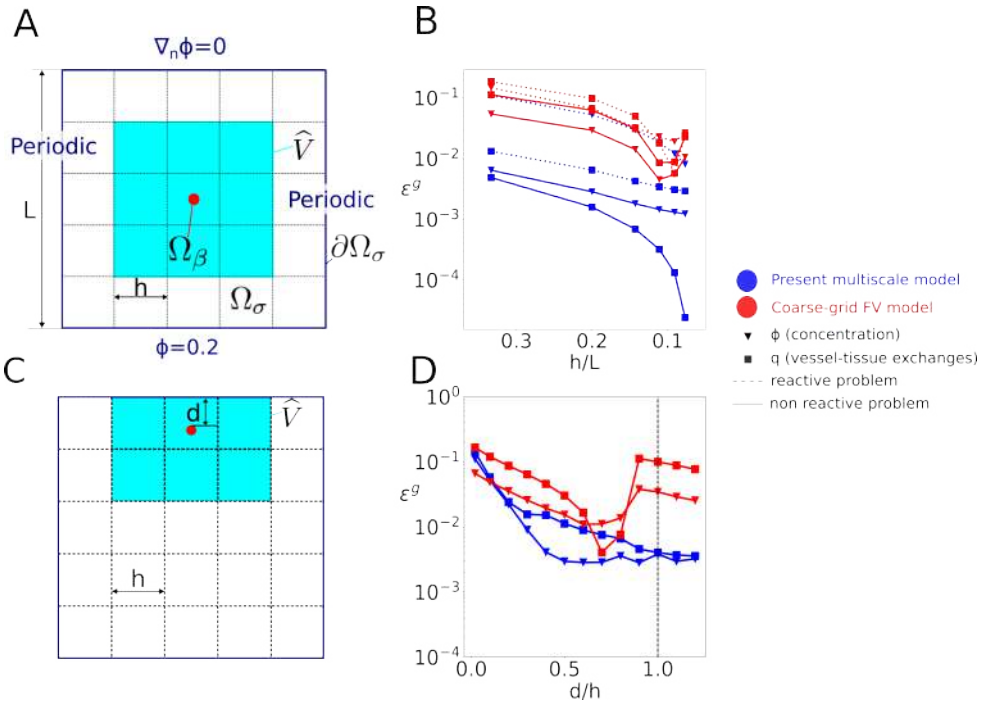

Fig 4. Error estimation for a single source: impact of discretization and boundary effects. A: schematics of the configuration under study, highlighting the detail of the boundary conditions. The domain size is $L = 240\mu$m, the source radius is $R = 4.8\mu$m, and the neighbourhood size is $(30R)^2$, i.e., $n = 3$ for a 5x5 grid (h/L=0.2); B: evolution of global errors as a function of grid size for the linear and non-linear problems, and for both the multiscale and the coarse-grid FV model (see legend); C: schematics of the boundary test, for which we use a mesh size $h/L = 0.2$, i.e., a 5x5 grid; D: evolution of global errors as a function of d, from $d = 0$ where the source is in contact with the no-flux boundary, to $d = 1.2h$ where the source lies in the contiguous grid-cell. The dashed vertical line illustrates the limit of the boundary cell.

When the radius of the source is a fifth of the side length of the grid-cell, the denominator in the above equation is equal to one, and the FV solution (Eq. 45) provides the same solution as the Peaceman well model. This occurs at the local minimum observed in Fig 4B, i.e. at approximately $h/L = 0.1$. The coarse-grid FV approach still exhibits errors between 10^{-2} and 10^{-1} for the smallest grid size considered in this study ($h \sim 4R$).

In contrast, a good balance between mesh-size and accuracy is achieved by the multiscale approach for the 5x5 grid ($h/L = 0.2$) with $n = 3$ (see Fig 4A), with errors on fluxes below 1% for both the linear and non-linear models (see Fig 4B). These parameters will thus be used next except as stated otherwise.

Because the source is located at the center of grid-cell V_k, the discrete value of the slow term in this grid cell $\widetilde{\mathfrak{z}}_k$ approximates well the local value of the slow term at source center $\mathfrak{z}(\mathbf{x}_k)$, so that the concentration $\widetilde{\phi}_k = \mathfrak{r}(\mathbf{x}_k) + \widetilde{\mathfrak{z}}_k$ directly enables the vessel-tissue exchanges to be evaluated using Eq. 27. However, this introduces inaccuracies when the source moves away from a grid-cell center, as illustrated in Fig A in S1 Figures, with errors ε_q^g up to 2.1% when the source is lying on a grid-cell corner. The interpolation scheme introduced in Section 2.3.3 reduces this errors to under 0.3% (Fig A in S1 Figures).

We now worsen the deviation from *Assumption 1* by reducing the distance d between the source and the no-flux boundary (*Cases 1.2* and *2.2*), as illustrated in Fig 4C. Errors reach up to $\approx 10\%$ when the source is in contact with the zero-flux boundary condition ($d = 0$), see Fig 4D. They decrease rapidly with increasing d, with $\varepsilon^q < 2\%$ as soon as there is half a grid-cell distance to the boundary. In contrast, the FV solution errors stay consistently around 10% even when the source belongs to a non-boundary grid-cell ($d/h > 1$), except for a minimum for $d/h \sim 0.7$. Similar to the Peaceman well model [39], the local minimum is likely obtained when the logarithmic decrease of the source potential is close to the discrete approximation of its gradient from values at the FV cell's center.

Overall, the single source test-cases highlight how coupling the analytical rapid term to the coarse-grid FV discretization of the slow term improves the numerical resolution of oxygen transport and metabolism within the tissue space. Importantly, these test-cases have been designed to push the limits of the corresponding underlying assumptions, by choosing small computational domains. Given the results shown in Fig 4, we expect to rarely find ourselves in conditions where $\varepsilon \geq 1\%$.

3.2 Single dipole

We now test the performance of the multiscale model for a single dipole, i.e., a single source ($\langle C_v \rangle_2 / \phi_{max} = 1$) and sink ($\langle C_v \rangle_1 = 0$). When these are placed close together in the same FV cell, we find ourselves in *Case 2.1*, and *Assumption 2* in Section 2.6 breaks down. In this case, models that don't integrate an analytical description of interactions among sources [37, 72] fail to capture the source to sink interactions. With increasing separation distance d between the source and sink, *Assumption 2* is recovered but, depending on the size of $\widehat{V}$, the deviation from *Assumption 1* may increase (*Case 1.3*). Thus, the dipole situation focuses on the interplay between source separation distance d and neighborhood size n and enables to compare the behavior of the model when the source and sink respective neighbourhoods overlap.

The local errors (equations 41 and 42) on the vessel-tissue exchanges are shown on Fig 5A as a function of the separation distance d, for the two neighborhood sizes presented in Panel B (n=3) and C ($n = 5$). In Panel D, we also show the reconstruction of the concentration field for $n = 3$ and $d = 60R$ using the interpolation function $\mathscr{I}_\phi$. This reconstruction closely approaches the FE reference solution obtained for a dense mesh of over $2,000$ grid cells (Fig B in S1 Figures), i.e, about 100 times the number of cells (5x5) needed to solve for the coarse-grid solution.

When the source and sink both lie in the same grid-cell, i.e., when d/R is below 40, the behavior of these local errors becomes similar whatever the neighbourhood size, since the cross-influence between their potentials is then calculated analytically by the rapid term. When there is no overlap between the two neighbourhoods (e.g. in Fig 5B and for d/R above 40 in the small neighborhood case, dark blue lines in Fig 5A), the errors increase significantly, reaching the upper-bound estimate of errors induced by localized formulation of the rapid term (Section 2.3.2), as evaluated by Eq. 36. In contrast, for a larger neighborhood size (light blue lines in Fig 5A and 5C), the errors quickly reach a plateau for an increasing separation distance d, consistent with the error obtained for a single source with similar discretization ($h/L = 0.2$ in Fig 4B). This underpins the residual error as the result of the coarse-grid resolution of the slow term and not of potential localization.

3.3 Multiple sources

We have shown how errors primarily build up when a source lies in the vicinity of a no-flux boundary (Fig 4B), and in lesser extent when two sources lie close to each other

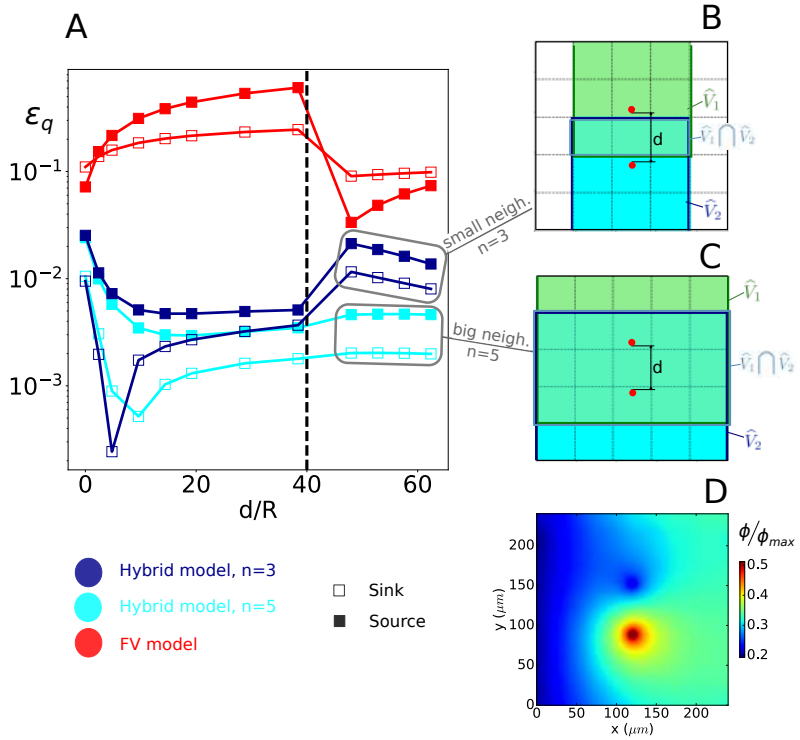

Fig 5. Error estimation for a single dipole: interplay between source/sink separation distance and neighborhood size. A: evolution of the local errors on vessel-tissue exchanges for the source (filled symbols) and for the sink (empty symbols) as a function of distance d between source and sink; B: schematics of the smaller-neighborhood configuration ($n = 3$); C: schematics of the large-neighborhood configuration ($n = 5$); D: reconstruction of the sub-grid concentration field for the case $n = 3$ and $d = 60 \cdot R$. The value of the concentration (ϕ) is non-dimensionalized by the value of the intravascular concentration in the source. The dashed vertical line in Panel A illustrates the transition between a situation where, for $n = 3$, the intersection of the source and sink neighborhoods contains both of them to a situation where the source and sink lie outside each other's neighborhood.

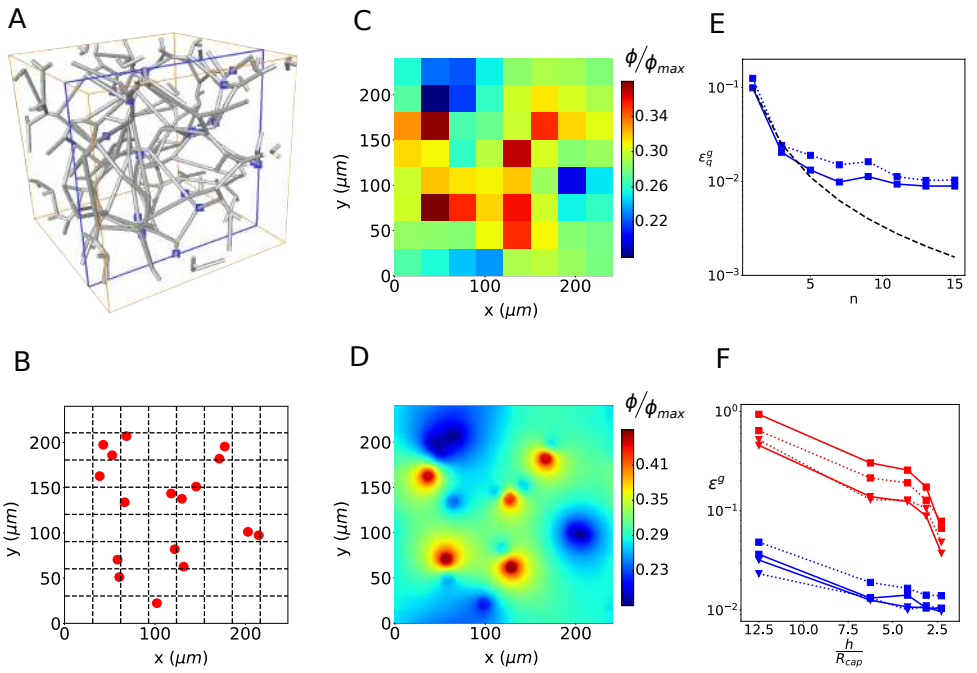

Fig 6. Error estimations for a realistic source distribution. A: synthetic capillary bed generated by the method of [60] with cutting plane highlighted in blue; B: intersections of each capillary vessel in A with the cutting plane (red dots) and coarse cartesian grid (dashed lines); C: coarse-grid solution for the concentration field $\widetilde{\phi}$ with metabolic consumption; D: sub-grid reconstruction of ϕ using $\mathscr{I}_\phi$ from Section 2.3.3. E: global errors on vessel-tissue exchanges estimations for a grid size $h = L/16$, therefore 256 FV cells in total. The curve $\frac{\kappa}{(n-1)^2}$ with $\kappa = 0.1$ is represented by the dashed black line; F: evolution of the errors in the estimation of the vessel-tissue exchanges and the concentration field with decreasing mesh cell size and with n chosen so that the size of $\widehat{V}$ is approximately $3L/5 = 30R$.

(Fig 5A), respectively. Both situations may arise frequently within the cortex, e.g., close to vessel bifurcations, where three vessel are connected in a single point.

Here, we thus consider a more realistic distribution of sources, obtained using a synthetic network that reproduces the structural and functional properties of cortical capillary beds, following [60] (Fig 6A). Briefly, we take a cross-section of such a network and map its intersections with each vessel (Fig 6A). We thus obtain a realistic map of source distribution, for which $S = 17$ (Fig 6B). We randomly assign one third of vessels to be sources and two third of vessels to be sinks, with periodic boundary conditions.

In Fig 6C and 6D, we show the coarse-grid concentration field and its reconstruction, respectively, for a 8x8 grid (h/L=0.125 and $h/R_{cap} = 6.25$) and $n = 5$. These clearly show that the model formulation enables enforcing the periodic boundary conditions for the reconstructed, highly-resolved, concentration field, as efficiently as the reference FE approach (Fig B in S1 Figures), even if periodicity at the boundaries doesn't propagate to the scale of the coarse-grid. Furthermore, the evolution of errors with neighbourhood size n (Fig 6E), follows the $1/n^2$ scaling predicted by Eq. 36, up to $n = 5$. For larger values of n, a plateau is reached, the value of which ($\sim 1\%$) corresponds to the residual error associated to deviations from *Assumption 2*, as shown in Sections 3.1 and 3.2. As a result, neither considering finer grid-cells nor increasing the neighborhood size n further reduce this residual errors (see Fig 6F and 6E, respectively).

Furthermore, we note that the numerical errors are only marginally affected when oxygen consumption is taken into consideration (dashed lines in Fig 6E and 6F), showing the robustness of our approach.

In contrast, errors corresponding to the coarse-grid FV model lie consistently one order of magnitude above than the one resulting from the multiscale approach.

4 Results: Periarteriolar oxygen concentration gradients

Now that we have shown the ability of our model to efficiently solve for the oxygen concentration field, including around vessels where gradients are the strongest, we turn to its exploitation in the context of brain metabolism. We specifically ask if variations of the radial peri-arteriolar concentration profiles that were recently measured across cortical layers in awake mice [10] could result from the layer-specific (laminar) increase of capillary density with cortical depth rather than from variations of baseline oxygen consumption.

For that purpose, we consider the typical case of a single penetrating arteriole (PA) and its surrounding tissue, as illustrated in Fig 7A. To account for the capillary-free space that encircles the PA, we include a cylindrical tissue region devoid of capillaries, with typical radius of 100 μm [10, 24]. Further away, we generate a random spatial distribution of sources with densities approximately matching the capillary density in cortical layer II (Table 2). We deduce the equivalent 2D source density (E2DSD) by using synthetic capillary networks similar to Section 3.3. We then create a randomized but statistically homogeneous distribution of sources following [60, 73]. We assign concentrations at the outer walls of the PA and capillaries, by using an asymptotically large value of K_{eff} and following experimental measurements in layer II [8]. For the capillaries, we assign a random distribution of normalized concentrations at capillary walls $\partial\Omega_{\beta,j}$, drawn from a Gaussian distribution with mean $\phi_{cap} = 0.45\phi_{PA}$ and standard deviation $\sigma = 0.1\phi_{PA}$, approximately corresponding to experimental measurements in layer II (Table 2). We also impose periodic boundary conditions on the limit of the domain to mimic the larger cortical space. Finally, the maximum metabolic rate of oxygen is chosen to be $M = 2.4\mu\text{mol} \cdot \text{cm}^{-3} \cdot \text{min}^{-1}$ (Table 1), an

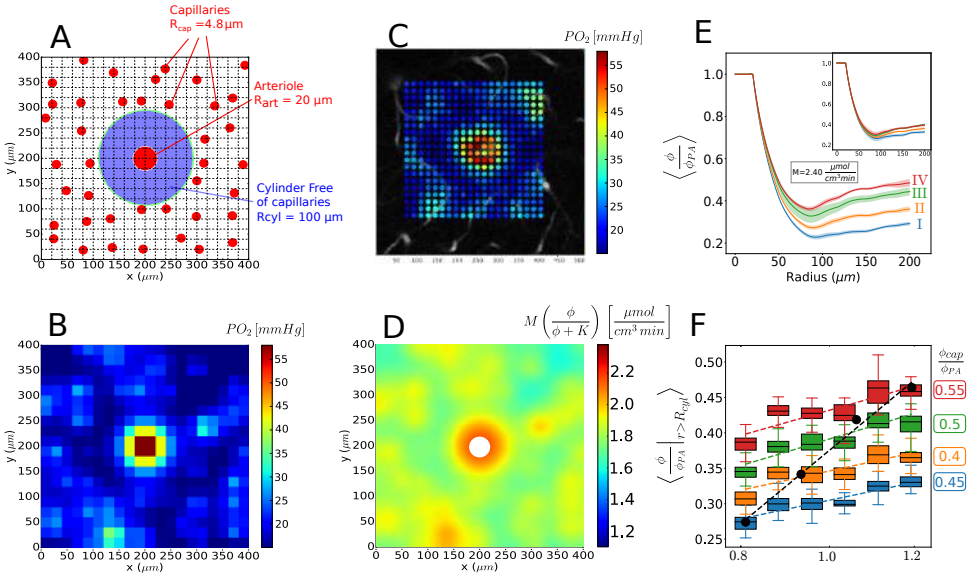

Fig 7. Effect of capillary density and intravascular concentration on radial periarteriolar concentration profiles. A: sketch of simulated configuration, with a random and homogeneous capillary bed for $r > R_{cyl}$ and a capillary-free region around the central PA. The cartesian grid of size 20x20 matches that of experimental sampling used in [10]. B: corresponding coarse-grid partial pressure deduced by linear transformation from the concentration field using the solubility of oxygen in brain tissue [10, 30, 37]. Capillary density and concentration correspond to layer II (Table 2) and $M = 2.4\mu\text{mol} \cdot \text{cm}^{-3} \cdot \text{min}^{-1}$. Note that all simulations (panels B, D, E, F) use the same value of M and $n = 10$; C: example of an experimentally sampled oxygen partial pressure field around a PA at 100μm under cortical surface, i.e. at the interface between layer I and II; D: estimated metabolic consumption deduced from Panel B; E: radial concentration profiles predicted in layers I to IV, each obtained by averaging the results of 30 simulations; Inset: result obtained when only variations of the capillary density are considered; F: resulting spatial average of the tissue concentration for $r > R_{cyl}$, as a function of capillary density for four values of the average capillary intravascular concentration (ϕ_{cap}/ϕ_{PA} from 0.4 to 0.55) corresponding to the four layers in Table 2; the black dots represent the resulting spatial average of the tissue concentration for $r > R_{cyl}$ for the four different layers, i.e., varying both capillary density and concentration. The black dashed line represents the associated linear fit ($\left\langle \frac{\phi}{\phi_{PA}}|_{r>R_{cyl}} \right\rangle = 1.12 \cdot 10^{-3} \cdot \text{CLD} - 0.118$).

intermediate value within the physiological range. Other transport parameters used to solve the non-linear problem (Eqs. 39 and 40) are deduced from reference values in the literature (Table 1).

A typical realization of the resulting coarse-grid concentration field, converted to partial pressure (PO_2) using the solubility of oxygen in brain tissue [10, 30, 37], is displayed in Fig 7B for a 20x20 grid ($h \sim 20\mu$m). This matches the experimental sampling used in [10] and results in a very good qualitative agreement with the field measured in a 100μm-deep plane perpendicular to a PA (see Fig 7C, data acquired following [10]). This field can be used to deduce the sub-grid concentration dynamics by interpolation (Eq. 30, see e.g. Figs C and D in S1 Figures), as well as the local cerebral metabolic rate of oxygen ($CMRO_2$, see Eq. 40 and Fig 7D). Interestingly, the cerebral metabolic rate of oxygen exhibits $\sim \pm 10\%$ variations in the outer region (around capillaries) and up to $\sim \pm 20\%$ in the periarteriolar region, in contrast to the common assumption of a spatial homogeneity [10, 23, 24, 74].

Moreover, the above results can be post-processed to deduce the azimuthal average of the normalized concentration around the PA, as displayed in Fig 7E as a function of the radial distance r to the PA center. In this figure, the plain orange line corresponds to the mean over 30 realizations of source distributions for layer II, while the faint orange areas shows the associated standard deviation. This radial concentration dynamics exhibits three regimes (Fig 7E): 1/ a constant value for $r \leq R_{\mathrm{PA}}$, i.e. within the PA, consistent with the source potential (Eq. 24); 2/ a fast decrease for $R_{\mathrm{PA}} \leq r \leq \sim 0.8 R_{\mathrm{cyl}}$ corresponding to the inner part of the region devoid of capillaries around the PA (see Fig 7A) and 3/ a re-increase followed by a slowly-varying region for larger values of r. The presence of a local minima, which can also be observed in the measurements (Fig 7C and Fig E in S1 Figures, dashed lines) suggests that the outer region of the capillary-free cylinder is both fed by the PA and the capillary bed.

Next, as the capillary density approximately increases linearly with depth in the cortex from layer I to layer IV [20], we increased the source density from 250 to 475 mm^{-2} (Table 2). This results in an increase in size of regions with high oxygen concentration around capillaries (see panel B vs. A in Fig C in S1 Figures) and therefore 1/ in a slight decrease of the steepness of radial periarteriolar PO_2 gradients averaged over 30 realizations and 2/ in a slight increase of the partial pressure in the plateau region ($r \geq R_{\mathrm{cyl}}$), see inset in Fig 7E. This increase can be quantified by plotting the spatial average $\langle PO_2/PO_{2,Art} \rangle_{r \geq r_{Cyl}}$ (see isocolor variations in Fig 7F).

Increases of the average intravascular PO_2 within the capillary bed (Table 2), which can be speculated based on depth-resolved experimental measurements of vascular oxygen within the cortex [9], result in a higher increase in size of regions with high oxygen concentration around capillaries (see panel C vs. A in Fig C in S1 Figures) and thus to higher increase of $\langle PO_2/PO_{2,Art} \rangle_{r \geq R_{Cyl}}$ (i.e. black dashed line vs. colored dashed lines in Fig 7F).

Combined together, the increase in capillary density and intravascular PO_2 that has been reported experimentally from layer I to layer IV in the cortex of living rodents leads to an even faster decrease of the perivascular concentration gradient (Fig 7E). This results in a faster increase of $\langle \phi/\phi_{2,PA} \rangle_{r \geq R_{Cyl}}$ from layer I to layer IV, see black dots in Fig 7F. For a constant value of M, this yields an increasing metabolic rate of oxygen from layer I to layer IV (panel D vs. A in Fig C in S1 Figures), consistent with the increased density of mitochondrial cytochrome oxidase through these layers [10, 75, 76].

Noteworthy, similar results have been obtained for different values of the maximal metabolic rate of oxygen M within the physiological range (Table 1), as illustrated in Fig D in S1 Figures. The only notable difference is that the amplitude of the dip in the radial concentration profile decreases with decreasing values of M (Fig E in S1 Figures). For the set of parameters representative of layers I and II, this leads to a monotonous

decrease of the average radial concentration followed by a region with nearly constant oxygen concentration, similar to experimental measurements reported in [10,24], as soon as $M \leq 1.2\mu\text{mol} \cdot \text{cm}^{-3} \cdot \text{min}^{-1}$ (Fig E in S1 Figures). As a result, the oxygen dynamics in the close vicinity of the arteriole ($r < R_{cyl}/2$) may be highly similar in different cortical layers for different values of M (e.g. $M = 2.4\mu\text{mol} \cdot \text{cm}^{-3} \cdot \text{min}^{-1}$ in layer IV, see red line in Fig 7E vs. $M = 1.6\mu\text{mol} \cdot \text{cm}^{-3} \cdot \text{min}^{-1}$ in layer I, see blue dashed-dotted line in Fig E in S1 Figures.)

Altogether, the present model suggests that laminar variations of the capillary density may be sufficient to explain the differences in periarteriolar radial oxygen profiles measured at different depths within the cortex [10], without any variation of the maximal cerebral metabolic rate of oxygen M. If laminar variations of intravascular capillary PO_2 are also considered, the predicted differences are even larger than the experimental ones. This demonstrates the interplay between metabolic consumption, capillary density and intravascular availability of oxygen in the capillary bed to determine the radial oxygen gradient in the vicinity of PAs. This makes it difficult to consider the steepness of the radial periarteriolar oxygen profile as a surrogate for the baseline oxygen consumption, with the potential to reconcile recent experimental measurements with the idea that laminar variations of capillary density could reveal underlying differences in metabolic load.

Layer	CLD $[\text{m}\,\text{mm}^{-3}]$	E2DSD $[\text{mm}^{-2}]$	Depth $[\mu\text{m}]$	$PO_{2,PA}$ [mmHg]	$PO_{2,cap}$ [mmHg]	ϕ_{cap}/ϕ_{PA}
I	0.8	250	[0-100]	99 ($= \phi_{max}/\alpha$)	39	0.4
II	0.94	325	[100-200]	92	42	0.45
III	1.08	400	[200-300]	87	44	0.5
IV	1.2	475	[300-400]	85	47	0.55

Table 2. Layer-specific (laminar) variations of capillary density and average intravascular capillary PO_2. The capillary length density (CLD) and depth of the corresponding layers are approximated from data in [20]. The equivalent two-dimensional source density (E2DSD) is deduced using synthetic capillary networks from [60] (Fig 6A). The ratio between arteriole and capillary concentration is approximated from data in [9].

5 Discussion

In this paper, we revisited the problem of oxygen transport and metabolism in the brain parenchyma, with the goal to introduce a simple, scalable and accurate numerical method for its direct resolution. Getting inspiration from previous work on blood flow and oxygen transport in the brain [22,30,45,64] and on mixed-dimensional problems in applied mathematics for geosciences [39,56,57] and biology [48], we applied the notion of operator-splitting, which allowed us to describe the oxygen concentration field in the parenchyma as the sum of a slow and a fast varying contributions. The slow contribution was treated using a classic finite volume approach on a coarse grid, while the fast contribution was described using Green's functions that allowed to analytically capture the sub-grid perivascular concentration gradients. This made it possible to locally bridge the scale gap between sources and the coarse-grid with higher flexibility than [39,41] regarding the position of the sources within the coarse grid-cells, including multiple sources within a single grid-cell, the proximity of the boundaries, and the control of the matrix sparsity thanks to the the size of the neighbourhood ($\widehat{V}$). Similarly to singularity removal approaches [45,48,57], this also made it possible to mix

the dimensionality reduction of the Green's functions approaches [30, 32, 51] with the versatility of FV methods [56, 57, 72]. Moreover, solving for a slowly varying background concentration field, thanks to a change of variable, offers a huge advantage with respect to the Green's functions resolution since it allows for a localization of the source potentials, thereby providing a much sparser system. In addition, this enable the use of a much coarser mesh that reduces considerably the size of the system compared to FV or FE methods, but without loss of precision thanks to the sub-grid reconstruction of the concentration field (Figs 5D and 6D). This, in turn allows the addition of non linear volume terms (metabolism) without significant loss of accuracy (Figs 4B, 4D and 6E).

To provide rigorous but still intelligible mathematical developments, we focused on a two-dimensional version of the problem (Section 2). In this way, we were able to introduce the localization scheme enabling us to control the bandwidth of the associated linear system of equations, by manipulating the size of the region over which the interactions with nearby vessels are accounted for analytically (scalability). We demonstrated the existence of an optimal size for this region, above which the errors induced by localization are smaller than those induced by deviations from local azimuthal symmetry of the concentration field around each vessel (see Fig 6E). This emphasizes the importance of comparing the results of any simplified model for oxygen transport in the brain parenchyma with a reference solution that is able to fully resolve these deviations. This is neither the case if only single vessels with Krogh-type configurations are considered for validation, as in [10, 23, 27, 37], or if the discrete version of the problem is compared to the corresponding continuous version (i.e., comparing the solution of Eqs. 33 to the solution of Eqs. 6 instead of Eqs. 1), as in [58, 66, 72, 77]. To our knowledge, such comparisons had never been performed before in this context. Crucially, they enabled to provide careful estimates of the numerical errors associated to the use of coarse meshes, demonstrating the unprecedented balance between reduction of problem size and minimization of errors associated to our method, compared to previous strategies in the literature (accuracy). With this regard, it is worth insisting that we designed test cases that enabled the origins of errors to be understood by purposefully choosing configurations with deviations from the model underlying assumptions (Section 3). Thus, all errors provide upper-bounds of the errors expected when considering larger, physiological-like problems. Moreover, the mathematical groundwork provided by the Green's function framework (Section B in S1 Methods) permitted to trace back the source of errors to specific modeling assumptions, which in turn offers a rationale for choosing the model parameters, including discretization and neighborhood size. Finally, the method makes use of a cartesian mesh independent of vessel locations, thereby belonging to the class of mesh-less approaches [38]. In contrast with the widespread semi-analytical methods [30, 32, 34, 51, 65] that require computationally intensive Fourier transforms to enforce conventional boundary conditions such as Neumann and Dirichlet [30], it also shows remarkable versatility with regard to the boundary conditions that can be handled (simplicity).

Of course, the two-dimensional version of the problem we considered doesn't enable coupling oxygen transport in the parenchyma with oxygen transport in blood vessels, because intersecting the vascular network with a plane yields disconnected vascular sources, as schematized in Fig 1. Thus, in the present work, intravascular concentrations have been treated as inputs, while in a three-dimensional version they should be treated as unknowns, with additional blocks in the final system accounting for intravascular transport, as highlighted in [45, 52, 66]. Together with previous work by our group that focused on revisiting intravascular transport [22], these will provide the foundations for an extension to three dimensions. The fact that the integrated potential arising from a circular source can be written analytically (Eq. 24 and Section B in S1 Methods) is a peculiar characteristic of the 2D model. In 3D, additional errors may

arise due to the approximations needed to estimate the potential of a small cylindrical element used to discretize the vascular networks, that will require careful evaluation in the spirit of [78, 79].

However, considering two-dimensional situations already offers the opportunity to investigate important physiological questions, as illustrated in Section 4. Thanks to the computational efficiency of our method, we were able to easily generate the large number of synthetic data (600 simulations per layer and 30 measurements per simulation) needed to incorporate statistical information about the capillary bed available in the literature [9, 20]. By this way, we shed new light on the interpretation of experimentally measured variations of periarteriolar oxygen profiles [10] in the context of laminar variations of capillary density and their relationships with baseline cerebral metabolic load. Due to the non-local nature of blood flow, understanding the measured variations of average intravascular concentration with depth will require a fully coupled three-dimensional analysis of oxygen exchange in the brain. In this regard, it is worth noting that the matrix assembly process only depends on the location of vessels in the considered domain and of the size of grid-cells and neighbourhood $\widehat{V}$, and requires to be performed only once when the structure of the vascular network is known. Besides parametric analyses, this will pave the way for the inverse modelling of brain metabolism from three-dimensional oxygen measurements. Inverse modelling indeed requires fast and precise forward model resolutions, overcoming the geometric simplifications of the Krogh cylinder type, which are at the basis of all current work that aims at measuring the cerebral metabolic rate of oxygen [10, 24, 26].

6 Conclusion

We developed a multi-scale model describing the spatial dynamics of oxygen transport in the brain that is simple, conservative, accurate and scalable. Our strategy was to consider that the oxygen concentration in the parenchyma is the result of a balance between contributions at local (cell metabolism, delivery by neighbouring arteriole) and larger (capillary bed) spatial scales. This allowed us to split the oxygen concentration field into a slow and a fast varying terms, underlying the separation of scales between local and distant contributions. Doing so allowed us to combine a coarse-grid approach for the slow-varying term to a Green's function approach for the fast-varying terms. This resulted in a computationally efficient model that was able to capture precisely gradients of concentration around microvessels and to describe boundary condition with flexibility (Dirichlet, Neumann, and periodic) along with the non-linear metabolic activity by the cells.

We then compared our model with reference solutions of the oxygen transport problem in scenarios of increasing complexity. We showed that our model was able to maintain small errors, even in scenario where the separation of scales was challenged or when azimuthal variations of flux were no longer negligible, demonstrating the robustness of the model.

While the present multi-scale model focused on two-dimensional problems, it has been designed to be easily extended to three-dimensional problems by adapting the expression for the source potential and by including an intravascular description of oxygen transport, both of which being available in the literature (see e.g. [22, 30, 45]).

Despite this limitation, we showed that the model was already capable of generating synthetic data reproducing the heterogeneous distribution of oxygen in the brain parenchyma. Doing so, we showed that periarteriolar gradients were the result of the balance between local cellular oxygen consumptionand supply by not only the neighbouring arteriole but also distant capillaries, thus reconciling recent measurements

of periarteriolar oxygen gradients across cortical layers with the fundamental idea that variations of vascular density within the depth of the cortex may reveal underlying differences in neuronal organization.

Code availability

All author-generated python code, as well as Comsol reference simulation data used for comparison are available from the Zenodo repository at
`https://doi.org/10.5281/zenodo.8383821`

Conflict of interest

The authors have declared that no competing interests exist.

Author's contribution

DP-A, SL and YD participated equally in all conceptual aspects of this work, with MB, MQ and FB providing scientific expertise on model development. DP derived the model, wrote the code, ran all simulations, prepared the figures and wrote a draft version of the manuscript. SL wrote the manuscript with feedback from DP and MB. NFT pointed out to the question of laminar variations of periarteriolar profiles and acquired and provided the associated experimental data. All authors reviewed and edited the manuscript.

Funding

The research leading to these results has received funding from the European Research Council under the European Union's Seventh Framework Program (FP7/2007-2013) Consolidator Brainmicroflow, ERC grant agreement no. 615102 to SL, from the NIH (awards R21CA214299 and 1RF1NS110054 to SL) and from Agence Nationale de la Recherche (J452IMF23174 to SL). It was performed using HPC resources from CALMIP (Grant 2016P1541). YD was partly funded by the H2020 program Starting Bebop, ERC grant agreement no. 803074. The funders had no role in study design, data collection and analysis, decision to publish, or preparation of the manuscript.

Acknowledgements

We gratefully acknowledge Maxime Pigou for technical help with the development and maintenance of the code and Franca Schmid for carefully reading our manuscript.

References

1. Dornbos D, Arthur AS. Current State of the Art in Endovascular Stroke Treatment. Neurologic Clinics. 2022;40(2):309–319. doi:10.1016/j.ncl.2021.11.008.

2. Iadecola C. The Pathobiology of Vascular Dementia. Neuron. 2013;80(4):844–866. doi:10.1016/j.neuron.2013.10.008.

3. Iturria-Medina Y, Sotero RC, Toussaint PJ, Mateos-Pérez JM, Evans AC, The Alzheimer's Disease Neuroimaging Initiative, et al. Early role of vascular dysregulation on late-onset Alzheimer's disease based on multifactorial data-driven analysis. Nature Communications. 2016;7(1):11934. doi:10.1038/ncomms11934.

4. Cruz Hernández JC, Bracko O, Kersbergen CJ, Muse V, Haft-Javaherian M, Berg M, et al. Neutrophil adhesion in brain capillaries reduces cortical blood flow and impairs memory function in Alzheimer's disease mouse models. Nature Neuroscience. 2019;22(3):413–420. doi:10.1038/s41593-018-0329-4.

5. Nortley R, Korte N, Izquierdo P, Hirunpattarasilp C, Mishra A, Jaunmuktane Z, et al. Amyloid beta oligomers constrict human capillaries in Alzheimer's disease via signaling to pericytes. Science. 2019;365(6450):eaav9518. doi:10.1126/science.aav9518.

6. Korte N, Nortley R, Attwell D. Cerebral blood flow decrease as an early pathological mechanism in Alzheimer's disease. Acta Neuropathologica. 2020;140(6):793–810. doi:10.1007/s00401-020-02215-w

7. Abdelfattah A, Allu SR, Campbell RE, Cheng X, Cižmár T, Costantini I, et al. Neurophotonic Tools for Microscopic Measurements and Manipulation: Status Report. Neurophotonics. 2022;9(S1). doi:10.1117/1.NPh.9.S1.013001

8. Lyons DG, Parpaleix A, Roche M, Charpak S. Mapping oxygen concentration in the awake mouse brain. eLife. 2016;5:e12024. doi:10.7554/eLife.12024.

9. Li B, Esipova TV, Sencan I, Kılıç K, Fu B, Desjardins M, et al. More homogeneous capillary flow and oxygenation in deeper cortical parenchyma to introduce a simple, scalable layers correlate with increased oxygen extraction. eLife. 2019;8:e42299. doi:10.7554/eLife.42299.

10. Mächler P, Fomin-Thunemann N, Thunemann M, Sætra MJ, Desjardins M, Kılıç K, et al. Baseline oxygen consumption decreases with cortical depth. PLOS Biology. 2022;20(10):e3001440. doi:10.1371/journal.pbio.3001440

11. Goirand F, Le Borgne T, Lorthois S. Network-driven anomalous transport is a fundamental component of brain microvascular dysfunction. Nature Communications. 2021;12(1):7295. doi:10.1038/s41467-021-27534-8.

12. Drew PJ. Neurovascular coupling: motive unknown. Trends in Neurosciences. 2022;45(11):809–819. doi:https://doi.org/10.1016/j.tins.2022.08.004.

13. Qi Y, Roper M. Control of low flow regions in the cortical vasculature determines optimal arterio-venous ratios. Proceedings of the National Academy of Sciences. 2021;118(34):e2021840118. doi:10.1073/pnas.2021840118

14. Duvernoy HM, Delon S, Vannson JL. Cortical blood vessels of the human brain. Brain Research Bulletin. 1981;7(5):519–579. doi:10.1016/0361-9230(81)90007-1.

15. Lauwers F, Cassot F, Lauwers-Cances V, Puwanarajah P, Duvernoy H. Morphometry of the human cerebral cortex microcirculation: General characteristics and space-related profiles. NeuroImage. 2008;39(3):936–948. doi:10.1016/j.neuroimage.2007.09.024.

16. Weber B, Keller AL, Reichold J, Logothetis NK. The Microvascular System of the Striate and Extrastriate Visual Cortex of the Macaque. Cerebral Cortex. 2008;18(10):2318–2330. doi:10.1093/cercor/bhm259.

17. Harik SI, Hritz MA, LaManna JC. Hypoxia-induced brain angiogenesis in the adult rat. The Journal of Physiology. 1995;485(2):525–530. doi:10.1113/jphysiol.1995.sp020748.

18. Harb R, Whiteus C, Freitas C, Grutzendler J. In Vivo Imaging of Cerebral Microvascular Plasticity from Birth to Death. Journal of Cerebral Blood Flow and Metabolism. 2013;33(1):146–156. doi:10.1038/jcbfm.2012.152.

19. Lacoste B, Comin C, Ben-Zvi A, Kaeser P, Xu X, Costa L, et al. Sensory-Related Neural Activity Regulates the Structure of Vascular Networks in the Cerebral Cortex. Neuron. 2014;83(5):1117–1130. doi:10.1016/j.neuron.2014.07.034.

20. Ji X, Ferreira T, Friedman B, Liu R, Liechty H, Bas E, et al. Brain microvasculature has a common topology with local differences in geometry that match metabolic load. Neuron. 2021;109(7):1168–1187.e13. doi:10.1016/j.neuron.2021.02.006.

21. Blinder P, Tsai PS, Kaufhold JP, Knutsen PM, Suhl H, Kleinfeld D. The cortical angiome: an interconnected vascular network with noncolumnar patterns of blood flow. Nature Neuroscience. 2013;16(7):889–897. doi:10.1038/nn.3426.

22. Berg M, Davit Y, Quintard M, Lorthois S. Modelling solute transport in the brain microcirculation: is it really well mixed inside the blood vessels? Journal of Fluid Mechanics. 2020;884:A39. doi:10.1017/jfm.2019.866.

23. Shaw K, Bell L, Boyd K, Grijseels DM, Clarke D, Bonnar O, et al. Neurovascular coupling and oxygenation are decreased in hippocampus compared to neocortex because of microvascular differences. Nature Communications. 2021;12(1):3190. doi:10.1038/s41467-021-23508-y.

24. Sakadžić S, Yaseen MA, Jaswal R, Roussakis E, Dale AM, Buxton RB, et al. Two-photon microscopy measurement of cerebral metabolic rate of oxygen using periarteriolar oxygen concentration gradients. Neurophotonics. 2016;3(4):045005. doi:10.1117/1.NPh.3.4.045005.

25. Mintun MA, Lundstrom BN, Snyder AZ, Vlassenko AG, Shulman GL, Raichle ME. Blood flow and oxygen delivery to human brain during functional activity: Theoretical modeling and experimental data. Proceedings of the National Academy of Sciences. 2001;98(12):6859–6864. doi:10.1073/pnas.111164398.

26. Sætra MJ, Solbrå AV, Devor A, Sakadžić S, Dale AM, Einevoll GT. Spatially resolved estimation of metabolic oxygen consumption from optical measurements in cortex. Neurophotonics. 2020;7(03). doi:10.1117/1.NPh.7.3.035005.

27. Secomb TW, Hsu R, Beamer NB, Coull BM. Theoretical Simulation of Oxygen Transport to Brain by Networks of Microvessels: Effects of Oxygen Supply and Demand on Tissue Hypoxia. Microcirculation. 2000;7(4):237–247. doi:10.1111/j.1549-8719.2000.tb00124.x

28. Goldman D. Theoretical Models of Microvascular Oxygen Transport to Tissue. Microcirculation. 2008;15(8):795–811. doi:10.1080/10739680801938289

29. Fang Q, Sakadžić S, Ruvinskaya L, Devor A, Dale AM, Boas DA. Oxygen advection and diffusion in a three-dimensional vascular anatomical network. Optics Express. 2008;16(22):17530. doi:10.1364/OE.16.017530.

30. Secomb TW, Hsu R, Park EYH, Dewhirst MW. Green's Function Methods for Analysis of Oxygen Delivery to Tissue by Microvascular Networks. Annals of Biomedical Engineering. 2004;32(11):1519–1529. doi:10.1114/b:abme.0000049036.08817.44.

31. Secomb TW. Blood Flow in the Microcirculation. Annual Review of Fluid Mechanics. 2017;49(1):443–461. doi:10.1146/annurev-fluid-010816-060302.

32. Sweeney PW, d'Esposito A, Walker-Samuel S, Shipley RJ. Modelling the transport of fluid through heterogeneous, whole tumours in silico. PLOS Computational Biology. 2019;15(6):e1006751. doi:10.1371/journal.pcbi.1006751.

33. Celaya-Alcala JT, Lee GV, Smith AF, Li B, Sakadžić S, Boas DA, et al. Simulation of oxygen transport and estimation of tissue perfusion in extensive microvascular networks: Application to cerebral cortex. Journal of Cerebral Blood Flow and Metabolism. 2021;41(3):656–669. doi:10.1177/0271678X20927100.

34. Xue Y, Georgakopoulou T, van der Wijk AE, Józsa TI, van Bavel E, Payne SJ. Quantification of hypoxic regions distant from occlusions in cerebral penetrating arteriole trees. PLOS Computational Biology. 2022;18(8):e1010166. doi:10.1371/journal.pcbi.1010166.

35. Sweeney PW, Walker-Samuel S, Shipley RJ. Insights into cerebral haemodynamics and oxygenation utilising in vivo mural cell imaging and mathematical modelling. Scientific Reports. 2018;8(1):1373. doi:10.1038/s41598-017-19086-z.

36. Secomb TW. A Green's function method for simulation of time-dependent solute transport and reaction in realistic microvascular geometries. Mathematical Medicine and Biology. 2016;33(4):475–494. doi:10.1093/imammb/dqv031.

37. Linninger AA, Gould IG, Marinnan T, Hsu CY, Chojecki M, Alaraj A. Cerebral Microcirculation and Oxygen Tension in the Human Secondary Cortex. Annals of Biomedical Engineering. 2013;41(11):2264–2284. doi:10.1007/s10439-013-0828-0.

38. Hartung G, Badr S, Moeini M, Lesage F, Kleinfeld D, Alaraj A, et al. Voxelized simulation of cerebral oxygen perfusion elucidates hypoxia in aged mouse cortex. PLOS Computational Biology. 2021;17(1):e1008584. doi:10.1371/journal.pcbi.1008584.

39. Peaceman DW. Interpretation of Well-Block Pressures in Numerical Reservoir Simulation. Society of Petroleum Engineers Journal. 1978;18(03):183–194.

40. Peaceman DW. Interpretation of Well-Block Pressures in Numerical Reservoir Simulation with Nonsquare Grid Blocks and Anisotropic Permeability. Society of Petroleum Engineers Journal. 1983;23(03):531–543. doi:10/cp86hz.

41. Aavatsmark I, Klausen RA. Well Index in Reservoir Simulation for Slanted and Slightly Curved Wells in 3D Grids. SPE-75275-PA. 2003;8(01):41–48. doi:10/fhfsrg.

42. Jayasinghe S, Darmofal DL, Dow E, Galbraith MC, Allmaras SR. A Discretization-Independent Distributed Well Model. SPE Journal. 2019;24(06):2946–2967. doi:10.2118/198898-PA.

43. Ding Y, Jeannin L. A Multi-Point Flux Approximation Scheme for the Well Modelling in Reservoir Simulations. 2000;doi:10/ghn49f.

44. Ding DY. Near-Well Upscaling for Reservoir Simulations. Oil Gas Science and Technology. 2004;59(2):157–165. doi:10/dpvbh3.

45. Gjerde IG, Kumar K, Nordbotten JM. A singularity removal method for coupled 1D–3D flow models. Computational Geosciences. 2020;24(2):443–457. doi:10.1007/s10596-019-09899-4.

46. Christopherson, D G and Southwell, R V . Relaxation methods applied to engineering problems. III. Problems involving two independent variables. Proceedings of the Royal Society of London Series A, Mathematical and Physical Sciences. 1938;168(934):317–350.

47. Woods LC. The relaxation treatment of singular points in Poisson's equation. The Quarterly Journal of Mechanics and Applied Mathematics. 1953;6(2):163–185. doi:10.1093/qjmam/6.2.163.

48. Drechsler F, Wolters CH, Dierkes T, Si H, Grasedyck L. A full subtraction approach for finite element method based source analysis using constrained Delaunay tetrahedralisation. NeuroImage. 2009;46(4):1055–1065. doi:10.1016/j.neuroimage.2009.02.024.

49. Holter KE, Kehlet B, Devor A, Sejnowski TJ, Dale AM, Omholt SW, et al. Interstitial solute transport in 3D reconstructed neuropil occurs by diffusion rather than bulk flow. Proceedings of the National Academy of Sciences. 2017;114(37):9894–9899. doi:10.1073/pnas.1706942114.

50. Nicholson C. Diffusion and related transport mechanisms in brain tissue. Reports on Progress in Physics. 2001;64(7):815–884. doi:10.1088/0034-4885/64/7/202.

51. Pozrikidis C, Farrow DA. A Model of Fluid Flow in Solid Tumors. Annals of Biomedical Engineering. 2003;31(2):181–194. doi:10.1114/1.1540103.

52. Koch T, Schneider M, Helmig R, Jenny P. Modeling tissue perfusion in terms of 1d-3d embedded mixed-dimension coupled problems with distributed sources. Journal of Computational Physics. 2020;410:109370. doi:10.1016/j.jcp.2020.109370.

53. Taylor R, Krishna R. Multicomponent mass transfer. Wiley series in chemical engineering. New York: Wiley; 1993.

54. Moinfar A, Varavei A, Sepehrnoori K, Johns RT. Development of a Novel and Computationally-Efficient Discrete-Fracture Model to Study IOR Processes in Naturally Fractured Reservoirs. In: All Days. Tulsa, Oklahoma, USA: SPE; 2012. p. SPE–154246–MS.

55. Yan X, Huang Z, Yao J, Li Y, Fan D. An efficient embedded discrete fracture model based on mimetic finite difference method. Journal of Petroleum Science and Engineering. 2016;145:11–21. doi:10.1016/j.petrol.2016.03.013.

56. Jenny P, Lee SH, Tchelepi HA. Adaptive Multiscale Finite-Volume Method for Multiphase Flow and Transport in Porous Media. Multiscale Modeling Simulation. 2005;3(1):50–64. doi:10.1137/030600795.

57. Wolfsteiner C, Lee SH, Tchelepi HA. Well Modeling in the Multiscale Finite Volume Method for Subsurface Flow Simulation. Multiscale Modeling Simulation. 2006;5(3):900–917. doi:10.1137/050640771.

58. Gjerde IG, Kumar K, Nordbotten JM, Wohlmuth B. Splitting method for elliptic equations with line sources. ESAIM: Mathematical Modelling and Numerical Analysis. 2019;53(5):1715–1739. doi:10.1051/m2an/2019027.

59. Weisstein EC. CRC Concise encyclopedia of mathematics. Boca Raton: CRC Press; 1998.

60. Smith AF, Doyeux V, Berg M, Peyrounette M, Haft-Javaherian M, Larue AE, et al. Brain Capillary Networks Across Species: A few Simple Organizational Requirements Are Sufficient to Reproduce Both Structure and Function. Frontiers in Physiology. 2019;10:233. doi:10.3389/fphys.2019.00233.

61. Pozrikidis C, Ferziger JH. Introduction to Theoretical and Computational Fluid Dynamics. Physics Today. 1997;50(9):72–74. doi:10.1063/1.881920.

62. Pozrikidis C, Davis JM. Blood Flow Through Capillary Networks. In: Transport in Biological Media. Elsevier; 2013. p. 213–252.

63. Roach GF. Green's Functions. 2nd ed. Cambridge: Cambridge University Press; 1982.

64. Peyrounette M, Davit Y, Quintard M, Lorthois S. Multiscale modelling of blood flow in cerebral microcirculation: Details at capillary scale control accuracy at the level of the cortex. PLOS ONE. 2018;13(1):e0189474. doi:10.1371/journal.pone.0189474.

65. Hsu R, Secomb TW. A Green's function method for analysis of oxygen delivery to tissue by microvascular networks. Mathematical Biosciences. 1989;96(1):61–78. doi:10.1016/0025-5564(89)90083-7.

66. Possenti L, Cicchetti A, Rosati R, Cerroni D, Costantino ML, Rancati T, et al. A Mesoscale Computational Model for Microvascular Oxygen Transfer. Annals of Biomedical Engineering. 2021;49(12):3356–3373. doi:10.1007/s10439-021-02807-x.

67. Atkins PW, De Paula J. Physical chemistry for the life sciences. 2nd ed. New York/Oxford: W.H. Freeman and Co./Oxford University Press; 2011.

68. Cooper C. Competitive, Reversible, Physiological? Inhibition of Mitochondrial Cytochrome Oxidase by Nitric Oxide. IUBMB Life. 2004;55(10):591–597. doi:10.1080/15216540310001628663.

69. Lecoq J, Parpaleix A, Roussakis E, Ducros M, Houssen YG, Vinogradov SA, et al. Simultaneous two-photon imaging of oxygen and blood flow in deep cerebral vessels. Nature Medicine. 2011;17(7):893–898. doi:10.1038/nm.2394.

70. Lorthois S, Duru P, Billanou I, Quintard M, Celsis P. Kinetic modeling in the context of cerebral blood flow quantification by H215O positron emission tomography: The meaning of the permeability coefficient in Renkin–Crones model revisited at capillary scale. Journal of Theoretical Biology. 2014;353:157–169. doi:10.1016/j.jtbi.2014.03.004.

71. Secomb TW, Bullock KV, Boas DA, Sakadžić S. The mass transfer coefficient for oxygen transport from blood to tissue in cerebral cortex. Journal of Cerebral Blood Flow and Metabolism. 2019;40(8):1634–1646. doi:10.1177/0271678X19870068.

72. Koch T, Helmig R, Schneider M. A new and consistent well model for one-phase flow in anisotropic porous media using a distributed source model. Journal of Computational Physics. 2020;410:109369. doi:10.1016/j.jcp.2020.109369.

73. Lorthois S, Cassot F. Fractal analysis of vascular networks: Insights from morphogenesis. Journal of Theoretical Biology. 2010;262(4):614–633. doi:10.1016/j.jtbi.2009.10.037.

74. Secomb TW. Krogh-Cylinder and Infinite-Domain Models for Washout of an Inert Diffusible Solute from Tissue. Microcirculation. 2015;22(1):91–98. doi:10.1111/micc.12180.

75. Santuy A, Turégano-L'opez M, Rodríguez JR, Alonso-Nanclares L, DeFelipe J, Merchán-Pérez A. A Quantitative Study on the Distribution of Mitochondria in the Neuropil of the Juvenile Rat Somatosensory Cortex. Cerebral Cortex. 2018;28(10):3673–3684. doi:10.1093/cercor/bhy159.

76. Lu X, Moeini M, Li B, Montgolfier Od, Lu Y, Bélanger S, et al. Voluntary exercise increases brain tissue oxygenation and spatially homogenizes oxygen delivery in a mouse model of Alzheimer's disease. Neurobiology of Aging. 2020;88:11–23. doi:https://doi.org/10.1016/j.neurobiolaging.2019.11.015.

77. D'Angelo C, Quarteroni A. On the coupling of 1D and 3D diffusion-reaction equations. Applications to tissue perfusion problems. Mathematical Models and Methods in Applied Sciences. 2008;18(08):1481–1504. doi:10.1142/S0218202508003108.

78. Pepper D, Kassab A, Divo E. Introduction to Finite Element, Boundary Element, and Meshless Methods: With Applications to Heat Transfer and Fluid Flow. ASME Press; 2014.

79. Aliabadi MH, Wen PH. Boundary element methods in engineering and sciences. No. 4 in Computational and experimental methods in structures. London: Imperial College Press; 2011.

Legend for supporting information files

- S1 Figures: contains supplementary figures A to E.
- S1 Methods: contains supplementary methods Sections A to E.

Supplementary methods for "Modeling oxygen transport in the brain: an efficient coarse-grid approach to capture perivascular gradients in the parenchyma".

David Pastor-Alonso[1], Maxime Berg[1,2], Franck Boyer[3], Natalie Fomin-Thunemann[4], Michel Quintard[1], Yohan Davit[1], Sylvie Lorthois*[1],

1 Institut de Mécanique des Fluides de Toulouse, UMR 5502, CNRS, University of Toulouse, Toulouse, France.
2 Department of Mechanical Engineering, University College London, London, UK
3 Institut de Mathématiques de Toulouse (IMT), CNRS and Université de Toulouse, 31400 Toulouse, France
4 Department of Biomedical Engineering, Boston University, Boston, Massachusetts, USA.

A Multiscale Finite Volume formulation

In the Finite Volume (FV) method, the main ideas are as follows:

1. **Discretization**: We divide the domain Ω_σ into a set of control volumes $\mathscr{F}$ where the variable are estimated at the geometrical center (node) of each control volume.
2. **Flux approximation**: We approximate the fluxes as a function of the nodal values to obtain a system involving only concentrations
3. **Closure of the system**: we impose flux and concentration continuity at each of the FV cell's interfaces

We begin by integrating the PDE 13a (see main text) over the control volume given by V_k:

$$\iint_{V_k} \nabla^2 \vartheta_k(\mathbf{x}) dS = 0 \quad \forall k \in \mathscr{F} \tag{46}$$

Recalling that V_k have been introduced in Section 2.3.2 to provide a tessellation of the parenchyma Ω_σ, we obtain, by applying the divergence theorem:

$$\sum_{m \in \mathscr{N}^k} \int_{\partial V_{k,m}} (\boldsymbol{\nabla} \vartheta_k \cdot \mathbf{n}) dl + \sum_{j \in E(V_k)} \oint_{\partial \Omega_{\beta,j}} (\boldsymbol{\nabla} \vartheta_k \cdot \mathbf{n}) dl = 0 \quad \forall k \in \mathscr{F} \tag{47}$$

The second integral term in the left hand side of Eq. 47 is always null due to the boundary condition 13c. Using the TPFA (Eq. 15) to estimate the slow term gradients and the mid-point rule to evaluate the integrals, we obtain:

$$-4\widetilde{\vartheta}_k + \sum_{m \in \mathscr{N}^k} \widetilde{\vartheta}_{k,m} = 0 \tag{48}$$

with

$$\mathscr{N}^k := \{n, s, e, w\} \tag{49}$$

Since the goal is to obtain a system of equations with one value of the slow term for each FV cell, we need to remove the dummy variables of the slow term (i.e. $\widetilde{\vartheta}_{k,m}$ and

$\widetilde{\jmath}_{m,k}$) at the interfaces of the FV cells. For that purpose, we use the local boundary conditions on each FV cell (Eqs 13d and 13e), which are rewritten below for ease of reading

$$\begin{cases} D\dfrac{\widetilde{\jmath}_{k,m}-\widetilde{\jmath}_k}{h/2} - D\dfrac{\widetilde{\jmath}_m-\widetilde{\jmath}_{m,k}}{h/2} = \dfrac{1}{h}\displaystyle\int_{\partial V_{k,m}} \mathbf{n}\cdot(D\boldsymbol{\nabla}\text{ɾ}_m(\mathbf{x}) - D\boldsymbol{\nabla}\text{ɾ}_k(\mathbf{x}))dl & \text{(50a)} \\ \widetilde{\jmath}_{k,m}-\widetilde{\jmath}_{m,k} = \dfrac{1}{h}\displaystyle\int_{\partial V_{k,m}} (\text{ɾ}_m - \text{ɾ}_k)dl & \text{(50b)} \end{cases}$$

We isolate $\widetilde{\jmath}_{m,k}$ in Eq. 50b and substitute it into Eq. 50 to obtain

$$\widetilde{\jmath}_{k,m} = \frac{\widetilde{\jmath}_k + \widetilde{\jmath}_m}{2} + \frac{J_{k,m}}{2} \tag{51}$$

where

$$J_{k,m} = \frac{1}{2}\int_{\partial V_{k,m}} \mathbf{n}\cdot(\boldsymbol{\nabla}\text{ɾ}_m - \boldsymbol{\nabla}\text{ɾ}_k)dl + \frac{1}{h}\int_{\partial V_{k,m}} (\text{ɾ}_m - \text{ɾ}_k)dl \tag{52}$$

Recalling that ɾ_k and ɾ_m are analytical functions of $\boldsymbol{q}$, we have written a system where the only unknowns are the values of the slow term in the FV grid ($\boldsymbol{\jmath}$) and the vessel-tissue exchanges ($\mathbf{q}$). Therefore, Eq. 16 results in

$$-4\widetilde{\jmath}_k + \sum_{m\in\mathcal{N}^k} \left(\widetilde{\jmath}_m + J_{k,m}\right) = 0 \tag{53}$$

where $J_{k,m} = J_{k,m}(\mathbf{q})$ since it only depends on the rapid term for each cell.

It is worth noting how Eq. 53 can be evaluated independently of the specific form of the rapid term. Additionally, the term $J_{k,m}$ is only evaluated at the interfaces of the cells V_k and V_m. This results in a more efficient and convenient formulation that allows for a flexible construction of the rapid term (see Section B) and a more efficient assembly of the system of equations compared to other models that impose a finite support to their respective analytical term [1, 2].

B Analytical derivation of potentials

To obtain Green's second identity, we multiply the concentration field in the parenchyma (ϕ) by a scalar field φ and apply the divergence theorem:

$$\int_{\Omega_\sigma} \varphi\nabla^2\phi - \phi\nabla^2\varphi dV = -\oint_{\partial\Omega_\sigma} (\varphi\boldsymbol{\nabla}\phi - \phi\boldsymbol{\nabla}\varphi)\cdot\mathbf{n}dS \tag{54}$$

where $\mathbf{n}$ follows the same convention as in figure 1 and represents the normal pointing inward to the domain Ω_σ, and $\partial\Omega_\sigma$ includes all the boundaries of the parenchyma (including the vascular walls) since $\partial\Omega_\sigma := \partial\Omega_\beta \bigcup \partial\Omega$.

We can obtain the Green's third identity by substituting the scalar field φ in equation 54 by the fundamental solution for the Laplace equation

$$G(\mathbf{x};\mathbf{x}^*) = \frac{1}{2\pi D}\ln\Big(\frac{a}{||\mathbf{x}-\mathbf{x}^*||}\Big) \tag{55}$$

where a is a constant of integration. This yields

$$D\nabla^2 G(\mathbf{x};\mathbf{x}^*) = -\delta(\mathbf{x}-\mathbf{x}^*) \quad in \quad \Omega \tag{56}$$

From equations 54 and 55,we obtain:

$$\phi(\mathbf{x}) = \oint_{\partial\Omega_\sigma} (\phi(\mathbf{x}^*)\boldsymbol{\nabla}G(\mathbf{x},\mathbf{x}^*)\cdot\mathbf{n}(\mathbf{x}^*) - G(\mathbf{x},\mathbf{x}^*)\boldsymbol{\nabla}\phi(\mathbf{x}^*)\cdot\mathbf{n}(\mathbf{x}^*))dS(\mathbf{x}^*) \tag{57}$$

which provides a description of the concentration field $\phi(\mathbf{x})$ through a superposition of a double layer potential and a single layer potential given as the first and second part of the integral, respectively. Note that here, the free space Green's function is used instead of the Green's function of the first or second kind due to the difficulty to calculate the later one. Practically, the approach used here is in line with the boundary element method literature [3–5]. Besides, we can decompose the integrals into a contribution from the external boundary $\partial\Omega$ and the vascular boundary $\partial\Omega_\beta$

$$\phi = \oint_{\partial\Omega} (\phi\boldsymbol{\nabla}G\cdot\mathbf{n} - G\boldsymbol{\nabla}\phi\cdot\mathbf{n})dl + \oint_{\partial\Omega_\beta} (\phi\boldsymbol{\nabla}G\cdot\mathbf{n} - G\boldsymbol{\nabla}\phi\cdot\mathbf{n})dl \tag{58}$$

where the integral over the boundary $\partial\Omega$ is expected to behave very regularly through space [2, 6–8] (*Assumption 1* in Section 2.6).

We now neglect the azimuthal variations of concentration around the sources (*Assumption 2* in Section 2.6). In 2D, this allows to strongly simplify the above expression since $\boldsymbol{\nabla}\phi\cdot\mathbf{n}$ and ϕ can be taken out of the integral. Then, the Green's function is integrated analytically over the source surface $\partial\Omega_{\beta,j}$

$$\oint_{\partial\Omega_{\beta,j}} G(\mathbf{x};\mathbf{x}^*)d\mathbf{x}^* = \begin{cases} R_j \ln\Big(\dfrac{R_j}{||\mathbf{x}-\mathbf{x}_j||}\Big) + K_1 & \text{if } ||\mathbf{x}-\mathbf{x}_j|| > R_j \\ K_1 & \text{if } ||\mathbf{x}-\mathbf{x}_j|| \leq R_j \end{cases} \tag{59}$$

where $\mathbf{x}_j$ is the center of the circular source ($\Omega_{\beta,j}$) and K_1 is a constant arising from the integration. Furthermore, due to the simplified Robin boundary condition (Eq. 2) we know that, on the outer surface of the source,

$$-\mathbf{n}\cdot(\boldsymbol{\nabla}\phi) = \frac{q_j}{2\pi R_j D} \tag{60}$$

Therefore, we obtain a non-integral expression for the single layer potential of each source as a function of the vessel-tissue exchanges (q_j)

$$-\oint_{\partial\Omega_{\beta,j}} (G(\mathbf{x};\mathbf{x}^*)\boldsymbol{\nabla}\phi(\mathbf{x}^*))\cdot\mathbf{n}(\mathbf{x}^*)d\mathbf{x}^* = \frac{q_j}{2\pi D}\ln\Big(\frac{R_j}{||\mathbf{x}-\mathbf{x}_j||}\Big) + K_1 \text{ for } \mathbf{x}\in\Omega_\sigma \tag{61}$$

For convenience we set $K_1 = \overline{\phi}_j$ so the potential always stays positive. Furthermore, since the sources in a 2D simulation are closed surfaces, the double layer potential is:

$$\oint_{\partial\Omega_{\beta,j}} (\boldsymbol{\nabla}G(\mathbf{x};\mathbf{x}^*)\cdot\mathbf{n}(\mathbf{x}^*))d\mathbf{x}^* = 0 \quad \forall\mathbf{x}\notin\Omega_{\beta,j} \tag{62}$$

Thus, Eq. 58 simplifies to:

$$\phi(\mathbf{x}) = \oint_{\partial\Omega} (\phi\boldsymbol{\nabla}G\cdot\mathbf{n} - G\boldsymbol{\nabla}\phi\cdot\mathbf{n})dl + \sum_{j\in E(\Omega)} P_j \tag{63}$$

with

$$P_j = \overline{\phi}_j + \frac{q_j}{2\pi D}\ln\Big(\frac{R_j}{||\mathbf{x}-\mathbf{x}_j||}\Big) \quad \text{if } ||\mathbf{x}-\mathbf{x}_j|| > R_j \ \forall\mathbf{x}\in\Omega_\sigma \tag{64}$$

We now make the link between the Green's formulation and the field splitting introduced in Section 2.2. When the neighbourhood of influence of each source is the whole domain ($\widehat{V}_k = \Omega \quad \forall k\in\mathscr{F}$)

$$\phi(\mathbf{x}) = \mathscr{s}(\mathbf{x}) + \sum_{j \in E(\Omega)} \Big(\overline{\phi}_j + \frac{q_j}{2\pi D} \ln\Big(\frac{R_j}{||\mathbf{x} - \mathbf{x}_j||} \Big) \Big) \tag{65}$$

Therefore,

$$\mathscr{s}(\mathbf{x}) = \oint_{\partial\Omega} (\phi \boldsymbol{\nabla} G \cdot \mathbf{n} - G \boldsymbol{\nabla} \phi \cdot \mathbf{n}) dl \tag{66}$$

demonstrating that the slow term carries the contribution of the boundary conditions.

We can reduce the size of $\widehat{V}$ to localize the potentials and increase the sparseness of the system, as the slow term then compensates for the contribution of sources lying further away. Essentially, when we decrease the size of $\widehat{V}$, we rely on the low gradients of the potentials far away from the sources to be accommodated by the slow term. In other words, when we decrease the size of $\widehat{V}$, the number of sources modeled analytically decreases and the gradient of the slow term increases (see Section 2.3.4 for an estimation of the numerical errors as a function of the the size of $\widehat{V}$, n). Nevertheless, the slow term behaves very regularly under most circumstances [1, 6, 9].

C Model conservativeness

Due to the approximated form for the source potentials given in Eq. 24, Eq. 9b is not satisfied point-wise when multiple sources lie close together. For ease of readability we recall the definition of the rapid term (Eq. 9):

$$\begin{cases} \nabla^2 \mathscr{r}_k = 0 & \text{in } \Omega_\sigma \quad (67a) \\ -\mathbf{n} \cdot (D \boldsymbol{\nabla} \mathscr{r}_k) = \dfrac{q_j}{2\pi R_j} & \text{on } \partial\Omega_{\beta,j} \, \forall j \in E(V_k) \quad (67b) \end{cases}$$

where $\mathscr{r}_k$ is composed by the linear sum of the sources potentials in the neighbhourhood (see Section 2.3.2 and B):

$$\mathscr{r}_k = \sum_{j \in E(\widehat{V}_k)} P_j \tag{68}$$

and the potential for each source is given by

$$P_j = \begin{cases} \overline{\phi}_j + \dfrac{q_j}{2\pi D} \ln\Big(\dfrac{R_j}{||\mathbf{x} - \mathbf{x}_j||} \Big) & \text{if } ||\mathbf{x} - \mathbf{x}_j|| > R_j \\ \overline{\phi}_j & \text{if } ||\mathbf{x} - \mathbf{x}_j|| \leq R_j \end{cases} \tag{69}$$

As a result of the choice of P_j, when two sources lie close together, Eq. 67b is not strictly satisfied anymore. To illustrate this, let us suppose there are two sources in the domain, both lying within the same mesh cell k i.e.$E(\Omega) = E(V_k) = \{1, 2\}$,. The rapid term reads

$$\mathscr{r}_k = P_1 + P_2 \tag{70}$$

We then evaluate Eq. 67b

$$\begin{cases} -\mathbf{n} \cdot (D \boldsymbol{\nabla} \mathscr{r}_k)|_{\partial\Omega_{\beta_1}} = \dfrac{q_1}{2\pi R_j} + \varepsilon^q_{2,1}(\mathbf{x}; q_2) & (71a) \\ -\mathbf{n} \cdot (D \boldsymbol{\nabla} \mathscr{r}_k)|_{\partial\Omega_{\beta_2}} = \dfrac{q_2}{2\pi R_j} + \varepsilon^q_{1,2}(\mathbf{x}; q_1) & (71b) \end{cases}$$

where $\varepsilon_{i,j}$ is the error caused by the potential of source i on source j, which stays undefined since we have not specified the position of each source. We can generalize the case for multiple sources:

$$-\mathbf{n}\cdot(D\boldsymbol{\nabla}\text{ר}_k) = \frac{q_i}{2\pi R_i} + \sum_{j\in E(\widehat{V}_k), j\neq i} \varepsilon^q_{i,j} \quad \text{on } \partial\Omega_{\beta,i} \quad \forall i \in E(V_k) \tag{72}$$

and

$$-\mathbf{n}\cdot(D\boldsymbol{\nabla}\text{ג}_k) = \sum_{j\in E(\widehat{V}_k), j\neq i} \varepsilon^q_{i,j} \quad \text{on } \partial\Omega_{\beta,i} \quad \forall i \in E(V_k) \tag{73}$$

However, as P_j are harmonic functions (Eq. 24), applying the divergence theorem we see that the integral contribution of these perturbations around source i is null

$$\oint_{\partial\Omega_{\beta,i}} \varepsilon^q_{i,j} dl = 0 \quad \text{for } i \neq j \tag{74}$$

ensuring that the model remains conservative. Therefore, we can conclude that Eq. 9 may not be satisfied point-wise, but the integral contribution of the associted error is null.

D Sub-grid interpolation of the concentration field

The purpose of the interpolation scheme is two-fold. Firstly, we need to estimate the wall concentration $\overline{\phi}$ to evaluate Eq. 3, and secondly, we aim at providing a sub-grid reconstruction of the concentration field from the values obtained at the grid nodes

$$\widetilde{\phi}_k = \widetilde{\text{ג}}_k + \text{ר}_k(\mathbf{x}_k) \quad \forall k \in \mathscr{T} \tag{75}$$

where $\mathscr{T}$ represents the set of all grid nodes $\mathscr{F}$ plus the boundary nodes, and $\mathbf{x}_k$ represents the position of each node. We want to preserve the logarithmic nature of the source potentials, therefore we define a dual neighbourhood $\widehat{V}^d$ that defines the sources whose potentials are reconstructed analytically. We use linear shape functions to interpolate the node values of the slow term. Since there are discontinuities across the mesh cell faces, a correction term $\mathbb{C}_i$ is added to preserve continuity of the interpolated field. We thus obtain:

$$\mathscr{I}_\phi(\mathbf{x}) = \sum_{i\in\mathscr{T}} \gamma_i(\mathbf{x})(\widetilde{\text{ג}}_i + \mathbb{C}_i) + \sum_{j\in E(\widehat{V}^d)} P_j(\mathbf{x}) \tag{76}$$

where $\mathscr{I}_\phi$ is the interpolation function and γ_i are the classic linear shape functions for a square element [5].

The choice of $\widehat{V}^d$ is arbitrary. In our case, we choose the union of the neighbourhoods ($\widehat{V}$) of all FV cells involved in the interpolation. Therefore, following the convention in Fig. 2, inside the red shaded space, we suggest:

$$\widehat{V}^d = \bigcup_{i\in\{k,e,s,se\}} \widehat{V}_i \tag{77}$$

To estimate the correction $\mathbb{C}_i$, we impose the constraint that:

$$\mathscr{I}_\phi(\mathbf{x}_k) = \widetilde{\phi}_k \quad \forall k \in \mathscr{T} \tag{78}$$

We further use Eqs. 78, 75 and 76 to solve for $\mathbb{C}_i$:

$$\mathbb{C}_i = -\sum_{j\in E(\widehat{V}^d)} \delta_{ji} P_j(\mathbf{x}_i) \tag{79}$$

where

$$\delta_{ji} = \begin{cases} 0 & \text{if} \quad j \in \widehat{V}_i \\ 1 & \text{else} \end{cases} \tag{80}$$

For ease of readability, we group all the potential terms into a extended rapid term:

$$\mathscr{r}_i^c(\mathbf{x}) = \sum_{j \in E(\widehat{V}^d)} (P_j(\mathbf{x}) - \delta_{ji} P_j(\mathbf{x}_i)) \tag{81}$$

to finally obtain the interpolation function

$$\mathscr{I}_\phi(\mathbf{x}) = \sum_{i \in \mathscr{T}} \gamma_i(\mathbf{x})(\widetilde{\mathscr{I}}_i + \mathscr{r}_i^c(\mathbf{x})) \tag{82}$$

E Metabolism

As written in section 2.4, the integrals inside vector $\mathbf{S_{metab}}$ are evaluated using the Simpson's rule of integration

$$\mathbf{S_{metab}} = \begin{Bmatrix} \frac{M}{D}\left(1 - Si_{V_1}\left(\frac{\phi_0}{\phi_0 + \widetilde{\mathscr{I}}_1 + \mathscr{r}_1(\mathbf{x})}\right)\right) \\ \frac{M}{D}\left(1 - Si_{V_2}\left(\frac{\phi_0}{\phi_0 + \widetilde{\mathscr{I}}_2 + \mathscr{r}_2(\mathbf{x})}\right)\right) \\ \frac{M}{D}\left(1 - Si_{V_2}\left(\frac{\phi_0}{\phi_0 + \widetilde{\mathscr{I}}_3 + \mathscr{r}_3(\mathbf{x})}\right)\right) \\ \vdots \\ \frac{M}{D}\left(1 - Si_{V_F}\left(\frac{\phi_0}{\phi_0 + \widetilde{\mathscr{I}}_F + \mathscr{r}_F(\mathbf{x})}\right)\right) \end{Bmatrix} \tag{83}$$

where Si refers to the second order accurate Simpson's rule of integration. We have the following system of equations for the iterative system

$$J(\boldsymbol{\mathscr{I}}^n, \mathbf{q}^n) \begin{Bmatrix} \Delta \boldsymbol{\mathscr{I}} \\ \Delta \mathbf{q} \end{Bmatrix} = - \begin{bmatrix} \mathbf{A} & \mathbf{B} \\ \mathbf{C} & \mathbf{E} \end{bmatrix} \cdot \begin{Bmatrix} \boldsymbol{\mathscr{I}}^n \\ \mathbf{q}^n \end{Bmatrix} - \begin{Bmatrix} \mathbf{b}_{\partial \boldsymbol{\Omega}} \\ \mathbf{b}_{\partial \boldsymbol{\Omega}_\beta} \end{Bmatrix} \tag{84}$$

where each new iteration is given by

$$\begin{Bmatrix} \boldsymbol{\mathscr{I}}^{n+1} \\ \mathbf{q}^{n+1} \end{Bmatrix} = \begin{Bmatrix} \boldsymbol{\mathscr{I}}^n \\ \mathbf{q}^n \end{Bmatrix} + \begin{Bmatrix} \Delta \boldsymbol{\mathscr{I}} \\ \Delta \mathbf{q} \end{Bmatrix} \tag{85}$$

and the Jacobian is calculated as

$$J(\boldsymbol{\mathscr{I}}^n, \mathbf{q}^n) = \begin{bmatrix} \mathbf{A} & \mathbf{B} \\ \mathbf{C} & \mathbf{E} \end{bmatrix} + \begin{bmatrix} \frac{\partial \mathbf{S_{metab}}}{\partial \boldsymbol{\mathscr{I}}^n} & \frac{\partial \mathbf{S_{metab}}}{\partial \mathbf{q}^n} \\ \mathbf{0} & \mathbf{0} \end{bmatrix} \tag{86}$$

$$\left[\frac{\partial \mathbf{S_{metab}}}{\partial \boldsymbol{\mathscr{I}}^n}\right]_{k,m} = \begin{cases} 0 & \text{if } k \neq m \\ -\frac{M}{D} Si_{V_k}\left(\frac{\phi_0}{(\phi_0 + \widetilde{\mathscr{I}}_k + \mathscr{r}_k(\mathbf{x}))^2}\right)) & \text{if } k = m \end{cases} \tag{87}$$

$$\left[\frac{\partial \mathbf{S_{metab}}}{\partial \mathbf{q}^n}\right]_{k,j} = \begin{cases} 0 & \text{if } j \notin E(\widehat{V}_k) \\ -\frac{M}{D} Si_{V_k}\left(\frac{1}{2\pi R_j} \ln\left(\frac{R_j}{||\mathbf{x} - \mathbf{x}_j||}\right) \frac{\phi_0}{(\phi_0 + \widetilde{\mathscr{I}}_k + \mathscr{r}_k(\mathbf{x}))^2}\right) & \text{if } j \in E(\widehat{V}_k) \end{cases} \tag{88}$$

The initial guess for the iterative system is the solution for the linear system with no metabolism

$$\begin{bmatrix} \mathbf{A} & \mathbf{B} \\ \mathbf{C} & \mathbf{E} \end{bmatrix} \cdot \begin{Bmatrix} \boldsymbol{\vartheta}^0 \\ \mathbf{q}^0 \end{Bmatrix} = \begin{Bmatrix} \mathbf{b_1} \\ \mathbf{b_2} \end{Bmatrix} \tag{89}$$

References

1. Gjerde IG, Kumar K, Nordbotten JM. A singularity removal method for coupled 1D–3D flow models. Computational Geosciences. 2020;24(2):443–457. doi:10.1007/s10596-019-09899-4.

2. Wolfsteiner C, Lee SH, Tchelepi HA. Well Modeling in the Multiscale Finite Volume Method for Subsurface Flow Simulation. Multiscale Modeling & Simulation. 2006;5(3):900–917. doi:10.1137/050640771.

3. Pozrikidis C, Farrow DA. A Model of Fluid Flow in Solid Tumors. Annals of Biomedical Engineering. 2003;31(2):181–194. doi:10.1114/1.1540103.

4. Aliabadi MH, Wen PH. Boundary element methods in engineering and sciences. No. 4 in Computational and experimental methods in structures. London: Imperial College Press; 2011.

5. Pepper D, Kassab A, Divo E. Introduction to Finite Element, Boundary Element, and Meshless Methods: With Applications to Heat Transfer and Fluid Flow. ASME Press; 2014.

6. Roach GF. Green's Functions. 2nd ed. Cambridge: Cambridge University Press; 1982.

7. Pozrikidis C, Davis JM. Blood Flow Through Capillary Networks. In: Transport in Biological Media. Elsevier; 2013. p. 213–252.

8. Ding DY. Near-Well Upscaling for Reservoir Simulations. Oil & Gas Science and Technology. 2004;59(2):157–165. doi:10/dpvbh3.

9. Pozrikidis C, Ferziger JH. Introduction to Theoretical and Computational Fluid Dynamics. Physics Today. 1997;50(9):72–74. doi:10.1063/1.881920.

Supporting Information for "Modeling oxygen transport in the brain: an efficient coarse-grid approach to capture perivascular gradients in the parenchyma".

David Pastor-Alonso[1], Maxime Berg[1,2], Franck Boyer[3], Natalie Fomin-Thunemann[4], Michel Quintard[1], Yohan Davit[1], Sylvie Lorthois*[1],

1 Institut de Mécanique des Fluides de Toulouse, UMR 5502, CNRS, University of Toulouse, Toulouse, France.
2 Department of Mechanical Engineering, University College London, London, UK
3 Institut de Mathématiques de Toulouse (IMT), CNRS and Université de Toulouse, 31400 Toulouse, France
4 Department of Biomedical Engineering, Boston University, Boston, Massachusetts, USA.

Supplementary figures

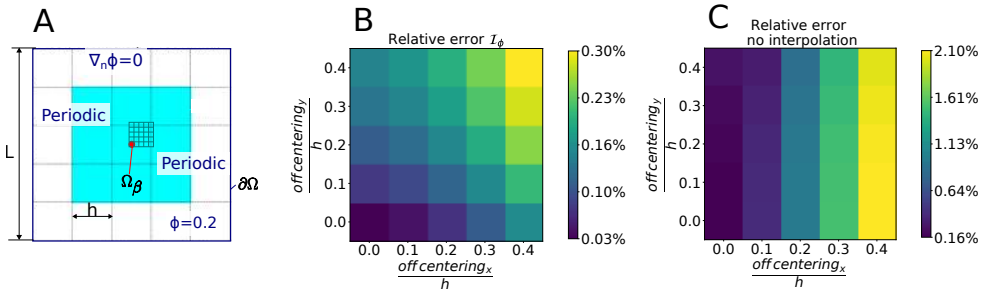

Fig S1. Flux rate errors are displayed for the off-centering of a source withing a FV cell. A: schematics of the test-case where the center of the source is moved throughout the grid contained in the upper right corner of the center cell. B and C: error on the vessel-tissue exchanges ($\mathbf{q}$) with interpolation ($\mathcal{I}_\phi$) in Panel B and without in Panel C. The asymmetry of errors is due to the set of boundary conditions imposed at the limits of the computational domain (see Panel A).

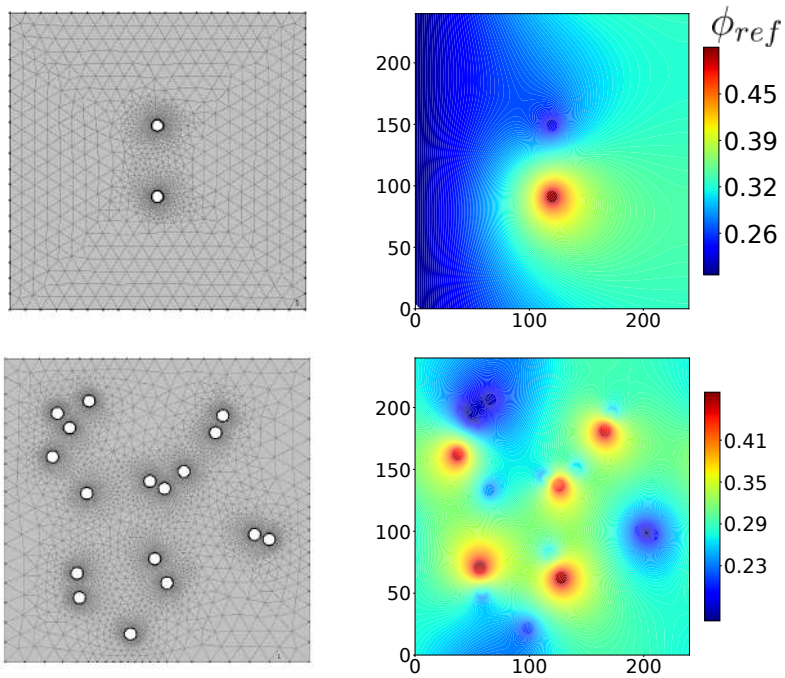

Fig S2. Fine mesh finite element (FE) reference concentration field (ϕ_{ref}) obtained with COMSOL Multiphysics for the original non-reactive BVP (eqs. ??). For the single dipole configuration, 2278 mesh elements have been used (upper panel), while 9468 elements have been used for the multiple source configurations (lower panel).

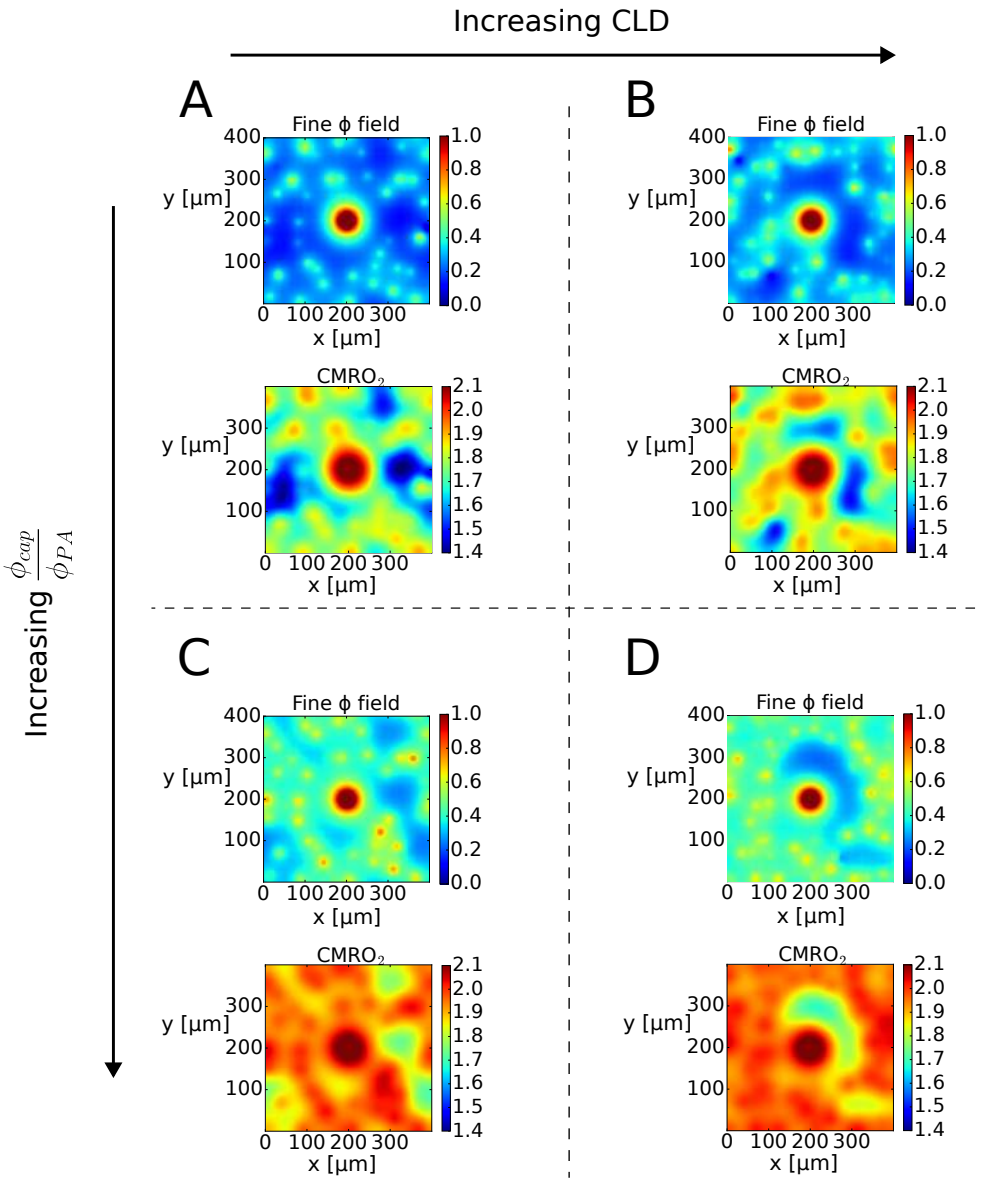

Fig S3. Sub-grid reconstructions of the concentration field (upper) and local cerebral metabolic rate $MC/(K+C)$ (lower) for varying capillary densities and oxygenations. M=2.4 $\frac{\mu mol}{cm^3 min}$. A: CLD=0.8 mmm^{-3} and ϕ_{cap}/ϕ_{PA}=0.4; B: CLD=1.2 mmm^{-3} and ϕ_{cap}/ϕ_{PA}=0.4; C: CLD=0.8 mmm^{-3} and ϕ_{cap}/ϕ_{PA}=0.55; D: CLD=1.2 mmm^{-3} and ϕ_{cap}/ϕ_{PA}=0.55. To facilitate comparison, panels with same CLD present the same realization of source/sink locations.

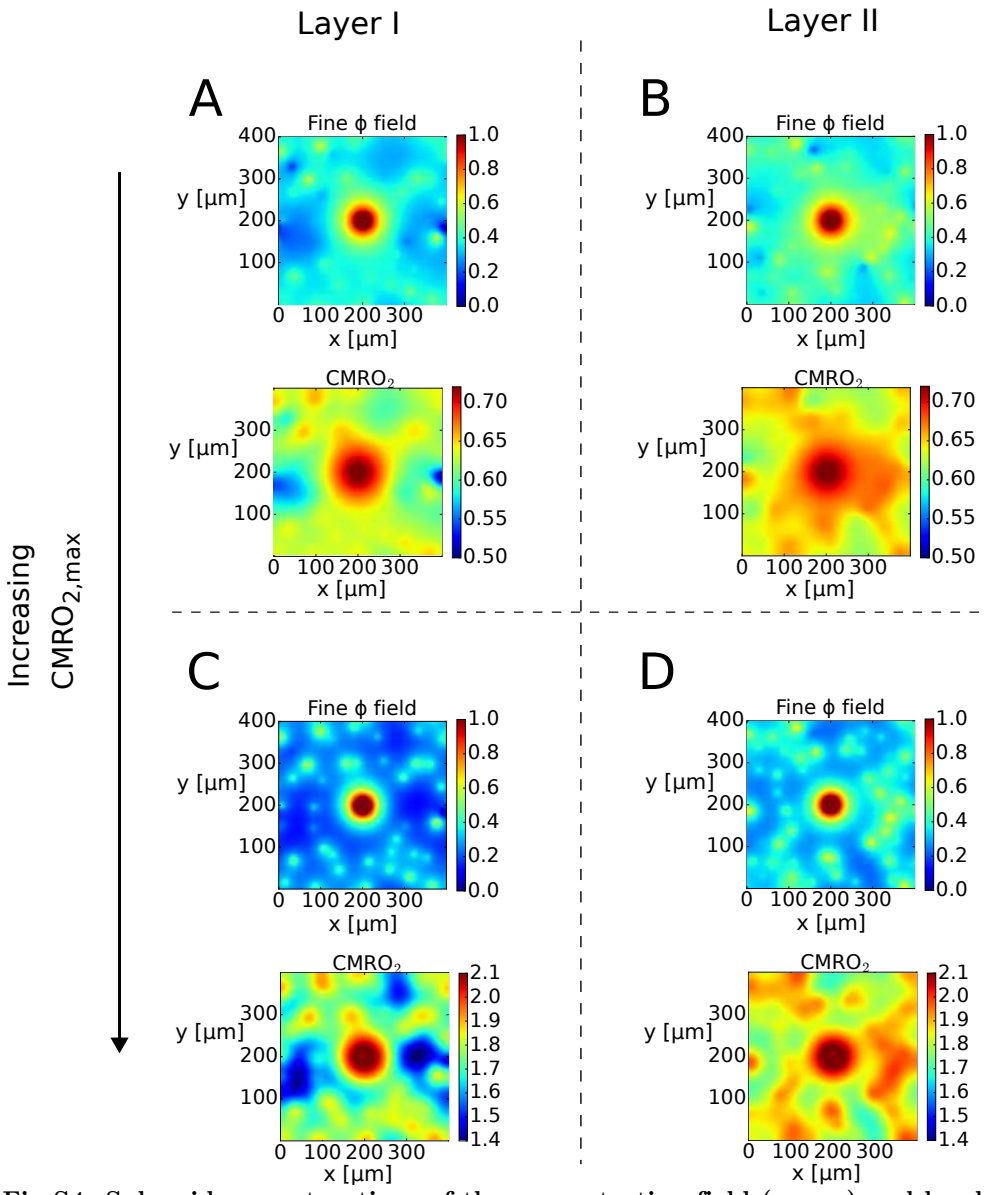

Fig S4. Sub-grid reconstructions of the concentration field (upper) and local cerebral metabolic rate $MC/(K+C)$ (lower) for varying values of the maximal cerebral rate of oxygen M. Layer I: CLD=0.8 mmm^{-3} and ϕ_{cap}/ϕ_{PA}=0.4; Layer II: CLD=0.94 mmm^{-3} and ϕ_{cap}/ϕ_{PA}=0.45; A and B: M=0.8 $\frac{\mu mol}{cm^3 min}$; C and D: M=2.4 $\frac{\mu mol}{cm^3 min}$. To facilitate comparison, panels with same CLD present the same realization of source/sink locations.

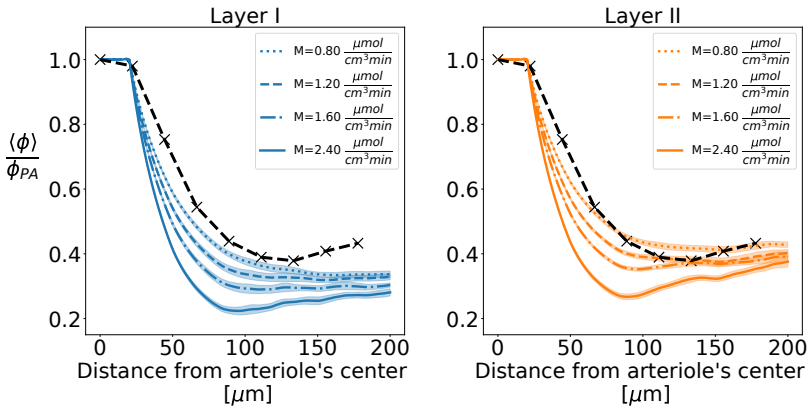

Fig S5. Radial concentration profiles predicted in layer I and layer II (thin continuous lines) together with experimental values obtained from post-processing the data in Fig. ??C (bold dashed line). The predicted profiles are obtained by averaging the results of 30 simulations for parameters for layer I (left) and layer II (right) as given in Table **??**, respectively, and for four physiologically realistic values of M (see legend in right panel). The experimental measurement were made $100\mu m$ under the cortical surface, i.e., at the interface between layer I and II.

Supplementary methods

S.1 Multiscale Finite Volume formulation

In the Finite Volume (FV) method, the main ideas are as follows:

1. **Discretization**: We divide the domain Ω_σ into a set of control volumes $\mathscr{F}$ where the variable are estimated at the geometrical center (node) of each control volume.
2. **Flux approximation**: We approximate the fluxes as a function of the nodal values to obtain a system involving only concentrations
3. **Closure of the system**: we impose flux and concentration continuity at each of the FV cell's interfaces

We begin by integrating the PDE **??** over the control volume given by V_k:

$$\iint_{V_k} \nabla^2 \mathscr{Z}_k(\mathbf{x}) dS = 0 \quad \forall k \in \mathscr{F} \tag{1}$$

Recalling that V_k have been introduced in Section **??** to provide a tessellation of the parenchyma Ω_σ, we obtain, by applying the divergence theorem:

$$\sum_{m \in \mathscr{N}^k} \int_{\partial V_{k,m}} (\boldsymbol{\nabla} \mathscr{Z}_k \cdot \mathbf{n}) dl + \sum_{j \in E(V_k)} \oint_{\partial \Omega_{\beta,j}} (\boldsymbol{\nabla} \mathscr{Z}_k \cdot \mathbf{n}) dl = 0 \quad \forall k \in \mathscr{F} \tag{2}$$

The second integral term in the left hand side of Eq. 2 is always null due to the boundary condition **??**. Using the TPFA (Eq. **??**) to estimate the slow term gradients and the mid-point rule to evaluate the integrals, we obtain:

$$-4\widetilde{\mathscr{Z}}_k + \sum_{m \in \mathscr{N}^k} \widetilde{\mathscr{Z}}_{k,m} = 0 \tag{3}$$

with

$$\mathscr{N}^k := \{n, s, e, w\} \tag{4}$$

Since the goal is to obtain a system of equations with one value of the slow term for each FV cell, we need to remove the dummy variables of the slow term (i.e. $\widetilde{\mathscr{Z}}_{k,m}$ and $\widetilde{\mathscr{Z}}_{m,k}$) at the interfaces of the FV cells. For that purpose, we use the local boundary conditions on each FV cell (Eqs **??**d and **??**e), which are rewritten below for ease of reading

$$\begin{cases} D\dfrac{\widetilde{\mathscr{Z}}_{k,m} - \widetilde{\mathscr{Z}}_k}{h/2} - D\dfrac{\widetilde{\mathscr{Z}}_m - \widetilde{\mathscr{Z}}_{m,k}}{h/2} = \dfrac{1}{h}\displaystyle\int_{\partial V_{k,m}} \mathbf{n} \cdot (D\boldsymbol{\nabla} \mathscr{r}_m(\mathbf{x}) - D\boldsymbol{\nabla} \mathscr{r}_k(\mathbf{x})) dl & \text{(5a)} \\ \widetilde{\mathscr{Z}}_{k,m} - \widetilde{\mathscr{Z}}_{m,k} = \dfrac{1}{h}\displaystyle\int_{\partial V_{k,m}} (\mathscr{r}_m - \mathscr{r}_k) dl & \text{(5b)} \end{cases}$$

We isolate $\widetilde{\mathscr{Z}}_{m,k}$ in Eq. 5b and substitute it into Eq. 5 to obtain

$$\widetilde{\mathscr{Z}}_{k,m} = \frac{\widetilde{\mathscr{Z}}_k + \widetilde{\mathscr{Z}}_m}{2} + \frac{J_{k,m}}{2} \tag{59}$$

where

$$J_{k,m} = \frac{1}{2}\int_{\partial V_{k,m}} \mathbf{n} \cdot (\boldsymbol{\nabla} \mathscr{r}_m - \boldsymbol{\nabla} \mathscr{r}_k) dl + \frac{1}{h}\int_{\partial V_{k,m}} (\mathscr{r}_m - \mathscr{r}_k) dl \tag{60}$$

Recalling that $\curlywedge_k$ and $\curlywedge_m$ are analytical functions of $\boldsymbol{q}$, we have written a system where the only unknowns are the values of the slow term in the FV grid ($\boldsymbol{\jmath}$) and the vessel-tissue exchanges ($\mathbf{q}$). Therefore, Eq. **??** results in

$$-4\widetilde{\jmath}_k + \sum_{m \in \mathcal{N}^k} \left(\widetilde{\jmath}_m + J_{k,m}\right) = 0 \tag{61}$$

where $J_{k,m} = J_{k,m}(\mathbf{q})$ since it only depends on the rapid term for each cell.

It is worth noting how Eq. 61 can be evaluated independently of the specific form of the rapid term. Additionally, the term $J_{k,m}$ is only evaluated at the interfaces of the cells V_k and V_m. This results in a more efficient and convenient formulation that allows for a flexible construction of the rapid term (see Section S.2) and a more efficient assembly of the system of equations compared to other models that impose a finite support to their respective analytical term [1, 2].

S.2 Analytical derivation of potentials

To obtain Green's second identity, we multiply the concentration field in the parenchyma (ϕ) by a scalar field φ and apply the divergence theorem:

$$\int_{\Omega_\sigma} \varphi\nabla^2\phi - \phi\nabla^2\varphi dV = -\oint_{\partial\Omega_\sigma} (\varphi\boldsymbol{\nabla}\phi - \phi\boldsymbol{\nabla}\varphi)\cdot\mathbf{n}dS \tag{62}$$

where $\mathbf{n}$ follows the same convention as in figure **??** and represents the normal pointing inward to the domain Ω_σ, and $\partial\Omega_\sigma$ includes all the boundaries of the parenchyma (including the vascular walls) since $\partial\Omega_\sigma := \partial\Omega_\beta \bigcup \partial\Omega$.

We can obtain the Green's third identity by substituting the scalar field φ in equation 62 by the fundamental solution for the Laplace equation

$$G(\mathbf{x};\mathbf{x}^*) = \frac{1}{2\pi D}\ln\Big(\frac{a}{||\mathbf{x}-\mathbf{x}^*||}\Big) \tag{63}$$

where a is a constant of integration. This yields

$$D\nabla^2 G(\mathbf{x};\mathbf{x}^*) = -\delta(\mathbf{x}-\mathbf{x}^*) \quad in \quad \Omega \tag{64}$$

From equations 62 and 63 [1], we obtain:

$$\phi(\mathbf{x}) = \oint_{\partial\Omega_\sigma} (\phi(\mathbf{x}^*)\boldsymbol{\nabla}G(\mathbf{x},\mathbf{x}^*)\cdot\mathbf{n}(\mathbf{x}^*) - G(\mathbf{x},\mathbf{x}^*)\boldsymbol{\nabla}\phi(\mathbf{x}^*)\cdot\mathbf{n}(\mathbf{x}^*))dS(\mathbf{x}^*) \tag{65}$$

which provides a description of the concentration field $\phi(\mathbf{x})$ through a superposition of a double layer potential and a single layer potential given as the first and second part of the integral, respectively. Besides, we can decompose the integrals into a contribution from the external boundary $\partial\Omega$ and the vascular boundary $\partial\Omega_\beta$

$$\phi = \oint_{\partial\Omega} (\phi\boldsymbol{\nabla}G\cdot\mathbf{n} - G\boldsymbol{\nabla}\phi\cdot\mathbf{n})dl + \oint_{\partial\Omega_\beta} (\phi\boldsymbol{\nabla}G\cdot\mathbf{n} - G\boldsymbol{\nabla}\phi\cdot\mathbf{n})dl \tag{66}$$

where the integral over the boundary $\partial\Omega$ is expected to behave very regularly through space [2, 6–8] (*Assumption 1* in Section **??**).

We now neglect the azimuthal variations of concentration around the sources (*Assumption 2* in Section **??**). In 2D, this allows to strongly simplify the above

[1] Here the free space Green's function is used instead of the Green's function of the first or second kind due to the difficulty to calculate the later one. Practically, the approach used here is in line with the boundary element method literature [3–5]

expression since $\boldsymbol{\nabla}\phi \cdot \mathbf{n}$ and ϕ can be taken out of the integral. Then, the Green's function is integrated analytically over the source surface $\partial\Omega_{\beta,j}$

$$\oint_{\partial\Omega_{\beta,j}} G(\mathbf{x};\mathbf{x}^*)d\mathbf{x}^* = \begin{cases} R_j \ln\Big(\dfrac{R_j}{||\mathbf{x}-\mathbf{x}_j||}\Big) + K_1 & \text{if } ||\mathbf{x}-\mathbf{x}_j|| > R_j \\ K_1 & \text{if } ||\mathbf{x}-\mathbf{x}_j|| \leq R_j \end{cases} \tag{67}$$

where $\mathbf{x}_j$ is the center of the circular source ($\Omega_{\beta,j}$) and K_1 is a constant arising from the integration. Furthermore, due to the simplified Robin boundary condition (Eq. **??**) we know that, on the outer surface of the source,

$$-\mathbf{n} \cdot (\boldsymbol{\nabla}\phi) = \frac{q_j}{2\pi R_j D} \tag{68}$$

Therefore, we obtain a non-integral expression for the single layer potential of each source as a function of the vessel-tissue exchanges (q_j)

$$-\oint_{\partial\Omega_{\beta,j}} (G(\mathbf{x};\mathbf{x}^*)\boldsymbol{\nabla}\phi(\mathbf{x}^*)) \cdot \mathbf{n}(\mathbf{x}^*)d\mathbf{x}^* = \frac{q_j}{2\pi D}\ln\Big(\frac{R_j}{||\mathbf{x}-\mathbf{x}_j||}\Big) + K_1 \text{ for } \mathbf{x} \in \Omega_\sigma \tag{69}$$

For convenience we set $K_1 = \overline{\phi}_j$ so the potential always stays positive. Furthermore, since the sources in a 2D simulation are closed surfaces, the double layer potential is:

$$\oint_{\partial\Omega_{\beta,j}} (\boldsymbol{\nabla}G(\mathbf{x};\mathbf{x}^*) \cdot \mathbf{n}(\mathbf{x}^*))d\mathbf{x}^* = 0 \quad \forall \mathbf{x} \notin \Omega_{\beta,j} \tag{70}$$

Thus, Eq. 66 simplifies to:

$$\phi(\mathbf{x}) = \oint_{\partial\Omega} (\phi\boldsymbol{\nabla}G \cdot \mathbf{n} - G\boldsymbol{\nabla}\phi \cdot \mathbf{n})dl + \sum_{j \in E(\Omega)} P_j \tag{71}$$

with

$$P_j = \overline{\phi}_j + \frac{q_j}{2\pi D}\ln\Big(\frac{R_j}{||\mathbf{x}-\mathbf{x}_j||}\Big) \quad \text{if } ||\mathbf{x}-\mathbf{x}_j|| > R_j \ \forall \mathbf{x} \in \Omega_\sigma \tag{72}$$

We now make the link between the Green's formulation and the field splitting introduced in Section **??**. When the neighbourhood of influence of each source is the whole domain ($\widehat{V}_k = \Omega \quad \forall k \in \mathscr{F}$)

$$\phi(\mathbf{x}) = \mathscr{s}(\mathbf{x}) + \sum_{j \in E(\Omega)} \Big(\overline{\phi}_j + \frac{q_j}{2\pi D}\ln\Big(\frac{R_j}{||\mathbf{x}-\mathbf{x}_j||}\Big)\Big) \tag{73}$$

Therefore,

$$\mathscr{s}(\mathbf{x}) = \oint_{\partial\Omega} (\phi\boldsymbol{\nabla}G \cdot \mathbf{n} - G\boldsymbol{\nabla}\phi \cdot \mathbf{n})dl \tag{74}$$

demonstrating that the slow term carries the contribution of the boundary conditions.

We can reduce the size of $\widehat{V}$ to localize the potentials and increase the sparseness of the system, as the slow term then compensates for the contribution of sources lying further away. Essentially, when we decrease the size of $\widehat{V}$, we rely on the low gradients of the potentials far away from the sources to be accommodated by the slow term. In other words, when we decrease the size of $\widehat{V}$, the number of sources modeled analytically decreases and the gradient of the slow term increases (see Section **??** for an estimation of the numerical errors as a function of the the size of $\widehat{V}$, n). Nevertheless, the slow term behaves very regularly under most circumstances [1, 6, 9].

S.3 Model conservativeness

Due to the approximated form for the source potentials given in Eq. **??**, Eq. **??**b is not satisfied point-wise when multiple sources lie close together. For ease of readability we recall the definition of the rapid term (Eq. **??**):

$$\begin{cases} \nabla^2 \text{ר}_k = 0 & \text{in } \Omega_\sigma \quad (75a) \\ -\mathbf{n} \cdot (D\boldsymbol{\nabla} \text{ר}_k) = \dfrac{q_j}{2\pi R_j} & \text{on } \partial\Omega_{\beta,j} \, \forall j \in E(V_k) \quad (75b) \end{cases}$$

where ר_k is composed by the linear sum of the sources potentials in the neighbhourhood (see Section **??** and S.2)

$$\text{ר}_k = \sum_{j \in E(\widehat{V}_k)} P_j \tag{68}$$

and the potential for each source is given by

$$P_j = \begin{cases} \overline{\phi}_j + \dfrac{q_j}{2\pi D} \ln\Big(\dfrac{R_j}{||\mathbf{x} - \mathbf{x}_j||}\Big) & \text{if } ||\mathbf{x} - \mathbf{x}_j|| > R_j \\ \overline{\phi}_j & \text{if } ||\mathbf{x} - \mathbf{x}_j|| \leq R_j \end{cases} \tag{69}$$

As a result of the choice of P_j, when two sources lie close together, Eq. 75b is not strictly satisfied anymore. To illustrate this, let us suppose there are two sources in the domain, both lying within the same mesh cell k i.e.$E(\Omega) = E(V_k) = \{1, 2\}$,. The rapid term reads

$$\text{ר}_k = P_1 + P_2 \tag{70}$$

We then evaluate Eq. 75b

$$\begin{cases} -\mathbf{n} \cdot (D\boldsymbol{\nabla} \text{ר}_k)|_{\partial\Omega_{\beta_1}} = \dfrac{q_1}{2\pi R_j} + \varepsilon^q_{2,1}(\mathbf{x}; q_2) & (71a) \\ -\mathbf{n} \cdot (D\boldsymbol{\nabla} \text{ר}_k)|_{\partial\Omega_{\beta_2}} = \dfrac{q_2}{2\pi R_j} + \varepsilon^q_{1,2}(\mathbf{x}; q_1) & (71b) \end{cases}$$

where $\varepsilon_{i,j}$ is the error caused by the potential of source i on source j, which stays undefined since we have not specified the position of each source. We can generalize the case for multiple sources:

$$-\mathbf{n} \cdot (D\boldsymbol{\nabla} \text{ר}_k) = \frac{q_i}{2\pi R_i} + \sum_{j \in E(\widehat{V}_k), j \neq i} \varepsilon^q_{i,j} \quad \text{on } \partial\Omega_{\beta,i} \quad \forall i \in E(V_k) \tag{68}$$

and

$$-\mathbf{n} \cdot (D\boldsymbol{\nabla} \text{ש}_k) = \sum_{j \in E(\widehat{V}_k), j \neq i} \varepsilon^q_{i,j} \quad \text{on } \partial\Omega_{\beta,i} \quad \forall i \in E(V_k) \tag{69}$$

However, as P_j are harmonic functions (Eq. **??**), applying the divergence theorem we see that the integral contribution of these perturbations around source i is null

$$\oint_{\partial\Omega_{\beta,i}} \varepsilon^q_{i,j} dl = 0 \quad \text{for } i \neq j \tag{70}$$

ensuring that the model remains conservative. Therefore, we can conclude that Eq. **??** may not be satisfied point-wise, but the integral contribution of the associted error is null.

S.4 Sub-grid interpolation of the concentration field

The purpose of the interpolation scheme is two-fold. Firstly, we need to estimate the wall concentration $\overline{\phi}$ to evaluate Eq. **??**, and secondly, we aim at providing a sub-grid reconstruction of the concentration field from the values obtained at the grid nodes

$$\widetilde{\phi}_k = \widetilde{\jmath}_k + \curlywedge_k(\mathbf{x}_k) \quad \forall k \in \mathscr{T} \tag{71}$$

where $\mathscr{T}$ represents the set of all grid nodes $\mathscr{F}$ plus the boundary nodes, and $\mathbf{x}_k$ represents the position of each node. We want to preserve the logarithmic nature of the source potentials, therefore we define a dual neighbourhood $\widehat{V}^d$ that defines the sources whose potentials are reconstructed analytically. We use linear shape functions to interpolate the node values of the slow term. Since there are discontinuities across the mesh cell faces, a correction term $\mathbb{C}_i$ is added to preserve continuity of the interpolated field. We thus obtain:

$$\mathscr{I}_\phi(\mathbf{x}) = \sum_{i \in \mathscr{T}} \gamma_i(\mathbf{x})(\widetilde{\jmath}_i + \mathbb{C}_i) + \sum_{j \in E(\widehat{V}^d)} P_j(\mathbf{x}) \tag{72}$$

where $\mathscr{I}_\phi$ is the interpolation function and γ_i are the classic linear shape functions for a square element [5].

The choice of $\widehat{V}^d$ is arbitrary. In our case, we choose the union of the neighbourhoods ($\widehat{V}$) of all FV cells involved in the interpolation. Therefore, following the convention in figure **??**, inside the red shaded space, we suggest:

$$\widehat{V}^d = \bigcup_{i \in \{k,e,s,se\}} \widehat{V}_i \tag{73}$$

To estimate the correction $\mathbb{C}_i$, we impose the constraint that:

$$\mathscr{I}_\phi(\mathbf{x}_k) = \widetilde{\phi}_k \quad \forall k \in \mathscr{T} \tag{74}$$

We further use Eqs. 74, 71 and 72 to solve for $\mathbb{C}_i$:

$$\mathbb{C}_i = - \sum_{j \in E(\widehat{V}^d)} \delta_{ji} P_j(\mathbf{x}_i) \tag{75}$$

where

$$\delta_{ji} = \begin{cases} 0 & \text{if} \quad j \in \widehat{V}_i \\ 1 & \text{else} \end{cases} \tag{76}$$

For ease of readability, we group all the potential terms into a extended rapid term:

$$\curlywedge_i^c(\mathbf{x}) = \sum_{j \in E(\widehat{V}^d)} (P_j(\mathbf{x}) - \delta_{ji} P_j(\mathbf{x}_i)) \tag{77}$$

to finally obtain the interpolation function

$$\mathscr{I}_\phi(\mathbf{x}) = \sum_{i \in \mathscr{T}} \gamma_i(\mathbf{x})(\widetilde{\jmath}_i + \curlywedge_i^c(\mathbf{x})) \tag{78}$$

S.5 Metabolism

As written in section **??**, the integrals inside vector $\mathbf{S_{metab}}$ are evaluated using the Simpson's rule of integration

$$\mathbf{S_{metab}} = \begin{Bmatrix} \frac{M}{D}\left(1 - Si_{V_1}\left(\frac{\phi_0}{\phi_0 + \widetilde{\jmath}_1 + \kappa_1(\mathbf{x})}\right)\right) \\ \frac{M}{D}\left(1 - Si_{V_2}\left(\frac{\phi_0}{\phi_0 + \widetilde{\jmath}_2 + \kappa_2(\mathbf{x})}\right)\right) \\ \frac{M}{D}\left(1 - Si_{V_2}\left(\frac{\phi_0}{\phi_0 + \widetilde{\jmath}_3 + \kappa_3(\mathbf{x})}\right)\right) \\ \vdots \\ \frac{M}{D}\left(1 - Si_{V_F}\left(\frac{\phi_0}{\phi_0 + \widetilde{\jmath}_F + \kappa_F(\mathbf{x})}\right)\right) \end{Bmatrix} \tag{79}$$

where Si refers to the second order accurate Simpson's rule of integration. We have the following system of equations for the iterative system

$$J(\boldsymbol{\jmath}^n, \mathbf{q}^n) \begin{Bmatrix} \Delta\boldsymbol{\jmath} \\ \Delta\mathbf{q} \end{Bmatrix} = - \begin{bmatrix} \mathbf{A} & \mathbf{B} \\ \mathbf{C} & \mathbf{E} \end{bmatrix} \cdot \begin{Bmatrix} \boldsymbol{\jmath}^n \\ \mathbf{q}^n \end{Bmatrix} - \begin{Bmatrix} \mathbf{b}_{\partial\boldsymbol{\Omega}} \\ \mathbf{b}_{\partial\boldsymbol{\Omega}_\beta} \end{Bmatrix} \tag{80}$$

where each new iteration is given by

$$\begin{Bmatrix} \boldsymbol{\jmath}^{n+1} \\ \mathbf{q}^{n+1} \end{Bmatrix} = \begin{Bmatrix} \boldsymbol{\jmath}^n \\ \mathbf{q}^n \end{Bmatrix} + \begin{Bmatrix} \Delta\boldsymbol{\jmath} \\ \Delta\mathbf{q} \end{Bmatrix} \tag{81}$$

and the Jacobian is calculated as

$$J(\boldsymbol{\jmath}^n, \mathbf{q}^n) = \begin{bmatrix} \mathbf{A} & \mathbf{B} \\ \mathbf{C} & \mathbf{E} \end{bmatrix} + \begin{bmatrix} \frac{\partial \mathbf{S_{metab}}}{\partial \boldsymbol{\jmath}^n} & \frac{\partial \mathbf{S_{metab}}}{\partial \mathbf{q}^n} \\ \mathbf{0} & \mathbf{0} \end{bmatrix} \tag{82}$$

$$\left[\frac{\partial \mathbf{S_{metab}}}{\partial \boldsymbol{\jmath}^n}\right]_{k,m} = \begin{cases} 0 & \text{if } k \neq m \\ -\frac{M}{D} Si_{V_k}\left(\frac{\phi_0}{(\phi_0 + \widetilde{\jmath}_k + \kappa_k(\mathbf{x}))^2}\right)) & \text{if } k = m \end{cases} \tag{83}$$

$$\left[\frac{\partial \mathbf{S_{metab}}}{\partial \mathbf{q}^n}\right]_{k,j} = \begin{cases} 0 & \text{if } j \notin E(\widehat{V}_k) \\ -\frac{M}{D} Si_{V_k}\left(\frac{1}{2\pi R_j} \ln\left(\frac{R_j}{||\mathbf{x} - \mathbf{x}_j||}\right) \frac{\phi_0}{(\phi_0 + \widetilde{\jmath}_k + \kappa_k(\mathbf{x}))^2}\right) & \text{if } j \in E(\widehat{V}_k) \end{cases} \tag{84}$$

The initial guess for the iterative system is the solution for the linear system with no metabolism

$$\begin{bmatrix} \mathbf{A} & \mathbf{B} \\ \mathbf{C} & \mathbf{E} \end{bmatrix} \cdot \begin{Bmatrix} \boldsymbol{\jmath}^0 \\ \mathbf{q}^0 \end{Bmatrix} = \begin{Bmatrix} \mathbf{b_1} \\ \mathbf{b_2} \end{Bmatrix} \tag{85}$$

References

1. Gjerde IG, Kumar K, Nordbotten JM. A singularity removal method for coupled 1D–3D flow models. Computational Geosciences. 2020;24(2):443–457. doi:10.1007/s10596-019-09899-4.

2. Wolfsteiner C, Lee SH, Tchelepi HA. Well Modeling in the Multiscale Finite Volume Method for Subsurface Flow Simulation. Multiscale Modeling & Simulation. 2006;5(3):900–917. doi:10.1137/050640771.

3. Pozrikidis C, Farrow DA. A Model of Fluid Flow in Solid Tumors. Annals of Biomedical Engineering. 2003;31(2):181–194. doi:10.1114/1.1540103.

4. Aliabadi MH, Wen PH. Boundary element methods in engineering and sciences. No. 4 in Computational and experimental methods in structures. London: Imperial College Press; 2011.

5. Pepper D, Kassab A, Divo E. Introduction to Finite Element, Boundary Element, and Meshless Methods: With Applications to Heat Transfer and Fluid Flow. ASME Press; 2014.

6. Roach GF. Green's Functions. 2nd ed. Cambridge: Cambridge University Press; 1982.

7. Pozrikidis C, Davis JM. Blood Flow Through Capillary Networks. In: Transport in Biological Media. Elsevier; 2013. p. 213–252.

8. Ding DY. Near-Well Upscaling for Reservoir Simulations. Oil & Gas Science and Technology. 2004;59(2):157–165. doi:10/dpvbh3.

9. Pozrikidis C, Ferziger JH. Introduction to Theoretical and Computational Fluid Dynamics. Physics Today. 1997;50(9):72–74. doi:10.1063/1.881920.

3.2 Discussion in the context of multiscale modeling of oxygen transport

In this chapter, we have established the foundation of a multiscale model designed to accurately and efficiently capture perivascular gradients and non-linear metabolic reactions in the brain parenchyma. Our particular focus was on integrating an analytical description of microscale dynamics into a structured cartesian mesh, significantly reducing the system's size compared to models with similar levels of detail. We introduced a 0DIV - 2DEV model to comprehensively test the underlying hypotheses of our multiscale approach. Leveraging the efficient integration of multiple sources and sinks in a 2D configuration, we applied this multiscale model to assist in interpreting tissue oxygenation data acquired through multiphoton microscopy [12; 13]. This enhanced efficiency indeed enabled us to reduce the computational cost of directly modeling the oxygen concentration field around a penetrating arteriole, facilitating the testing of various configurations to achieve a representation of the average radial concentration profile around penetrating arterioles that matches experimental data.

Furthermore, the 2D configuration allowed us to isolate the impact of radial concentration gradients around the vessels without needing to consider the three-dimensional architecture of the microvascular network or axial transport along the vessels' axis. As a result, we thoroughly analyzed and validated the most challenging aspect of solute transport in the microcirculation, i.e., perivascular concentration gradients, within the operator splitting framework. This analysis paves the way for extending the multiscale model to 1DIV-3DEV configurations, with a precise estimation of the errors introduced by the analytical-numerical framework proposed in this chapter for describing radial transport. Therefore, in the next chapter, we expand this multiscale model to include the third dimension, introducing new challenges related to the coupling with intravascular transport, network discretization, and the evaluation of source potentials within a given discretization.

3.3 References

[1] D W Peaceman. Interpretation of Well-Block Pressures in Numerical Reservoir Simulation. *Society of Petroleum Engineers*, page 17, 1978. 47

[2] I. Aavatsmark and R.A. Klausen. Well Index in Reservoir Simulation for Slanted and Slightly Curved Wells in 3D Grids. *SPE-75275-PA*, 8(01) :41–48, March 2003. Publisher : Society of Petroleum Engineers. 47

[3] Myriam Peyrounette, Yohan Davit, Michel Quintard, and Sylvie Lorthois. Multiscale modelling of blood flow in cerebral microcirculation : Details at capillary scale control accuracy at the level of the cortex. *PLOS ONE*, 13(1) :e0189474, January 2018. 47

[4] Rebecca J Shipley, Amy F Smith, Paul W Sweeney, Axel R Pries, and Timothy W Secomb. A hybrid discrete–continuum approach for modelling microcirculatory blood flow. *Mathematical Medicine and Biology : A Journal of the IMA*, March 2019. 47

[5] T.W. Secomb, R. Hsu, N.B. Beamer, and B.M. Coull. Theoretical Simulation of Oxygen Transport to Brain by Networks of Microvessels : Effects of Oxygen Supply and Demand on Tissue Hypoxia. *Microcirculation*, 7(4) :237–247, August 2000. 47

[6] Daniel Goldman. Theoretical Models of Microvascular Oxygen Transport to Tissue. *Microcirculation*, 15(8) :795–811, January 2008. 47

[7] Qianqian Fang, Sava Sakadžić, Lana Ruvinskaya, Anna Devor, Anders M. Dale, and David A. Boas. Oxygen advection and diffusion in a three-dimensional vascular anatomical network. *Optics Express*, 16(22) :17530, October 2008. 47

[8] Grant Hartung, Shoale Badr, Mohammad Moeini, Frédéric Lesage, David Kleinfeld, Ali Alaraj, and Andreas Linninger. Voxelized simulation of cerebral oxygen perfusion elucidates hypoxia in aged mouse cortex. *PLOS Computational Biology*, 17(1) :e1008584, January 2021. 47

[9] C. Pozrikidis and D. A. Farrow. A Model of Fluid Flow in Solid Tumors. *Annals of Biomedical Engineering*, 31(2) :181–194, February 2003. 47

[10] Timothy W. Secomb, Richard Hsu, Eric Y. H. Park, and Mark W. Dewhirst. Green's Function Methods for Analysis of Oxygen Delivery to Tissue by Microvascular Networks. *Annals of Biomedical Engineering*, 32(11) :1519–1529, November 2004. 47

[11] Sava Sakadžić, Emiri T. Mandeville, Louis Gagnon, Joseph J. Musacchia, Mohammad A. Yaseen, Meryem A. Yucel, Joel Lefebvre, Frédéric Lesage, Anders M. Dale, Katharina Eikermann-Haerter, Cenk Ayata, Vivek J. Srinivasan, Eng H. Lo, Anna Devor, and David A. Boas. Large arteriolar component of oxygen delivery implies a safe margin of oxygen supply to cerebral tissue. *Nature Communications*, 5(1) :5734, December 2014. 47

[12] Philipp Mächler, Natalie Fomin-Thunemann, Martin Thunemann, Marte Julie Sætra, Michèle Desjardins, Kıvılcım Kılıç, Layth N. Amra, Emily A. Martin, Ichun Anderson Chen, Ikbal Şencan Eğilmez, Baoqiang Li, Payam Saisan, John X. Jiang, Qun Cheng, Kimberly L. Weldy, David A. Boas, Richard B. Buxton, Gaute T. Einevoll, Anders M. Dale, Sava Sakadžić, and Anna Devor. Baseline oxygen consumption decreases with cortical depth. *PLOS Biology*, 20(10) :e3001440, October 2022. 47, 101

[13] Sava Sakadžic, Mohammad A. Yaseen, Rajeshwer Jaswal, Emmanuel Roussakis, Anders M. Dale, Richard B. Buxton, Sergei A. Vinogradov, David A. Boas, and Anna Devor. Two-photon microscopy measurement of cerebral metabolic rate of oxygen using periarteriolar oxygen concentration gradients. *Neurophotonics*, 3(4) :045005, October 2016. 101

Chapter 4

Oxygen transport in the parenchyma : 3D configuration

In this Chapter, we propose a strategy to efficiently solve the 1DIV-3DEV coupled mass transport problem as is described in Chapter 2, with the goal to model large microvascular networks. The development and the results from the previous 0DIV-2DEV formulation of the same problem (Chapter 3) will resurface often throughout the Chapter to alleviate the technical developments since many aspects of the numerical approach remain unchanged. The first main difference between the 0DIV-2DEV and 1DIV-3DEV configurations is the inclusion of intravascular transport, which in the 0DIV-2DEV model was irrelevant due to the sources not being connected among them. The other main difference between the two models is the estimation of the potentials that make up the rapid term, which will comprise the bulk of the new content presented in this Chapter (Sections 4.2.3-4.2.6).

In Section 4.1, we set up the problem with the operator splitting approach that already proved useful in modeling the large gradients caused by the vascular sources, thereby strongly reducing the computational requirements for the resolution of the problem. Subsequently, in Section 4.2, we show the developments to obtain an efficient system of discrete algebraic equations associated to the coupled molecular transport problem. Finally, in Section 3, we apply the model to a single vessel in order to compare the results with a reference solution and validate the model, and afterward, we test large networks encompassing multiple vessels.

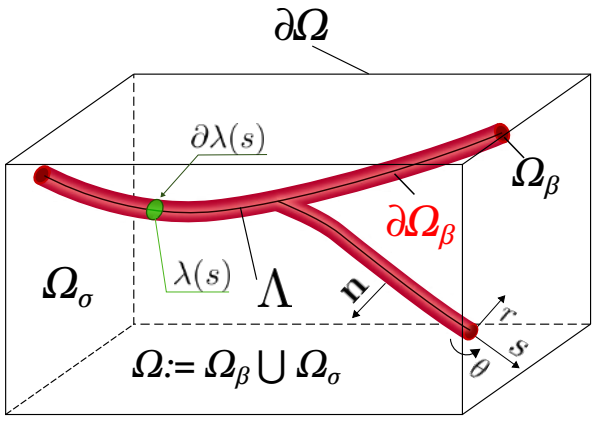

FIGURE 4.1 – **Terminology and notations for parenchyma and vessel spaces in the 3D configuration.** We show a 3D region Ω of brain tissue, which includes the parenchyma Ω_σ and the vascular space Ω_β. The external boundary is denoted by $\partial\Omega$, the vessel walls denoted by $\partial\Omega_\beta$, the vessels' center-lines by Λ, the curvilinear coordinate system for the vessels by (s, r, θ), and the normal $\mathbf{n}$ to the boundary $(\partial\Omega_\beta)$ pointing toward the parenchyma. The new terms introduced exclusively to handle 3D networks include $\lambda(s)$ that denotes the vessel cross-section, and $\partial\lambda(s)$ that denotes its circumference.

4.1 Problem formulation

Similar to the previous Chapter, we present an operator splitting approach based on the boundary integral equation (BIE), which is derived using the method of Green's functions. In this Section, we apply the operator splitting framework to reframe the extravascular boundary value problem (BVP) for the concentration field. The resulting BVP, after reformulation in terms of a slow term, can be effectively solved using a coarse mesh. As demonstrated in the previous Chapter, the accuracy of the coarse grid resolution is tightly connected to the definition of the rapid term, which we explore in detail in Section 4.2.

Moving on to Section 4.1.1, we define the two coupled intravascular and extravascular problems, using the formulations for the intravascular transport introduced in Chapter 2. In Section 4.1.2, we briefly describe the model used to obtain the velocity field in microvascular networks that is needed to deduce the effective properties of the intravascular transport. Finally, in Section 4.1.3, we replicate the same development as the previous Chapter to propose a BVP for the slow term.

4.1.1 Coupled Transport Problem

We consider a region of tissue $\Omega \subset \mathbb{R}^3$ that comprises the parenchyma $\Omega_\sigma \subset \mathbb{R}^3$ and the vascular compartment $\Omega_\beta \subset \mathbb{R}^3$, as shown in Fig. 4.1. We consider diffusion as the main driving mechanism for transport in the parenchyma [1–4]. Accordingly, the BVP with respect to the concentration ϕ in the parenchyma reads :

$$\begin{cases} \nabla^2\phi = 0 & \text{in } \Omega_\sigma \quad (4.1a) \\ -\mathbf{n}\cdot(D\boldsymbol{\nabla}\phi) = \dfrac{q(s)}{2\pi R(s)} & \text{on } \partial\Omega_{\beta,j}\ \forall j \in E(\Omega) \quad (4.1b) \\ \phi = \phi_D & \text{on } \partial\Omega_D \quad (4.1c) \end{cases}$$

where ϕ [mol m^{-3}] represents the molar extravascular concentration, D [m^2 s^{-1}] represents the diffusion coefficient in the parenchyma assumed to be homogeneous and isotropic, and $R(s)$ represents the radius of the vessel at the curvilinear abscissa s along the vessel network, as

illustrated in Fig. 4.1. Transport in the parenchyma is coupled to the intravascular compartment by the diffusive flux traversing the vessel wall, which we denominate the vessel-tissue exchanges $q(s)$ [mol m^{-1} s^{-1}].

$$q(s) = K_{eff}(\langle C_v \rangle(s) - \overline{\phi}(s)) \tag{4.2}$$

where K_{eff} [m^2 s^{-1}] represents the effective permeability of the vessel wall. We estimate the vessel wall concentration $\overline{\phi}$ as the average concentration ϕ over the circumference $\partial\lambda(s)$:

$$\overline{\phi}(s) = \frac{1}{2\pi R(s)} \int_{\partial\lambda(s)} \phi(\mathbf{x}) d\mathbf{x} \tag{4.3}$$

and the average intravascular concentration $\langle C_v \rangle$ as the average over the vessel cross-section $\lambda(s)$:

$$\langle C_v \rangle(s) = \frac{1}{\pi R(s)^2} \iint_{\lambda(s)} \phi(\mathbf{x}) d\mathbf{x} \tag{4.4}$$

which constitutes the assumption of local axisymmetry made in the previous Chapter. Equation 4.3 results in neglecting locally the tangential gradients in the normal derivative (i.e., molecular flux) of the parenchymal concentration (see equations 4.1b and 4.2). However, thanks to the multiple source simulations shown in the previous Chapter, we concluded that this axisymmetry condition provides very low errors (under 1% for the estimation of q) on the estimation of the radial flow even in configurations lacking symmetry around the sources. We remind the reader how the previous Chapter served as the foundation for the development introduced here. The thorough testing provided done for the 0DIV-2DEV configurations provides the groundwork that now furnishes us with the upper bound estimate of the errors generated by the axisymmetry hypothesis.

Moreover, for the intravascular transport i.e., 1DIV, we use a 1D effective equation that reads [5],

$$\begin{cases} U_{eff} \dfrac{\partial \langle C_v \rangle(s)}{\partial s} - D_{eff} \dfrac{\partial^2 \langle C_v \rangle(s)}{\partial s^2} + \dfrac{q(s)}{\pi R(s)^2} = 0 & \text{on } \Lambda & \text{(4.5a)} \\ \langle C_v \rangle(s) = C_D & \text{on } \Lambda_D & \text{(4.5b)} \\ \dfrac{\partial \langle C_v \rangle(s)}{\partial s} = N & \text{on } \Lambda_N & \text{(4.5c)} \end{cases}$$

where Λ_D and Λ_N represent the inlets and outlets of the network where the Dirichlet C_D, or Neumann N boundary conditons (BCs) are imposed, respectively. The effective transport coefficients, i.e., U_{eff} [m s^{-1}], D_{eff} [m^2 s^{-1}], and K_{eff} [m^2 s^{-1}], account for the coupling between the radial gradients of concentration and the radial gradients of velocity when diffusion is possible through the vessel wall. These coefficients thus provide a generalization of Taylor's dispersion, and match with the corresponding coefficients when the diffusive permeability of the vessel wall is null. In the limit case of weak couplings (see [5] for more details), their expression is given in A.1. Here, building up on Berg et al. [5], we assume that, even outside of this regime, these expression provide a better and more general approximation of intravascular transport than the usual well-mixed model [6–10].

4.1.2 Flow model

Here, we revisit the flow model used to obtain the velocity map in the vascular network. For a deeper explanation we suggest to revisit Section 2.2 and [11]. The effective velocity parameter in equation 4.5a is strongly dependent on the flow field in the intravascular compartment. Blood flow in the vessels is considered to be uncoupled from the transport problem due to the low permeability of the Blood Brain Barrier (BBB), thus, it can be computed beforehand. We estimate the blood flow through a vessel by a linear relationship with the pressure difference between the initial P_β and final P_γ vertices.

$$\pi R^2 \langle U \rangle_{\beta\gamma} = \mathscr{G}_{\beta\gamma}(P_\beta - P_\gamma) \tag{4.6}$$

where $\langle U \rangle$ represents the average cross-sectional velocity and $\mathscr{G}$ is the vessel conductance that is calculated using the following relationship

$$\mathscr{G}_{\beta\gamma} = \frac{\pi R^4}{8\mu^{app} l} \tag{4.7}$$

where μ^{app} is the apparent viscosity, R is the radius of the vessel, and l represents the curvilinear length of the vessel. Writing equation 4.6 for each vessel with known pressure or flow rates at the network boundary leads to a sparse linear system, the solution of which is later used to calculate the effective coefficients of the intravascular transport equation. This is known as the network approach and it is widely used in the literature [5–8; 11; 12]

4.1.3 Field Splitting

Based on similar arguments as in the previous Chapter, we expect strong concentration gradients to build up in the vicinity of the vessels that we aim to capture through a rapid term that is defined analytically. The remaining slow background field is solved numerically. Therefore, we split the concentration field into two contributions :

$$\phi(\mathbf{x}) = \mathscr{s}(\mathbf{x}) + \mathscr{r}(\mathbf{x}) \tag{4.8}$$

The developments to obtain a BVP for the slow term is identical to the 0DIV-2DEV case. For ease of reading, we repeat here the crucial steps. We divide the domain of computation Ω into a set $\mathscr{F}$ of F volumes that represent the volumes created by the cartesian grid used for the finite volume (FV) discretization. The slow and rapid terms are composed of continuous functions over each volume $V_k \subset \mathscr{F}$

$$\mathscr{r}(\mathbf{x}) = \sum_{k \in \mathscr{F}} \mathscr{r}_k(\mathbf{x}) \quad \text{with} \quad \mathscr{r}_k(\mathbf{x}) = 0 \ \forall \mathbf{x} \notin V_k \tag{4.9a}$$

$$\mathscr{s}(\mathbf{x}) = \sum_{k \in \mathscr{F}} \mathscr{s}_k(\mathbf{x}) \quad \text{with} \quad \mathscr{s}_k(\mathbf{x}) = 0 \ \forall \mathbf{x} \notin V_k \tag{4.9b}$$

Furthermore, we define the rapid term as a harmonic function inside each V_k that quantifies the gradients caused by the vessel tissue exchanges.

$$\begin{cases} \nabla^2 \text{ר}_k = 0 & \text{in } V_k \quad (4.10a) \\ -\mathbf{n} \cdot (D \boldsymbol{\nabla} \text{ר}_k) = \dfrac{q(s)}{2\pi R(s)} & \text{on } \partial\Omega_{\beta,j} \, \forall j \in E(V_k) \quad (4.10b) \end{cases}$$

which results in the following BVP for each ש_k :

$$\begin{cases} \nabla^2 \text{ש}_k = 0 & \text{in } V_k \quad (4.11a) \\ \text{ש}_k = \phi_D - \text{ר}_k & \text{on } \partial\Omega \quad (4.11b) \\ \mathbf{n} \cdot \boldsymbol{\nabla} \text{ש}_k = 0 & \text{on } \partial\Omega_\beta \quad (4.11c) \\ \mathbf{n} \cdot (\boldsymbol{\nabla} \text{ש}_k - \boldsymbol{\nabla} \text{ש}_m)\big|_{\partial V_{k,m}} = \mathbf{n} \cdot (\boldsymbol{\nabla} \text{ר}_m - \boldsymbol{\nabla} \text{ר}_k)\big|_{\partial V_{k,m}} & (4.11d) \\ (\text{ש}_k - \text{ש}_m)\big|_{\partial V_{k,m}} = (\text{ר}_m - \text{ר}_k)\big|_{\partial V_{k,m}} & (4.11e) \end{cases}$$

Therefore, the fully coupled system is composed, firstly, by the mass conservation equation in the parenchyma (equation 4.11), which arises from applying the splitting to equation 4.1 ; secondly, by the vessel tissue exchanges calculated through equation 4.2 ; and lastly, by the mass conservation in the intravascular compartment, equation 4.5. We thus obtain a system of 3 coupled systems of equations as opposed to two in the previous Chapter due to the addition of the intravascular transport problem. For ease of reading, the full coupled BVP is illustrated in Box 1 :

Box 1

$$\begin{cases} \nabla^2 \text{ש}_k = 0 & \text{in } V_k \quad (4.12a) \\ \text{ש}_k = \phi_D - \text{ר}_k & \text{on } \partial\Omega \quad (4.12b) \\ \mathbf{n} \cdot \boldsymbol{\nabla} \text{ש}_k = 0 & \text{on } \partial\Omega_\beta \quad (4.12c) \\ \mathbf{n} \cdot (\boldsymbol{\nabla} \text{ש}_k - \boldsymbol{\nabla} \text{ש}_m)\big|_{\partial V_{k,m}} = \mathbf{n} \cdot (\boldsymbol{\nabla} \text{ר}_m - \boldsymbol{\nabla} \text{ר}_k)\big|_{\partial V_{k,m}} & (4.12d) \\ (\text{ש}_k - \text{ש}_m)\big|_{\partial V_{k,m}} = (\text{ר}_m - \text{ר}_k)\big|_{\partial V_{k,m}} & (4.12e) \end{cases}$$

$$\begin{cases} U_{eff} \dfrac{\partial \langle C_v \rangle(s)}{\partial s} - D_{eff} \dfrac{\partial^2 \langle C_v \rangle(s)}{\partial s^2} + \dfrac{q(s)}{\pi R(s)^2} = 0 & \text{on } \Lambda \quad (4.13a) \\ \langle C_v \rangle(s) = C_D & \text{on } \Lambda_D \quad (4.13b) \\ \dfrac{\partial \langle C_v \rangle(s)}{\partial s} = N & \text{on } \Lambda_N \quad (4.13c) \end{cases}$$

$$q(s) = K_{eff}(\langle C_v \rangle(s) - \overline{\phi}(s)) \quad (4.14)$$

4.2 Assembly of the system of discrete algebraic equations

We follow the same paradigm as in the previous Chapter where we assemble each equation of the linear system in a different block of the matrix associated. In this case, one block of matrices is added to represent the intravascular transport problem. We show a preview of the final structure of the numerical model in Fig. 4.2, where the first line of matrices (**A B 0**) models mass transport in the parenchyma (discrete version of the system of equations 4.12) ;

the second line (**D E F**) models the vessel tissue exchanges (discrete version of equation 4.14) ; lastly, the third line (**0 H I**) models the intravascular transport where the matrix **I** contains the discrete advection diffusion transport part of the system of equations 4.13 and **H** contains the reaction part (molecular flux leaving the vessel).

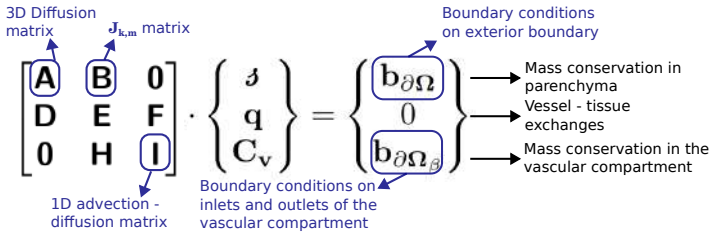

FIGURE 4.2 – **Schematics of the final coupled linear system in matrix form.**

Fig. 4.2 represents the discrete version of the coupled boundary value problem (BVP) made up by the intra and extra vascular transport problems introduced in the previous Section. The rest of this Section deals with the assembly of the individual linear blocks illustrated in Fig. 4.2 and proceeds as follows : in Section 4.2.1, we deal with the numerical model for the intravascular transport problem, i.e., the discrete version of the system of equations 4.13 and the third line in Fig. 4.2. In Section 4.2.2, we deal with the assembly of the extravascular diffusion problem, i.e., the discrete version of the system of equations 4.12 and the first line in Fig. 4.2. The rest of the Section tackles the challenge of obtaining a compact formulation for the source potentials (rapid term).

4.2.1 Finite volume discretization of the intravascular transport problem

We discretize the vascular domain into a set $\mathcal{S}$ of open cylinders denominated by the subindex j, i.e., $j \in \mathcal{S}$ and $\bigcup_{j\in\mathcal{S}} \partial\Omega_{\beta,j} = \partial\Omega_\beta$, where $\partial\Omega_{\beta,j}$ denotes the surface of an open cylinder with fixed radius and length given by R_j and $h_{\Lambda,j}$ respectively. In the same way, each cylinder is associated with a centerline Λ_j where $\bigcup_{j\in\mathcal{S}} \Lambda_j = \Lambda$, and $||\Lambda_j|| = h_{\Lambda,j}$. Accordingly, the discretization size of the vascular system is represented by the length of the cylinders $h_{\Lambda,j}$.

We integrate equation 4.13a to obtain a mass balance over each cylinder, which reduces to :

$$\pi R_j^2 \int_{\Lambda_j} \left(U_{eff} \frac{\partial \langle C_v \rangle(s)}{\partial s} - D_{eff} \frac{\partial^2 \langle C_v \rangle(s)}{\partial s^2} + \frac{q(s)}{\pi R_j^2} \right) ds = 0 \tag{4.15}$$

We further approximate the derivative of the concentration using the Two Point Flux Approximation (TPFA) for the gradients and use an upwind scheme for the advective term to obtain the following discrete PDE for intravascular transport :

$$U_{eff,j}(C_{v,j} - C_{v,j-1}) + D_{eff,j} \left(\frac{-C_{v,j-1} + 2C_{v,j} - C_{v,j-1}}{h_{\Lambda,j}} \right) + q_j \frac{h_{\Lambda,j}}{\pi R_j^2} = 0 \tag{4.16}$$

where $C_{v,j}$, $C_{v,j-1}$, $C_{v,j+1}$ are the concentrations of the current, upstream and downstream cylinders, respectively. $U_{eff,j}$ and $D_{eff,j}$ are the effective advection and diffusion coefficients for the current cylinder, and q_j represents the average molecular flux exchanged through the surface $\partial\Omega_{\beta,j}$ [1] . Thus far, we have discretized the flow and transport problems in the vascular

1. Following the notation illustrated in Fig. 4.1, $\partial\Omega_{\beta,j}$ represents the surface (i.e., BBB) of the open cylinder j.

compartment ; in the next Section, we deal with its coupled counterpart in the parenchyma.

4.2.2 FV discretization of the slow term

This Section focuses on the discrete version of the mass conservation problem in the parenchyma. Following the same strategy as the previous Chapter, we mesh the whole domain of computation Ω with a cartesian mesh, where we use the finite volume (FV) method to discretize the slow field equations (system of equations 4.12). We integrate over each control volume V_k and apply the TPFA to approximate the cell-to-cell fluxes. Thus, we obtain the following discretization of the PDE (equation 4.12a)

$$h_\Omega \sum_{m \in \mathcal{N}^k} (\widetilde{\jmath}_m - \widetilde{\jmath}_k + J_{k,m}) = 0 \tag{4.17}$$

For simplicity, we assume each FV cell is a cube, where h_Ω represents the side length of a single FV cell. Furthermore, the source term induced by the discontinuity of the rapid field across the FV cells interface is given by :

$$J_{k,m} = \frac{1}{2h} \iint_{\partial V_{k,m}} \mathbf{n} \cdot (\boldsymbol{\nabla} \wr_m - \boldsymbol{\nabla} \wr_k) dS + \frac{1}{h^2} \iint_{\partial V_{k,m}} (\wr_m - \wr_k) dS \tag{4.18}$$

As in the previous Chapter, $J_{k,m}$ bridges the discontinuity created by the finite support (i.e., $\widehat{V}$) of each source's potential. Essentially, $J_{k,m}$ can be considered as a source term appearing at the FV cell's interfaces that ensures equation 4.17 actually models mass conservation within each FV cell.

4.2.3 Green's function method and the bounary integral equation

The operator splitting framework is built on the idea that the rapid term accurately represents the perivascular concentration gradients. To acheive that, we represent the rapid term as a sum of source potentials.

$$\wr_k = \sum_{j \in E(\widehat{V}_k)} P_j \quad \forall j \in E(\widehat{V}_k) \tag{4.19}$$

One of the fundamental differences with the 0DIV-2DEV model is the estimation of the source potentials P_j that make up the rapid term. As mentioned previously, the 0DIV-2DEV model is considerably simpler than its 1DIV-3DEV counterpart since the estimation of each source potential (in 2D) can be done exactly, which allows to isolate the impact of the other modeling assumptions (e.g., assumption of axisymmetry of the flux field around each source). However, in the 1DIV-3DEV case, the estimation of the potential arising from an open cylinder cannot be estimated with an exact analytical expression, thus approximations are usually employed [6; 10; 13–16].

Through Green's third identity [17–19], we obtain the following boundary integral equation (BIE)

$$\phi(\mathbf{x}) = \oint_{\partial \Omega_\sigma} (\phi(\mathbf{x}^*) \boldsymbol{\nabla} G(\mathbf{x}, \mathbf{x}^*) \cdot \mathbf{n}(\mathbf{x}^*) - G(\mathbf{x}, \mathbf{x}^*) \boldsymbol{\nabla} \phi(\mathbf{x}^*) \cdot \mathbf{n}(\mathbf{x}^*)) dS(\mathbf{x}^*) \tag{4.20}$$

where G represents the free space Green's function, i.e., the fundamental solution

$$D \nabla^2 G(\mathbf{x}; \mathbf{x}^*) = -\delta(\mathbf{x} - \mathbf{x}^*) \quad in \quad \Omega \tag{4.21}$$

with

$$G(\mathbf{x};\mathbf{x}^*) = \frac{1}{4\pi D||\mathbf{x}-\mathbf{x}^*||} \tag{4.22}$$

which represents the concentration field created by an infinitely small source of mass in an infinite domain. We note that when the evaluation point $\mathbf{x}$ approaches the pole $\mathbf{x}^*$, the Green's function exhibits a singularity.

Equation 4.20 provides the concentration field in the parenchyma as the potential arising from a series of infinitesimally small sources (G) and dipoles ($\nabla G \cdot \mathbf{n}$) distributed over the boundary of the parenchyma. Moreover, we divide the boundary of the parenchyma $\partial\Omega_\sigma$ into the boundary with the vascular domain $\partial\Omega_\beta$ and the rest $\partial\Omega$. Skipping the variable $\mathbf{x}$ and $\mathbf{x}^*$ for readability, we have

$$\phi = \int_{\partial\Omega} (\phi \boldsymbol{\nabla} G \cdot \mathbf{n} - G \boldsymbol{\nabla}\phi \cdot \mathbf{n}) dS + \int_{\partial\Omega_\beta} (\phi \boldsymbol{\nabla} G \cdot \mathbf{n} - G \boldsymbol{\nabla}\phi \cdot \mathbf{n}) dS \tag{4.23}$$

The numerical approach developed here is rooted on the classic boundary element method (BEM). The underlying concept involves constructing a BVP for unknown quantities situated at the boundary, utilizing the boundary integral equation (BIE) as depicted in equation 4.23. The crucial difference with the conventional BEM [19–22] lies in the fact that the first integral over the contour of the domain $\partial\Omega$ (first integral on the right hand side (RHS) of equation 4.23) is considered within the slow field, as shown in the previous Chapter. The slow behavior of the contribution of the first integral is well understood [17; 18; 23], and considering the uncertain nature of boundary conditions within the brain microcirculation, the operator splitting framework offers a means to estimate this uncertain contribution through a coarsely resolved mesh for the slow term. The appropriate behaviour expected of the slow term nevertheless depends on the accurate estimation of the source potentials, i.e., the accurate estimation of the second integral of the RHS of equation 4.23. If achieved, this approach provides a unprecedented flexibility in evaluating the contribution of the boundary conditions, i.e., first integral in the RHS of equation 4.23.

To obtain a generic evaluation of the BIE for any vascular geometry we perform the following three steps (modified from Pozrikidis [20]) :

1. Divide the boundary ($\partial\Omega_\beta$ [2]) into discrete boundary elements, and approximate the boundary integrals by summing integrals across these components.
2. Write the discrete version of the BIE, i.e., introduce approximations for the unknown functions over the boundary.
3. Approximate integration of the single- and double-layer potential over the boundary elements and compute the discrete BIE to obtain a discrete equation for each element.
4. Implement the discrete system of equations arising from the BIE into the splitting framework.

2. We reiterate that in this case, the boundary corresponds to the vessel wall $\partial\Omega_\beta$, whereas in the classic BEM, the boundary consists of the whole boundary of the parenchyma $\partial\Omega_\sigma := \partial\Omega_\beta \bigcup \partial\Omega$. This elucidates the great advantage of the operator splitting where it allows to treat only the vessel wall $\partial\Omega_\beta$ in classic BEM fashion, while the integral over the exterior boundary $\partial\Omega$ (first integral in the RHS of equation 4.23) is evaluated via a coarse-grid FV approach for the slow term

The three steps cited above are often referenced throughout the Chapter to elucidate how far along the assembly of the problem we find ourselves. In the first step, we refer to the boundary created by the vascular wall, i.e., $\partial\Omega_\beta$, since the boundary integral over the exterior boundary i.e., $\partial\Omega$, is included in the slow term. The first step results in spatial discretization of the vascular wall, which was the topic of Section 4.2.1, where we modeled the vascular compartment as a series of open cylinders with constant radius. The second step consists of estimating the boundary values on such cylinders. For that purpose, we take advantage of the BIE (equation 4.23) and we choose the simplest implementation that consists of approximating both boundary distributions with constant functions over each element : $\overline{\phi}_j$ and q_j. Thus, we estimate the potential arising from each individual boundary element (i.e., cylinder) as follows

$$P_j(\mathbf{x}) = \overline{\phi}_j \iint_{\partial\Omega_{\beta,j}} G(\mathbf{x};\mathbf{x}^*)\cdot\mathbf{n}(\mathbf{x}^*)dS(\mathbf{x}^*) + \frac{q_j}{2\pi R_j}\iint_{\partial\Omega_{\beta,j}} \boldsymbol{\nabla} G(\mathbf{x};\mathbf{x}^*)dS(\mathbf{x}^*) \tag{4.24}$$

Introducing G_j and H_j as the single and double layer influence coefficients, respectively :

$$G_j(\mathbf{x}) = \iint_{\partial\Omega_{\beta,j}} G(\mathbf{x};\mathbf{x}^*)dS(\mathbf{x}^*) \tag{4.25}$$

$$H_j(\mathbf{x}) = \iint_{\partial\Omega_{\beta,j}} \boldsymbol{\nabla} G(\mathbf{x};\mathbf{x}^*)\cdot\mathbf{n}(\mathbf{x}^*)dS(\mathbf{x}^*) \tag{4.26}$$

we get

$$P_j(\mathbf{x}) = \frac{q_j}{2\pi R_j}G_j(\mathbf{x}) + \overline{\phi}_j H_j(\mathbf{x}) \tag{4.27}$$

The coefficients G_j and H_j allow to define the potentials everywhere in the parenchyma Ω_σ provided that the values of the concentration ($\overline{\phi}$) and its normal derivative (q) over the vessel wall are known. Their estimation represents the biggest difference between the 1DIV-3DEV and 0DIV-2DEV models. The estimation of the surface integrals in equations 4.25 and 4.26 is indeed challenging, but it proves to be crucial for the accuracy of the model and this challenge becomes the central focus of the subsequent Section 4.2.4.

Before going further, let us take a step back and unify the potential formulation presented in this Section with the operator splitting framework of the previous Section. Equations 4.8 and 4.9 express the concentration field as a composite of rapid and slow potentials. Via equations 4.19 and 4.27, we defined the rapid potential as a sum of single and double layer potentials originating from nearby sources. Thus, we represented the concentration field as a sum of potentials in the following manner :

$$\phi(\mathbf{x}) = \sum_{j\in E(\widehat{V}_k)} \left(\frac{q_j}{2\pi R_j}G_j(\mathbf{x}) + \overline{\phi}_j H_j(\mathbf{x})\right) + \mathfrak{z}(\mathbf{x}) \quad \forall \mathbf{x}\in V_k \tag{4.28}$$

where $\mathfrak{z}$ represents the contribution of far away sources and the integrals over the outer domain ($\partial\Omega$) in the same spirit as in the previous Chapter. Equation 4.28 represents the operator splitting version of the BIE. Furthermore, the potential-based formulation equips us with the formal definition of the slow term ; from equation 4.28 and Green's third identity

(equation 4.20) we indeed obtain :

$$\mathfrak{z}(\mathbf{x}) = \sum_{j \notin E(\widehat{V}_k)} \left(\frac{q_j}{2\pi R_j} G_j(\mathbf{x}) + \overline{\phi}_j H_j(\mathbf{x}) \right) + \int_{\partial\Omega} (\phi \boldsymbol{\nabla} G \cdot \mathbf{n} - G \boldsymbol{\nabla} \phi \cdot \mathbf{n}) dS \quad \forall \mathbf{x} \in V_k \tag{4.29}$$

which, thanks to the results of the previous Chapter, we know that $\mathfrak{z}$ is a slowly varying field everywhere in Ω, even in small domains of computation (where the boundary conditions have a greater influence over the field and provide a more rapidly varying slow term). We have now written a boundary integral equation that describes the concentration field anywhere in the parenchyma. Provided the boundary values over the cylinders, and the slow field, we can fully reconstruct the concentration field in the parenchyma using equation 4.28. Thus, the goal resides in setting up a system to solve for the boundary values, since we have already set up the mass balance equation that solves for the slow term values on the FV grid in equation 4.17.

4.2.4 Green's function method for the estimation of the potentials

Having defined the discrete BIE (equation 4.28), we now focus on the evaluation of the single and double layer coefficients (equations 4.25 and 4.26). The potential of any given cylinder j (equation 4.25) is commonly approximated as a the potential created by an equivalent point source placed on the barycenter of the cylinder, which effectively reduces the vascular domain as a collection of point sources located on the centerline of the vessels, as commonly done in the literature [6; 10; 13; 24], which reduces equation 4.25 to

$$G_i^{point}(\mathbf{x}) = 2\pi R_i h_{\Lambda,i} G(\mathbf{x}, \mathbf{x}_i) \tag{4.30}$$

where $\mathbf{x}_i$ represents the barycenter of the cylinder i where the point source is located. This effectively approximates the integral in equation 4.25 via the midpoint rule. Substituting equation A.27 into equation 4.30 yields

$$G_i^{point}(\mathbf{x}) = \frac{R_i h_{\Lambda,i}}{2d(\mathbf{x})} \tag{4.31}$$

where $d(\mathbf{x})$ represents the distance between the point source $\mathbf{x}_i$ and the evaluation point $\mathbf{x}$

$$d_i(\mathbf{x}) = ||\mathbf{x} - \mathbf{x}_i|| \tag{4.32}$$

Another viable approximation consists of reducing the cylinder to a line source, as in [25]

$$G_i^{line}(\mathbf{x}) = 2\pi R_i \int_{\Lambda_i} G(\mathbf{x}, \mathbf{x}_i) ds \tag{4.33}$$

The integral on the right hand side can be evaluated analytically (see Section A.2). Therefore, we write :

$$G_i^{line}(\mathbf{x}) = \frac{R_i}{2} ln \left(\frac{max(d_{i-1/2}, d_{i+1/2}) + h_{\Lambda,i}/2 + \langle \mathbf{x}_i - \mathbf{x}, \boldsymbol{\tau} \rangle}{min(d_{i-1/2}, d_{i+1/2}) - h_{\Lambda,i}/2 + \langle \mathbf{x}_i - \mathbf{x}, \boldsymbol{\tau} \rangle} \right) \tag{4.34}$$

where $d_{i-1/2}$ and $d_{i+1/2}$ represent the distances to the initial and final points of the centerline

of the cylinder.

Line sources offer virtually no improvement of accuracy compared to point sources (see figure 4.3A), we use them regardless since they do not add any considerable complexity to the code. Therefore, we use the line approximation to estimate the integral of the single layer coefficient in equation 4.25.

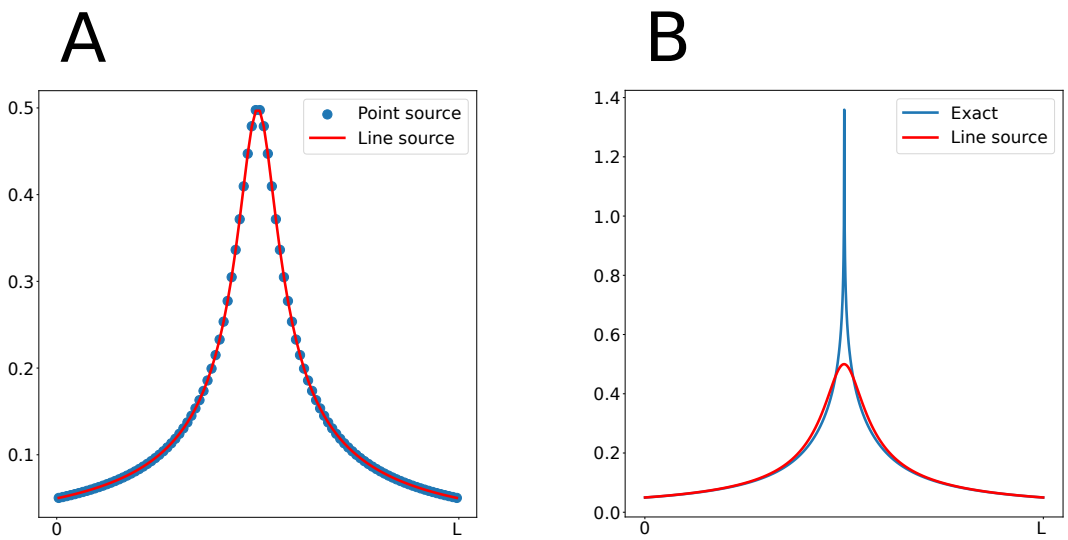

FIGURE 4.3 – **Estimation of the single layer influence coefficient using point, line and exact formulation.** Panel A shows the single layer potential over the centerpoint of the vessel calculated through the exact formulation, and the two approximations (line and point) which are essentially superposed. Panel B shows the same plot but comparing the exact estimation and the line approximation.

Furthermore, these same approximation, substituted in equation 4.28, lead to a null value of the double layer potential, due to the collapse of the cylinder into lower dimensional objects. Thus, we have

$$H_i^{line} = H_i^{point} = 0 \quad in \quad \Omega \tag{4.35}$$

These approximations for the coefficients in the discrete BIE are easy to evaluate anywhere in the parenchyma without the need to perform any type of integration.

These simplifications are often used in the literature for the computation of the single layer potential [6; 10; 16; 24]. As detailed above, they are introduced by the geometrical simplifications that decrease the complexity of the necessary computations to evaluate the BIE (equation 4.28). In contrast, in the previous Chapter, the integral over each source wall could be evaluated analytically, and the double potential was null. Therefore, no approximations where introduced regarding the layer potentials. The innacuracies introduced by the geometrical simplifications (illustrated in Fig. 4.3) are the topic of the next Section 4.2.5.

4.2.5 Analyzing Approximations : Understanding Their Impact on Potentials

We have completed the first two steps of four needed to obtain a system of algebraic equations as highlighted in Section 4.2.3. First, we represented the vasculature as an ensemble of cylinders (Section 4.2.3). Second, we approximated the boundary fields (concentration and flux over the vascular wall) with constant functions over each element (Section 4.2.4), which resulted in the discrete version of the BIE given in equation 4.28. Now, we focus on

the approximations of the potentials i.e., line and point approximations, to understand the magnitude of the errors introduced (especially near the pole of the Green's function).

The potentials intervene in the mass conservation equation in the parenchyma via the source terms $J_{k,m}$ in the mass balance equation 4.17. The source potential is defined in equation 4.27, which, using the line approximation, results in :

$$P_i^{line}(\mathbf{x}) = \frac{q_i}{2\pi R_i} G_i^{line}(\mathbf{x}) \tag{4.36}$$

We remind that the sum of the potentials from individual sources constitutes the rapid term

$$\curlyvee_k = \sum_{i \in E(\widehat{V}_k)} P_i \quad \forall i \in E(\widehat{V}_k) \tag{4.37}$$

where $\widehat{V}_k$ represents an extension to V_k that guarantees the sufficient smoothness of $\jmath$. We also remind (see Chapter 3) the fact that $\widehat{V}_k$ is greater in size than V_k so that the kernels of the integrals in $J_{k,m}$ in equation 4.18 are non-null only for sources that lie far away from the given interface ($\partial V_{k,m}$). The reasoning behind this result lies in the fact that, in the integral kernels of equation 4.18, the contributions from the sources in $\widehat{V}_m$ and $\widehat{V}_k$ are subtracted from each other. Therefore, the only sources that will provide a non-null contribution are the sources $j \in (E(\widehat{V}_k) \backslash E(\widehat{V}_m)) \bigcup (E(\widehat{V}_m) \backslash E(\widehat{V}_k))$, which, by definition, all lie far away from $\partial V_{k,m}$. This fact has important implications because we can safely assume that the point/line approximation (equations 4.31 and 4.34) will be accurately integrated for the mass conservation equation given that the evaluation surfaces of the rapid term always lie far away from the source. Additionally, the same argument can be made for neglecting the double layer potential [3]. We note that the model remains conservative as long as the source's potentials are of harmonic functions in the parenchyma.

Additionally, the potentials intervene in the vessel tissue exchanges where we need to evaluate the average extravascular concentration over the source to estimate the exchange flux :

$$q_j = K_{eff,j}(\langle C_v \rangle_j - \overline{\phi}_j) \tag{4.38}$$

where we recall that q_j is the average molecular flux exchanged through the wall (equation 4.14), $\langle C_v \rangle_j$ is the average intravascular concentration inside the cylinder (equation 4.4), and $\overline{\phi}_j$ represents the average extravascular wall concentration (equation 4.3), which now, applying the operator splitting framework yields :

$$\overline{\phi}_j = \frac{1}{|\partial\Omega_{\beta,j}|} \iint_{\partial\Omega_{\beta,j}} \left[\sum_{i \in E(\widehat{V}_k)} \left(\frac{q_i}{2\pi R_i} G_i(\mathbf{x}) + \overline{\phi}_i H_i(\mathbf{x}) \right) + \jmath(\mathbf{x}) \right] dS \quad \forall j \in E(V_k) \tag{4.39}$$

Let us recall Fig. 4.2 where we showed the structure of the discrete linear system ; the rapid term is involved in matrices **B** and **E**. The matrix **B** represents the portion of mass conservation in the parenchyma containing the computation of the source terms $J_{k,m}$. As previously stated, the kernels of those integrals contain only remote sources, with the distance depending

3. The double layer potential decays faster than the single layer potential. We can safely assume the value of the double layer potential to remain fairly constant on any mesh cell interface that lies sufficiently far from the source.

on the size of $\widehat{V}$. In contrast, in matrix $\mathbf{E}$ we estimate the average value of the rapid term over the vessel wall (i.e., the integral of G_j and H_j in equation 4.39) for each cylinder which represents the discrete version of equation 4.2. In this case, replacing G_i and H_i in equation 4.39 by the line approximation will introduce errors due to the fact that the evaluation point ($\mathbf{x} \in \partial\Omega_{\beta,j}$) does not necessarily lie far away from the original cylinder $\partial\Omega_{\beta,i}$. This deviation is illustrated in Fig. 4.3 around the center of the vessel (around L/2). Therefore, we must consider the possibility that the double layer potential might not be negligible and the line approximation might fail since they are evaluated very near the surface of the source (thus, very near the singularity). The task now consists of providing appropriate estimations for the single and double layer coefficients that do not require brute-force evaluation of the integrals in equations 4.25 and 4.26 but render the model accurate when estimating the boundary values at the vessel wall. Particularly, we focus on the cases when the evaluation point lies closest to the cylinder, which is especially true when evaluating the self-influence i.e., the integral of the coefficients G_i and H_i over the surface of the same cylinder $\partial\Omega_{\beta,i}$, which corresponds with the peak in Fig. 4.3 where the line and exact formulation differ the most. This constitutes the main topic of the next Section.

4.2.6 Self-influence coefficients

The objective of this Section is to provide an estimation of the layer potentials coefficients (equations 4.25 and 4.26) in order to evaluate equation 4.39 accurately. First, let us define the average values over the cylinder j of the slow term ($\mathfrak{s}_j$), the single layer potential of cylinder i (G_{ij}), and the double layer potential of cylinder i (H_{ij}), to render equation 4.39 more readable

$$\mathfrak{s}_j = \frac{1}{|\partial\Omega_{\beta,j}|} \iint_{\partial\Omega_{\beta,j}} \mathfrak{s}(\mathbf{x}) dS \tag{4.40}$$

$$G_{ij} = \frac{1}{|\partial\Omega_{\beta,j}|} \iint_{\partial\Omega_{\beta,j}} \left(\iint_{\partial\Omega_{\beta,i}} G(\mathbf{x};\mathbf{x}^*) dS(\mathbf{x}^*) \right) dS(\mathbf{x}) \tag{4.41}$$

$$H_{ij} = \frac{1}{|\partial\Omega_{\beta,j}|} \iint_{\partial\Omega_{\beta,j}} \left(\iint_{\partial\Omega_{\beta,i}} \nabla G(\mathbf{x};\mathbf{x}^*) \cdot \mathbf{n}(\mathbf{x}^*) dS(\mathbf{x}^*) \right) dS(\mathbf{x}) \tag{4.42}$$

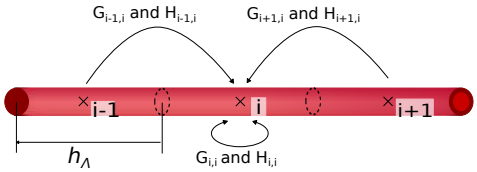

FIGURE 4.4 – **Schematic of the influence coefficients.** In a hypothetical vessel discretized into 3 cylinders with IDs $i-1$,i and $i+1$, we show all the influence coefficients acting over the cylinder i.

The single and double layer potentials have an influence over the whole parenchyma, notably, they are relevant only over the closest points due to the rapid decay of the Green's function and its normal derivative. For instance, in the case shown in Fig. 4.4, the larger value corresponds to the coefficients G_{ii} and H_{ii}, due to its greater proximity from the evaluation point to the pole. We denote them as self-influence coefficients.

Equations 4.40-4.49 allow us to rewrite the average vessel wall concentration for any cylinder

j (equation 4.39) in a concise manner

$$\overline{\phi}_j = \sum_{i \in E(\widehat{V}_k)} \left(\frac{q_i}{2\pi R_i} G_{ij} + \overline{\phi}_i H_{ij} \right) + \mathfrak{s}_j \tag{4.43}$$

To clarify even further, let us substitute equation 4.43 into equation 4.38 to obtain an explicit expression of q_j :

$$q_i = \frac{1}{\left(\frac{1 - H_{ii}}{K_{eff,i}} - \frac{G_{ii}}{2\pi R_i} \right)} \left[(1 - H_{ii}) \langle Cv \rangle_i + \mathfrak{s}_i - \sum_{\substack{j \in E(\widehat{V}_k) \\ i \neq j}} \left(\frac{q_j}{2\pi R_j} G_{ji} + \overline{\phi}_j H_{ji} \right) \right] \tag{4.44}$$

where G_{ii} and H_{ii} are commonly called the self-influence coefficients and they involve the integration of the Green's function and its normal derivative over their poles (equations 4.47 and 4.49 when $i = j$). The self-influence coefficient is expected to behave quite differently from the approximated forms since the later exhibit no singularity.

Let us focus on the single layer potential, and only a couple of separated cylinders i and j as illustrated in Fig. 4.4, i.e., let us consider the cross-influence single layer coefficient (G_{ij}). We first deal with the average over the current cylinder, i.e., integral over $\partial\Omega_{\beta,j}$. Due to the harmonic properties of the Green's function and the high aspect ratio of the vessels in the brain microcirculation, we estimate the average over the cylinder wall as the value at its barycenter [4] :

$$G_{ij} \approx \iint_{\partial\Omega_{\beta,i}} G(\mathbf{x}; \mathbf{x}_j) dS(\mathbf{x}^*) \tag{4.45}$$

And using the line approximation :

$$G_{ij} \approx G_i^{line}(\mathbf{x}_j) \tag{4.46}$$

where $\mathbf{x}_j$ represents the barycenter of the cylinder j. equation 4.45 represents the exact form of the cross-influence coefficient (granted we estimated the average over the open cylinder equal to the average value of an equivalent closed cylinder), and equation 4.46 represents the line approximation of the cross-influence coefficient.

We note that in this Section, we are dealing with the estimation of the first integral in equations 4.41 and 4.49 (over $\partial\Omega_{\beta,i}$, the source cylinder), whereas in Section 4.2.4 we were approximating the second integral over $\partial\Omega_j$ (the cylinder over which the influence of i is estimated). Clearly, the integral over $\partial\Omega_{\beta,i}$ constitutes the main challenge since it includes integrating over the singularity.

It is clear now that, when we deal with the self-influence coefficient, i.e., $i = j$, strong

4. We approximate the average value of the single layer potential over the open cylinder as equal to the average value over a close cylinder. This renders the evaluation of any harmonic function over the cylinders straight-forward. The Gauss theorem dictates that the average of a harmonic function over a closed surface equals the value of the harmonic function at the barycenter of the closed surface.

deviations occur when using the approximate forms (defined by equation 4.46) since the exact form integrates over the pole of the Green's function and in the approximate forms we do not (see Fig. 4.3B). This results in a strong deviation for the self influence coefficients G_{ii} as shown in Fig. 4.3. For that reason, we use the line approximation for the cross influence coefficients, and we preserve the surface integral for the self influence, which can be evaluated analytically for straight cylinders.

$$G_{ij} = \begin{cases} G_i^{line}(\mathbf{x}_j) & \text{if } i \neq j \\ \dfrac{1}{|\partial\Omega_{\beta,i}|} \displaystyle\iint_{\partial\Omega_{\beta,i}} \left(\iint_{\partial\Omega_{\beta,i}} G(\mathbf{x};\mathbf{x}^*) dS(\mathbf{x}^*) \right) dS(\mathbf{x}) & \text{if } i = j \end{cases} \tag{4.47}$$

This fully defines the single layer potential of a source anywhere in the parenchyma. Regarding the double layer potential, due to the very rapid decay to zero of the double layer potential, we estimate it analytically for the cylinders that lie within the same vessel, and neglect it for the rest.

$$H_{ij} = \frac{1}{|\partial\Omega_{\beta,j}|} \iint_{\partial\Omega_{\beta,j}} \left(\iint_{\partial\Omega_{\beta,i}} \boldsymbol{\nabla} G(\mathbf{x};\mathbf{x}^*) \cdot \mathbf{n}(\mathbf{x}^*) dS(\mathbf{x}^*) \right) dS(\mathbf{x}) \tag{4.48}$$

when i and j belong to the same vessel. equation 4.48 can be evaluated analytically as long as both cylinders share a centerline, i.e., the vessel is not tortuous. The integrals in equations 4.47 and 4.48 have a singularity when integrating over the pole. The one on equation 4.47 is weakly singular and can be evaluated with a change in coordinates, and the one on 4.48 is a diverging singularity and is evaluated as a Cauchy principal value integral [19; 20] :

$$H_{ij} = \frac{1}{|\partial\Omega_{\beta,j}|} \iint_{\partial\Omega_{\beta,j}}^{PV} \left(\iint_{\partial\Omega_{\beta,i}} \boldsymbol{\nabla} G(\mathbf{x};\mathbf{x}^*) \cdot \mathbf{n}(\mathbf{x}^*) dS(\mathbf{x}^*) \right) dS(\mathbf{x}) + 0.5 \tag{4.49}$$

For an explanation of the evaluation of equations 4.47 and4.49 see Section A.3. We now have all the ingredients to evaluate the boundary fields $\overline{\phi}$ as a function of the unknowns of the system, i.e., $\mathfrak{s}$, q, $\langle C_v \rangle$. We have successfully completed the third step in the application of the BEM to the current problem.

4.2.7 Sub-grid reconstruction to estimate vessel-tissue exchanges

In the previous Chapter, we showed how thanks to the rapid term and the TPFA, we were able to very accurately estimate the concentration gradients on the FV cells' interfaces, which rendered the extravascular model accurate, conservative, and permitted a coarse grid discretization. Nevertheless, we underline that a point-wise estimation of the concentration field anywhere in the parenchyma lacks accuracy since the FV formulation provides a single value of the slow term per grid cell. As a result, we could expect an accurate prediction of the average concentration within a single FV cell, but not an accurate point-wise estimation of the concentration field on the vessel walls, which posed a problem regarding the accuracy of the vessel tissue exchanges (equations 4.43 and 4.44). In this Section, we follow the same strategy as the previous Chapter to provide an interpolation scheme that allows us to reconstruct the concentration field anywhere in Ω based on the values of the slow term in the coarse grid. We then use the interpolated value to precisely assess the vessel tissue exchanges from equations 4.43 and

The FV scheme provides a second order accurate estimation of the slow field $\mathfrak{z}$ [26] at the cells' centers. Thus, following the standard FV formulation [18; 26; 27], we approximate the value on the cell's center as its average value over the given grid cell. Therefore, we can write the concentration on the cell center :

$$\widetilde{\phi}_k = \widetilde{\mathfrak{z}}_k + \mathscr{r}_k(\mathbf{x}_k) \quad \forall k \in \mathscr{T} \tag{4.50}$$

To interpolate the value of the concentration field on every point $\mathbf{x}$ of Ω, we define the set of the closest all FV cell centers ($\mathscr{T}(\mathbf{x})$). We thus have

$$\mathscr{I}_\phi(\mathbf{x}) = \sum_{i \in \mathscr{T}(\mathbf{x})} \gamma_i(\mathbf{x})(\widetilde{\mathfrak{z}}_i + \mathbb{C}_i) + \sum_{j \in \widehat{V}^d} P_j(\mathbf{x}) \tag{4.51}$$

where γ_i represents the Q^1 element in 3 dimensions that equals 1 on the center of FV cell i and zero on all the other cells i.e., providing bilinear interpolation of the values at the cells' centers, and $\mathbb{C}_i$ is a correction term that will be introduced subsequently. We define the dual neighbourhood $\widehat{V}_d$ as a combination of the neighbourhoods of the 8 relevant FV cells in $\mathscr{T}(\mathbf{x})$

$$\widehat{V}^d = \bigcup_{i \in \mathscr{T}(\mathbf{x})} \widehat{V}_i \tag{4.52}$$

In equation 4.51, we added the correction term $\mathbb{C}_i$ to bridge the discontinuities created by the localization scheme, i.e., the finite size of $\widehat{V}$, in the specific case where $\widehat{V} = \Omega$ we would have $\mathbb{C}_i = 0 \, \forall i \in \mathscr{F}$. With these definitions, we are equipped with the tools to calculate $\mathbb{C}_i$. For that purpose, we first set the interpolation to be equal to the cell center concentration :

$$\mathscr{I}_\phi(\mathbf{x}_k) = \widetilde{\phi}_k \quad \forall k \in \mathscr{T} \tag{4.53}$$

Then, to estimate $\mathbb{C}_i$ we use equations 4.50-4.53, and the definition of the rapid term 4.37, to obtain :

$$\mathbb{C}_i = - \sum_{j \in E(\widehat{V}^d)} \delta_{ji} P_j(\mathbf{x}_i) \tag{4.54}$$

where

$$\delta_{ji} = \begin{cases} 0 & \text{if} \quad j \in \widehat{V}_i \\ 1 & \text{else} \end{cases} \tag{4.55}$$

For ease of reading, we define the corrected rapid term that considers the sources in the dual neighbourhood

$$\mathscr{r}_i^c(\mathbf{x}) = \sum_{j \in E(\widehat{V}^d)} (P_j(\mathbf{x}) - \delta_{ji} P_j(\mathbf{x}_i)) \tag{4.56}$$

to finally obtain the interpolation function

$$\mathcal{J}_\phi(\mathbf{x}) = \sum_{i\in\mathcal{T}} \gamma_i(\mathbf{x})(\widetilde{\jmath}_i + \kappa_i^c(\mathbf{x})) \tag{4.57}$$

Therefore, equations 4.39 can be rewritten as

$$\overline{\phi}_i \approx \mathcal{J}_\phi(\mathbf{x}_i) = \sum_{i\in\mathcal{T}} \gamma_i(\mathbf{x}) \left[\widetilde{\jmath}_i + \sum_{j\in E(\widehat{V}^d(\mathbf{x}))} (P_j(\mathbf{x}) - \delta_{ji} P_j(\mathbf{x}_i)) \right] \tag{4.58}$$

which provides an interpolation function capable of reconstructing the concentration field anywhere in the parenchyma and takes advantage of both the regular nature of the slow term and the analytical description of the potentials. We recall that each source's potential is determined the estimation of the single layer and double layer potentials (equation 4.27).

4.2.8 Metabolic Consumption

In the previous Chapter, we showed how to iteratively solve the extravascular transport problem to include the non-linear metabolic consumption estimated through Michaelis-Menten kinetics. The underlying structure of the mass conservation problem formulation in the 2D and 3D models is virtually the same. However, in this Chapter, for simplicity, we model metabolic consumption as proportional to the concentration to preserve the linearity of the problem. We include the metabolic sink in the mass conservation equation 4.1a that results

$$\nabla^2\phi - \frac{M}{D}\phi = 0 \quad in \quad \Omega_\sigma \tag{4.59}$$

Subsequently, we apply the operator splitting framework (equation 4.11a) to obtain

$$\nabla^2\jmath_k - \frac{M}{D}(\jmath_k + \kappa_k) = 0 \quad in \quad V_k \tag{4.60}$$

After discretizing, this leads to

$$h_\Omega \sum_{m\in\mathcal{N}^k} (\widetilde{\jmath}_m - \widetilde{\jmath}_k + J_{k,m}) - \frac{M}{D}\widetilde{\jmath}_k - \frac{M}{D}\widetilde{\kappa}_k = 0 \tag{4.61}$$

where $\widetilde{\kappa}_k$ represents the averaged rapid term over a FV cell given by :

$$\widetilde{\kappa}_k \approx \iiint_{V_k} \kappa_k(\mathbf{x}) \tag{4.62}$$

4.2.9 Assembly of the system

The BEM provides an ideal framework that allows us to model the vascular system as sources of solute embedded in the parenchyma. In this framework, we can trace back every term in our formulation to Green's third identity. For this reason, we can estimate the errors by comparing the approximations introduced in the model with the exact formulation given by the BIE in equation 4.23. Furthermore, we can also trace back the physical meaning of the slow and rapid terms to the BIE, thus providing the mathematical groundwork for a

continuous reconstruction of the concentration field in the parenchyma (Section 4.2.7), which is often missing in other coarse-grid models [7; 11; 28].

The numerical model developed in this Chapter shares several characteristics with the 2D model, such as the splitting of the concentration field and the localization approach. However, the most notable difference between the two lies in the estimation of the source potentials. This difference arises due to the necessary geometrical simplifications associated with the 3D geometry.

In this Section, we sum up the development carried out to obtain a system of discrete algebraic equations for the coupled 1DIV-3DEV problem (Box 1), and we write given system is matrix form. Firstly, we solve the extravascular problem by enforcing mass conservation (described by the BVP in equations 4.11) through the discrete formulation given by equations 4.17 and 4.18. The mass conservation in the parenchyma is discretized via FV yielding :

$$h_\Omega \sum_{m \in \mathcal{N}^k} (\widetilde{\jmath}_m - \widetilde{\jmath}_k + J_{k,m}) = 0 \tag{4.63}$$

with the source terms given by

$$J_{k,m} = \frac{1}{2h} \iint_{\partial V_{k,m}} \mathbf{n} \cdot (\boldsymbol{\nabla} \wp_m - \boldsymbol{\nabla} \wp_k) dS + \frac{1}{h^2} \iint_{\partial V_{k,m}} (\wp_m - \wp_k) dS \tag{4.64}$$

and the rapid term defined by

$$\wp_k = \sum_{j \in E(\widehat{V}_k)} P_j \quad \forall j \in E(\widehat{V}_k) \tag{4.65}$$

Second, we model the vessel tissue exchanges, where we introduce the interpolation scheme used to estimate the wall concentration (equation 4.58) inside the linear relationship that quantifies the exchanges (equation 4.38) and using the definition of the sources' potentials (equation 4.27) :

$$\begin{aligned} \frac{q_j}{K_{\text{eff},j}} - \langle C_v \rangle_j = - \sum_{i \in \mathscr{T}(\mathbf{x}_j)} \gamma_i(\mathbf{x}_j) \Bigg[\widetilde{\jmath}_i + \sum_{k \in E(\widehat{V}^d(\mathbf{x}_i))} \Bigg[\left(q_k \left(\frac{G_{kj}}{2\pi R_k} - \frac{H_{kj}}{K_{\text{eff}_k}} \right) + \langle C_v \rangle_j H_{kj} \right) \\ - \delta_{ji} \left(q_k \left(\frac{G_k(\mathbf{x}_i)}{2\pi R_k} - \frac{H_k(\mathbf{x}_i)}{K_{\text{eff}_k}} \right) + \langle C_v \rangle_j H_{kj} \right) \Bigg] \Bigg] \end{aligned} \tag{4.66}$$

This provides the vessel tissue exchanges for a given cylinder j as a function of the unknowns of the system (q_j and $\langle C_v \rangle_j$). Moreover, the estimation of the layer potentials are given by :

$$G_{ij} = \begin{cases} G_i^{line}(\mathbf{x}_j) & \text{if } i \neq j \\ \dfrac{1}{|\partial\Omega_{\beta,i}|} \displaystyle\iint_{\partial\Omega_{\beta,i}} \left(\iint_{\partial\Omega_{\beta,i}} G(\mathbf{x};\mathbf{x}^*) dS(\mathbf{x}^*) \right) dS(\mathbf{x}) & \text{if } i = j \end{cases} \tag{4.67}$$

$$H_{ij} = \frac{1}{|\partial\Omega_{\beta,j}|} \iint_{\partial\Omega_{\beta,j}}^{PV} \left(\iint_{\partial\Omega_{\beta,i}} \boldsymbol{\nabla} G(\mathbf{x};\mathbf{x}^*) \cdot \mathbf{n}(\mathbf{x}^*) dS(\mathbf{x}^*) \right) dS(\mathbf{x}) + 0.5 \tag{4.68}$$

Finally, the discrete intravascular transport PDE :

$$U_j(C_{v,j} - C_{v,j-1}) + D_j\left(\frac{-C_{v,j-1} + 2C_{v,j} - C_{v,j-1}}{h}\right) + q_j\frac{h_{\Lambda,j}}{\pi R_j^2} = 0 \tag{4.69}$$

providing a fully coupled formulation between the intravascular and extravascular transport. We have now fully defined the discrete coupled problem and is assembled in matrix form as follows :

The full discrete system is therefore

$$\begin{cases} \mathbf{A}\cdot\boldsymbol{\mathfrak{z}} + \mathbf{B}\cdot\mathbf{q} + \mathbf{C}\cdot\mathbf{C_v} = \mathbf{b}_{\partial\boldsymbol{\Omega}} & \text{(4.70a)} \\ \mathbf{D}\cdot\boldsymbol{\mathfrak{z}} + \mathbf{E}\cdot\mathbf{q} + \mathbf{F}\cdot\mathbf{C_v} = 0 & \text{(4.70b)} \\ \mathbf{H}\cdot\mathbf{q} + \mathbf{I}\cdot\mathbf{C_v} = \mathbf{b}_{\partial\boldsymbol{\Omega}_\beta} & \text{(4.70c)} \end{cases}$$

The matrix $\mathbf{C}$ represents the contribution of the double layer potential to the rapid term in the mass conservation equation. The double layer potential under physiological conditions is negligible even at short distances (studied in Section 4.3.1), consequently its influence on the final system (matrix $\mathbf{C}$) is neglected [6; 10]. Therefore, the matrix associated with the linear system reads

$$\mathbf{L} = \begin{bmatrix} \mathbf{A} & \mathbf{B} & \mathbf{0} \\ \mathbf{D} & \mathbf{E} & \mathbf{F} \\ \mathbf{0} & \mathbf{H} & \mathbf{I} \end{bmatrix} \tag{4.71}$$

and the full linear system is

$$\mathbf{L}\cdot\begin{Bmatrix} \boldsymbol{\mathfrak{z}} \\ \mathbf{q} \\ \mathbf{C_v} \end{Bmatrix} = \begin{Bmatrix} \mathbf{b}_{\partial\boldsymbol{\Omega}} \\ 0 \\ \mathbf{b}_{\partial\boldsymbol{\Omega}_\beta} \end{Bmatrix} \tag{4.72}$$

as schematized in Fig. 4.2.

To summarize the approach developed in this Chapter : we base our developments in the BEM where the transport problem is modeled via a BIE. We discretize the BIE and use the operator splitting framework to localize the influence of the layer potentials and to estimate the integral over the exterior boundary $\partial\Omega$. The localization scheme results in jumps across the FV mesh cells' interfaces ; this poses problems when interpolating the concentration field in the parenchyma, therefore, we designed an interpolation scheme that adds a correction term to bridge such discontinuities. Finally, we assembled the mass conservation equations in both compartments with the vessel-tissue exchange equation to obtain the matrix of the coupled linear system.

4.2.10 Numerical implementation

The multiscale model is coded from scratch in Python due to its flexibility in object-oriented programming. The library Numba [29] for scientific computations allows to translate the python code to machine code, thereby severely accelerating the assembly of the system which currently represents the main bottleneck of the model. Additionally, we choose among the large variety of numerical solvers available in the Scipy library [30] for the resolution of linear

systems. Particularly, we use the GMRES iterative method for the simulations including networks, and the standard direct linear solver for single vessel simulations.

The Green's portion of the model i.e., the rapid term, is non-local, meaning that the influence of a single source needs to be calculated far away from its location. That distance depends on the size of $\widehat{V}$. The larger $\widehat{V}$ the greater the accuracy (as shown in the previous Chapter), but the longer the assembly time. This process is greatly accelerated using the library Numba.

In this Section, we analyze the computational requirements when assembling and solving the system to provide an estimation of the capabilities of the model and a deeper perspective on the numerical efficiency of the model. First, we discuss the assembly of each of the three equations of the linear system (each of the three lines in equations 4.70 and 4.71).

Mass conservation equation

The first line of equations 4.70a represents the matrix version of the mass conservation within each FV cell, which is given by the discrete equation 4.17 where the term $J_{k,m}$ bridges the discontinuities of the rapid term across FV cells. This formulation allows to localize the source potentials (i.e., the rapid term), thereby providing a sparse model. The localization approach based on the size of $\widehat{V}$ dictates on how many interfaces ($\partial V_{k,m}$) the term $J_{k,m}$ is relevant (see explanation in Section 4.2.5). Thus, we can estimate the complexity of the assembly of matrix $\mathbf{B}$ as the total number of non-null entries $\mathscr{P}$ in the matrix

$$\mathscr{P}_{\mathbf{B}} = O(F6n^2\rho h_\Omega^3) \tag{4.73}$$

where ρ represents the density of sources per volume (m^{-3}), and we remind that F is the total number of FV cells of the cartesian grid, n is the side length (in discrete FV cells) of the neighbourhood $\widehat{V}$ and h_Ω is the side length of the cube made by a FV cell.

The computation of $\mathbf{A}$ is simpler since each line contains the conventional diffusion stencil in three dimensions, therefore it requires one computation for each FV cell ($O(F)$), which pales in comparison with equation 4.73. Furthermore, the code is implemented in Python, so we take advantage of vectorized calculations to further accelerate the assembly of $\mathbf{A}$.

Vessel-tissue exchanges

The source-to-source interactions contribute to a significant amount of computational complexity in the assembly of the matrix version of the vessel-tissue exchanges (second line of the linear system in equation 4.70). For any two sources that lie within each others neighbourhood ($\widehat{V}$), the source-to-source interactions need to be accounted for, which, due to the great vascular density in the brain, constitute one of the main bottlenecks in the assembly of the linear system. In a similar manner as in the previous Section, we can estimate the amount of computations needed

$$\mathscr{P}_{\mathbf{EF}} = O(8S(n+1)^3\rho h_\Omega^3) \tag{4.74}$$

where we remind that S represents the total amount of sources, i.e., discrete cylinders in the domain of computation. Furthermore, the matrix $\mathbf{D}$ contains the bilinear interpolation of the values at each FV cell (see Section 4.2.7), i.e., the estimation shape functions γ_i for the Q^1

element that is used, this yields the following amount of computations for the matrix $\mathbf{D}$

$$\mathscr{P}_{\mathbf{D}} = O(8S) \tag{4.75}$$

that corresponds to the eight non-null shape functions (from each of the eight nearest FV cells), for each source in the problem.

Intravascular transport

Similarly to the assembly of $\mathbf{A}$, the assembly of the discrete intravascular transport problem (third line in equations 4.70 and 4.71) is not computationally expensive due to the local nature of the FV scheme used. We estimate the amount of computations as the same order of magnitude as the amount of sources in the domain of computation

$$\mathscr{P}_{\mathbf{I}} = O(S) \tag{4.76}$$

It is clear now how the majority of computing time is spent in the assembly of the matrices $\mathbf{D}$, $\mathbf{E}$ and $\mathbf{F}$. Overall, these estimations allow to know a-priori the assembly time of any simulation and allow to compare the improvements offered by the multiscale model with respect to others in the literature.

4.2.11 Solution of the numerical system

The operator splitting approach introduced in this Chapter results in a strongly coupled system, i.e., the discrete equations are assembled in a single matrix (equation 4.71) that simultaneously contains the intravascular and extravascular problems. We can simplify the problem by writing it only in terms slow term $\mathfrak{z}$ and C_v. The matrix $\mathbf{H}$ can be easily inverted since it is diagonal (see equation 4.69), which allows us to write the vessel-tissue exchanges as a function of the intravascular concentration field :

$$\mathbf{q} = \mathbf{H}^{-1}(\mathbf{b}_{\partial\Omega_\beta} - \mathbf{I} \cdot \mathbf{C_v}) \tag{4.77}$$

Therefore, the matrix associated to the full linear system as a function of the concentrations yields :

$$\widetilde{\mathbf{L}} = \begin{bmatrix} \mathbf{A} & -\mathbf{B}\mathbf{H}^{-1}\mathbf{I} \\ \mathbf{D} & \mathbf{F} - \mathbf{E}\mathbf{H}^{-1}\mathbf{I} \end{bmatrix} \tag{4.78}$$

and the full linear system is given by

$$\widetilde{\mathbf{L}} \cdot \begin{Bmatrix} \mathfrak{z} \\ \mathbf{C_v} \end{Bmatrix} = \begin{Bmatrix} \mathbf{b}_{\partial\Omega} - \mathbf{B}\mathbf{H}^{-1}\mathbf{b}_{\partial\Omega_\beta} \\ -\mathbf{E}\mathbf{H}^{-1}\mathbf{b}_{\partial\Omega_\beta} \end{Bmatrix} \tag{4.79}$$

4.3 Results

In this Section, our attention is directed towards evaluating the accuracy of the 1DIV-3DEV multiscale model introduced in this Chapter, specifically those features exclusive to the 3D model that were not explored in the previous Chapter, i.e., computation of the source potentials. It's worth reminding that the intention behind the 2D simulations presented in the

previous Chapter served to 1) propose an operator splitting framework applicable to brain microcirculation, and 2) examine limit cases and establish an upper estimation of the framework's potential errors. Now that the ranges wherein the multiscale model is applicable and the errors introduced are clear, our focus shifts to the new 3D features. We recall the fact that the 0DIV-2DEV cases enabled an assessment of the framework's effectiveness in computing the radial diffusive fluxes, which constitute the main challenge of the molecular transport models in the brain, and the main reason why Green's functions approaches are popular for these types of problems [6; 9; 10; 13; 24; 31]. Consequently, in this Section our focus swifts towards axial transport as it constitutes the innovation of the Chapter. In short, the previous Chapter focused on evaluating the numerical strategy adopted, including operator splitting, localization, the local axisymmetry hypothesis, and addressing the slow term through a coarse grid. Meanwhile, this Chapter delves into the challenging estimation of the rapid term in a novel way.

In Section 4.3.1, we study the errors associated to the multiscale model and evaluate the influence of the approximations used for the influence coefficients (equations 4.67 and 4.68). Subsequently, in Section 4.3.2, we use synthetically generated networks mimicking the structure and function of the capillary bed to serve as a demonstration case for large microvascular networks. Here, for validation purposes, we implemented a finely meshed finite element (FE) model using COMSOL for a single vessel in the same spirit as [32]. Due to the difficulty of solving the coupled 1DIV-3DEV model, we opt for solving them separately in the validation stage. That is, we impose the concentration profile inside the vessel and evaluate the resulting parenchymal field, or we impose a the value of the vessel wall concentration in the parenchyma and evaluate the resulting cross-sectional average concentration within the vessels. This permits the use of commercial software (COMSOL) for meshing and computation without the need to develop a new fine grid model.

4.3.1 Single vessel

In this Section, we focus on the validation of the new 1DIV-3DEV multiscale model introduced in this Chapter. We use the aforementioned validation procedure where, to validate the extravascular field, we use a finely meshed model of the parenchyma and impose the intravascular concentration profile as a boundary condition. On the other hand, to validate the intravascular model (i.e., the FV method applied to the intravascular compartment used to assemble matrices $\mathbf{H}$ and $\mathbf{I}$), we use analytical solution of the 1D transport equation. For all the simulations in this Section with the multiscale model, we used a 3D coarse grid discretization of grid cell size $h_\Omega = L/5$ where L represents the length of a single vessel.

First, we assess the approximation of the single layer potential via equation 4.67. We design a case where three straight vessels share a centerline and have constant intravascular concentration (see Fig. 4.5A). That way, we achieve the following : the double layer potential is null so we can focus on the single layer potential. Moreover, we set the permeability of the first and last vessels to zero (grey lines along the vessel wall in Fig. 4.5A) to minimize boundary effects. We also set the metabolic consumption to zero, with Dirichlet boundary conditions on the faces parallel to the vessels set to $\phi = 0$ in order to guarantee rapid decay of the concentration field around the vessels mimicking the microcirculation. We set Neumann boundary conditions on the faces perpendicular to the vessels with $\boldsymbol{\nabla}_n \phi = 0$. Fig. 4.5B shows three cross-sections of the extravascular concentration field. This configuration allows to isolate the estimation of the single layer potential to compare the improvements achieved by

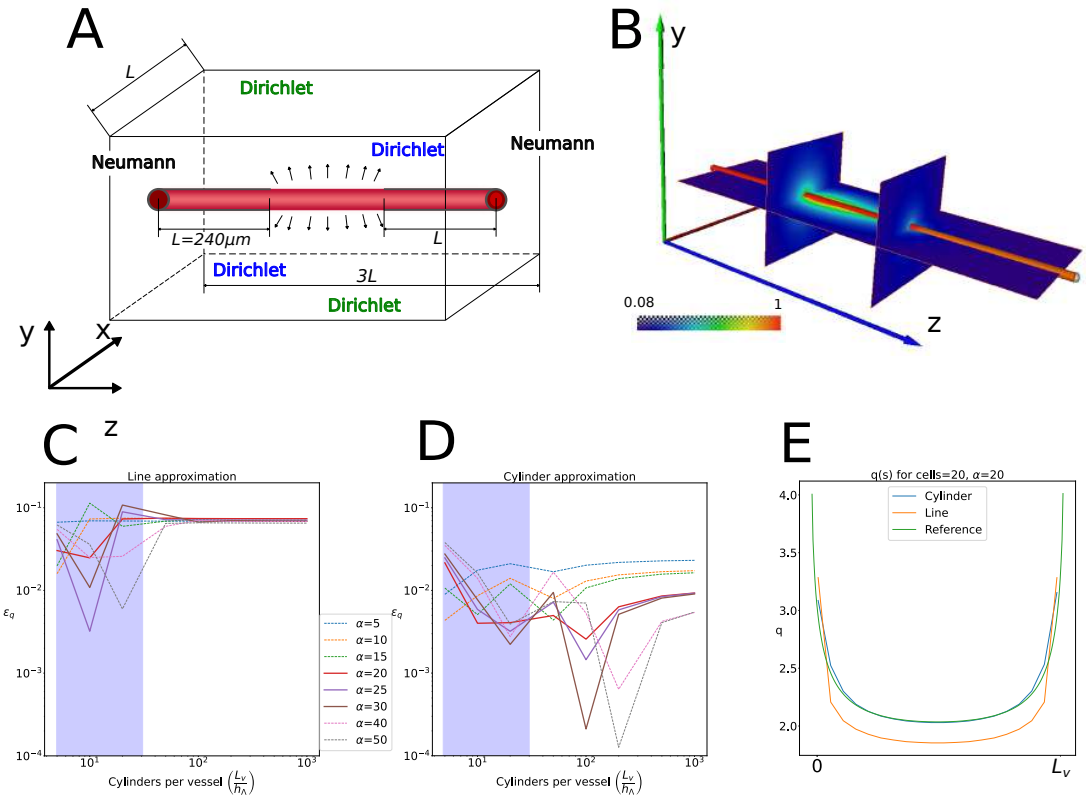

FIGURE 4.5 – **Impact of the approximation of the self-influence coefficient.** Panel A shows the schematic of the solved problem ; we assemble three vessels where the first and last have null permeability to avoid boundary effects, and only the middle one exchanges with the parenchyma. Panel B shows the contour plots of the concentration field. Panels C and D show the errors in the estimation of the exchanges via the exact formulation and the line approximation, respectively, for multiple discretizations, and multiple aspect ratios. Panel E contains the legend for the aspect ratios (α). In panels D and E, the continuous lines represent the most common aspect ratios applicable for a model of the brain microcirculation, and the blue shaded areas represent the reasonable discretizations used for large scale simulations. Panel E shows the difference in the vessel-tissue exchanges (for the middle vessel), between the COMSOL reference solution, the exact estimation, and the line approximation for a case with 20 discrete cylinders per vessel and an aspect ratio of 20 ($\frac{R}{L} = 20$).

the cylinder approximation for the self-influence coefficient (equation 4.67) when compared with the conventional line approximation (equation 4.34) often used in 1DIV-3DEV models [16; 25].

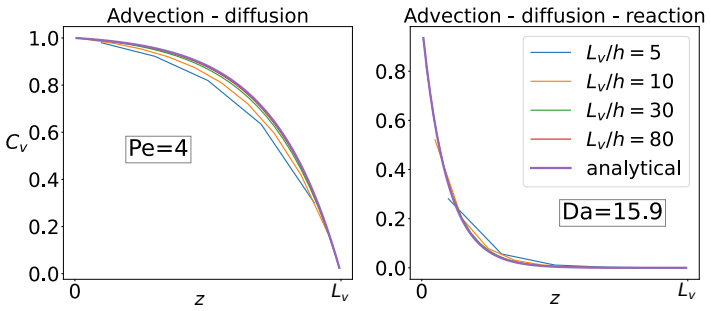

FIGURE 4.6 – **Assessment of equation 4.16 for the intravascular transport**. Comparison of the numerical resolution for different discretizations of the vessel. Left panel shows the solution for the problem with no reaction i.e., $Da = 0$. Right panel shows the solution for the same Peclet number ($Pe = 4$) and a fixed reaction rate $Da = 15.9$.

Furthermore, we test multiple vessel aspect ratios given by $\alpha = R/L$, and multiple vessel discretizations given by the amount of cylinders per vessel L/h_Λ. In Fig. 4.5C, we can appreciate how the line approximation for the single layer (equation 4.34) converges toward errors of the order of 10^{-1} regardless of the aspect ratio of the vessel. We remind the reader the errors obtained in the previous Chapter using no coupling condition are of the smae order of magnitude. Therefore, we can conclude that neglecting the volume of the vessel in a multiscale model based on the Green's functions results in errors of similar magnitude as neglecting the perivascular gradients all together. Thus, the line approximation (equation 4.34) introduces important errors due to its failure to accurately evaluate the single layer potential near the pole as illustrated in Fig. 4.3.

In contrast, in Fig. 4.5D, we can appreciate the better estimation achieved when using the cylinder approximation (equation 4.67), especially for reasonable values of the vessel discretization [5] (shaded in blue in panels C and D). Furthermore, in Fig. 4.5E, we can appreciate the difference in the estimation of the vessel tissue exchanges (q) for a reasonable choice of discretization size (L/h_Λ=20) and aspect ratio ($\alpha = 20$) for both, the cylinder approximation (equation 4.67), and the line approximation (equation 4.34). We obtain remarkable accuracy for the cylinder approximation, whereas the line approximation commonly used in literature provides an overestimation of the concentration at the vessel wall, thus underestimating the value of the vessel-tissue exchanges.

We now focus on the intravascular transport equation. The conventional FV method is used for the assembly of 1D transport. We therefore use the intravascular simulations to assess the error introduced by the model with different discretization sizes. We use a single vessel and impose Dirichlet BCs $\phi = 1$ on the inlet, and $\phi = 0$ on the outlet. We show a specific example for values for Peclet ($Pe = \dfrac{U \cdot L}{D}$) and Damköhler ($Da = \dfrac{K_{eff} \cdot L}{D \cdot R_v}$). Fig. 4.6 shows the nice agreement between the solution obtained with equation 4.16 and the analytical solution.

We now shift the focus to the double layer potential. We come back to the three vessel

5. With reasonable values we mean the discretizatios that can be used in large microvascular network simulations. Only a model that is accurate for discretizations $L/h_\Lambda < 20$ and aspect ratios $\alpha < 50$ can be applicable to the brain microcirculation.

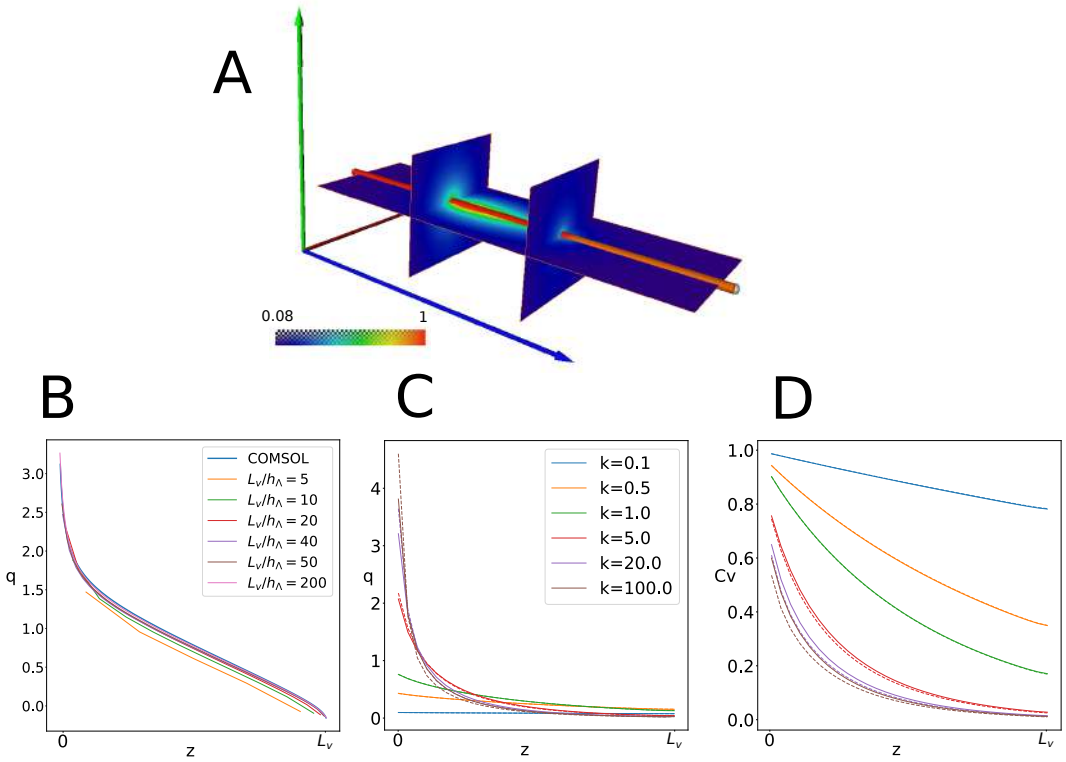

FIGURE 4.7 – **Analysis of the influence of the double layer potential for an aspect ratio $\alpha = 20$.** Panel A shows the contour plot of the concentration field. Panel B shows the comparison between the formulation developed in this paper and the reference solution for the vessel tissue exchanges. Panel C and D show the impact of neglecting the dipoles for multiple values of the vessel wall permeability, where $k = \dfrac{K_{eff}}{2\pi RD}$. The plots show the quantities for the middle vessel of the three, which is the only one that has non-null vessel wall permeability.

framework of Fig. 4.5A, but this time we set a variable intravascular concentration profile to ensure a non-null double layer potential. In Fig. 4.7B, we fix the intravascular concentration to decay linearly along the center vessel from $\phi = 1$ at the inlet to $\phi = 0$ at the outlet. Furthermore, we show the convergence of the numerical model using different discretizations confirming the proper estimation of the double layer potential. The results highlight that the model results in low errors for reasonable discretizations (e.g., $L/h_\Lambda = 10$).

We have now assessed the accuracy of the double layer potential via equation 4.68. Now the task consists in assessing the relevancy of the double layer potential in our simulations. Fig. 4.7C and D compare the results of the fully coupled model with (straight lines) and without (dotted lines) the double layer in the potential estimation. The parameters of the simulation include, $L/h_\Lambda = 10$, $\phi = 0$ at the inlet and $\boldsymbol{\nabla}_n\phi = 0$ at the outlet and only the middle vessel is permeable to avoid boundary effects. Furthermore, we test a wide range of vessel permeabilities around the physiological range, which for a small capillary would fall around $k = 1$ i.e., green line, since it was found to have the greatest impact over the magnitude of the double layer potential [10]. We can observe the low impact of the double layer potential on the accuracy of the solution, even for very large values of the vessel wall permeability as predicted by Pozrikidis and Farrow [10]. Therefore, in the rest of the manuscript, we neglect the influence of the double layer potential due to its low impact on the results and lack of an acceptable estimation for non-straight vessels.

4.3.2 Synthetic Networks

Once assessed the accuracy of the newly developed concepts, we step foot into the multiple vessel models that constitute the main objective of this thesis. We now focus on the task of assessing the capabilities of the multiscale model regarding the scale of the networks that can be tackled. Subsequently, we provide an assessment of the improvements our model can offer with respect to the ones developed in the literature.

Firstly, we generate a synthetic network that mimics the properties of the capillary bed [33] to produces a cube of tissue containing 558 vessels of 10 μm in diameter. The side length of the cube of tissue is $300\mu m$, and the vessels have an average length of approximately $60\mu m$. We set periodic BCs on the parenchyma and Dirichlet BCs on the network inlets and Neumann on the outlets. For each inlet of the vessels the concentration is set to its maximum ($\phi = 1$) mimicking oxygenated incoming blood, and $\nabla_n \phi = 0$ on the outlets [34]. Additionally, we set a constant metabolic rate throughout the parenchyma of 2 $\mu molcm^{-2}s^{-1}$.

Furthermore, we obtain the velocity field by imposing a gradient of pressure along the z-axis, that provides a velocity field within the ranges found in the brain microcirculation [5]. The resulting concentration fields are shown in Fig. 4.8, where we can appreciate the radial oxygen gradients around the capillaries. The vascular system was discretized with an average cylinder size of $h_{\Lambda,j} = 6\mu m$, which resulted in approximately 6000 sources in the model, where the bifurcations were handled as detailed in Section A.4 to avoid the over estimation of the surface created by the intersection of three cylinders. The cartesian grid included $5 \times 5 \times 5$ cells, and $n = 3$, which results in $h_\Omega = 60\mu m$ and $||\widehat{V}|| = 180 \times 180 \times 180 \mu m^3$. The assembly and resolution of the problem took around 4 minutes for the compilation of the code [6], the assembly of the problem and the resolution of the linear system with a Dell laptop using an intel Core i7 processor and 16 Gb of RAM.

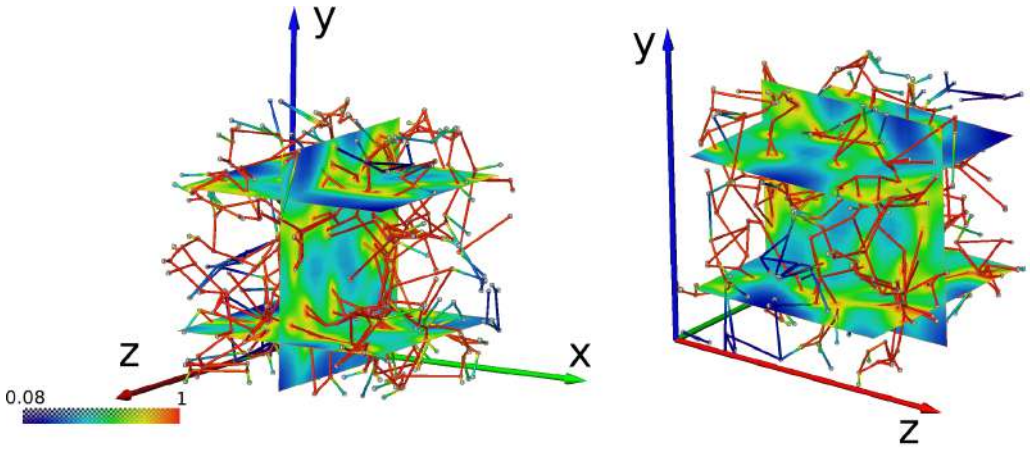

FIGURE 4.8 – **Contour plot of the concentration field in both compartments for a synthetic capillary network with 556 vessels** The concentration field in the parenchyma and in the vessels is shown. And two different views are shown of the same simulation. The concentration field in the parenchyma is given through three cross-sections, and the concentration field in the vessels is provided by the coloring of the graph which represents the averaged concentration for each vessel.

The simulation shown in Fig. 4.8 provides a test for the multiscale model allowing to qualitatively assess the radial concentration gradients around the capillaries. However, one cannot

6. Normally, Python codes do not need compilation. In this case, we used the Numba library to accelerate the assembly of the system. Essentially, Numba translates certain functions to machine code which requires a compilation. This does not offer time advantages for small networks, but it is crucial for large ones.

appreciate large scale effects such as the decay in concentration caused by the deoxygenation of blood flowing through the network. For that, we increase the size of the simulation domain to $1\mu m^3$ which includes 18000 vessels as shown in Fig. 4.9. We impose the same BCs on the network and on the parenchyma as in the previous simulation in Fig. 4.8. The problem is solved with a mesh of 15x15x15 and $n = 3$ which results in $h_\Omega = 66.6\mu m$ and $||\widehat{V}|| = 200x200x200\mu m^3$. The assembly of the matrix system took approximately 9 hours to complete and the resolution of the linear system using the GMRES algorithm took around 30 minutes with a Dell laptop using an intel Core i7 processor and 16 Gb of RAM.

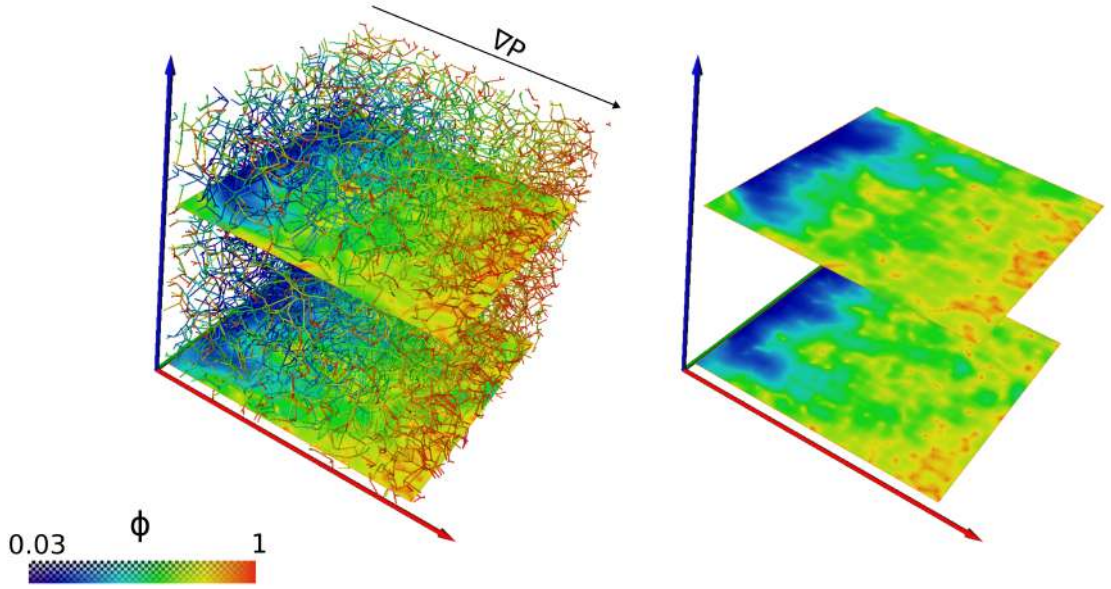

FIGURE 4.9 – **Contour plot of the concentration field in both compartments for a synthetic capillary network with 18000 vessels** Left panel shows the average vessel concentration superposed to two cross-sections of the reconstructed concentration in the parenchyma. Right panel shows the same two cross-sections of the reconstructed concentration field in the parenchyma

4.4 Discussion

We have introduced a multiscale model for molecular transport in the brain microcirculation based on a operator splitting approach combined with a Green's function formulation that allows an accurate estimation of the challenging perivascular concentration gradients. The improvements of this model are apparent when solving a large network of 18000 capillaries in under 30 minutes with a single processor while using a 3D mesh containing just 2700 cells. For comparison, the FE model used as reference for the single vessel simulation used a mesh of the parenchyma of over $4 \cdot 10^5$ elements (solved using COMSOL Multiphysics) shown in Fig. A.4. Furthermore, the accuracy of the model is evaluated with the single vessel simulations that demonstrates that the newly introduced single layer potential computation reduces the errors an order of magnitude when compared with the conventional line approximation used in Gjerde et al. [16; 25].

Moreover, we confirmed the low impact of the double layer potential even for very high values of the vessel wall permeability. This allows to severely simplify the computation of the source potentials, thus the rapid term, and the overall assembly of the linear problem. In this Chapter, we focused on axial transport which required a new framework for the computation of the potentials that make up the rapid term since we assessed the accuracy of

the multiscale model regarding radial transport in the previous Chapter with the 0DIV-2DEV simulations. We followed the same validation procedure by using a reference solution of the original physical problem in the same spirit as [32]. To our knowledge, we are the first to perform the validation using the original physical problem, i.e., using the real volume of the vessel and no assumed symmetry around the capillary wall. This step by step development allowed us to test the underlying assumptions of the model (e.g., constant value of the wall concentration on each cylinder's wall, low magnitude of the gradients of the slow term), thus enabling us to confidently apply the multiscale model to large networks (Fig. 4.8 and 4.9) with a good estimate of the errors committed.

When compared with the semi-analytical models based on the Green's function formulation [6; 10; 13; 14], the multiscale model provides an efficient way to simplify the computation of the bounded Green's function by the use of the operator splitting approach. This strongly reduces the assembly time of the problem since the computation of the bounded Green's function constitutes the most expensive computation of the semi-analytical methods [13]. Furthermore, the localization procedure allows for a sparse system, which severely reduces the resolution time of the linear system. Additionally, the use of a 3D grid allows for straight forward computation of metabolic consumption in the parenchyma without the need to modify the fundamental solution of the problem (equation A.27).

With respect the fine-grid FE simulations [8; 35; 36] and many others, our approach differs significantly. With fine-grid models, the lack of a coupling scheme allows for a local formulation that permits a more accurate estimation of the metabolic term and also allows the easier inclusion of other non-linearities such as the oxygen dissociation from the blood [8]. Nevertheless, the fine refinement required around the vessels increases the computational requirements substantially, to the point that simulations as the ones shown here (O(10000) vessels) would be impossible without substantial loss of accuracy. Furthermore, the line approximation has been shown here to be highly inaccurate ; such inaccuracy depends strongly on the analytical function used to interpolate the values of the source over the coarse grid. No information can be extrapolated from the results shown in Fig. 4.5 to these FE schemes other than the cases where they use logarithmic shape functions for their elements. However, caution is advised when using such geometrical approximations since the volume of the vessels in the microcirculation is small, but non negligible.

The closest performance reduction is achieved by the coarse grid models employing some type of analytical coupling scheme model the perivascular concentration gradients [16; 25; 28; 37]. Such models can be applied to large microvascular networks bridging the gap between the sources and the coarse grid. In the case of well models [38–40], the main drawback is the considerable increase in source density and chaotic structure of the microcirculation when compared to oil and water reservoirs. We estimate that the pre-processing step to compute the coupling models and the interaction between sources in a microvascular network in using such models would render the pre-processing stem unfeasible for large networks.

Flexible coupling models such as the one used by [28] offer a useful alternative. However the smoothing operator needed for localizing the source potentials produces the background field to be faster varying, thus requiring further discretization of the 3D mesh, which increases considerably the size of the system (a volume mesh increases size with a complexity of N^3, where N represents the refinement of the mesh). Additionally, the model in [28] succeeds in spreading and incorporating the delta singularity of a vessel source into the grid. However, such an approach cannot handle interactions between multiple sources unless treated indivi-

dually, which either introduces errors in the model, or increases severely the pre-processing step in the same way as well models.

Lastly, we discuss the operator splitting models proposed in [15; 16; 39; 41]. Such models deal with the sources as infinitesimally thin lines, which introduces strong errors comparable to a lack of coupling model all together as shown in Fig. 4.5. Furthermore, similarly to [39; 41], but differently to [16; 25], we introduced a FV foundation to the resolution of the slow term. This allows the localization of the potentials via the rapid terms (equation 4.18) to be computed at the interfaces. This severely reduces the computation requirements of the assembly of the problem as discussed in Section 4.2.10. Currently, this is the bottleneck of the simulations where the assembly of the problem shown in Fig. 4.9 takes over 20 times longer than the resolution of the linear system, totalling at around 10 hours. We estimate that a model not based on a FV approach would increase this computation time by an order of magnitude.

The resolution time of the linear system is not the only roadblock in obtaining efficient large scale models of the brain microcirculation. Due to the great size of microvascular networks, the assembly of the linear model (matrix $\mathbf{L}$ in equation 4.71) requires serious computational time, especially in models such as the one developed in this Chapter. The foundation on the Green's function formulation has great advantages such as better accuracy than other coupling models, or the possibility to provide a reconstruction based on the actual solution of the BVP. On the other hand, it requires the computation of source-to-source interactions (matrices $\mathbf{E}$ and $\mathbf{F}$) and a great amount of fluxes (matrix $\mathbf{B}$). Out of the 9 hours that took the assembly of the biggest network shown in Fig. 4.9, the majority (around 6 hours), was spent on the computation of the cell to cell fluxes of matrix $\mathbf{B}$.

Other coarse mesh modeling approaches differ in their ability to reduce the size and density of the system, capture microscale dynamics and offer an overall improvement in performance compared to semi-analytical [6; 24] or fine scale methods. Koch et al. [42] implemented an analytical kernel to couple the sources from the vasculature to the containing mesh cell, which can be considered as another generalization of the Peaceman well model for any geometry [40; 43]. This approach captures perivascular gradients similarly to our model, but requires a much finer extravascular mesh to avoid large errors in the coupling term. Gjerde et al. [16] incorporated the microscale dynamics into the extravascular mesh using a kernel based on the free space Green's function. However, their non-localized problem does not offer performance improvements compared to traditional semi-analytical methods [10; 13] beyond the explicit treatment of boundary conditions. Moreover, the localized model [25] relies on a modification of the free-space Green's function, which yields source terms in the coarse mesh that must be explicitly calculated for each source. For very large networks, the estimation of these source terms becomes exceedingly large. In contrast, our model does not modify the free-space Green's function which leads into $J_{k,m}$ in equation 4.18. This reduces the computation of the source terms by several orders of magnitude and significantly increases the sparseness of the system. Other coarse mesh approaches such as Linninger et al. [7] and Hartung et al. [44] struggle capturing microscale dynamics due to the lack of an analytical coupling strategy.

Overall, to our knowledge, the multiscale model introduced in this Chapter offers the greatest reduction in computational complexity for the problem of 1DIV-3DEV in the brain microcirculation. In the previous Chapter, we focused on the development of an operator splitting approach that serves as the foundation of a local, coarse-grid numerical scheme, while in this Chapter, we focused on the accurate estimation of the sources' potentials. We showed how the estimation of the sources' potentials can be done basing the numerical model on the BIE ob-

tain via Green's third identity. This allows to obtain an accurate estimation of the potentials and avoid introducing errors by using other common forms for the rapid term as shown in Fig. 4.5E. We also tested the impact of the double layer potential on the simulations relevant for the brain microcirculation, obtaining a negligible impact which allowed us to neglect its computation. In the next Chapter, we discuss thoroughly the challenges addressed by the multiscale model, its place within the literature, and the future perspectives.

Certainly, here's an improved version of your concluding paragraph :

In summary, the multiscale model introduced in this Chapter represents a significant breakthrough in addressing the computational complexity associated with the 1DIV-3DEV problem in brain microcirculation. In the previous Chapter, our focus was on the development of an operator splitting approach that forms the cornerstone of a localized, coarse-grid numerical scheme. In contrast, in this Chapter, we shift the attention towards the precise estimation of source potentials. We demonstrated the efficacy of estimating these potentials by rooting the numerical model within the BIE derived from Green's third identity. This approach ensures accurate potential estimation and minimizes errors that may arise from alternative forms of the rapid term, as illustrated in Fig. 4.5E. Additionally, we conducted comprehensive tests on the influence of the double layer potential on brain microcirculation simulations, revealing a negligible impact that justifies its exclusion from computation.

In the upcoming Chapter, we will delve into a detailed explanation of the challenges addressed by our multiscale model, its place within the existing literature, and our vision for future research prospects.

4.5 References

[1] T.W. Secomb, R. Hsu, N.B. Beamer, and B.M. Coull. Theoretical Simulation of Oxygen Transport to Brain by Networks of Microvessels : Effects of Oxygen Supply and Demand on Tissue Hypoxia. *Microcirculation*, 7(4) :237–247, August 2000. 104

[2] Charles Nicholson. Diffusion and related transport mechanisms in brain tissue. *Reports on Progress in Physics*, 64(7) :815–884, July 2001.

[3] Daniel Goldman. Theoretical Models of Microvascular Oxygen Transport to Tissue. *Microcirculation*, 15(8) :795–811, January 2008.

[4] Karl Erik Holter, Benjamin Kehlet, Anna Devor, Terrence J. Sejnowski, Anders M. Dale, Stig W. Omholt, Ole Petter Ottersen, Erlend Arnulf Nagelhus, Kent-André Mardal, and Klas H. Pettersen. Interstitial solute transport in 3D reconstructed neuropil occurs by diffusion rather than bulk flow. *Proceedings of the National Academy of Sciences*, 114(37) :9894–9899, September 2017. 104

[5] Maxime Berg, Yohan Davit, Michel Quintard, and Sylvie Lorthois. Modelling solute transport in the brain microcirculation : is it really well mixed inside the blood vessels ? *Journal of Fluid Mechanics*, 884 :A39, February 2020. 105, 106, 128

[6] Timothy W. Secomb, Richard Hsu, Eric Y. H. Park, and Mark W. Dewhirst. Green's Function Methods for Analysis of Oxygen Delivery to Tissue by Microvascular Networks. *Annals of Biomedical Engineering*, 32(11) :1519–1529, November 2004. 105, 109, 112, 113, 121, 124, 130, 131

[7] A. A. Linninger, I. G. Gould, T. Marinnan, C.-Y. Hsu, M. Chojecki, and A. Alaraj. Cerebral Microcirculation and Oxygen Tension in the Human Secondary Cortex. *Annals of Biomedical Engineering*, 41(11) :2264–2284, November 2013. 120, 131

[8] Luca Possenti, Alessandro Cicchetti, Riccardo Rosati, Daniele Cerroni, Maria Laura Costantino, Tiziana Rancati, and Paolo Zunino. A Mesoscale Computational Model for Microvascular Oxygen Transfer. *Annals of Biomedical Engineering*, 49(12) :3356–3373, December 2021. 106, 130

[9] Yidan Xue, Theodosia Georgakopoulou, Anne-Eva van der Wijk, Tamás I. Józsa, Ed van Bavel, and Stephen J. Payne. Quantification of hypoxic regions distant from occlusions in cerebral penetrating arteriole trees. *PLOS Computational Biology*, 18(8) :e1010166, August 2022. 124

[10] C. Pozrikidis and D. A. Farrow. A Model of Fluid Flow in Solid Tumors. *Annals of Biomedical Engineering*, 31(2) :181–194, February 2003. 105, 109, 112, 113, 121, 124, 127, 130, 131

[11] Myriam Peyrounette, Yohan Davit, Michel Quintard, and Sylvie Lorthois. Multiscale modelling of blood flow in cerebral microcirculation : Details at capillary scale control accuracy at the level of the cortex. *PLOS ONE*, 13(1) :e0189474, January 2018. 106, 120

[12] Franca Schmid, Philbert S. Tsai, David Kleinfeld, Patrick Jenny, and Bruno Weber. Depth-dependent flow and pressure characteristics in cortical microvascular networks. *PLOS Computational Biology*, 13(2) :e1005392, February 2017. 106

[13] Richard Hsu and Timothy W. Secomb. A Green's function method for analysis of oxygen delivery to tissue by microvascular networks. *Mathematical Biosciences*, 96(1) :61–78, September 1989. 109, 112, 124, 130, 131

[14] Timothy W Secomb. Blood Flow in the Microcirculation. page 21, 2016. 130

[15] Ingeborg G. Gjerde, Kundan Kumar, and Jan M. Nordbotten. A Singularity Removal Method for Coupled 1D-3D Flow Models. Technical Report arXiv :1812.03055, arXiv, August 2019. arXiv :1812.03055 [cs, math] type : article. 131

[16] Ingeborg G. Gjerde, Kundan Kumar, Jan M. Nordbotten, and Barbara Wohlmuth. Splitting method for elliptic equations with line sources. *ESAIM : Mathematical Modelling and Numerical Analysis*, 53(5) :1715–1739, September 2019. 109, 113, 126, 129, 130, 131

[17] G.F. Roach. *Green's Functions*. Second edition, 1989. 109, 110

[18] Costas Pozrikidis and Joel H. Ferziger. Introduction to Theoretical and Computational Fluid Dynamics. *Physics Today*, 50(9) :72–74, September 1997. 110, 118

[19] D. Pepper, A. Kassab, and E. Divo. *Introduction to Finite Element, Boundary Element, and Meshless Methods : With Applications to Heat Transfer and Fluid Flow*. ASME Press, 2014. 109, 110, 117

[20] C. Pozrikidis. *A practical guide to boundary element methods with the software library BEMLIB*. Chapman & Hall/CRC, Boca Raton, 2002. 110, 117

[21] Lothar Gaul, Martin Kögl, and Marcus Wagner. *Boundary Element Methods for Engineers and Scientists*. Springer Berlin Heidelberg, Berlin, Heidelberg, 2003.

[22] M. H. Aliabadi and P. H. Wen. *Boundary element methods in engineering and sciences*. Number 4 in Computational and experimental methods in structures. Imperial College Press, London, 2011. 110

[23] Dean G. Duffy. *Green's functions with applications*. Studies in advanced mathematics. Chapman & Hall/CRC, Boca Raton, Fla, 2001. 110

[24] Paul W. Sweeney, Angela d'Esposito, Simon Walker-Samuel, and Rebecca J. Shipley. Modelling the transport of fluid through heterogeneous, whole tumours in silico. *PLOS Computational Biology*, 15(6) :e1006751, June 2019. 112, 113, 124, 131

[25] Ingeborg G. Gjerde, Kundan Kumar, and Jan M. Nordbotten. A singularity removal method for coupled 1D–3D flow models. *Computational Geosciences*, 24(2) :443–457, April 2020. 112, 126, 129, 130, 131

[26] Robert Eymard, Thierry Gallouet, and Raphaele Herbin. January 2019. This manuscript is an update of the preprint n0 97-19 du LATP, UMR 6632, Marseille, September 1997 which appeared in Handbook of Numerical Analysis, P.G. Ciarlet, J.L. Lions eds, vol 7, pp 713-1020. 2019. 118

[27] H. K. Versteeg and W. Malalasekera. *An introduction to computational fluid dynamics : the finite volume method*. Pearson Education Ltd, Harlow, England ; New York, 2nd ed edition, 2007. OCLC : ocm76821177. 118

[28] Timo Koch, Martin Schneider, Rainer Helmig, and Patrick Jenny. Modeling tissue perfusion in terms of 1d-3d embedded mixed-dimension coupled problems with distributed sources. *Journal of Computational Physics*, 410 :109370, June 2020. 120, 130

[29] Siu Kwan Lam, Antoine Pitrou, and Stanley Seibert. Numba : a LLVM-based Python JIT compiler. In *Proceedings of the Second Workshop on the LLVM Compiler Infrastructure in HPC*, pages 1–6, Austin Texas, November 2015. ACM. 121

[30] Pauli et al. Virtanen. SciPy 1.0 : fundamental algorithms for scientific computing in Python. *Nature Methods*, 17(3) :261–272, March 2020. 121

[31] Timothy W. Secomb. A Green's function method for simulation of time-dependent solute transport and reaction in realistic microvascular geometries. *Mathematical Medicine and Biology*, 33(4) :475–494, December 2016. 124

[32] Qianqian Fang, Sava Sakadžić, Lana Ruvinskaya, Anna Devor, Anders M. Dale, and David A. Boas. Oxygen advection and diffusion in a three-dimensional vascular anatomical network. *Optics Express*, 16(22) :17530, October 2008. 124, 130

[33] Amy F. Smith, Vincent Doyeux, Maxime Berg, Myriam Peyrounette, Mohammad Haft-Javaherian, Anne-Edith Larue, John H. Slater, Frédéric Lauwers, Pablo Blinder, Philbert Tsai, David Kleinfeld, Chris B. Schaffer, Nozomi Nishimura, Yohan Davit, and Sylvie Lorthois. Brain Capillary Networks Across Species : A few Simple Organizational Requirements Are Sufficient to Reproduce Both Structure and Function. *Frontiers in Physiology*, 10 :233, March 2019. 128

[34] maxime Berg. Modélisation de l'écoulement sanguin et du transport de molécules dans la microcirculation sanguine cérébrale : impact des occlusions capillaires dans la maladie d'Alzheimer. page 160, 2019. 128

[35] C. D'Angelo and A. Quarteroni. On the coupling of 1D and 3D diffusion-reaction equations. Applications to tissue perfusion problems. *Mathematical Models and Methods in Applied Sciences*, 18(08) :1481–1504, August 2008. 130

[36] Carlo D'Angelo. Finite Element Approximation of Elliptic Problems with Dirac Measure Terms in Weighted Spaces : Applications to One- and Three-dimensional Coupled Problems. *SIAM Journal on Numerical Analysis*, 50(1) :194–215, January 2012. 130

[37] D W Peaceman. Interpretation of Well-Block Pressures in Numerical Reservoir Simulation. *Society of Petroleum Engineers*, page 17, 1978. 130

[38] I. Aavatsmark and R.A. Klausen. Well Index in Reservoir Simulation for Slanted and Slightly Curved Wells in 3D Grids. *SPE-75275-PA*, 8(01) :41–48, March 2003. Publisher : Society of Petroleum Engineers. 130

[39] Christian Wolfsteiner, Seong H. Lee, and Hamdi A. Tchelepi. Well Modeling in the Multiscale Finite Volume Method for Subsurface Flow Simulation. *Multiscale Modeling & Simulation*, 5(3) :900–917, January 2006. 131

[40] Savithru Jayasinghe, David L. Darmofal, Eric Dow, Marshall C. Galbraith, and Steven R. Allmaras. A Discretization-Independent Distributed Well Model. *SPE Journal*, 24(06) :2946–2967, December 2019. 130, 131

[41] P. Jenny, S. H. Lee, and H. A. Tchelepi. Adaptive Multiscale Finite-Volume Method for Multiphase Flow and Transport in Porous Media. *Multiscale Modeling & Simulation*, 3(1) :50–64, January 2005. 131

[42] Timo Koch, Rainer Helmig, and Martin Schneider. A new and consistent well model for one-phase flow in anisotropic porous media using a distributed source model. *Journal of Computational Physics*, 410 :109369, June 2020. 131

[43] D. Y. Ding. Near-Well Upscaling for Reservoir Simulations. *Oil & Gas Science and Technology*, 59(2) :157–165, March 2004. 131

[44] Grant Hartung, Shoale Badr, Mohammad Moeini, Frédéric Lesage, David Kleinfeld, Ali Alaraj, and Andreas Linninger. Voxelized simulation of cerebral oxygen perfusion elucidates hypoxia in aged mouse cortex. *PLOS Computational Biology*, 17(1) :e1008584, January 2021. 131

Chapter 5

General conclusions and perspectives

Modeling solute transport in the brain microcirculation is a crucial step in order to improve our understanding of the development of multiple diseases such as AD and vascular mediated dementias [1–5]. Particularly, large scale models of oxygen transort and consumption can shed light on the emergence of hypoxic regions in the brain, considering the impact of non-local effects [6] that are not captured by theoretical models [7; 8]. In the context of imaging techniques centered around oxygen delivery and the estimation of oxidative metabolism at the macroscopic scale [9–11], or at the microscopic scale [12–15] there is a clear need for integrating the theoretical principles that govern the movement of molecules across scales in order to provide clear interpretation of experimental data and improve the understanding of multiple physiological principles such as neurovascular coupling [4; 16].

Thus, the problem of solute transport in the brain microcirculation has been a long standing challenge with notable contributions in the last decades [12; 17–21]. However, due to the complex geometry of the vascular system, solving the transport equations for solutes that cross the blood brain barrier (BBB) proves difficult, and current accurate models remain only applicable to small networks [12; 19; 22–24]. In this thesis, we tackled the complex problem of accurately modeling the microscale dynamics while simultaneously solving the solute transport problem in large vascular networks, i.e., several thousand vessels.

For that purpose, we have developed a multiscale method that combines analytical approaches, based on Green's third identity, with numerical approaches such as the multiscale finite volume method (MSFV). The main idea is to leverage the boundary integral equation (BIE) to provide an analytical description of the microscale dynamics in the neighbourhood of the vessel. By also tailoring the numerical model to integrate the analytical description, we achieve a remarkable decrease in the computational cost when compared with models with a similar level of detail. Specifically, in the case of the 0DIV (intravascular)-2DEV (extravascular) and 1DIV-3DEV configurations, the fine-grid finite element (FE) solution results in a matrix problem that is two to three orders of magnitude larger. This increased efficiency effectively bridges the spatial scale gap between transport dynamics at the capillary scale and large microvascular networks, a significant step toward enabling whole-brain simulations. Nonetheless, challenges remain, including the incorporation of temporal dynamics and the development of an exchange law that more accurately represents molecular dynamics within red blood cells (RBCs). In this Chapter, our primary focus is on the challenges addressed by the multiscale model and the improvements it offers within the paradigm of solute transport models (Section 5.1). Subsequently, we explore potential future research directions and exten-

sions of our current model (Section 5.2) based on the operator splitting framework introduced in Chapter 3.

5.1 General conclusions

In this Section, we assess the performance and novelty of the multiscale model, and discuss the extent to which the research objectives are met. To this end, we begin by revisiting the primary challenges that hindered accurate simulations at the microvascular network scale, as detailed in Section 5.1.1. Subsequently, in Section 5.1.2, we provide a concise overview of the key features of our multiscale model and offer rationale for the main assumptions made throughout the development in Chapter 3. We also discuss the place of the obtained multiscale model within the landscape of solute transport models in the literature.

5.1.1 Challenges

The main issue hindering progress in the development of numerical models of the brain microcirculation is the challenging task of integrating microscale phenomena in models of large volumes as discussed throughout this thesis. This stems from the complex and convoluted geometry of the brain's vascular system. This intricate network prevents simplification of the governing equations through conventional upscaling methods, making it exceptionally challenging to devise a comprehensive solution. Therefore, our focus centered on efficiently solving large networks of vessels, as detailed in Chapter 4. In doing so, we focused on the following challenges which we consider to be the main roadblocks :

— **Accurate estimation of perivascular gradients**. These gradients play a crucial role in driving extravascular transport, and any inaccuracies in their quantification can result in significant errors, as illustrated in Chapter 3, Figs. 4-6. The rapid fluctuations in concentration fields near blood vessels create complex configurations that are often difficult to address using traditional numerical methods.

— **Multiscale nature and high density of the cerebral microcirculation.** The previous challenge becomes even more pronounced when dealing with the seemingly chaotic and densely packed microvascular networks. The high spatial density of these microvessels often renders certain approaches, such as the analytical coupling models (discussed in Section 2.4.2), impractical due to the complex interactions between individual vessels. Also, these configurations often render fine-grid models (discussed in Section 2.4.2 and 2.4.2) very computationally expensive, thus not applicable to large microvascular networks.

— **Inclusion of non-linear metabolic consumption**. The non-linear Michaelis-Menten expression introduces important complications in some of the models often applied to the brain such as the ones based on the Green's function of the problem due to their inherent linear nature.

— **Lack of a reference solution**. The solute transport literature for the brain microcirculation lacks of a gold standard model. This severely complicates the validation procedure especially when attempting a comparison with existing models. We perform the validation using a fine-grid FE model in the same spirit as [12], as it provides the highest fidelity to the original problem.

Although not exhaustive, the list above summarizes the main barriers towards large scale models of molecular transport in microvascular networks. Failure to tackle one of these challenges would result in an incomplete model. For instance, failure to include the non-linear metabolic consumption would provide a model that might be interesting for bridging the scale gap, but would not be useful with regards to the main applications cited in Chapter 1, i.e., study of the development of AD, aid in the understanding of neurovascular and neurometabolic coupling, etc. Next, in Section 5.1.2 we discuss the characteristics of the multiscale model developed in this thesis in relation to the above mentioned challenges.

5.1.2 A new multiscale model

In this thesis, we proposed a novel model that leverages the developments in multiple research fields into the cerebral microcirculation. The combination of the MSFV method with the Green's function approaches (i.e., semi-analytical approaches) allows the development of a sparse and efficient method that includes a novel localization scheme for the source potentials inspired by that of Jenny et al. [25]. The finite volume (FV) discretization forms the foundation of our method, enabling us to address the slow term and localize potentials using a coarse cartesian grid. Additionally, our use of Green's functions allows us to analytically compute source potentials, offering a significant time-saving advantage compared to other methods that rely on numerical computations (e.g., MSFV [26]). The substantial computational gain obtained by the multiscale method stems from the following :

— **Analytical computation of the source potentials through a Green's function framework.** Green's third identity is leveraged to obtain an explicit description of the rapid and slow terms characteristic of the operator splitting approach. This provides an analytical expression for the source potentials that strongly simplifies the computation of the rapid term.

— **Strong coupling between analytical and numerical parts via the interface fluxes of the FV method.** The simple formulation of the FV method allows to couple the analytical approach for the computation of the rapid term with the coarse grid numerical solution for the slow term. This, in turn, allows an efficient localization of the source potentials, which is needed to obtain a sparse system, while preserving the conservative nature of the FV method.

— **Coarse grid computation of the boundary conditions.** Commonly, the primary challenge of semi-analytical methods based on the Green's function approach is the satisfaction of the boundary conditions. This can be achieved by either using the bounded fundamental solution or by choosing a numerical approach such as the boundary element method. When dealing with the brain microcirculation, the former is widespread [18; 19; 27–29]. In this case, the computation of the bounded fundamental solution constitutes the most computationally demanding calculation of the model [17]. Our multiscale model avoids this all together by using a coarse grid contributing to a small proportion of the computational resources needed for the solution of the problem (the majority of unknowns come from the 1D mesh of the vascular system).

— **Cartesian grid**. The cartesian grid serves a dual purpose : it facilitates the precise fulfillment of the boundary conditions, it also offers a structured framework for incorporating non-linear volume reaction terms within the parenchyma. In contrast, purely semi-analytical methods encounter significant challenges when dealing with non-linear reactions in the parenchyma because they do not utilize the operator splitting frame-

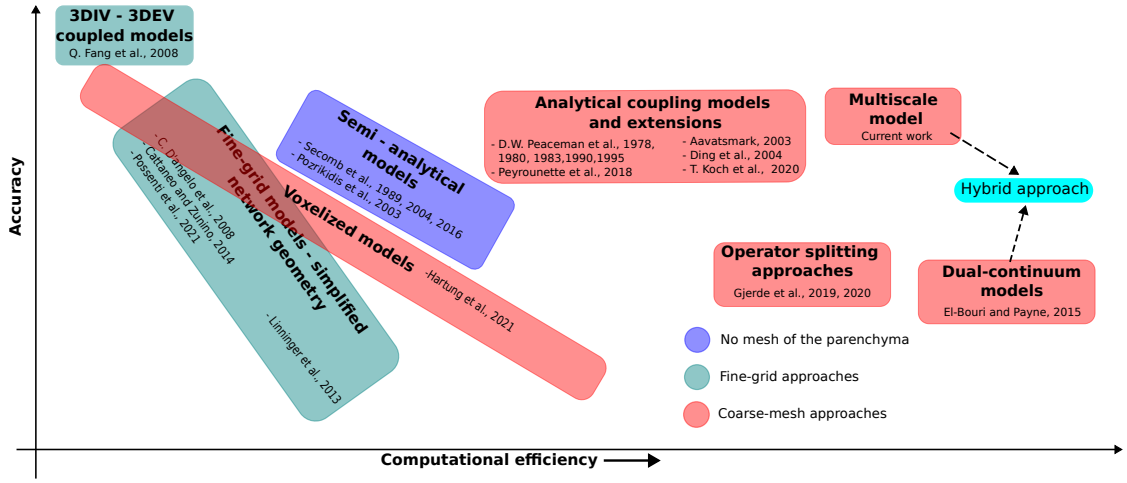

FIGURE 5.1 – **Approximative assessment of the accuracy and computational efficiency of the published models for molecular transport in the brain microcirculation.** The most popular models used in the molecular transport in the brain microcirculation are compared with each other. Those in the upper right corner represents an ideal balance of accuracy and computational efficiency. The following models are included in the assessment [12; 17–20; 22–24; 26; 30–38]

work and, as a result, do not use a volume mesh. In their work, Secomb et al. [19] addressed this issue by introducing point sinks of mass whose intensity depend on the surrounding concentration field. This approach effectively introduces as many unknowns into the system as a cartesian grid, while providing an approximation of the volumic sink term associated with metabolism through a concentrated point sink, which is not ideal.

It is worth noting that the choice of a coarse cartesian grid and the simplified calculation of the source potentials through the assumption of local axisymmetry introduces slight errors around 1% as shown in Chapters 3 and 4. These choices are made deliberately to maximize the reduction in computational complexity while introducing minimal errors in the process, i.e., excellent balance between accuracy and computational efficiency (Fig. 5.1). This results in a remarkable reduction in calculation time, where the coupled intra- extra- vascular problem in a volume containing 18.000 vessels took 30 minutes to solve with a Dell laptop using an intel Core i7 processor and the conventional Scipy library of linear solvers. Evaluating the computational efficiency and accuracy of previous models for comparison purposes is not easy. However, based on the underlying assumptions of the available models, we provide in Fig. 5.1 the landscape of the different approaches to the solute transport problem in the brain microcirculation.

In the upper left corner of the model spectrum in Fig. 5.1, we find the model proposed by Fang et al. [12], which makes minimal modeling assumptions, thus, provides the highest fidelity to the miscrovascular geometry and transport processes. While this model yields the most accurate results, it is also expected to be the most time-consuming due to its complicated meshing procedure and great quantity of unknowns. Consequently, it serves as the reference solution for validation in this thesis used in Chapter 3 and 4. Moving towards models with lower accuracy, we encounter the fine-grid models with simplified network geometry [1]. Their accuracy and complexity depend significantly on factors such as mesh type (e.g., non-

1. Simplified network geometry refers to the representation of the network within the parenchyma. Some authors choose to reduce the vascular network to a collection of line sources, thus reducing the complexity of the mesh of the parenhcyma

structured, cartesian) and size. For instance, Possenti et al. [24] uses a fine mesh for volumes containing under one hundred vessels. On the opposite end spectrum, we find Linninger et al. [20], who perform coarse grid simulations without meticulous consideration of perivascular concentration gradients. This approach is estimated to introduce larger errors, approximately around 10%, as discussed in Chapter 3 where it was used as comparison. Slightly more efficient models include the voxelized method by [31; 39] and semi-analytical models [17–19; 32]. The former can provide high accuracy provided extremely refined meshes, even capturing fine details such as the epithelial wall around vessels. The latter, as discussed extensively in this thesis, performs accurately and efficiently for linear problems. However, their scalability is limited due to their non-local nature, the time-consuming computations required for boundary conditions, and challenges in incorporating non-linear phenomena within the parenchyma

The models discussed above employ diverse strategies to address the complex task of evaluating vessel wall concentration in the parenchyma, utilizing either fully numerical [12; 24] or analytical [19] approaches. However, several approaches combine these two different strategies to handle rapid near-source gradients analytically and the slower background field numerically. Such strategies are denoted as ”analytical coupling models and extensions” in Fig. 5.1, which have evolved considerably over the past 45 years. Although there are clear distinctions between subsurface reservoirs and brain microcirculation, some core principles can be adapted to propose new strategies. For instance, Koch et al. [40] uses an analytical kernel to spread the slender mass source generated by vessels, thereby regularizing the concentration field and reducing the reliance on highly refined irregular meshes. However, due to the approximate nature of the kernel and framework characteristics, this model still necessitates a fine mesh of comparable size to capillaries' diameters, limiting its computational efficiency while maintaining relatively high accuracy.

Alternatively, an operator splitting approach is demonstrated in Gjerde et al. [22; 41], which achieves a similar reduction in system size as our multiscale model. Key distinctions include the computation of the self-influence coefficient, the localization scheme, and the incorporation of metabolic consumption. It is worth noting that their vessel geometry simplification introduces potential errors of approximately 10%, similar to the error introduced by neglecting perivascular concentration gradients entirely (see Fig. 4.5). Moreover, their localization technique relies on a smoothing function that converges to zero at a distance far from the source, necessitating the calculation of a source term in every element within the source's vicinity. This approach leads to substantial assembly time within the microcirculation. Additionally, the model lacks an inclusion of metabolic consumption terms in its formulation. For those reasons, we expect it to provide lower accuracy than our multiscale model while offering also lower computational efficiency.

Lastly, we include the dual continuum models [21] that provide an upscaled description of the transport equations. This results in a two equation model that can be solved in a coarse grid of similar size as the one used for the slow term in the multiscale model. However, as previously mentioned, the upscaling required for the two equation model necessitates the existence of a representative elementary volume (REV) of the microvasculature, which generally, cannot be found. We discuss this further in Section 5.2.2 where we suggest a hybrid approach (in blue in Fig. 5.1), that will combine the multiscale model for regions where an REV cannot be found, with an upscaled model for the more homogeneous and quasi-periodic regions of the microvasculature, in the same spirit as [37].

5.2 Perspectives

This thesis focused on the intricate spatial constraints imposed by the brain's angioarchitecture. Our primary objective was to establish a versatile framework capable of facilitating large-scale, efficient simulations. The development of our multiscale model holds promise for diverse applications, ranging from investigating the progression of hypoxia in diseased brain tissue to analyzing experimental data concerning tissue oxygenation. However, it's important to acknowledge that the model's development involved certain assumptions that may not be necessarily accurate at a physiological level. In this Section, we first suggest some modifications to include in the multiscale model framework to render it more realistic (Section 5.2.1). Then, we suggest two extensions to the multiscale model (Section 5.2.2).

5.2.1 Extensions to the multiscale model

In this Section, we explore two fundamental assumptions of the multiscale model and propose a logical evolution to better capture the intricacies of molecular exchanges within physiological processes. Throughout this thesis, we have primarily operated under the assumption of steady-state conditions. The primary obstacle stemmed from the complex spatial arrangements, which posed challenges for applying numerical methods to solve large networks. Consequently, we simplified the problem by neglecting temporal dynamics, as they were comparatively simpler contrasted with the spatial complexities. In this Section, we briefly explore the challenges arising when incorporating temporal dynamics and suggest potential strategies to address these challenges.

Another fundamental assumption is that blood is treated as a continuous medium in which oxygen is dissolved. However, as discussed in Section 2.2, blood is primarily consists of red blood cells (RBCs) and plasma. In Section 5.2.1, we discuss some existing modeling strategies to include the interplay between the oxygen molecules and the hemoglobin protein inside RBCs. Finally, Section 5.2.1 focuses on other molecules that cannot freely diffuse within the parenchyma, and we discuss the incorporation of non-isotropic diffusion within the multiscale model.

Temporal variations

In Chapters 3 and 4, we have mainly focused on studying the transport problem in steady-state configurations. However, it's important to consider time-related variations, especially in the context of functional imaging, e.g., BOLD fMRI. This becomes particularly significant when examining neurovascular or neurometabolic coupling, as different time scales come into play. To address these temporal aspects, we suggest continuing to utilize the conventional unsteady FV approach, a well-established method in computational fluid dynamics for handling steady and unsteady problems [42; 43]. However, when it comes to the rapid term (i.e., sources' potentials), some adjustments are necessary. This is because the fundamental solution (i.e., the Green's function) employed in our multiscale model solves the steady-state Poisson's equation. To accommodate temporal variations, we need to update the source potentials by incorporating the unsteady fundamental solution.

The unsteady Green's function $G_u(\mathbf{x} - \mathbf{x}^*, t - t^*)$ represents the concentration at a point $\mathbf{x}$ and time t resulting from an instantaneous point source at point $\mathbf{x}^*$ and time t^*, or the solution to

$$\frac{\partial G_u}{\partial t} - D\nabla^2 G_u = \delta(\mathbf{x} - \mathbf{x}^*)\delta(t - t^*) \tag{5.1}$$

where δ denotes the dirac delta function. The fundamental solution reads

$$G_u(\mathbf{x}-\mathbf{x}^*, t-t^*) = (4\pi D(t-t^*))^{-3/2}\exp\left[\frac{-||\mathbf{x}-\mathbf{x}^*||^2}{4D(t-t^*)}\right] \tag{5.2}$$

The rapid term can now be computed in the same way as in Chapters 3 and 4. We recall that the rapid term is composed of the individual source potentials (P_j) that are computed through integration of the fundamental solution along the wall of the open cylinder ($\partial\Omega_{\beta,j}$)

$$P_j(\mathbf{x}) = -\int_0^t \iint_{\partial\Omega_{\beta,j}} (G_u(\mathbf{x}-\mathbf{x}^*, t-t^*)\boldsymbol{\nabla}\phi(\mathbf{x}^*)\cdot\mathbf{n})\, d\mathbf{x}^* dt^* \tag{5.3}$$

The source potentials can be integrated into the numerical framework in the same manner as described in Chapters 3 and 4. Utilizing a time-stepping approach is suitable for these computations. The localization of the source potentials, as introduced in Chapter 3, eliminates the need to store numerous time steps (as required by the first integral in equation 5.3). However, a new challenge arises in calculating the influence coefficients, as equation 5.2 significantly differs from the fundamental solution for the Poisson equation (equation A.27). Nevertheless, the localization framework, based on the underlying FV scheme, remains unchanged. Therefore, to incorporate temporal variations, the primary challenge involve computing the source potentials using the unsteady fundamental solution and implementing a time-stepping procedure.

Vessel - tissue oxygen exchange

The multiscale approach considered in this thesis focuses on bridging the gap between the capillary scale and spatial scale of larger microvascular networks. Nevertheless, there are phenomena at the cellular level that we considered in an upscaled manner. For instance, diffusion in the parenchyma represents the upscaled description of the random walk of molecules, which is the topic of next Section. Another important phenomenon at the cellular level is the binding of oxygen with the hemoglobin contained inside the RBCs. As mentioned in Section 2.2, oxygen is available in the blood as dissolved oxygen (C_{plasma}) and hemoglobin-bound oxygen (C_{RBC}), i.e., oxygen actively binds to the hemoglobin molecule inside the RBCs. The total oxygen concentration is the addition of the two :

$$C_v = C_{plasma} + C_{RBC} \tag{5.4}$$

Given the scope of our research, the molecular interactions inside the RBCs were not explicitly considered, and blood was modeled as a continuum. Nevertheless, the hemoglobin-oxygen interactions manifest themselves in a non linear relationship between oxygen saturation within the RBCs and concentration, given by Hill's law :

$$S(C_b) = \frac{C_b^n}{C_b^n + C_{50}^n} \tag{5.5}$$

where C_{50} is the concentration at 50% saturation, n is a constant commonly taken as $n = 0.55$ for oxygen and hemoglobin [19; 20; 24; 44] and S represents the saturation of oxygen in RBCs. Furthermore, the effective solubility of oxygen in blood to relate the partial pressure

to concentration is given by :

$$\alpha_{eff} = (1 - H_D)\alpha_{plasma} + H_D\alpha_{RBC} \tag{5.6}$$

where α_{RBC} and α_{plasma} are the solubility of oxygen in RBCs and in plasma respectively, and H_D is the discharge hematocrit.

The incorporation of this phenomenon introduces a non-linear relationship (as shown in equation 5.5) that must be integrated into the model. This non-linear behavior specifically impacts the equation related to vessel-tissue exchanges, found in the second line of equation 4.71, where Hill's equation plays a crucial role in accurately estimating intravascular oxygen concentrations. While the overall problem assembly remains largely unchanged, its resolution will now need an iterative process tailored to addressing this new non-linearity. Especially, when combined with the non-linear estimation of metabolic consumption. Testing is essential to determine whether a strongly coupled resolution within a single matrix (as demonstrated in Chapters 3 and 4) is the optimal approach or if an iterative procedure, where intravascular and extravascular problems are addressed separately, would be more suitable.

Non-isotropic diffusion

We have assumed through the development of the model the diffusivity of the solute to be isotropic within the parenchyma. This may hold true for small molecules such as oxygen or carbon dioxide, but not for other larger molecules (e.g., glucose, proteins) or charged ions (e.g., Na^+, Ca^{2+}). The molecules that penetrate the BBB but cannot cross the lipid bilayer that encloses the cells diffuse through the extra-cellular space (ECS). Hindered diffusion through tortuous channels arises often in porous media. Commonly, the pore equations (in this case the diffusion within the micropores created by the extracellular space (ECS)) are upscaled and an effective diffusion tensor is obtained

$$\mathbf{D}^{eff} = \begin{bmatrix} D_{xx} & D_{xy} & D_{xz} \\ D_{yx} & D_{yy} & D_{yz} \\ D_{zx} & D_{zy} & D_{zz} \end{bmatrix} \tag{5.7}$$

which permits the modeling of diffusion at the scale of large porous regions (as we have done with the multiscale model) while accounting for the microscale tortuosity. Complexifying the diffusion properties of the parenchyma does not interfere with the structure of the code. The final assembly of the problem, i.e., equation 4.71, does not have to include substantial changes besides the computation of $\mathbf{A}$ and $\mathbf{B}$ that needs to accommodate the anisotropy of the diffusion tensor. Moreover, FV schemes already exists that include anisotropy [42].

Furthermore, if the effective diffusion tensor is spatially homogeneous, we propose following the approach outlined in Chapter 2, where the development for obtaining the boundary value problem (BVP) for the slow term remains unaltered. However, when dealing with the FV discretization of the problem, it's crucial to consider the anisotropic diffusivity, as is commonly done in existing FV schemes as noted in [42]. When we account for the tortuous geometry of the extracellular matrix, it is unlikely that the diffusivity tensor remains spatially homogeneous. In such cases, the fundamental solution may not exist. Therefore, we propose adopting a similar approach to that suggested in [34], where the potentials (i.e., the fundamental solution) are computed using an average diffusivity value for the surrounding tissue.

Consequently, the slow term will need to compensate for the approximation made by using this average diffusivity, leading to modifications in the computation of **A** and **B** in equation 4.71. If the heterogeneity of diffusivity is significant, the compensation required by the slow term may be substantial, resulting in a more rapidly varying slow field. To maintain accuracy in such cases, a finer mesh may be necessary.

5.2.2 Future directions

The multiscale model achieves remarkable computational efficiency when solving the solute transport problem in the microcirculation. We managed to solve the primary spatial constraints through a localized scheme that provides a sparse matrix associated to the coupled linear problem. Nevertheless, we recall that the coarse mesh used in our simulations remains of an approximate size $50 \times 50 \times 50\,\mu\text{m}^3$. That would require billions of unknowns for entirely meshing the whole brain. Considering the 1D mesh used for the intravascular transport problem is commonly larger than the 3D mesh due to the high density of sources, whole brain simulations remain inaccessible, especially if human configurations are to be achieved. In this Section, we first suggest a line of research that builds upon the multiscale model and has the potential to provide an approach that renders full brain solute transport simulations feasible (Section 5.2.2). We then suggest a physics based estimation of metabolic consumption from experimental oxygen concentration data (Section 5.2.2). And finally, we discuss the implementation of our multiscale model within an high performance computing (HPC) framework (Section 5.2.2)

Coupling with upscaled equations for the capillary bed

A common strategy in multiscale problems is to treat the system as a continuous medium whose effective properties can be calculated. The procedure to obtain the effective properties of the medium is called upscaling and it is meant to obtain a set of macroscopic equations in which the effect at smaller scales are represented. This method requires partial differential equations to be solved on a REV of the microscopic scale. The computation of an REV requires the satisfaction of certain regularity conditions such as homogeneity and quasi-periodicity, which are satisfied in the capillary bed [21; 37; 45].

Upscaling techniques are highly efficient strategies that involve representing the medium, e.g., the capillary bed [37], as a continuum. This approach is frequently employed for various solutes within the parenchyma, akin to the upscaling of the tortuous paths in the extracellular space (ECS) within the parenchyma as discussed in Section 5.2.1. They are also often used to upscale the flow equations in a porous medium where Darcy's law is applied instead of solving the detailed Stokes equations within the microstructure [37; 46; 47].

In contrast, the arterio-venular trees that feed and drain the capillary bed exhibit continuous variations of scale that severely challenge the computation of an REV. Due to this limitation, one approach to simulating large microvascular volumes involves upscaling the transport equations within the capillary bed while maintaining an explicit description of the arterio-venular trees using the current multiscale model. A similar strategy was employed for flow equations in [37], where the network model introduced in Chapter 2 was used to simulate blood flow in the arterio-venular trees, while an upscaled description of flow through Darcy's law was applied to simulate flow in the capillary bed.

The extension of the solute transport equations is considerably more challenging than the

blood flow equations. In a healthy brain, blood remains within the vessels, which requires a one equation description of flow. When modeling transport however, as elucidated throughout this thesis, we have two media, blood and parenchyma, coupled together. Therefore, local upscaling of the transport equations in the capillary bed and surrounding parenchyma results in a non-equilibrium two equation upscaled description as discussed in [48]. The general form of the continuous equations are [49] :

$$\begin{aligned}\varepsilon_\beta \partial_t \langle C_v\rangle^\beta + (\varepsilon_\beta \langle \mathbf{u}\rangle^\beta - \mathbf{u}_{\beta\beta}) \cdot \nabla \langle C_v\rangle^\beta - \mathbf{u}_{\beta\sigma} \cdot \boldsymbol{\nabla}\langle\phi\rangle^\sigma \\ = \boldsymbol{\nabla} \cdot (D_{\beta\beta} \cdot \langle C_v\rangle^\beta) + \boldsymbol{\nabla} \cdot (D_{\beta\sigma} \cdot \langle\phi\rangle^\sigma) + \tau_m(\langle\phi\rangle^\sigma - \langle C_v\rangle^\beta) + \varepsilon_\beta S_\beta \end{aligned} \tag{5.8a}$$

$$\begin{aligned}\varepsilon_\sigma \partial_t \langle\phi\rangle^\sigma - \mathbf{u}_{\sigma\sigma} \cdot \boldsymbol{\nabla}\langle\phi\rangle^\sigma - \mathbf{u}_{\sigma\beta} \cdot \boldsymbol{\nabla}\langle C_v\rangle^\beta \\ = \boldsymbol{\nabla} \cdot (D_{\sigma\sigma} \cdot \langle\phi\rangle^\sigma) + \boldsymbol{\nabla} \cdot (D_{\sigma\beta} \cdot \langle C_v\rangle^\beta) - \tau_m(\langle\phi\rangle^\sigma - \langle C_v\rangle^\beta) + \varepsilon_\sigma S_\sigma \end{aligned} \tag{5.8b}$$

where σ and β represent the parenchyma and blood respectively, $\langle\cdot\rangle$ represents the averaging operator within the REV [2], D_{ij} represent effective diffusion tensors, τ_m represents an exchange coefficient that is strongly dependent on the vessel wall permeability, ε represents the porosity of each media, S represent sources or sinks of mass and $\mathbf{u}_{ij}$ are effective velocity vectors.

Once we have obtained an upscaled description of the transport equations within the capillary bed, we face the challenge of coupling the explicit model of the arterio-venular trees with this upscaled description. In the work by Peyrounette et al. [37], the transition between the semi-fractal arteriolar and venular trees with the space-filling capillary bed is represented a small volumic source of flow in the upscaled flow equations for the capillary bed.

In a similar manner, we suggest to treat this transition points between the arteriolar or venular trees and the capillary bed as coupling points. These coupling points represent sources or sinks of mass in the upscaled equation for the blood compartment (denoted by the term S_β in equation 5.8a). We suggest adopting a strategy similar to that in Peyrounette et al. [37] to bridge the scale gap between the 1D intravascular transport to the 3D upscaled description provided by equation 5.8.

Additionally, there is the added challenge of coupling the upscaled description of transport in the parenchyma (equation 5.8b) with the explicit description of transport in the arterio-venular trees. To address this, an operator splitting similar to the one introduced in this thesis can be implemented to avoid the need for fine meshing in the numerical solution of equation 5.8b around the relevant vessels.

In summary, the operator splitting framework introduced in this thesis serves as the foundation for the extension to an upscaled description of mass transport within the capillary bed. The Green's function approach helps quantify the microscale dynamics, such as source terms arising from the explicit description of the arterio-venular trees or large perivascular gradients arising in the upscale description of tissue transport (equation 5.8b). On the other hand, the numerical resolution slow term aids in the determining boundary conditions, localizing the sources's potentials, quantifying volume reaction (i.e., metabolism) and assessing volume exchange terms (i.e., exchange terms $\tau_m(\langle\phi\rangle^\sigma - \langle C_v\rangle^\beta)$ in equations 5.8).

2. different from the cross-sectional average operator used throughout this thesis for the blood concentration

Inverse problem

In Chapter 3, we developed the foundation of the multiscale problem by coupling the Green's function approach with a FV model for the parenchyma. The main goal of this coupling is to decrease the complexity of the 3D mesh by permitting the use of a cartesian, non-conforming mesh. A secondary advantage of this model is the localization of the potentials thanks to the flux formulation of the FV discretization. This particular resolution provides a concentration field in a cartesian grid that shows uncanny resemblance to the experimental measurements of oxygen concentration around arterioles, which prompted the application of the multiscale model for synthetic data generation to analyze the experimental data. In short, the specific knowledge of the concentration gradients arising around the penetrating arteriole, combined with the coarse grid cartesian mesh provides an ideal research tool for the evaluation of experimental data of cortical oxygenation.

It is common to find one- or two- parameter models used to fit a curve to the data obtained with two-photon microscopy [14; 15; 50]. The fitting consists in an optimization procedure of the parameters of a function resembling the perivascular concentration gradients around an arteriole. Then, the fitted parameters are used to deduce the metabolic consumption within the parenchyma. The fitting of a one variable (distance from the arteriole) function to a 2D grid of concentration data obtained from a 3D vascular network necessitates strong modeling assumptions that may not represent the actual transport dynamics. Thus, we suggest to leverage the formulation of the multiscale model, which pays careful attention to the perivascular gradients and to the metabolic consumption.

We suggest to extend the 2D model developed in Chapter 3 to generate an inverse model that takes the coarse grid concentration field as input and outputs the constant of the Michaelis-Menten consumption term. Evidently, since there are more equations than grid cells, we need to make some modeling assumptions, notably related to the capillary bed and the boundary conditions. Nevertheless, this strategy promises to predict a more physiological metabolic consumption that allows a more sophisticated consideration of the capillary bed and the reaction field.

Parallel implementation of the multiscale model

Throughout the development of the multiscale model, our primary objective has been to provide a highly efficient numerical scheme suitable for large microvascular networks. This is exemplified by the implementation of a novel and efficient localization scheme for the sources' potentials, the analytical computation of these potentials, and many other careful considerations that result in a highly sparse and local matrix system (equation 4.71).

One notable achievement is the localization scheme, which provides a framework that enables control over the expansion of source-to-source and source-to-grid interactions. This attribute makes the multiscale model well-suited for HPC through parallelization, potentially increasing the scope of solute transport simulations by an order of magnitude.

The problem assembly, currently the most time-consuming task, is readily parallelizable due to the independence of each equation from the rest. Additionally, the resolution of the linear system, expected to consume more time as the size increases, can potentially benefit from the separation of Intravascular (IV) and Extravascular (EV) systems within the matrix formulation. To this end, we propose utilizing an iterative technique, such as Picard's method [51], to further enhance the performance of conventional linear solvers.

5.3 References

[1] Xiulian Sun, Guiqiong He, Hong Qing, Weihui Zhou, Frederick Dobie, Fang Cai, Matthias Staufenbiel, L. Eric Huang, and Weihong Song. Hypoxia facilitates Alzheimer's disease pathogenesis by up-regulating *BACE1* gene expression. *Proceedings of the National Academy of Sciences*, 103(49) :18727–18732, December 2006. 137

[2] Roderick A. Corriveau, Francesca Bosetti, Marian Emr, Jordan T. Gladman, James I. Koenig, Claudia S. Moy, Katherine Pahigiannis, Salina P. Waddy, and Walter Koroshetz. The Science of Vascular Contributions to Cognitive Impairment and Dementia (VCID) : A Framework for Advancing Research Priorities in the Cerebrovascular Biology of Cognitive Decline. *Cellular and Molecular Neurobiology*, 36(2) :281–288, March 2016.

[3] Brina Snyder, Brent Shell, J. Thomas Cunningham, and Rebecca L. Cunningham. Chronic intermittent hypoxia induces oxidative stress and inflammation in brain regions associated with early-stage neurodegeneration. *Physiological reports*, 5(9), May 2017. Place : United States.

[4] Costantino Iadecola. The Neurovascular Unit Coming of Age : A Journey through Neurovascular Coupling in Health and Disease. *Neuron*, 96(1) :17–42, 2017. 137

[5] Patrick J. Drew. Neurovascular coupling : motive unknown. *Trends in Neurosciences*, 45(11) :809–819, 2022. 137

[6] Florian Goirand, Tanguy Le Borgne, and Sylvie Lorthois. Network-driven anomalous transport is a fundamental component of brain microvascular dysfunction. *Nature Communications*, 12(1) :7295, December 2021. 137

[7] August Krogh. The number and distribution of capillaries in muscles with calculations of the oxygen pressure head necessary for supplying the tissue. *The Journal of Physiology*, page 7, 1919. 137

[8] Daniel Goldman. Theoretical Models of Microvascular Oxygen Transport to Tissue. *Microcirculation*, 15(8) :795–811, January 2008. 137

[9] Richard B. Buxton, Eric C. Wong, and Lawrence R. Frank. Dynamics of blood flow and oxygenation changes during brain activation : The balloon model. *Magnetic Resonance in Medicine*, 39(6) :855–864, June 1998. 137

[10] Richard B. Buxton. Interpreting oxygenation-based neuroimaging signals : the importance and the challenge of understanding brain oxygen metabolism. *Frontiers in Neuroenergetics*, 2010.

[11] Nikos K. Logothetis and Brian A. Wandell. Interpreting the BOLD Signal. *Annual Review of Physiology*, 66(1) :735–769, March 2004. 137

[12] Qianqian Fang, Sava Sakadžić, Lana Ruvinskaya, Anna Devor, Anders M. Dale, and David A. Boas. Oxygen advection and diffusion in a three-dimensional vascular anatomical network. *Optics Express*, 16(22) :17530, October 2008. 137, 138, 140, 141

[13] Sava Sakadžić, Emiri T. Mandeville, Louis Gagnon, Joseph J. Musacchia, Mohammad A. Yaseen, Meryem A. Yucel, Joel Lefebvre, Frédéric Lesage, Anders M. Dale, Katharina Eikermann-Haerter, Cenk Ayata, Vivek J. Srinivasan, Eng H. Lo, Anna Devor, and

David A. Boas. Large arteriolar component of oxygen delivery implies a safe margin of oxygen supply to cerebral tissue. *Nature Communications*, 5(1) :5734, December 2014.

[14] K. Shaw, L. Bell, K. Boyd, D. M. Grijseels, D. Clarke, O. Bonnar, H. S. Crombag, and C. N. Hall. Neurovascular coupling and oxygenation are decreased in hippocampus compared to neocortex because of microvascular differences. *Nature Communications*, 12(1) :3190, May 2021. 147

[15] Philipp Mächler, Natalie Fomin-Thunemann, Martin Thunemann, Marte Julie Sætra, Michèle Desjardins, Kıvılcım Kılıç, Layth N. Amra, Emily A. Martin, Ichun Anderson Chen, Ikbal Şencan Eğilmez, Baoqiang Li, Payam Saisan, John X. Jiang, Qun Cheng, Kimberly L. Weldy, David A. Boas, Richard B. Buxton, Gaute T. Einevoll, Anders M. Dale, Sava Sakadžić, and Anna Devor. Baseline oxygen consumption decreases with cortical depth. *PLOS Biology*, 20(10) :e3001440, October 2022. 137, 147

[16] Berislav V. Zlokovic. Neurovascular mechanisms of Alzheimer's neurodegeneration. *Trends in Neurosciences*, 28(4) :202–208, 2005. 137

[17] Richard Hsu and Timothy W. Secomb. A Green's function method for analysis of oxygen delivery to tissue by microvascular networks. *Mathematical Biosciences*, 96(1) :61–78, September 1989. 137, 139, 140, 141

[18] C. Pozrikidis and D. A. Farrow. A Model of Fluid Flow in Solid Tumors. *Annals of Biomedical Engineering*, 31(2) :181–194, February 2003. 139

[19] Timothy W. Secomb, Richard Hsu, Eric Y. H. Park, and Mark W. Dewhirst. Green's Function Methods for Analysis of Oxygen Delivery to Tissue by Microvascular Networks. *Annals of Biomedical Engineering*, 32(11) :1519–1529, November 2004. 137, 139, 140, 141, 143

[20] A. A. Linninger, I. G. Gould, T. Marinnan, C.-Y. Hsu, M. Chojecki, and A. Alaraj. Cerebral Microcirculation and Oxygen Tension in the Human Secondary Cortex. *Annals of Biomedical Engineering*, 41(11) :2264–2284, November 2013. 140, 141, 143

[21] Wahbi K. El-Bouri and Stephen J. Payne. Multi-scale homogenization of blood flow in 3-dimensional human cerebral microvascular networks. *Journal of Theoretical Biology*, 380 :40–47, September 2015. 137, 141, 145

[22] Ingeborg G. Gjerde, Kundan Kumar, and Jan M. Nordbotten. A Singularity Removal Method for Coupled 1D-3D Flow Models. Technical Report arXiv :1812.03055, arXiv, August 2019. arXiv :1812.03055 [cs, math] type : article. 137, 140, 141

[23] Timo Koch, Martin Schneider, Rainer Helmig, and Patrick Jenny. Modeling tissue perfusion in terms of 1d-3d embedded mixed-dimension coupled problems with distributed sources. *Journal of Computational Physics*, 410 :109370, June 2020.

[24] Luca Possenti, Alessandro Cicchetti, Riccardo Rosati, Daniele Cerroni, Maria Laura Costantino, Tiziana Rancati, and Paolo Zunino. A Mesoscale Computational Model for Microvascular Oxygen Transfer. *Annals of Biomedical Engineering*, 49(12) :3356–3373, December 2021. 137, 140, 141, 143

[25] P. Jenny, S. H. Lee, and H. A. Tchelepi. Adaptive Multiscale Finite-Volume Method for Multiphase Flow and Transport in Porous Media. *Multiscale Modeling & Simulation*, 3(1) :50–64, January 2005. 139

[26] Christian Wolfsteiner, Seong H. Lee, and Hamdi A. Tchelepi. Well Modeling in the Multiscale Finite Volume Method for Subsurface Flow Simulation. *Multiscale Modeling & Simulation*, 5(3) :900–917, January 2006. 139, 140

[27] Paul W. Sweeney, Angela d'Esposito, Simon Walker-Samuel, and Rebecca J. Shipley. Modelling the transport of fluid through heterogeneous, whole tumours in silico. *PLOS Computational Biology*, 15(6) :e1006751, June 2019. 139

[28] Yidan Xue, Theodosia Georgakopoulou, Anne-Eva van der Wijk, Tamás I. Józsa, Ed van Bavel, and Stephen J. Payne. Quantification of hypoxic regions distant from occlusions in cerebral penetrating arteriole trees. *PLOS Computational Biology*, 18(8) :e1010166, August 2022.

[29] Chang Sub Park and Stephen J. Payne. Modelling the effects of cerebral microvasculature morphology on oxygen transport. *Medical Engineering & Physics*, 38(1) :41–47, January 2016. 139

[30] C. D'Angelo and A. Quarteroni. On the coupling of 1D and 3D diffusion-reaction equations. Applications to tissue perfusion problems. *Mathematical Models and Methods in Applied Sciences*, 18(08) :1481–1504, August 2008. 140

[31] Grant Hartung, Shoale Badr, Mohammad Moeini, Frédéric Lesage, David Kleinfeld, Ali Alaraj, and Andreas Linninger. Voxelized simulation of cerebral oxygen perfusion elucidates hypoxia in aged mouse cortex. *PLOS Computational Biology*, 17(1) :e1008584, January 2021. 141

[32] Timothy W Secomb. Blood Flow in the Microcirculation. page 21, 2016. 141

[33] D W Peaceman. Interpretation of Well-Block Pressures in Numerical Reservoir Simulation. *Society of Petroleum Engineers*, page 17, 1978.

[34] Donald W Peaceman. Interpretation of Well-Block Pressures in Numerical Reservoir Simulation with Nonsquare Grid Blocks and Anisotropic Permeability. *Society of Petroleum Engineers Journal*, 23(03) :531–543, 1983. Publisher : Society of Petroleum Engineers. 144

[35] D.W. Peaceman. Interpretation of Wellblock Pressures in Numerical Reservoir Simulation : Part 3 – Off-Center and Multiple Wells Within a Wellblock. *SPE Reservoir Engineering*, 5(02) :227–232, May 1990.

[36] D.W. Peaceman. A New Method for Representing Multiple Wells With Arbitrary Rates in Numerical Reservoir Simulation. *SPE Reservoir Engineering*, 10(04) :253–258, November 1995.

[37] Myriam Peyrounette, Yohan Davit, Michel Quintard, and Sylvie Lorthois. Multiscale modelling of blood flow in cerebral microcirculation : Details at capillary scale control accuracy at the level of the cortex. *PLOS ONE*, 13(1) :e0189474, January 2018. 141, 145, 146

[38] D. Y. Ding. Near-Well Upscaling for Reservoir Simulations. *Oil & Gas Science and Technology*, 59(2) :157–165, March 2004. 140

[39] Thomas Ventimiglia and Andreas A Linninger. MESH-FREE HIGH-RESOLUTION SIMULATION OF CEREBROCORTICAL OXYGEN SUPPLY WITH FAST FOURIER PRECONDITIONING. preprint, Bioengineering, January 2023. 141

[40] Timo Koch, Rainer Helmig, and Martin Schneider. A new and consistent well model for one-phase flow in anisotropic porous media using a distributed source model. *Journal of Computational Physics*, 410 :109369, June 2020. 141

[41] Ingeborg G. Gjerde, Kundan Kumar, Jan M. Nordbotten, and Barbara Wohlmuth. Splitting method for elliptic equations with line sources. *ESAIM : Mathematical Modelling and Numerical Analysis*, 53(5) :1715–1739, September 2019. 141

[42] H. K. Versteeg and W. Malalasekera. *An introduction to computational fluid dynamics : the finite volume method*. Pearson Education Ltd, Harlow, England ; New York, 2nd ed edition, 2007. OCLC : ocm76821177. 142, 144

[43] Robert Eymard, Thierry Gallouet, and Raphaele Herbin. January 2019. This manuscript is an update of the preprint n0 97-19 du LATP, UMR 6632, Marseille, September 1997 which appeared in Handbook of Numerical Analysis, P.G. Ciarlet, J.L. Lions eds, vol 7, pp 713-1020. 2019. 142

[44] A R Pries, T W Secomb, P Gaehtgens, and J F Gross. Blood flow in microvascular networks. Experiments and simulation. *Circulation Research*, 67(4) :826–834, October 1990. 143

[45] Rebecca J Shipley, Amy F Smith, Paul W Sweeney, Axel R Pries, and Timothy W Secomb. A hybrid discrete–continuum approach for modelling microcirculatory blood flow. *Mathematical Medicine and Biology : A Journal of the IMA*, March 2019. 145

[46] Christophe C. Frippiat and Alain E. Holeyman. A comparative review of upscaling methods for solute transport in heterogeneous porous media. *Journal of Hydrology*, 362(1-2) :150–176, November 2008. 145

[47] Stephen Whitaker. Flow in porous media I : A theoretical derivation of Darcy's law. *Transport in Porous Media*, 1(1) :3–25, 1986. 145

[48] Sylvie Lorthois, Paul Duru, Ian Billanou, Michel Quintard, and Pierre Celsis. Kinetic modeling in the context of cerebral blood flow quantification by H215O positron emission tomography : The meaning of the permeability coefficient in Renkin–Crones model revisited at capillary scale. *Journal of Theoretical Biology*, 353 :157–169, July 2014. 146

[49] Azita Ahmadi, Michel Quintard, and Stephen Whitaker. Transport in chemically and mechanically heterogeneous porous media V. Two-equation model for solute transport with adsorption. page 28, 1998. 146

[50] Sava Sakadžic, Mohammad A. Yaseen, Rajeshwer Jaswal, Emmanuel Roussakis, Anders M. Dale, Richard B. Buxton, Sergei A. Vinogradov, David A. Boas, and Anna Devor. Two-photon microscopy measurement of cerebral metabolic rate of oxygen using periarteriolar oxygen concentration gradients. *Neurophotonics*, 3(4) :045005, October 2016. 147

[51] Terry Feagin. Matrix formulation of the Picard method for parallel computation. 1982. 147

Annexe A

Annexes

A.1 Effective coefficients

In this section we focus on the development of an analytical expression for the effective coefficients of intravascular transport for the limit case of weak couplings, with a flow profile parametrized via a one parameter model.

The explicit expression of U_{eff}, D_{eff} and K_{eff} can be derived for a generic polynomial expression of the velocity profile. The following corresponds to the development in Berg et al. [1] to obtain the analytical expressions. We consider the following polynomial approximation for the velocity profile :

$$U^* = \sum_{i=0}^{i=N} w_i \left(\frac{r}{2\alpha}\right)^i \tag{A.1}$$

with w_i chosen so that $\langle U^* \rangle = 1$, and α is the aspect ratio of the vessel given by $\alpha = R/L$. The effective velocity varies linearly with the Péclet as dictated by the following expression [1] :

$$U_{eff} = Pe(1 + U_+) \tag{A.2}$$

where U_+ represents an apparent overspeed defined by :

$$U_+ = -\frac{42\alpha Da_m}{2\alpha Da_m + 4} \sum_i w_i \frac{i}{(i+2)(i+4)} + \frac{2(2\alpha Da_m)^2}{(2\alpha Da_m + 4)^2} \sum_i w_i \left(\frac{i^2 + 2i + 8}{(i+2)(i+4)(i+6)}\right) \tag{A.3}$$

We proceed similarly for the effective diffusion, the analytical expression is the following :

$$D_{eff} = 1 + \frac{(2\alpha Pe)^2}{Pe_c^2} \tag{A.4}$$

where $2\alpha Pe$ represents the radial Péclet number and Pe_c is a critical Péclet number defined

by :

$$
\begin{aligned}
Pe_c^{-2} = -2\sum_i\sum_j \frac{w_i w_j}{(i+2)(j+2)}\left(\frac{j}{(i+4)(i+j+4)} - \frac{j}{4(j+4)}\right) \\
- \frac{22\alpha Da_m}{2\alpha Da_m + 4}\sum_i\sum_j \frac{w_i w_j}{(i+2)(j+2)(j+4)}\left(\frac{2(j+2)}{i+j+6} - \right. \\
\left. \frac{j+4}{i+j+4} - \frac{2j}{i+4} + \frac{(j+2)^2}{2(j+6)}\right) \\
+ \frac{2(2\alpha Da_m)^2}{(2\alpha Da_m+4)^2}\sum_i\sum_j \frac{w_i w_j (j^2+2j+8)i}{4(i+2)(i+4)(j+2)(j+4)(j+6)}
\end{aligned}
$$

Finally, the effective reaction rate is :

$$K_{eff} = \frac{16\alpha^{-1} Da_m}{\epsilon Da_m + 4} \tag{A.5}$$

which does not depend on the velocity profile and monotonically increases with the membrane Damköhler number.

A.2 Integration for the line approximation

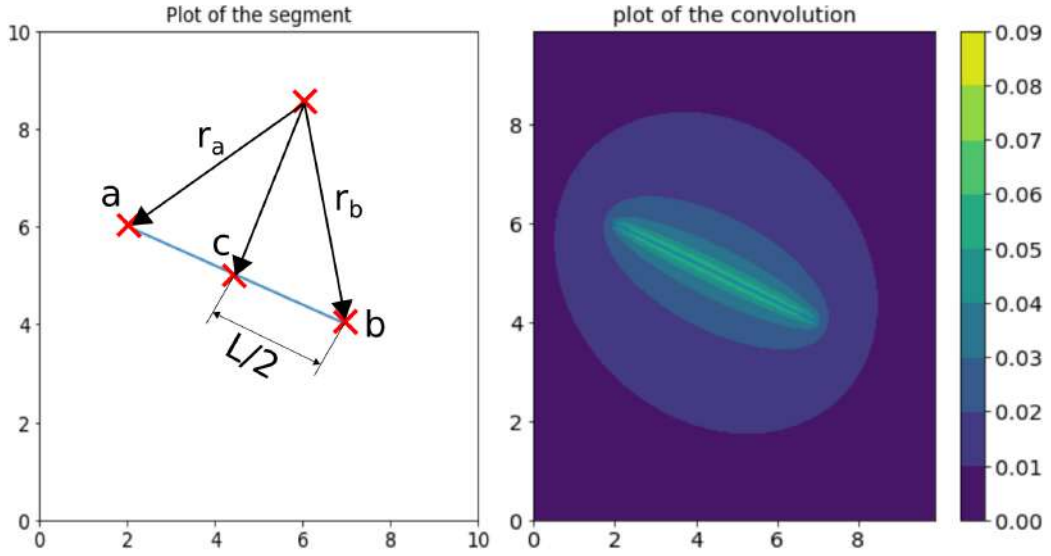

FIGURE A.1 – Plot of the segment over which the Green's function is integrated with the terminology used on the left. On the right, the contour plot of the final integration. The plot is artificially modified to remove the singularities on the points shown in equation A.23

On equation 1 we have the parametrization of the segment given by $\mathbf{y}$

$$\mathbf{y} = \mathbf{c} + \boldsymbol{\tau} s \tag{A.6}$$

where $\mathbf{a}$ is the initial point of the segment, and $\boldsymbol{\tau}$ represents the unitary vector parallel to the segment ($\boldsymbol{\tau} = \frac{\mathbf{b}-\mathbf{a}}{||\mathbf{b}-\mathbf{a}||}$)

The vessel coordinate is given by s :

$$s \in [-L/2, L/2] \tag{A.7}$$

The distance from any random point in space $\mathbf{x}$ to another point on the segment is given by the variable d :

$$d(s) = ||\mathbf{x} - \mathbf{y}(s)|| \tag{A.8}$$

Manipulating the description of the distance so to work with scalar variables :

$$d(s) = ||\mathbf{x} - \mathbf{c} - \boldsymbol{\tau} s||$$

$$d(s) = \sqrt{||\mathbf{r_c}||^2 - 2\langle \mathbf{r_c}, \boldsymbol{\tau} \rangle s + s^2}$$

where $||\cdot||$ represents the norm of a vector, and $\langle \cdot, \cdot \rangle$ represents the scalar product between two vectors. For simplicity, let us define the scalar product between $\mathbf{r_c}$ and $\boldsymbol{\tau}$ as h :

$$h = \langle \mathbf{r_c}, \boldsymbol{\tau} \rangle \tag{A.9}$$

Therefore, the integral is written as :

$$I = \int_{-L/2}^{L/2} \frac{1}{4\pi} \frac{1}{d(s)} ds \tag{A.10}$$

$$I = \int_{-L/2}^{L/2} \frac{1}{4\pi} \frac{1}{\sqrt{||\mathbf{r_c}||^2 - 2hs + s^2}} ds \tag{A.11}$$

The following change of variable is implemented to simplify the denominator :

$$t + s = d \tag{A.12}$$

elevating each side to square power yields

$$d^2 = t^2 + 2ts + s^2 \tag{A.13}$$

and substituting into the value of d

$$||\mathbf{r_c}||^2 - 2hs + s^2 = t^2 + 2ts + s^2 \tag{A.14}$$

Equation A.2 is manipulated to make s explicit and subsequently substitute in A.11

$$||\mathbf{r_c}||^2 - t^2 = 2s(t + h) \tag{A.15}$$

$$s = \frac{||\mathbf{r_c}||^2 - t^2}{2(t + h)} \tag{A.16}$$

The same process is done for the differential :

$$\frac{ds}{dt} = \frac{1}{2}\Big(\frac{-2t(t+h) - (||\mathbf{r_a}^2|| - t^2)}{(t+h)^2}\Big) \tag{A.17}$$

$$\frac{ds}{dt} = -\frac{1}{2}\Big(\frac{t^2 + 2th + ||\mathbf{r_a}^2||}{(t+h)^2}\Big) \tag{A.18}$$

Substituting both inside A.11 :

$$I(t) = \frac{1}{4\pi}\int \frac{1}{d(s)}ds = \frac{1}{4\pi}\int \frac{1}{t + \frac{||\mathbf{r_a}||^2 - t^2}{2(t+h)}}\Big(-\frac{1}{2}\frac{t^2 + 2th + ||\mathbf{r_a}||^2}{(t+h)^2}\Big)dt \tag{A.19}$$

$$I = \frac{1}{4\pi}\int -\frac{1}{t+h}dt = -\frac{1}{4\pi}ln(|t+h|) \tag{A.20}$$

Undoing the change of variable

$$I = -\frac{1}{4\pi}ln(|d(s) - s + h|)\Big|_{-L/2}^{L/2} \tag{A.21}$$

Including the limits in the results and substituting A.9, we obtain the final expression for A.11

$$I = -\frac{1}{4\pi}ln\Big(\frac{||\mathbf{r_a}|| + L/2 + \langle \mathbf{r_c}, \boldsymbol{\tau}\rangle}{||\mathbf{r_b}|| - L/2 + \langle \mathbf{r_c}, \boldsymbol{\tau}\rangle}\Big) \tag{A.22}$$

Equation A.2 is not properly defined everywhere, since for the points $\mathbf{z}$ such that :

$$\langle \mathbf{z}, \boldsymbol{\tau}\rangle = ||\mathbf{z}|| \quad \& \quad \langle \mathbf{z}, \boldsymbol{\tau}\rangle < \langle \mathbf{c}, \boldsymbol{\tau}\rangle - L/2 \tag{A.23}$$

since the numerator inside the logarithm of equation A.2 becomes zero for such points.

A.3 Integration of the single and double layer coefficients

The purpose of this section is to evaluate the coefficients appearing in the potential arising from an open cylinder in an accurate manner near the singularity. We recall the expression for the potential of a cylinder i over another cylinder j

$$P_{ij} = \frac{q_i}{2\pi R_i}G_{ij} + \overline{\phi}H_{ij} \tag{A.24}$$

where G_{ij} and H_{ij} represent the average value over the surface of the cylinder j of the single layer and double layer coefficients respectively. We focus on the self-influence coefficients since they pose the difficulty due to the presence of a singularity in both the single layer and the double layer coefficients.

A.3.1 Single layer potential

First, we remind that the single layer potential arising from a single cylinder (equation 4.25) is given by :

$$G_i = \iint_{\partial\Omega_{\beta,i}} G(\mathbf{x}, \mathbf{x}^*) d\mathbf{x} \tag{A.25}$$

which cannot be evaluated analytically. In this Section, the focus lies over the self-influence coefficient due to the larger errors committed when using geometrical approximations. Let us suppose we are evaluating the value of the self-influence single layer coefficient for a cylinder i (G_{ii}), as illustrated in Fig. A.3.1. The strategy is to evaluate the integral over the abscisa coordinate numerically, and the integral over the cross-section analytically.

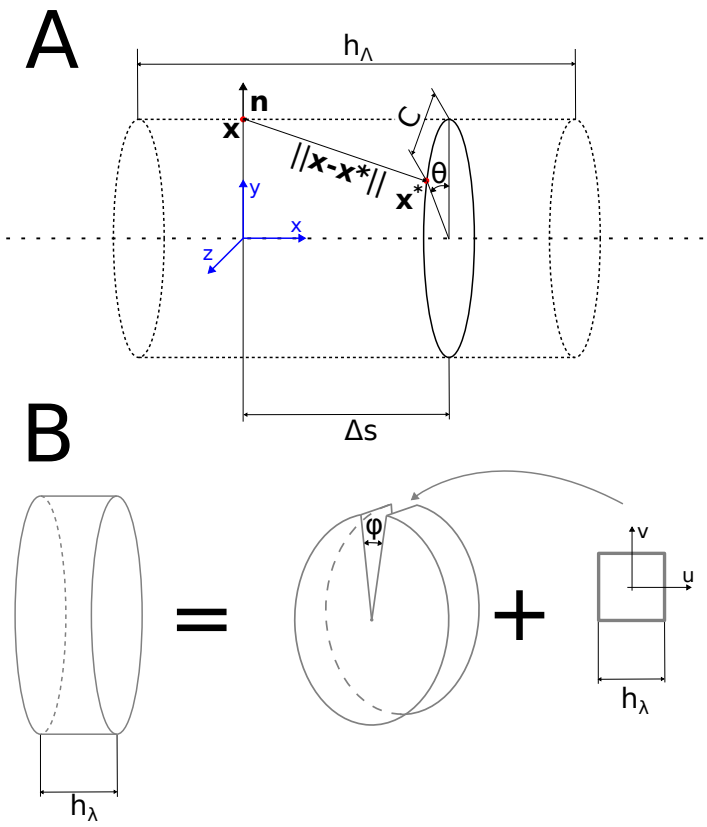

FIGURE A.2 – **Schematics used for the evaluation of the self-influence coefficients**. Panel A : illustration of the cylinder whose self-influence coefficients we are interested in calculating. The two variables of integration $\mathbf{x}$ and $\mathbf{x}^*$ are illustrated. The separation between the two can be given by a cylindrical coordinate system $(\Delta s, \theta)$. Both points $\mathbf{x}$ and $\mathbf{x}^*$ lie on the surface of the cylinder ($\partial\Omega_\beta$). Panel B : schematic of the technique used to evaluate the integrals near the singularity. A small square containing the pole is subtracted from the cross-section (whose width is given by h_λ), in order to evaluate the integral easily. The angle of the subtracted square (φ) can be calculated as a function of the radius R and the width of the cross-section h_λ. The integral over the pole over the flat square can be approximated for both the single and double layer coefficients and the integral over the (non-singular) remaining surface can be evaluated since it constitutes an incomplete elliptic integral.

The integral of the single layer potential over a single (infinitely thin) cross-section constitutes a complete elliptic integral. We denote the integral of the single layer potential of a thin cross-section over a point of the same cylinder ($\mathbf{x}$) as :

$$\widehat{G}(\Delta s) = \int_{\partial\lambda(s)} G(\mathbf{x}, \mathbf{x}^*) d\mathbf{x} \tag{A.26}$$

where G is the fundamental solution repeated here for ease of reading

$$G(\mathbf{x}; \mathbf{x}^*) = \frac{1}{4\pi D||\mathbf{x} - \mathbf{x}^*||} \tag{A.27}$$

Equation A.26 allows to evaluate numerically the full integral using the mid-point rule.

$$G_{ii} = \sum_{\Delta s=-h_\Lambda/2}^{\Delta s=h_\Lambda/2} \widehat{G}(\Delta s) h_\lambda \tag{A.28}$$

where h_λ is a virtual thickness for the numerical integration, and h_Λ is the total width of the cylinder, i.e., discretization size of the intravascular problem. This results in an elliptic integral of the first kind when $\mathbf{x}$ and $\mathbf{x}^*$ lie on the surface of the same cylinder, which is the focus here.

In order to write $\widehat{G}$ as a two variable function, we follow the terminology of Fig. A.3.1 and we write

$$\frac{C^2}{4} + R^2 \left(cos\frac{\theta}{2}\right)^2 = R^2 \tag{A.29}$$

which results in

$$C(\theta) = (4R^2 \left(sin\frac{\theta}{2}\right)^2)^{1/2} \tag{A.30}$$

We can now write the distance between the evaluation point and the pole of the fundamental solution as a function of θ and Δs.

$$||\mathbf{x} - \mathbf{x}^*|| = (\Delta s^2 + 4R^2 sin^2\frac{\theta}{2})^{1/2} \quad \forall \quad \theta \in (0, 2\pi] \tag{A.31}$$

Then, substituting, we obtain the analytical form of $\widehat{G}(\Delta s)$

$$\widehat{G}(\Delta s) = \int_{\partial\lambda(s)} \frac{1}{4\pi||\mathbf{x} - \mathbf{x}^*||} = \frac{R}{4\pi} \int_0^{2\pi} \frac{1}{\left(\Delta s^2 + 4R^2 sin^2\frac{\theta}{2})\right)^{1/2}} d\theta \tag{A.32}$$

which can be simplified to the following elliptic integral [1] :

$$\widehat{G}(\Delta s) = \frac{k}{2\pi} \left(\int_0^{\pi/2} \frac{d\alpha}{(1 - k^2 sin^2\alpha)} \right) \tag{A.33}$$

Then, we substitute into equation A.28 to obtain the expression for the computation of the self-influence coefficient

1. We have used the following trigonometric identity $sin^2\frac{\theta}{2} = 1 - sin^2\left(\frac{\theta + \pi}{2}\right)$

$$G_{ii} = \sum_{\Delta s=-h_\Lambda/2}^{\Delta s=h_\Lambda/2} \left(\frac{k}{2\pi} \left(\int_0^{\pi/2} \frac{d\alpha}{(1-k^2 sin^2\alpha)} \right) \right) \tag{A.34}$$

where $k = \left(\frac{\Delta s^2}{4R^2} + 1 \right)^{-1/2}$, and α represents a change of variable used to write the elliptic integral in standard form $\alpha = \frac{\theta + \pi}{2}$

A.3.2 Double layer potential

For the self-influence for the double layer potential, we proceed similarly as for the single layer potential.

$$H_i = \iint_{\partial\Omega_{\beta,i}} \boldsymbol{\nabla}_n G(\mathbf{x}, \mathbf{x}^*) d\mathbf{x} \tag{A.35}$$

which cannot be evaluated analytically. Let us suppose we are evaluating the value of the self-influence single layer coefficient for a cylinder i (H_{ii}), as illustrated in Fig. A.3.1. Similarly, we use $\widehat{H}$ to evaluate the integral over the cross-section $\partial\lambda$

$$\widehat{H}(\Delta s) = \int_{\partial\lambda(s)} \boldsymbol{\nabla}_n G(\mathbf{x}, \mathbf{x}^*) d\mathbf{x} \tag{A.36}$$

where

$$\boldsymbol{\nabla}_n G(\mathbf{x}, \mathbf{x}^*) d\mathbf{x} = \frac{(\mathbf{x} - \mathbf{x}^*) \cdot \mathbf{n}}{4\pi D ||\mathbf{x} - \mathbf{x}^*||^3} \tag{A.37}$$

In the same manner as with the single layer potential. We split the integral into two : The integral over the cross-section ($\widehat{H}$) that can be evaluated efficiently, and the integral along the cylinder's axis.

$$H_{ii} = \sum_{\Delta s=-h_\Lambda/2}^{\Delta s=h_\Lambda/2} \widehat{H}(\Delta s) h_\lambda \tag{A.38}$$

Using the terminology shown in Fig.A.3.1, and some algebraic manipulation, we arrive to the final expression for $\widehat{H}$

$$\widehat{H}_(\Delta s) = \frac{R}{4\pi} \int_0^{2\pi} \frac{R(1 - cos(\theta))}{[\Delta s^2 + (2R sin\frac{\theta}{2})^2]^{3/2}} d\theta \tag{A.39}$$

A.3.3 Evaluation of the singularity when $\Delta s = 0$

Both expressions for the single and double layer potentials exhibit a singularity when $\Delta s = 0$, i.e., the functions $\widehat{G}$ and $\widehat{H}$ must be integrated over the poles. According to the terminology of Fig. A.3.1, we subtract a square from the cross-section containing the singularity :

$$\widehat{G}(0) = h_\lambda R \int_0^{2\pi} G d\theta = h_\lambda R \int_{\varphi/2}^{2\pi-\varphi/2} G d\theta + h_\lambda R \int_{-\varphi/2}^{\varphi/2} G d\theta \tag{A.40}$$

and

$$\widehat{H}(0) = h_\lambda R \int_0^{2\pi} \boldsymbol{\nabla}_n G d\theta = h_\lambda R \int_{\varphi/2}^{2\pi-\varphi/2} \boldsymbol{\nabla}_n G d\theta + h_\lambda R \int_{-\varphi/2}^{\varphi/2} \boldsymbol{\nabla}_n G d\theta \tag{A.41}$$

where the subtracted angle φ can be calculated

$$\varphi = 2sin^{-1}\left(\frac{h_\lambda}{2R}\right) \tag{A.42}$$

The discretization size for the numerical integration along the axis h_λ is assumed to be very small. For that reasonm we can safely assume the square is a flat surface. That allows to consider the singular integral, i.e., second integral of the right hand side of equation A.41 to be zero.

$$\int_{-\varphi/2}^{\varphi/2} \boldsymbol{\nabla}_n G d\theta = 0 \tag{A.43}$$

with coincides with the estimations found in the literature [2–4]. On the other hand, for the single layer potential, this singularity can be evaluated using a simple change of coordinate system, using a cartesian coordinates centered on the square as illustrated in Fig. A.3.1B.

$$\widehat{G}(0) = h_\lambda R \int_0^{2\pi} \frac{1}{4\pi||\mathbf{x}-\mathbf{x}^*(\theta)||} d\theta \approx h_\lambda R \int_{\varphi/2}^{2\pi-\varphi/2} \frac{1}{4\pi||\mathbf{x}-\mathbf{x}^*(\theta)||} d\theta + \int_{-h_\lambda/2}^{h_\lambda/2}\int_{-h_\lambda/2}^{h_\lambda/2} \frac{1}{4\pi\left(u^2+v^2\right)} dudv \tag{A.44}$$

$$\begin{Bmatrix} u \\ v \end{Bmatrix} = \begin{Bmatrix} \rho\, cos\alpha \\ \rho\, sin\alpha \end{Bmatrix} \tag{A.45}$$

$$\int_{-h_\lambda/2}^{h_\lambda/2}\int_{-h_\lambda/2}^{h_\lambda/2} \frac{1}{4\pi\left(u^2+v^2\right)} dudv = 8\int_0^{\pi/4}\int_0^{r(\alpha)} \frac{1}{4\pi} d\rho d\alpha \tag{A.46}$$

$$r(\alpha) = \frac{h_\lambda}{2\,cos(\alpha)} \tag{A.47}$$

$$\int_{-h_\lambda/2}^{h_\lambda/2}\int_{-h_\lambda/2}^{h_\lambda/2} \frac{1}{4\pi\left(u^2+v^2\right)} dudv = \frac{h_\lambda}{\pi}\int_0^{\pi/4} \frac{d\alpha}{cos\,\alpha} = 0.28 h_\Lambda \tag{A.48}$$

$$\int \frac{1}{cos\,\alpha} d\alpha = ln\left(\frac{sin\frac{\alpha}{2}+cos\frac{\alpha}{2}}{sin\frac{\alpha}{2}-cos\frac{\alpha}{2}}\right) + constant \tag{A.49}$$

A.4 Treatment of the bifurcations

In Section 4.2.6, we have ensured the approximation of the cylinders' potentials remain accurate even for the self-influence coefficients which are challenging to approximate. This entails taking into account the volume occupied by the vessels, which poses challenges when several vessels intersect, such as in bifurcations. In Fig. A.3, we show an illustration of a bifurcation reconstructed using a graph of the network. For simplicity, we assume the diameters of the vessels remain constant, although including variability does not change the rationel for the accomodation of the bifurcations. Without special treatment, the bifurcation geometry overestimates the surface area of the contact between cylinders and parenchyma. For that reason, in bifurcations we follow a strategy similar to Berg [5]. As illustrated in Fig. A.3, the cylinder of the smallest vessel out of the three is uncoupled from the parenchyma. That is, $K_{eff,j} = 0$ for the smallest cylinder out of the three intersecting. This method allows us to

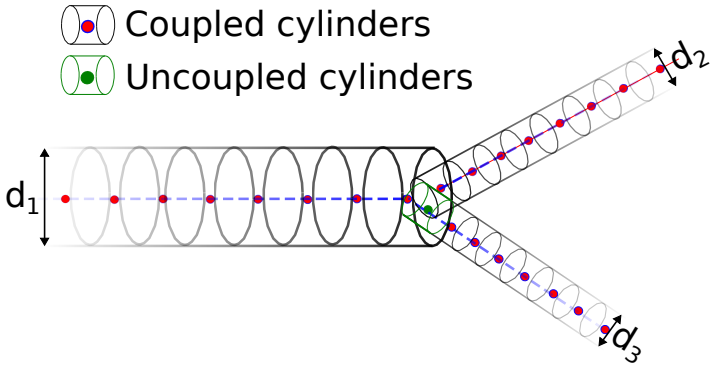

FIGURE A.3 –

approach the real value of the intersection between the three cylinders without systematically overestimating the contact surface as other 1DIV-3DEV methods do [6–9], which introduces important errors [10].

A.5 Example of the fine-grid finite element mesh used for validation

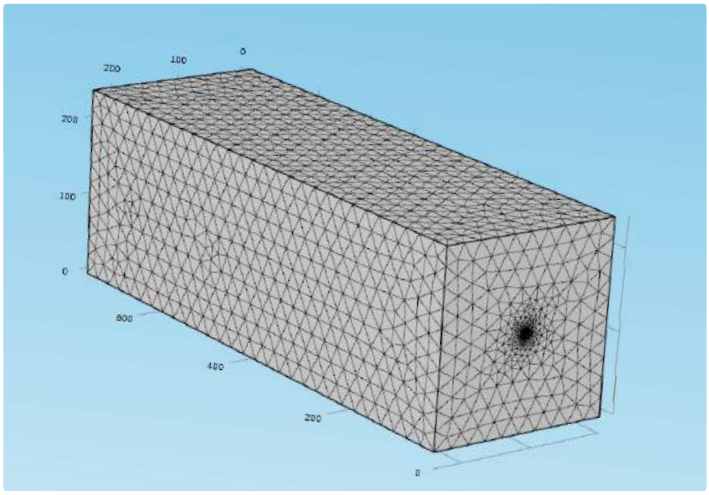

FIGURE A.4 – **Fine-grid used for the FE validation with over $4 \cdot 10^5$ elements**

A.6 References

[1] Maxime Berg, Yohan Davit, Michel Quintard, and Sylvie Lorthois. Modelling solute transport in the brain microcirculation : is it really well mixed inside the blood vessels ? *Journal of Fluid Mechanics*, 884 :A39, February 2020. I

[2] Costas Pozrikidis and Joel H. Ferziger. Introduction to Theoretical and Computational Fluid Dynamics. *Physics Today*, 50(9) :72–74, September 1997. VIII

[3] D. Pepper, A. Kassab, and E. Divo. *Introduction to Finite Element, Boundary Element, and Meshless Methods : With Applications to Heat Transfer and Fluid Flow.* ASME Press, 2014.

[4] M. H. Aliabadi and P. H. Wen. *Boundary element methods in engineering and sciences.* Number 4 in Computational and experimental methods in structures. Imperial College Press, London, 2011. VIII

[5] maxime Berg. Modélisation de l'écoulement sanguin et du transport de molécules dans la microcirculation sanguine cérébrale : impact des occlusions capillaires dans la maladie d'Alzheimer. page 160, 2019. VIII

[6] Luca Possenti, Alessandro Cicchetti, Riccardo Rosati, Daniele Cerroni, Maria Laura Costantino, Tiziana Rancati, and Paolo Zunino. A Mesoscale Computational Model for Microvascular Oxygen Transfer. *Annals of Biomedical Engineering*, 49(12) :3356–3373, December 2021. IX

[7] Ingeborg G. Gjerde, Kundan Kumar, and Jan M. Nordbotten. A Singularity Removal Method for Coupled 1D-3D Flow Models. Technical Report arXiv :1812.03055, arXiv, August 2019. arXiv :1812.03055 [cs, math] type : article.

[8] A. A. Linninger, I. G. Gould, T. Marinnan, C.-Y. Hsu, M. Chojecki, and A. Alaraj. Cerebral Microcirculation and Oxygen Tension in the Human Secondary Cortex. *Annals of Biomedical Engineering*, 41(11) :2264–2284, November 2013.

[9] Timothy W. Secomb, Richard Hsu, Eric Y. H. Park, and Mark W. Dewhirst. Green's Function Methods for Analysis of Oxygen Delivery to Tissue by Microvascular Networks. *Annals of Biomedical Engineering*, 32(11) :1519–1529, November 2004. IX

[10] Timo Koch. Projection-based resolved interface 1D-3D mixed-dimension method for embedded tubular network systems. 2022. IX